Developments Towards a Scaled-Up One-Dimensional Directional Dark Matter Detector

Andrew Scarff

Department of Physics & Astronomy
University of Sheffield

A thesis submitted in partial fulfilment for the degree of
Doctor of Philosophy

November 2017

Abstract

There are many forms of evidence that point towards an unknown form of matter, known as dark matter, making up $\sim$85% of the mass in the universe. Many dark matter candidates have been proposed with the Weakly Interacting Massive Particle (WIMP) being among the most favoured. There are many groups around the world actively looking for WIMPs with direct, indirect and collider searches with specific interest here in annual modulation and directional searches.

The DRIFT-IId detector is the world's largest directional dark matter detector and is operational in Boulby Mine in the UK. Members of the directional community have come together to form the CYGNUS collaboration, looking towards larger detectors with better directional sensitivity. This thesis looks towards the future scale up to larger directional detectors, specifically low-pressure gas detectors.

Improvements have been made to a system used to measure the radon emanation of materials, with emanation tests taken of potential components for CYGNUS detectors. Measurements have also been taken with a small scale THGEM TPC in both CF_4 and SF_6 gas. The results from CF_4 showed the high gas gains achievable from the THGEM detector and allowed a direct measurement of the Townsend coefficients of the gas. Gains of up to 8600 ± 150 have been achieved in low pressure SF_6 with a resolution of 19%, both of these figures are the highest achieved to date.

The directional sensitivity of 1D readouts has been tested with initial signals of head-tail shown in a THGEM TPC in SF_6. A head-tail signature is also seen in a simplified 1D DRIFT-IId readout mode. Exclusion limits from both the full and simplified DRIFT readouts have been produced from over 100 days of background data. The result of 0.16 pb from the full analysis is the lowest limit produced by any directional detector. These results show that a one-dimensional readout may be feasible for directional WIMP detection removing the need for many hundreds or thousands of read out channels required for 3D reconstruction.

Acknowledgements

Firstly I would like to acknowledge my supervisor Neil Spooner for giving me the opportunity to undertake this PhD and for his help and guidance throughout the process. I would also like to thank the rest of the Sheffield DRIFT team including Dan Walker, Leonid Yuriev, Steve Sadler and Warren Lynch with special thanks being owed to Anthony Ezeribe and Fred Mouton for all of their help in many forms throughout my time working on DRIFT.

I would like to say acknowledge the Boulby team for hosting me so many times and doing their best to help in any way they could; it was very much appreciated especially Sean Paling, for all the help he has provided and all the conversations over countless meals in Whitby. An extra thanks is required for Chris Toth from Boulby for going above and beyond to keep DRIFT running and for an incredibly entertaining and productive Google chat!

I would also like to thank the wider DRIFT collaboration with special thanks going to Dan Snowden-Ifft and Jean-Luc Gavreaux at Oxy for many conversations about all things DRIFT ops. I spent 2 weeks working at the University of New Mexico and would like to thank everyone there especially Dinesh Loomba and Nguyen Phan who welcomed me with open arms and helped me to really enjoy my time there, as well as teaching me about all things THGEM. I would also like to thank the DM-Ice, COSINE and CYGNUS collaborations for their help with associated work; I enjoyed my time working with everyone.

I would like to thank the whole Sheffield Physics Dept. for providing the funding for this PhD and the HEP group for all the help and guidance they have provided, especially John Mac for teaching me countless things about radiation among a great deal of other things. I would also like to thank the HEP computing team for all their help, especially Matt Robinson for helping with many analysis, cluster and DAQ issues. I also need to acknowledge everyone in my year of HEP: Anthony, Karl, Calum, Matt, Dave & Mike for all the help provided and good times along the way.

I want to thank all of my friends from elsewhere within physics and in the wider world for supporting me through this; one special thanks needs to go to Amy Moores for helping me get to grips with MATLAB. I would also like to thank my parents and all the members of my family for their support and for not asking ‘Have you found it yet?’ too many times.

Finally a very special thanks must go to Joanna for putting up with me and being amazing throughout the whole time we’ve been together!

Author's Contributions

Chapter 2. The author wrote the analysis code for the background and light yield estimations for the SICCAS crystal as part of the DM-Ice collaboration. This provided the first results from crystals grown by SICCAS and will provide a benchmark for future crystals from the group.

Chapter 4. The modifications to allow DRIFT to run in a fully flowing, fiducialised mode were performed by the author in collaboration with Daniel Walker. The cooling system was designed in collaboration with Jean-Luc Gavreaux and was then constructed and tested by the author and the gas samples were collected and analysed by the author providing a first measurement of the contamination of the collected CS_2.

Chapter 5. All of the improvements to the radon emanation system and all measurements were made by the author with assistance from undergraduate project students. The tests of the internal RAD7 components were made in collaboration with Steve Sadler at Durridge UK.

Chapter 6. The author constructed the THGEM TPC and optimised both the charge and optical readouts. The measurements of the Townsend coefficients in CF_4 is a first with a THGEM-based TPC and were taken by the author. The optical results, calibration and analysis were performed by the author.

Chapter 7. The construction of the back-to-back THGEM TPCs was by the author. The measurements of the THGEM operation in SF_6 were performed by the author and the gain measurements are the highest of any low-pressure gas detector to the author's knowledge. The head-tail analysis from the THGEM is the first known measurement of this signature both in SF_6 and in a one-dimensional detector and all the data taking and analysis was performed by the author. The results from the head-tail measurements are also an important part of work towards a scaled up detector, with the tests of the large-area THGEM at Boulby being another part of this. The author helped to install and perform tests on the large-area THGEM at Boulby.

Chapter 8. The analysis of the simplified DRIFT readout was performed by the author building upon previous work by Anthony Ezeribe. The head-tail measurement in a single channel readout is a first with MWPCs and was performed by the author. The analysis of the shielded data and neutron calibrations and production of the WIMP limits in both the simplified and normal DRIFT modes was the author's work.

Other Contributions. The author led the UK side of DRIFT-IId operations from January 2014 with over 80 days spent working underground at Boulby. The author has also presented 4 conference talks on behalf of the DRIFT collaboration as well as 4 other talks on the other work contained in this thesis such as the radon emanation system and the THGEM TPC. The author has also contributed to weekly conference calls with the DRIFT, DM-Ice, COSINE and CYGNUS collaborations and is a co-author on 8 papers with the DRIFT & DM-Ice collaborations. The author also taught in a variety undergraduate courses for 3.5 years as part of the PhD scholarship from the University of Sheffield physics department.

Table of contents

List of figures **xi**

List of tables **xix**

1 Introduction to Dark Matter **1**

1.1 Evidence for Dark Matter 1

1.2 DM Candidates 9

1.2.1 WIMPs 10

1.2.2 Axions 12

1.2.3 Sterile Neutrinos 12

1.3 Direct Detection of Dark Matter 13

1.3.1 Direct Detection Theory 14

1.3.2 Direct Detection Experiments 20

1.4 Alternative Methods of Dark Matter Detection 27

1.5 Conclusions 28

2 Galactic Signals of Dark Matter **29**

2.1 Annual Modulation 29

2.1.1 DAMA/LIBRA 30

2.1.2 DM-Ice 32

2.1.3 Other Annual Modulation Experiments 33

2.1.4 Low-Background Crystal R&D 35

2.2 Directional Detection 44

2.2.1 Directional detectors 49

2.2.2 The CYGNUS Collaboration 52

2.3 Conclusions 53

3 DRIFT-IId Detector **56**

3.1 The Detector 56

3.2 Boulby Underground Laboratory 59
3.3 Background-Free Operation 60
3.3.1 Texturised Thin-Film Cathode 61
3.3.2 Z-fiducialisation 62
3.4 Recent Results from DRIFT-IId 64
3.4.1 Direction Sensitivity 64
3.4.2 Efficiency Improvement 68
3.4.3 Measurements of Neutrons from Boulby Rock 68
3.4.4 Latest WIMP Limit 71
3.5 Conclusions 72

4 Operations and Modifications of the DRIFT-IId Detector 73
4.1 Detector Operations 73
4.2 Modification of Gas System for O_2 74
4.2.1 Mass Flow Controllers 74
4.2.2 Flashback Arrestors 75
4.2.3 Nitrogen 76
4.3 CS_2 Cooling 76
4.4 Residual Gas Analyser Tests Towards CS_2 Recirculation 79
4.5 Conclusions 81

5 Radon Emanation Measurements 82
5.1 Radon in Low Background Experiments 82
5.2 Radon Emanation System 83
5.3 Emanation System Improvements 86
5.3.1 Activated Charcoal Filter 86
5.3.2 Multiple Detectors 87
5.3.3 Component Swaps on Emanation Chamber 87
5.3.4 Desiccant 88
5.3.5 Final Post-Improvements System 88
5.4 Emanation Measurements 89
5.4.1 Samples for Low Background Experiments 90
5.4.2 Emanation Measurements of RAD7 Components 90
5.5 Conclusions 96

6 Operation of THGEM Detectors in CF_4 Gas with Charge and Optical Readouts 97
6.1 Introduction to THGEM Detectors 97

6.2 Operation of a THGEM TPC in Low Pressure CF_4 99
6.2.1 Description of THGEM TPC 99
6.2.2 Gain Calibration 102
6.2.3 Calculation of Rose-Korff Coefficients 105
6.3 A CCD-Based Optical Readout with a THGEM TPC 107
6.3.1 Detection of Alpha Tracks 108
6.3.2 Optical Energy Calibration 111
6.4 Optical Observation of Nuclear Recoils 116
6.5 Conclusions 116

7 Head-Tail Measurements from a THGEM Detector in SF_6 118
7.1 Operation in SF_6 118
7.1.1 SF_6 Gas 118
7.1.2 Detector Setup & Data Acquisition 119
7.1.3 Gain Calculation & Calibration 121
7.2 Head-Tail Measurements with Single Plane THGEM Readout 125
7.3 Testing a Large Area THGEM 129
7.4 Conclusions 131

8 Directionality and WIMP Limit with a Simplified DRIFT-IId Readout 133
8.1 The Simplified Readout Mode 133
8.2 Head-Tail Sensitivity with the Simplified Readout 135
8.3 Calculation of a WIMP Limit 140
8.3.1 Efficiency Map 140
8.3.2 Calculation of a WIMP Limit 144
8.4 Conclusions 147

9 Conclusions 148

References 151

Appendix A DRIFT Data used for Analysis 164

List of figures

1.1 Rotation curve of objects in the Andromeda galaxy, M31. Image from Rubin and Ford [7]. 3

1.2 Observations made of the Bullet Cluster, with an image from Chandra of the x-ray emission with overlaid contours of mass inferred from weak lensing. Image from Clowe et al. [11]. 4

1.3 Observations made of the Abell-2744 cluster, with x-ray emission shown in red and results from weak lensing shown in blue. Both are overlaid on the optical results [15]. Credit: NASA/CXC/SAO. 4

1.4 A diagram showing the 2D analogues to the curvature of the universe for differing values of Ω. Credit: NASA / WMAP Science Team 5

1.5 A plot of the CMB power spectrum (left) and an image of the CMB. Both images are from the Planck collaboration [6]. 6

1.6 This plot shows the predicted abundances from BBN along with the observed abundance measurements (yellow boxes) as well as other measurements of the baryon density. Image from the Particle Data Group [21]. 8

1.7 Comparison of the results from the Millennium simulation (red) with astrophysical observations from SDSS, CfA2 and 2dFGRS (all blue). Image from Frenk and White [23]. 9

1.8 Simplified diagrams of example 3rd generation squark production and decay methods, resulting in an LSP. Diagrams from the ATLAS collaboration [30]. 11

1.9 Plot of current axion bounds from both experiments and astrophysical sources, with the expected band from theory also shown. Plot from Daw [41]. 13

1.10 These diagrams show the interactions for the three main methods of dark matter detection. These are, from left to right, direct detection, indirect detection and collider production. 14

1.11 Plot of form factor against qr_N [46]. The dotted line shows an approximation of $\exp[-(qr_N)^{2/3}/3]$. The dashed line shows the form factor using the first Bessel function, the solid line shows the described approximate fit to this using Equation 1.28. The white circles are the result of a single-particle model for ^{131}Xe and the asterisks are a single-particle model for Nb. 18

1.12 Plot of form factor against recoil energy for several spin-dependant targets used in direct dark matter searches. 18

1.13 The operation principle of the dual-phase Xe detectors is shown [48] with the initial interaction in the bulk liquid giving prompt scintillation light (S1) and the secondary scintillation (S2) coming from the ionised electrons avalanching when they reach the upper gas volume. 22

1.14 A schematic of the DEAP-3600 detector is shown with the active LAr held in the spherical acrylic vessel and instrumented on all sides with PMTs connected to light guides [59]. 23

1.15 The latest spin-independent WIMP cross-section limits are shown from the liquid noble detectors, with the lowest limit at time of writing coming from the LUX collaboration. The grey shaded area is the preferred parameter space of the SUSY CMSSM (constrained minimal supersymmetric model). Figure from Akerib et al. [52]. 24

1.16 The projected WIMP limits from the SuperCDMS SNOLAB detectors are shown for both the iZIP detectors and the HV mode along with recent limits from other collaborations. Plot from Calkins [64]. The limit from the Si detectors are shown in blue with the Ge limits in red. 25

1.17 This plot shows the latest limit from the PICO-60 detector (blue) along with previous direct detection results from PICO-60 (red), PICO-2L (purple), Panda-X (cyan), SIMPLE (orange) and PICASSO (green). Also plotted are indirect limits set by IceCube (pink) and SuperK (black) with the purple shaded region showing the favoured parameter space for the CMSSM SUSY model. Plot and limits from Ref. [71] and references therein. 26

2.1 Diagram of the change in modulation amplitude with recoil energy. Figure from Freese et al. [92]. 30

2.2 Diagram of the earth travelling around the Sun over a year, causing a rise in WIMP interactions. Image credit: Sheffield Dark Matter Research 31

2.3 Plot of the modulation signal seen across the DAMA/NaI and DAMA/LIBRA searches. Plot from Bernabei et al. [95]. 31

2.4 Diagram and photographs of a single 8.5 kg detector from DM-Ice17 before being deployed in the South Pole ice. Diagram from Cherwinka et al. [102]. 33

2.5 Plot of the latest exclusion limits from the DM-Ice17 detectors running at the South Pole, together with the DAMA preferred regions and predicted future sensitivity. Figure from Barbosa de Souza et al. [105]. 34
2.6 Plot of the latest results from the KIMS CsI(Tl) detectors from Lee et al. [106]. It can be seen that KIMS is cutting into the DAMA allowed region. 35
2.7 A Photograph SICCAS crystal on the left and the AS1 crystal from DM-Ice37 on the right. 36
2.8 Image of the SICCAS crystal inside a NAIAD box, inside the lead castle with the optically coupled Hamamatsu PMTs on either side. 37
2.9 A plot of alpha events against time from the KIMS study from Adhikari et al. [114]. The red line and associated 68% error band (green) show a fit to a model assuming a single instantaneous contamination event. The best fit line shows a match between the start date of the increase and the date of crystal growth. 37
2.10 A plot of average waveforms from muon, gamma and alpha events from Cherwinka et al. [103]. The difference between pulse shape of alphas provides the basis of the calculation of the τ parameter. 38
2.11 Plot of integral vs pulse height for PMT-A (left) and PMT-B (right). 38
2.12 Plot of integral vs pulse height for PMT-B showing the chosen alpha events. . . . 39
2.13 Plots of τ (tau) vs integral for PMT-A and PMT-B at both high and low gains. . . . 40
2.14 Plots of τ vs integral for PMT-A and PMT-B at high gain, showing the chosen alpha events. 40
2.15 Spectra of alpha events for PMT-A and PMT-B at high gain. 41
2.16 Calibration spectra for PMT-A. 42
2.17 Calibration spectra for PMT-B. 43
2.18 Diagram of the movement of an earth-based detector compared to the WIMP-wind due to the Earth's rotation. Image credit: Sheffield Dark Matter Research. 44
2.19 Plot of the expected WIMP signal in the galactic frame, with the incoming direction of WIMPs on the left and the reconstructed nuclear recoil direction on the right. Plot from Mayet et al. [91]. 45
2.20 An example plot of the WIMP mass against cross-section parameter space showing the neutrino floor (orange dashed line) along with current and future spin-independant limits set by direct dark matter searches from Cushman et al. [119]. Detectors with a sensitivities high enough to probe below this line are expected to start seeing coherent neutrino scatters. 46

2.21 Plot of the expected WIMP and solar neutrino signals in the lab frame from Mayet et al. [91]. In this plot the WIMP signal is on the left of the neutrinos in the upper row of images, corresponding to February 26, and on the right in the lower row, corresponding to September 6 2015. The plots from left to right represent different energy bins with 0-1.6667 keV on the left, 1.6667-3.3333 keV in the centre and 3.3333-5 keV on the right. 47
2.22 The left plot shows how the discovery limit of a 6 GeV WIMP changes with increasing detector mass, and therefore increasing numbers of ^{8}B neutrino interactions for different levels of directional sensitivity. The right plot shows the limits set in the WIMP mass vs cross-section parameter space for changing levels of directional sensitivity and the inclusion of head-tail sense recognition. Plots from Mayet et al. [91]. 48
2.23 Diagram of the m^3 DMTPC detector. Figure from Leyton [132]. 50
2.24 Diagram of the NEWAGE 0.3b' detector from Nakamura et al. [134]. 51
2.25 A 'sky-map' plot from NEWAGE, showing the incoming particle directions in alt-az co-ordinates (red), also shown is the position of Cygnus through the run (blue). Plot from Nakamura et al. [134]. 51
2.26 Diagram of the MIMAC detector from Santos et al. [136]. 52
2.27 Diagram of the CYGNUS test vessel to be built and run in Kamioka from Miuchi [141]. 53

3.1 Diagram of the DRIFT detector, showing positions of cathode and MWPCs with dimensions in mm. Diagram from S. Burgos et al. [149]. 58
3.2 A diagram of the guard and veto wires on one side of the anode plane (a) and the veto wires on one side of the inner grid plane (b). 59
3.3 Photograph of the DRIFT-IId detector outside the vacuum vessel in Boulby Underground Laboratory. 60
3.4 A diagram of the ^{222}Rn decay chain which is the basis for the RPR backgrounds in the DRIFT-IId detector. Figure from [151]. 61
3.5 Image of the 0.9 μm aluminised-mylar thin-film central cathode. In this image the cathode is shown in place in the DRIFT-IId field cage. 62
3.6 Diagram of the effect from bead blasting the thin-film central cathode From Battat et al. [146]. The maximum contained length of an alpha particle from an RPR event is shown. This length is shorter than the length of an alpha track so the alpha particle enters the gas volume. 62
3.7 Plot of the minority peaks appearing in a dataset from DRIFT-IId from Snowden-Ifft [148]. 63

3.8 A figure showing the background free fiducial volume from a 45.4 day shielded run with the DRIFT-IId detector in the z vs NIPs (Number of Ion Pairs) plane from Battat et al. [127]. The fiducial volume is enclosed in the tan box with the RPR population seen around the cathode. 64
3.9 An example event showing the method for calculating the head-tail parameters. Plot from Battat et al. [123]. 65
3.10 The positions of the neutron source for each of the runs are shown, with the ±z runs being the optimal direction and the –x and –y directions being the anti-optimal directions used for an expected null result. Plot from Battat et al. [123]. 67
3.11 Results from the head tail analysis, with the results from the ±z runs in blue, the –x & –y runs in red and the results from Ref. [122] in black. Plot from Battat et al. [123]. 67
3.12 Efficiency maps of the DRIFT detector from a 30 mV threshold (a) and a 15 mV threshold (b) are shown. Plots from Battat et al. in Refs [145] and [127] respectively. 69
3.13 Plot of z vs NIPs for the 45.4 days of unshielded data. There are 14 events seen passing all cuts inside the fiducial volume. Plot from Battat et al. [127]. 69
3.14 Results from a comparison of gamma spectra from GEANT4 from Battat et al. [127]. The spectra from rock gammas is shown in blue with that of ^{60}Co shown in red. . . 70
3.15 The latest SD WIMP exclusion limit from the DRIFT detector is shown, along with previous limits from the DRIFT collaboration and other notable results from other groups. The plot is taken from Battat et al. [127]. 71

4.1 Diagram of the gas mixing system used with the DRIFT-IId detector. Positions of flashback arrestors are shown in blue. Figure modified from Ref. [159]. 75
4.2 Diagram of the water trap used to capture CS_2. Image credit: Chris Toth 76
4.3 Image of the cooling system components with the Peltier with heatsink in (a) and the copper plate with copper tubes in (b). 78
4.4 Plot of the temperature drop of the insulated cooling system after power was applied to the Peltier cooler. 79
4.5 Plot of the proportion of CS_2 and water in the sample. The level of CS_2 is shown in blue with the level of water shown in red. 80

5.1 An image of the Durridge RAD7 detector is shown in (a) with a diagram of the internal dome and detector shown in (b). Image (b) from Durridge [173]. 83
5.2 The small, 3.5 litre, and the large, 35 litre, emanation chambers are shown in (a) and (b) respectively. 84
5.3 Diagram of the emanation system described above. Figure from Sadler [166]. . . . 85
5.4 Diagram of the emanation system including all described improvements. 89

5.5 Plot of the radon emanation from the pump setup over the 7 day test. 94

6.1 (a) A magnified image of a GEM foil. (b) A diagram of the electric fields through a GEM. Image and diagram from CERN's Gaseous Detector Development Group [186]. 98
6.2 Image of a THGEM detector and the rims around the holes from Shalem et al. [182]. 99
6.3 A diagram of the dimensions of the CERN THGEMs used in this work. 100
6.4 A photograph of the THGEM used in this work. 101
6.5 Setup of THGEM TPC inside the 10 litre vacuum vessel. Also shown are the ^{241}Am and ^{55}Fe sources used for calibration. 101
6.6 A diagram of the electronics setup used with the THGEM TPC. 102
6.7 An example energy spectrum from the 5.89 keV ^{55}Fe x-rays is shown (green) along with a background measurement for comparison (blue). These data were taken in 30 minute runs with 100 Torr CF_4. The voltage across the THGEM was 750 V with a drift field of 300 V/cm. 103
6.8 Plot of the gain against ADC of the MCA from the calibration with a test pulses. . 104
6.9 Plot of THGEM gain against voltage across the THGEM for different pressures of CF_4 gas. 105
6.10 Plot of the ln(ln(gain)) against the reciprocal of the amplification field inside the THGEM holes for different pressures of CF_4 gas. 106
6.11 Setup of THGEM TPC inside the vessel with CCD camera positioned above the quartz window. 108
6.12 A photograph of the CCD camera positioned above the quartz window. 109
6.13 Example alpha track. 109
6.14 Example profile across an alpha track. 110
6.15 Plot of track width against drift distance with errors included. Best fit line shown in red. 111
6.16 Example ^{55}Fe events in 100 Torr CF_4 112
6.17 Plots from TRIM of alpha particles in 100 Torr CF_4. (a) shows the distance travelled by the particles and (b) shows the energy deposited along the track. 113
6.18 Histogram of the sum of recoil energy deposited after the maximum of the Bragg peak. Energies calculated from TRIM. 113
6.19 An example alpha event with the results of the track finding algorithm. The maximum points from the Gaussian fit are shown (red) along with the linear fit made to these points to reconstruct the track direction (white). 115
6.20 An example multiple-event image with the results of the track finding algorithm. It is seen that the extra track confuses the algorithm. 115
6.21 Example nuclear recoil events from a ^{252}Cf run in 100 Torr CF_4. 116

7.1 An averaged waveform from Phan et al. [194] showing the SF_5 peak at about 2150 μs, along with the main SF_6 peak ($\sim$2350 μs). 119
7.2 A diagram of the experimental setup used in this work; the major difference from the setup shown in Chapter 6 is the addition of the lower THGEM electrode. . . . 120
7.3 A photograph of the experimental setup used in this work showing the upper and lower THGEM electrodes in place either side of the cathode. 120
7.4 A diagram of the electronics and power supplies used with the upper THGEM. An identical setup is used for the lower THGEM. 121
7.5 A plot of an example raw waveform (red) along with the baseline corrected waveform (blue). It can be seen that the restoration accurately brings the baseline to 0 V. . . 122
7.6 A spectrum of the integral charge from a 300 mV pulse in the preamp test input. . 123
7.7 ^{55}Fe spectra in pressures of 20 - 50 Torr of SF_6. 124
7.8 Diagram of the ^{252}Cf source locations for the directed neutron exposures. 126
7.9 An example event from the +z run showing the areas used for η_1 (red) and η_2 (green). This calculation is the main basis of the head-tail analysis looking in the difference in charge in the start and end of the tracks. 127
7.10 A diagram of a THGEM plane with a 0.5 cm veto around the edge. This would be a vital part of background rejection in one-dimensional THGEM readouts. 129
7.11 A photograph of the 50 x 50 cm THGEM at Boulby (a) and a diagram of the THGEM TPC setup inside the vessel, showing the 1 cm drift gap between THGEM and cathode and the placement of the ^{241}Am alpha source. 130
7.12 An example alpha spectrum from the latest runs with the large area THGEM. The spectrum was taken in 50 Torr CF_4 with 700 V across the THGEM [197] and recorded on an Ortec 926 ADCAM MCB. 131

8.1 An example event from the DRIFT-IId detector. The labels represent the left/right anode channels (LA/RA), left/right grid channels (LG/RG) and the left/right anode and grid veto channels(LVA/RVA/LVG/RVG). The other channels shown are known as the 'sum lines'. These lines are the sum of all the respective channels, for example the left anode sum (LAS) is the sum of all left anode channels (LA1 to LA8) . . . 134
8.2 The waveform of the event that passed the cuts to appear in the fiducial volume. It can be seen that there was a hit on the LVA veto line that indicates a background event.138
8.3 The neutron events passing all the cuts from the full DRIFT analysis are shown in z vs. NIPs parameter space. 141
8.4 The neutron events passing all the cuts from the simplified DRIFT analysis are shown in z vs. NIPs parameter space. 141

8.5 A map of efficiency showing how the neutron detection efficiency changes for the full DRIFT analysis with varying position in the detector and deposited energy. . . 142
8.6 A map of efficiency showing how the neutron detection efficiency changes for the simplified DRIFT analysis with varying position in the detector and deposited energy. 143
8.7 A plot of efficiency against NIPs for both analyses, with the full analysis shown in blue and the simplified analysis shown in red. 143
8.8 A plot of z against NIPs showing that no events in the fiducial volume passed the cuts from the full DRIFT analysis. The fiducial volume is shown by the black box. 144
8.9 A plot of z against NIPs showing no thatevents in the fiducial volume passed the cuts in the simplified DRIFT analysis. The fiducial volume is shown by the black box. 145
8.10 The exclusion limits set on the spin dependant WIMP-proton cross section as a function of WIMP mass. Here both the full analysis (blue) and the simplified analysis (red) are shown. 146

List of tables

2.1 Contamination results for SICCAS crystal from number of alpha events. . . 41
2.2 Light yield estimates for SICCAS crystal and AS1/2 crystals from DM-Ice37. 43
2.3 A table comparing the main four directional dark matter detectors. Table modified from Battat et al. [116] with information from references within. . 55

3.1 Results of ^{238}U (ppb) & ^{232}Th contamination from measurements in Boulby. Table reproduced from Battat et al. [127]. 70

4.1 Values for the constants of the Antoine equation for CS_2 [163, 164]. 77
4.2 Comparisons of temperatures and corresponding vapour pressures of CS_2. . 78
4.3 Drop in vapour pressure from use of Peltier cooler. 79

5.1 Results from tests using the activated charcoal filter. 87
5.2 Comparison between background results from old and new emanation systems. 89
5.3 Emanation results from G10 sample tests. 91
5.4 Results from all material emanation tests made with improved system. . . . 91
5.5 Results from the emanation tests of the pods. 92
5.6 Results from the emanation tests of the pod gaskets. 92
5.7 Results from the emanation tests of the dome gaskets. 93
5.8 Results from the emanation tests of the internal pumps. 94
5.9 Total contribution of radon emanation from the internal RAD7 components. This should be compared to the RAD7 background of $<$ 0.01 atoms/min given by Durridge. 95
5.10 Results for comparing the background levels before and after the dome gasket swap of the RAD7. 96

6.1 Calibration numbers 104
6.2 Values for the gas constants for different pressures of CF_4. 107

7.1 Gain measurements for different pressures of SF_6. 123

7.2 Results of the head-tail measurements from the THGEM detector in 30 Torr SF_6. 128

8.1 Live time of the directed neutron runs. 136
8.2 Results of the head-tail measurements from the simplified DRIFT-IId readout. 139

A.1 Datasets corresponding to the directed neutron runs. 164
A.2 Datasets corresponding to the shielded background runs. 165
A.3 Datasets corresponding to the neutron calibration runs. 166

Chapter 1

Introduction to Dark Matter

This chapter will provide an overview of dark matter. The evidence for dark matter will be discussed before looking at possible candidates for what the dark matter is composed of. Finally a review will be made of the methods for detecting dark matter, with an emphasis on the direct detection of dark matter, which is one of the main motivations for the work presented in this thesis.

1.1 Evidence for Dark Matter

Coma Cluster

The first signs that the universe was not made purely of the matter we see around us came in 1933. Fritz Zwicky [1, 2] was looking at the motion of galaxies in the Coma cluster and saw something unexpected when he compared two different methods to calculate the mass of the cluster. He used the luminosity of the galaxies, and using the mass-luminosity relation he could calculate the mass of the cluster and found it to be $2.55\times 10^{11} M_\odot$ [3].

The second method he used was the Virial Theorem. This gives the relation

$$E_{KE} = -\frac{1}{2} E_{GPE}, \tag{1.1}$$

where E_{KE} is the total kinetic energy and E_{GPE} is the gravitational potential energy of the system, both averaged over time. Substituting values for E_{KE} and E_{GPE} here, assuming that there is a uniform spherically symmetric distribution of galaxies gives an expression for the mass as

$$M = \frac{5r\langle v^2 \rangle}{3G}, \tag{1.2}$$

where M is the mass of the cluster, r is the radius, $\langle v^2 \rangle$ is the average squared velocity of the galaxies in the cluster and G is the gravitational constant. Using this method Zwicky obtained a cluster mass of 4.5 $\times 10^{13} M_{\odot}$, a value more than two orders of magnitude higher than that from the luminosity. From this discrepancy he suggested that there must be some 'dunkle Materie' (dark matter) in the cluster making up the majority of the mass. Since Zwicky's original measurements more accurate measurements have been made of both the mass of the baryonic matter in the cluster (1.6 $\times 10^{14} M_{\odot}$ [4]) and the mass from the virial method (1.9 $\times 10^{15} M_{\odot}$ [4]). From these more recent values it can be seen that although the difference in the mass estimates is now smaller than Zwicky's, there is still an order of magnitude difference pointing towards some unseen mass.

Zwicky's work is now widely regarded as the first real evidence for dark matter being the dominant form of mass in the universe, but this work was largely ignored until more evidence was published in 1970. In the editorial note to the reprint of Zwicky's paper [5], Ehlers explains that much of the physics in the paper was not well known at the time, and has since been shown to be wrong. The physicists at the time, including Zwicky, knew that some of this physics was not completely correct so may have thought that the evidence of extra mass would disappear once the other physics was better understood. One example of such an inaccuracy is the value of the Hubble constant. Zwicky used 558 km s^{-1} Mpc $^{-1}$ where the latest result from the Planck Collaboration calculates it to be 67.8 ± 0.9 km s^{-1} Mpc $^{-1}$ [6], almost an order of magnitude difference between the two results.

Rotation Curves

In 1970 Vera Rubin and Kent Ford [7] were studying the orbital velocities of different objects in galaxies and found that the rotation curves remained flat out to large radii. If the luminous matter in the galaxy were dominant the rotational velocities are expected to follow Kepler's third law and decrease with increasing distance from the galactic centre as $v_c \propto r^{-\frac{1}{2}}$. This is seen to agree very well with the orbits of the planets in the solar system where the orbital velocity decreases with distance [8]. However, the results from Rubin and Ford, shown in Figure 1.1, instead show that the velocity curves stay flat out to large radii. This flatness of the rotation curve implies that $\rho(r) \propto 1/r^2$. This is inconsistent with the stellar distribution where $\rho(r) \propto e^{r/r_0}$ and so implies that the dominant form of mass must be some unknown matter, and not the luminous mass of the galaxy as expected.

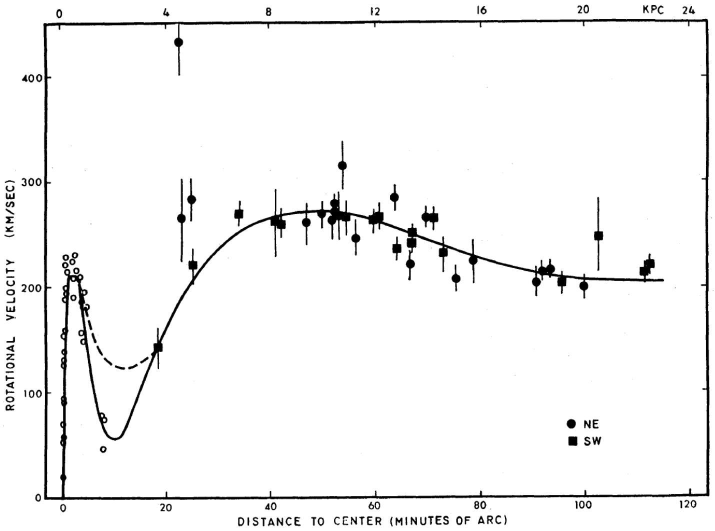

Fig. 1.1 Rotation curve of objects in the Andromeda galaxy, M31. Image from Rubin and Ford [7].

Lensing and Cluster Mergers

More evidence for dark matter being the dominant mass in the universe comes from looking at mergers of galaxy clusters. In 2004 evidence of a merger between the main cluster and a sub-cluster was seen in the Bullet Cluster [9–11]. By comparing the observations of x-ray emission (from baryonic matter) from the Chandra X-ray Observatory with the results of weak lensing after the collision, it can be seen that the position of the baryonic matter does not match up to the contours of where the main component of mass is shown to be. The mass is inferred from weak lensing and this result is shown in Figure 1.2.

This shows that, as the merger occurs, the baryonic matter interacts and slows down but the majority of the mass, from the dark matter, does not interact as much and the two components of the cluster separate. These results have been confirmed by similar findings in other cluster mergers, such as A1758N [12], A2146 [13], A520 [14] and A2744 [15]. The results from A2744 are shown in Figure 1.3. As in the Bullet Cluster, it can be seen that after the merger the mass inferred from lensing, shown in blue, is in a different position from the luminous matter from x-ray observations, shown in red.

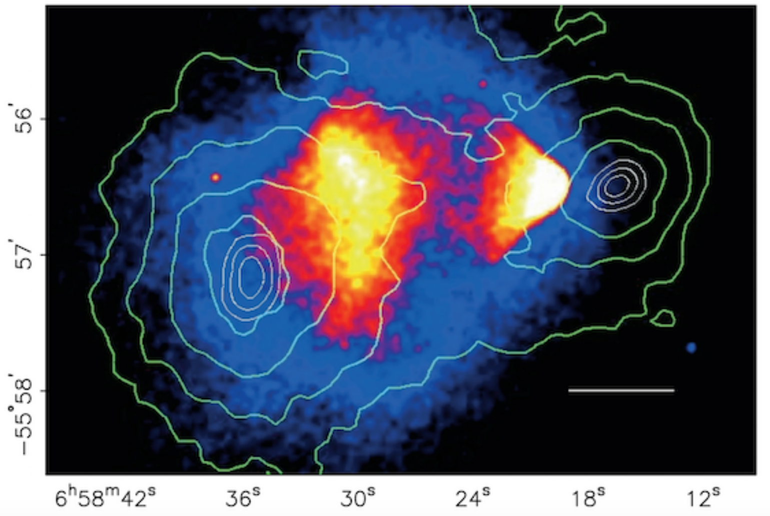

Fig. 1.2 Observations made of the Bullet Cluster, with an image from Chandra of the x-ray emission with overlaid contours of mass inferred from weak lensing. Image from Clowe et al. [11].

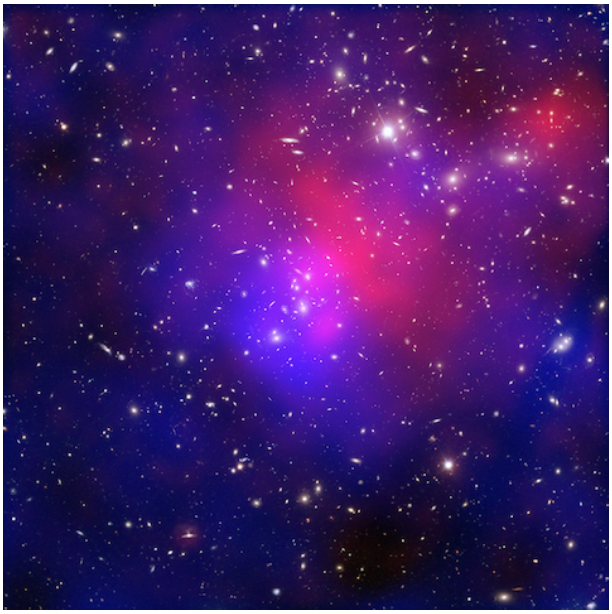

Fig. 1.3 Observations made of the Abell-2744 cluster, with x-ray emission shown in red and results from weak lensing shown in blue. Both are overlaid on the optical results [15]. Credit: NASA/CXC/SAO.

CMB and ΛCDM

The Cosmic Microwave Background (CMB) is a thermal relic coming from the expansion of the universe predicted from the Big Bang theory. 380,000 years after the Big Bang, the universe had expanded and the temperature dropped below 3000 K. This allowed photons to decouple. Since this time, and due to the further expansion of the universe, the photons have been redshifted into the microwave band of the electromagnetic spectrum and the temperature now has been measured at 2.73 K [6]. The CMB was first measured in 1965 by Penzias and Wilson [16] who found it as a background while working with the Holmdel Horn Antenna in New Jersey, USA. At the same time Dicke et al. were actively looking for the CMB and, after hearing of Penzias and Wilson's results, they identified the signal they were seeing as the CMB [17].

The CMB was linked to dark matter in the 1980s when the Cold Dark Matter (CDM) theory was proposed [18]. The favoured model currently is ΛCDM [6], where the Λ represents the presence of dark energy in the model [19]. A key input to the ΛCDM model is the value of the density parameter, $\Omega(t)$, defined by

$$\Omega(t) = \frac{\rho(t)}{\rho_c(t)} \tag{1.3}$$

where $\rho_c(t)$ is the critical density, the density at which the universe is flat, and $\rho(t)$ is the current energy density of the universe. The value of $\Omega(t)$ defines the curvature of the universe, with $\Omega = 1$ giving a flat universe, $\Omega > 1$ giving an open universe and $\Omega < 1$ giving a closed universe; a representation of these possibilities is shown in Figure 1.4. Results from experiments such as Planck [6] show excellent agreement with a flat universe.

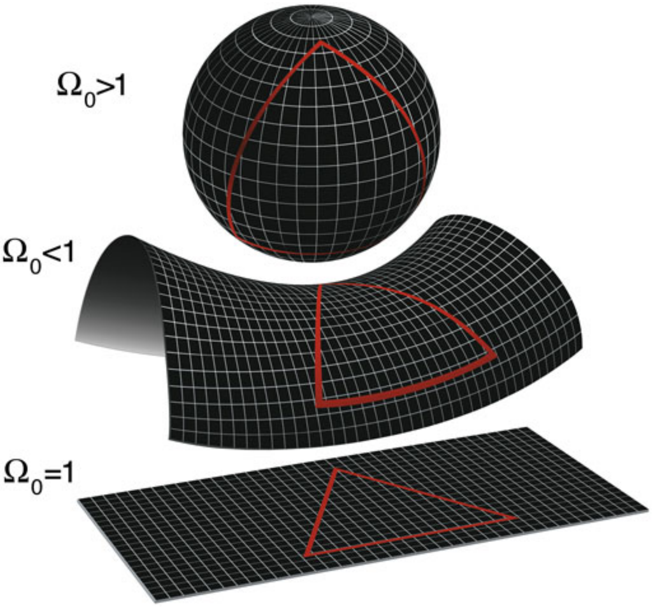

Fig. 1.4 A diagram showing the 2D analogues to the curvature of the universe for differing values of Ω. Credit: NASA / WMAP Science Team

The components dominating the value of Ω for the present day are

$$\Omega = \Omega_\Lambda + \Omega_m, \tag{1.4}$$

where Ω_Λ is the density of dark energy in the universe and Ω_m is the density of matter. Ω_m can also be written in terms of its constituent parts as

$$\Omega_m = \Omega_b + \Omega_{DM}, \tag{1.5}$$

where Ω_b is the matter made of baryonic material and Ω_{DM} is the dark matter component.

The model predicts that there will be fluctuations in the CMB and these will be related to Ω_m at the time of freeze out. These predicted fluctuations were first discovered in 1994 by the Cosmic Background Explorer (COBE) satellite [20]. The latest results of the CMB power spectrum come from the Planck collaboration and are shown in Figure 1.5. The power spectrum is generated from the temperature fluctuations at differing angles across the sky. In Figure 1.5a the x-axis shows the multipole moment, ℓ, this corresponds to the angular separation, with lower ℓ corresponding to larger angles.

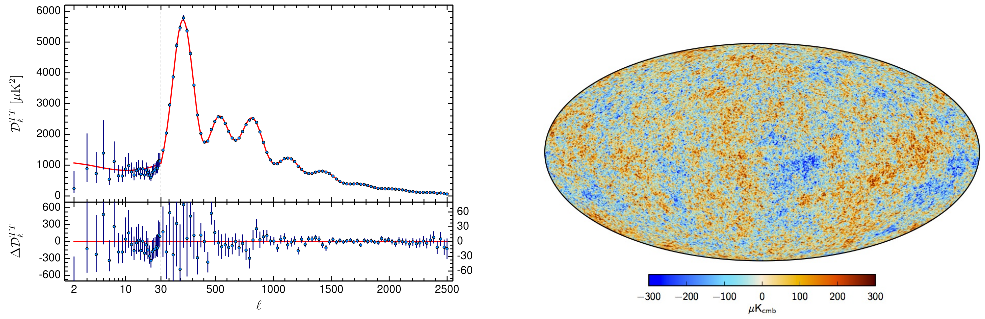

(a)

(b)

Fig. 1.5 A plot of the CMB power spectrum (left) and an image of the CMB. Both images are from the Planck collaboration [6].

The positions and relative heights of the peaks in the CMB power spectrum give information about the density of matter in the universe and the baryon density in the universe. The position of the first peak gives Ω_m and the relative heights of the first two peaks gives the value for Ω_b. From the Planck results Ω_m is measured to be 0.308 ± 0.012 and Ω_b is measured to be 0.0048 ± 0.007 [6].

From these results it can be seen that the matter in the universe only makes up 30.8% of the total energy density and only 4.8% of that is from baryonic matter. That also shows that $\sim$ 85% of the matter in the universe is non-baryonic, implying a large dark matter component. The results from the CMB spectrum are in agreement with the ΛCDM cosmological model, but they are model dependant so using a model other than ΛCDM may give you different values for these parameters [6]. Another independent test can be made to confirm these claims by looking at the abundances of light nuclei in the early universe, as shown below.

Big Bang Nucleosynthesis

Big Bang Nucleosynthesis (BBN) [21] describes the creation of light elements in the first three minutes after the Big Bang. In the first second after the Big Bang, the weak interactions were in thermal equilibrium: this gave a fixed neutron-to-proton ratio. After 1 s, with a corresponding temperature of 1 MeV, the interactions were no longer in equilibrium and there was a freeze out of the n/p ratio at 1/6. From this time the only change in this ratio came from neutron decay via beta emission: by the time nuclear fusion begins at 100 s (T = 0.1 MeV) the n/p ratio has dropped to 1/7. From 100 s from the Big Bang to 180 s the protons and neutrons can interact to form deuterons. The deuteron, along with the remaining free neutrons and protons, can then interact to form the heavier elements: ^{3}H, ^{3}He, ^{4}He and ^{7}Li. After the first three minutes since the Big Bang, the temperature has dropped sufficiently for these nuclear interactions to stop, and the abundances of the early elements become fixed. After this time ^{4}He makes up 25% of the primordial mass due to the stable nature of the isotope. The remaining 75% is composed of free protons and traces of the other light elements.

The rate of interactions and thus the final abundance ratios are dependant on the density of baryons. This is often expressed as the baryon-to-photon ratio, η, where $\eta = n_b/n_\gamma$. The value of n_γ is fixed and can be found from the current temperature of the CMB (T = 2.73 K). From using the relative abundances of the different light elements in the universe it is then possible to calculate a value for η and then a value for Ω_b.

The BBN model, assuming the standard model, has only η as a free parameter; given a fixed n_γ it is then possible to simulate the abundances of the different elements for changing η. These simulations are compared to astronomical measurements in Figure 1.6. The plot shows the simulated lines from D, ^{3}He, ^{4}He and ^{7}Li in blue, red, pink and green respectively. These are plotted along with the allowed regions from observations seen in the yellow bands, which correspond to a 2σ confidence level. A limit is shown for the BBN results in the pink striped band and this is compared to the corresponding value for Ω_b from the CMB measurements. Both the BBN and CMB bands are at a 95% confidence level.

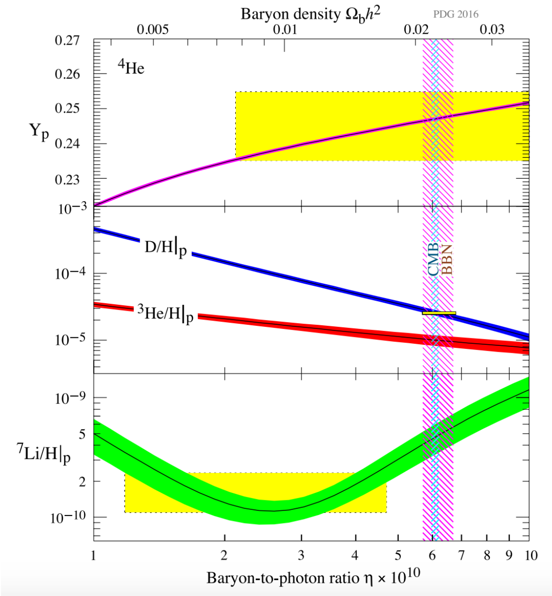

Fig. 1.6 This plot shows the predicted abundances from BBN along with the observed abundance measurements (yellow boxes) as well as other measurements of the baryon density. Image from the Particle Data Group [21].

It is seen that there is a very good agreement between the abundance measurements and the BBN model in general with good agreement also seen with the independent CMB measurements. There is a discrepancy in the results from ^{7}Li measurements; the exact cause of this is under investigation [22]. It could be from systematic errors, for example the different techniques used to study the temperature of the stellar atmospheres in which the ^{7}Li line is formed [21]. Other possible reasons for the discrepancies are the uncertainties in the astrophysical or nuclear inputs used in the model or possibly there is some new physics that is not yet understood.

Using the results from the BBN, Ω_b is found to lie in the range $0.046 < \Omega_b < 0.052$ (95% CL) [21], which is in agreement with the CMB showing that only $\sim$5% of the universe is made of baryonic matter, and, given the measurement of Ω_m, is further evidence for non-baryonic dark matter making up the majority of the matter in the universe.

Large Scale Structure Formation

Since the turn of the millennium computational power has reached a level where simulations of the formation of the universe have become possible. Using these simulations it is possible to include astrophysical assumptions and compare the results to what can be seen today in telescope surveys. Using ΛCDM models it has been shown that these produce a very similar universe to the one we see today [23]. This is shown in the comparison of data and simulations seen in Figure 1.7 which shows results from the Millennium simulation along with astrophysical observations from the SDSS (Sloan Digital Sky Survey) [24], CfA2 (Center for Astrophysics) Redshift Survey [25] and 2dFGRS (Two-degree-Field Galaxy Redshift Survey) [26]. The image and data used in the figure are from Ref. [23] and references therein.

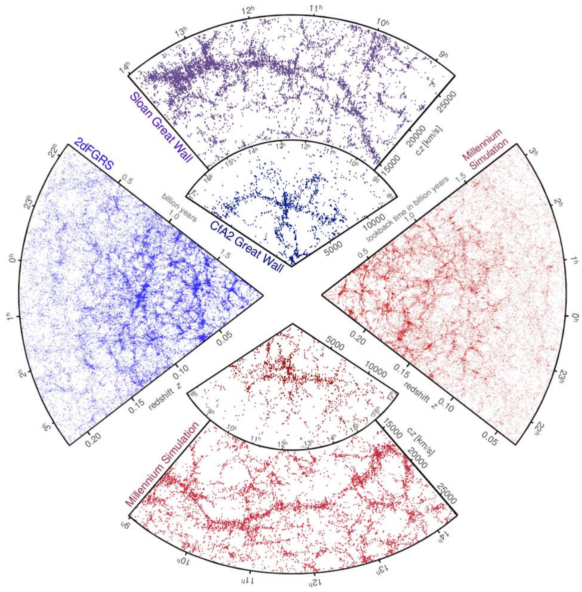

Fig. 1.7 Comparison of the results from the Millennium simulation (red) with astrophysical observations from SDSS, CfA2 and 2dFGRS (all blue). Image from Frenk and White [23].

1.2 DM Candidates

The evidence for dark matter discussed in Section 1.1 gives some constraints on the nature of dark matter. In 2007 Taoso, Bertone and Masiero [27] devised a list of 10 questions to narrow down prospective dark matter particles. These questions are shown below. For a particle to be considered a dark matter candidate it must give a ‘yes’ as the answer to every question.

1. Does it match the appropriate relic density
2. Is it cold?
3. Is it neutral?
4. Is it consistent with Big Bang nucleosynthesis (BBN)?
5. Does it leave stellar evolution unchanged?
6. Is it compatible with constraints on self-interactions?
7. Is it compatible with direct DM searches?
8. Is it compatible with gamma-ray constraints?
9. Is it compatible with other astrophysical bounds?
10. Can it be probed experimentally?

These constraints, while ruling out some options, still allow several possible candidates for dark matter. Some of the leading candidates are described in more detail in this section.

1.2.1 WIMPs

One theorised candidate for dark matter, and the main study of this thesis, is the Weakly Interacting Massive Particle (WIMP). The WIMP is a particle that is neutral, massive and one that only interacts weakly, with a low interaction cross-section. The WIMP fits with all ten of the previously mentioned points and can come from one of a few different theories such as Supersymmetry (SUSY) [28] and Universal Extra Dimensions (UED) [29]. These will be the only theories discussed in more detail here.

Supersymmetry

Supersymmetry, specifically the Minimal Supersymmetric Standard Model (MSSM) [28], gives rise to a particle known as the Lightest Supersymmetric Particle (LSP). The MSSM is the most simple form of supersymmetry in that it only considers the minimum number of particles required for a working supersymmetric extension of the standard model. One key part of this model for a DM candidate perspective is the conservation of R-parity [28]. R-parity (R_p) is a parameter defined by

$$R_p = (-1)^{3B+L+2S}, \tag{1.6}$$

where B is the baryon number, L is the lepton number and S is the spin. If R-parity was not included in the model then the lifetime of the proton is expected to be short, however this has not been observed with the decay time of the proton known to be over 10^{32} years [28]. The R_p for a supersymmetric particle is –1, and for a standard model particle it is +1. Conservation of R-parity gives two main consequences: the first is that supersymmetric particles can only be made in pairs; this is what would occur if they were created in the LHC for example. The second consequence of R-parity conservation is that the decay of a supersymmetric particle must contain an odd number of supersymmetric particles. This leads to the final decay stage containing a supersymmetric particle that is both neutral and stable; this particle is the LSP and is a good WIMP dark matter candidate. Figure 1.8 shows some example supersymmetric decays of a pair of 3rd generation squark particles produced in a collider such as the LHC. Here $\tilde{\chi}_1^0$ is the LSP.

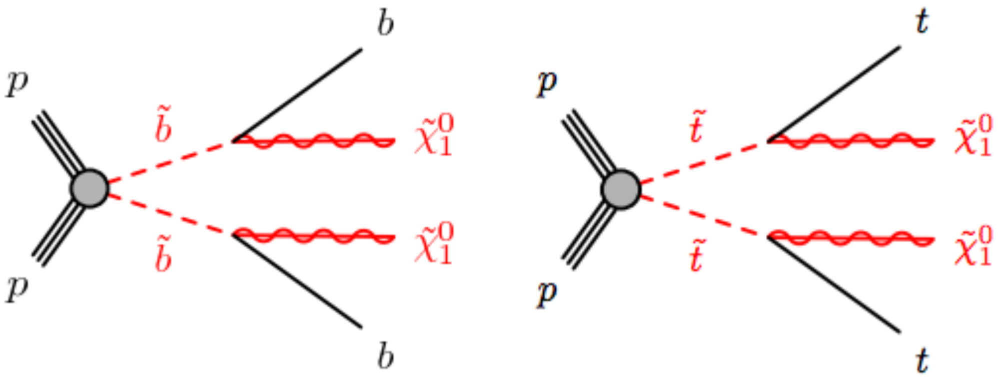

Fig. 1.8 Simplified diagrams of example 3rd generation squark production and decay methods, resulting in an LSP. Diagrams from the ATLAS collaboration [30].

Universal Extra Dimensions

The universal extra dimensions (UED) theory [29] can produce the Lightest Kaluza-Klein Particle (LKP) which is also a possible candidate for a WIMP particle. Initial extra dimension theories were developed as a way to unify Maxwell’s equations with general relativity in 5 dimensional space-time. The first of these was proposed by Kaluza in 1921 [31] in a fully classical interpretation, with Klein giving a quantum interpretation to the theory in 1926 [32, 33]. This theory was built on in the following years and eventually resulted in UED which also had the aim of solving the gauge hierarchy problem [34]. In UED there is a conservation of KK-parity, defined by

$$KK_p = (-1)^n, \tag{1.7}$$

where n is the KK number. For SM particles $n = 0$, for KK states $n = 1$. This conservation results in the lightest particle, the LKP, being stable, or else the parity would be violated, as with R-parity in SUSY models. The LKP is then a good candidate for WIMP dark matter with recent results constraining the mass to be > 950 GeV [35].

1.2.2 Axions

Axions are hypothetical particles associated with the breakdown of the global quasi-symmetry postulated by Peccei and Quinn in their work trying to explain the strong CP problem [36], where no CP violation is seen in QCD interactions. The mass of axions, unlike WIMPs, is known within a range of masses, thanks to bounds being set by both astrophysical, e.g. SN1987A, and experimental results, e.g. ADMX and CAST. These set bounds for the parameter space into which axions can fit, which is slowly being tested, a plot of the latest bounds is shown in Figure 1.9 along with the predictions from the most commonly quoted theories: KSVZ (Kim-Shifman-Vainshtein-Zakharov) [37, 38] and DFSZ (Dine-Fischler-Srednicki-Zhitnitsky) [39, 40].

1.2.3 Sterile Neutrinos

The SM [21] predicts that there should be three flavours of neutrinos (e, μ, τ) which are all massless and do not mix with each other. It has since been shown that all 3 flavours of neutrino do oscillate, which requires that they must have mass. One example of this came from the SNO (Sudbury Neutrino Observatory) detector [42], where the number of solar electron neutrinos (ν_e) detected was lower than the number of neutrinos of all flavours. As only ν_es are expected from the Sun, this showed that they had oscillated to another form of neutrino. A suggestion for the origin of the neutrino mass is through the see-saw mechanism. This is where the neutrinos would have a similar form to the other mass terms with both the observed left-handed triplet and a right-handed singlet. This singlet is often know as a sterile neutrino and the mass of which is linked to the masses of the triplet neutrinos, with a higher

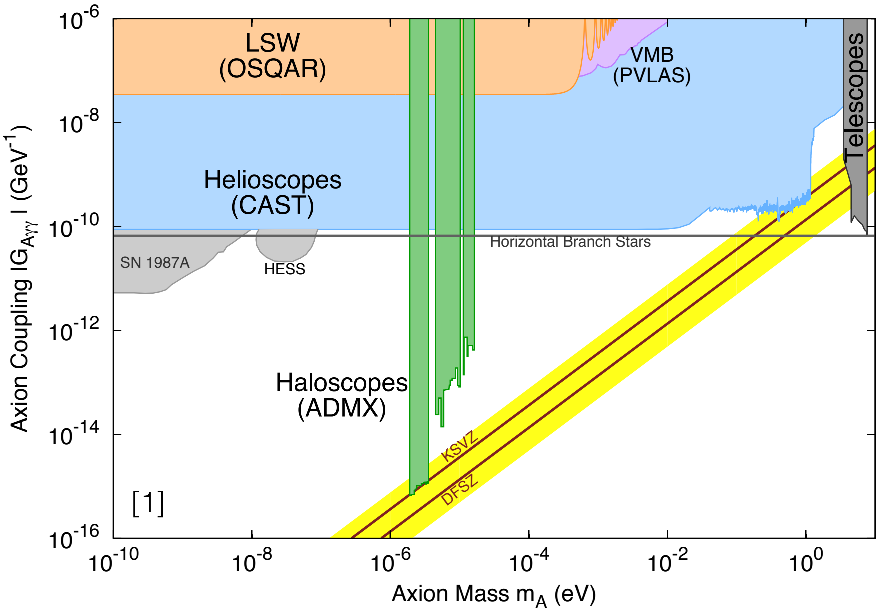

Fig. 1.9 Plot of current axion bounds from both experiments and astrophysical sources, with the expected band from theory also shown. Plot from Daw [41].

singlet mass leading to a smaller triplet mass [43]. One specific extension to the SM that includes this sterile neutrino is the neutrino minimal standard model (νMSM) [44], which has many advantages to it in explaining physics beyond the SM, including a natural candidate for dark matter. This extension produces sterile neutrinos as singlet Majorana fermions, the lightest of which is a good dark matter candidate, with a mass $\mathscr{O}(10)$ keV.

1.3 Direct Detection of Dark Matter

There are three main paths to detecting dark matter: the first is to detect the interaction of dark matter scattering off normal matter, known as direct detection; he second is to detect the by-products of DM interactions/annihilation, known as indirect detection, and the final method is to measure the production of DM in collider experiments such as the LHC. A diagram showing these interaction methods is shown in Figure 1.10. The subject of this thesis will be the direct detection of dark matter and that topic will be discussed in detail in this section. Section 1.4 presents a brief discussion of both indirect searches and the latest results from collider searches.

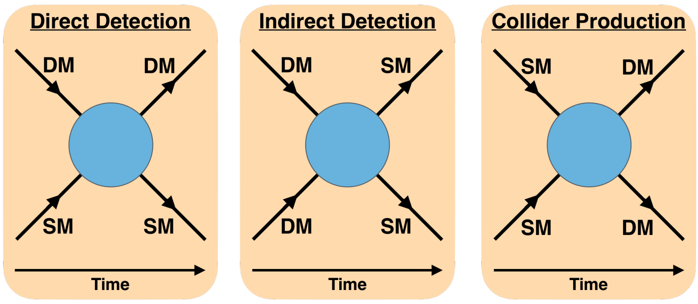

Fig. 1.10 These diagrams show the interactions for the three main methods of dark matter detection. These are, from left to right, direct detection, indirect detection and collider production.

1.3.1 Direct Detection Theory

Searches for the direct detection of WIMP dark matter are looking for an interaction between WIMPs and the target detector material. As both the mass and interaction cross-section of WIMPs are unknown, we want to be able to find a way to find limits on these to constrain the parameter space or to be able to calculate the mass and cross-section in the case of a positive result. The derivation below follows Daw [45]. To be able to claim a detection of WIMPs or set a limit on the mass and cross-section of WIMP interactions, first one needs to understand the interaction of WIMPs in the chosen detector. The rate of scatters in a detector is given by

$$R = \frac{N_W N_N v \sigma}{L^3}, \tag{1.8}$$

where L is the length of a side for a cubic detector, v is the velocity of the incoming WIMP particle, σ is the interaction cross-section and $N_{W,N}$ is the number of WIMPs/nuclei in the detector volume,

$$N_W = \frac{10^6 L^3 \rho_W}{M_W}, \tag{1.9}$$

$$N_N = 10^3 N_A M_D, \tag{1.10}$$

where ρ_W is the local density of WIMPs in GeV/cm^3, N_A is Avogadro's Constant, M_W is the WIMP mass in GeV/c^2 and M_D is the detector mass in kg. Substituting values for N_W and N_N into Equation 1.8 gives

$$R = \frac{10^9 N_A \rho_W M_D v \sigma}{M_W}. \tag{1.11}$$

For a realistic detector there will be an energy threshold that needs to be taken into account. This is done by integrating the differential rate over the energy limits of the detector:

$$R_{det} = \int_{E_{min}}^{E_{max}} \frac{dR}{dE_R} dE_R. \tag{1.12}$$

Here

$$\frac{dR}{dE_R} = Rp(E_R), \tag{1.13}$$

where $p(E_R)$ is the probability density of the WIMP inducing a recoil energy of E_R and is given by [46]

$$p(E_R) = \frac{M_N}{2\mu_{WN}^2 v_{min}^2}, \tag{1.14}$$

where M_N is the mass of the target nucleus and μ_{WN} is the reduced mass of the WIMP-nucleus interaction, shown in Equation 1.15.

$$\mu_{WN} = \frac{M_W M_N}{M_W + M_N}, \tag{1.15}$$

and v_{min} is the minimum velocity required to produce a recoil of energy E_R, where

$$E_R = \frac{\mu_{WN}^2 v^2}{M_N}(1 - \cos(\theta)), \tag{1.16}$$

where θ is the angle between the recoil direction and the initial WIMP direction. From equation 1.16, $v = v_{min}$ when $\theta = 180$, resulting from a head-on collision resulting in maximum energy transfer. This implies that

$$v_{min} = \sqrt{\frac{E_R M_N}{2\mu_{WN}^2}}. \tag{1.17}$$

Substituting Equations 1.11 and 1.14 into Equation 1.13 gives

$$\frac{dR}{dE_R} = \frac{10^9 N_A \rho_W M_N M_D \sigma}{2 M_W \mu_{WN}^2 v}. \tag{1.18}$$

Velocity Distribution

The next two sections follow the method of Lewin and Smith [46]. Assuming that the WIMP-halo velocity distribution follows a Maxwell-Boltzmann distribution then we can define the $\frac{1}{v}$ from Equation 1.18 by

$$\frac{1}{v} = \int_{v_{min}}^{v_{esc}} \frac{f(v)}{v}, \tag{1.19}$$

where $f(v)$ is the velocity distribution with the velocity taking a value between v_{min} and v_{esc} the escape velocity of the Galaxy, thus setting the upper limit on the velocity of WIMPs gravitationally bound to the Galaxy [46]. We assume that $f(v)$ is given by

$$f(v) = \frac{4v^2}{v_o^3\sqrt{\pi}} e^{-(\frac{v}{v_o})^2}, \tag{1.20}$$

where v_o is the average circular velocity of objects in the Galactic halo. By substituting $V_{esc} \to \infty$ and calculating the integral [46] this gives

$$\frac{1}{v} = \frac{2}{v_o\sqrt{\pi}} e^{-(\frac{v_{min}}{v_o})^2}. \tag{1.21}$$

Substituting this into Equation 1.18 gives

$$\frac{dR}{dE_R} = \frac{10^9 N_A \rho_W M_N M_D \sigma}{M_W \mu_{WN}^2 v_o \sqrt{\pi}} e^{-(\frac{v_{min}}{v_o})^2}. \tag{1.22}$$

Nuclear Form Factor

The previous model is for a collision of solid spheres and only holds true if $\lambda \gg r_N$, where r_N is the radius of the target nucleus and λ is the de Broglie wavelength. If λ is not $\gg r_N$ then it would be sensitive to the structure of the nucleus. λ is given by [46]

$$\lambda = \frac{2\pi\hbar}{q}, \tag{1.23}$$

where q is the momentum of the recoiling nucleus in the lab frame. As the particle recoil is non-relativistic it can be expressed as

$$q = \sqrt{2M_N E_R}. \tag{1.24}$$

For a 100 GeV WIMP colliding with a fluorine nucleus this gives λ = 53.8 fm. The radius of a nucleus is given by

$$r_N = r_o A^{\frac{1}{3}}, \tag{1.25}$$

where r_0 = 1.2 fm. Using this the radius of a fluorine nucleus is found to be 3.2 fm. As there is only one order of magnitude between λ and r_N, the solid spheres approximation cannot be said to be true. To correct for this a nuclear form factor is associated with the cross-section, σ, where $\sigma \to \sigma_0 F(qr_N)$. Here σ_0 is the limit on σ for the zero momentum-transfer case and $F(qr_N)$ is the nuclear form factor.

For interactions that are spin-dependant, such as interactions with ^{19}F found in the DRIFT detector, the form factor must include details of the spin of the interaction. In the case of a fluorine target, the spin, J, is $\frac{1}{2}$.

If we approximate particles as plane waves, also known as the first Born approximation [46], the form factor can be expressed as

$$F(qr_N) = j_0(qr_N), \tag{1.26}$$

where j_0 is the first Bessel function for a thin shell, $j_0(x) = \frac{\sin(x)}{x}$. Here the thin shell is an approximation of the outer shell of a nucleus, so applies only for spin-dependant interactions. For a spin-independent interaction a Bessel function of a solid sphere would be used to approximate the entire nucleus. The form factor for this would be described by

$$F(qr_N) = \frac{3j_1(qr_N)}{qr_N} = \frac{3(\sin(qr_N) - qr_N\cos(qr_N))}{(qr_N)^3}. \tag{1.27}$$

As the main focus of this thesis will be using spin-dependant targets, only the spin-dependant interactions will be discussed from here.

It has been shown by Lewin and Smith [46] that for a spin dependant interaction the first minimum can be approximated to the second maximum when the coupling to all ‘odd-group’ nucleons is accounted for. From this the form factor between $0 < qr_N < 6$ can be expressed as

$$F^2(qr_N) = \begin{cases} j_o^2(qr_N) & (qr_N < 2.55 \text{ or } qr_N > 4.5) \\ 0.047 & (2.55 < qr_N < 4.5) \end{cases} \tag{1.28}$$

The calculation of a single particle model with ^{131}Xe show good agreement with this approximation between $2.55 < qr_N < 4.5$, shown in Figure 1.11.

Figure 1.12 shows how the form factor changes with recoil energy for different spin-dependant target nuclei used in direct dark matter searches. It can be seen that, in the main energy window of interest (0–300 keV), the form factor has only a small effect for lighter targets such as ^{19}F and ^{23}Na, but for heavy targets such as ^{127}I and ^{131}Xe there is a large effect on the form factor as the recoil energy increases.

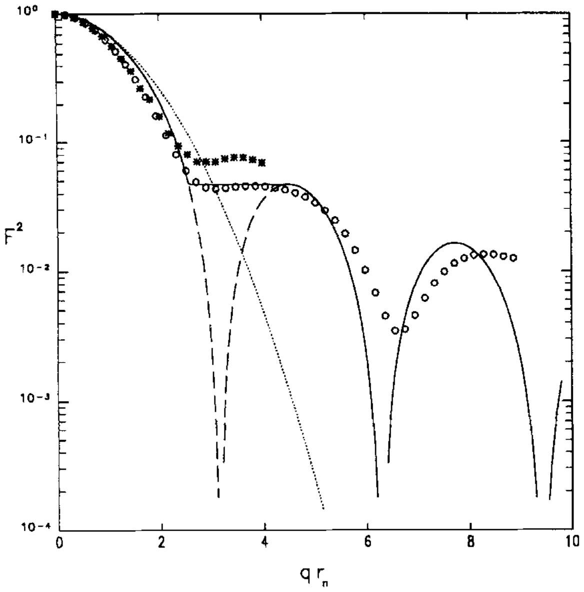

Fig. 1.11 Plot of form factor against qr_N [46]. The dotted line shows an approximation of $\exp[-(qr_N)^{2/3}/3]$. The dashed line shows the form factor using the first Bessel function, the solid line shows the described approximate fit to this using Equation 1.28. The white circles are the result of a single-particle model for ^{131}Xe and the asterisks are a single-particle model for Nb.

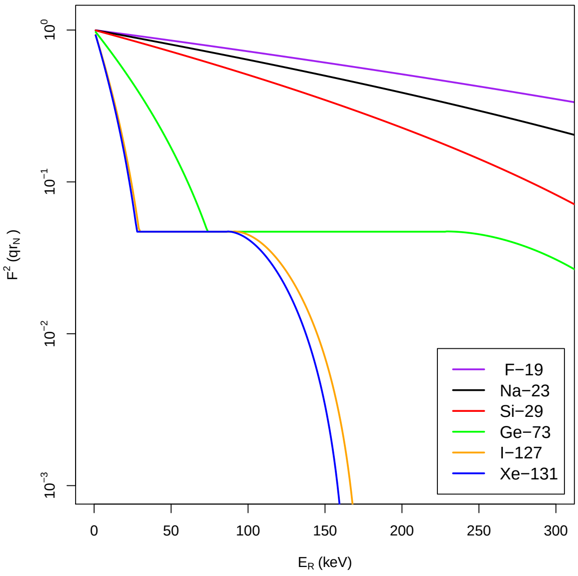

Fig. 1.12 Plot of form factor against recoil energy for several spin-dependant targets used in direct dark matter searches.

WIMP-Nucleon Cross-Section

We now need to calculate the the cross-section, σ. To be able to compare results of experiments using different targets and masses, it is useful to express this in terms of the proton or neutron cross-section following Tovey et al. [47]:

$$\sigma_{WN} = (\sqrt{\sigma_{Wp}} + \sqrt{\sigma_{Wn}})^2, \tag{1.29}$$

in which

$$\sigma_{Wp} = 4G_F^2 \mu_{Wp}^2 C_{Wp} \tag{1.30}$$

and

$$\sigma_{Wn} = 4G_F^2 \mu_{Wn}^2 C_{Wn}, \tag{1.31}$$

where G_F is the Fermi coupling ($1.166 \times 10^{-5}\mathrm{GeV}^{-2}$ [21]), μ_{Wp} (μ_{Wn}) is the WIMP-proton (WIMP-neutron) reduced mass and C_{Wp} (C_{Wn}) are the contributions of the proton (neutron) to the total enhancement factor, C_{WN}, defined as

$$C_{WN} = \frac{8}{\pi}(|a_p\langle S_p\rangle| \pm |a_n\langle S_n\rangle|)^2 \frac{J+1}{J}, \tag{1.32}$$

with

$$C_{Wp(n)} = \frac{8}{\pi}|a_{p(n)}\langle S_{p(n)}\rangle|^2 \frac{J+1}{J}. \tag{1.33}$$

Here $\langle S_{p(n)}\rangle$ is the expectation value for the spin of the proton(neutron), J is the nuclear spin and $a_{p(n)}$ is the WIMP-proton(neutron) coupling from the chosen WIMP model.

If the nuclear cross-section is proton or neutron dominated, this can be made independent of the WIMP model. This is the case for the fluorine target used in DRIFT, where $\sigma_{WN} \sim \sigma_{Wp}$. One can then define an effective cross section

$$\sigma_{Wp}^{eff} = \sigma_{WN} \frac{\mu_{Wp}^2 C_{Wp}^{eff}}{\mu_{WN}^2 C_{WN}}, \tag{1.34}$$

where C_{Wp}^{eff} is obtained by setting $\langle S_p\rangle = J = \frac{1}{2}$ into Equation 1.33. This gives

$$C_{Wp}^{eff} = \frac{6a_p^2}{\pi} \tag{1.35}$$

and hence

$$\frac{C_{WN}}{C_{Wp}^{eff}} = \frac{4}{3}\langle S_p\rangle^2 \frac{J+1}{J}. \tag{1.36}$$

The a_p^2 factor containing the WIMP model dependence cancels, and therefore this result holds for any WIMP model.

Substituting this into Equation 1.34 and rearranging for σ_{WN} gives

$$\sigma_{WN} = \sigma_{Wp}^{eff} \frac{4}{3} \frac{\mu_{WN}^2}{\mu_{Wp}^2} \langle S_p \rangle^2 \frac{J+1}{J}. \tag{1.37}$$

This can be substituted into Equation 1.22 using $\sigma = \sigma_{WN}$ and including the form factor giving

$$\frac{dR^{SD}}{dE_R} = \frac{10^9 N_A \rho_W M_N M_D F^2(qr_N)}{M_W \mu_{WN}^2 v_o \sqrt{\pi}} \sigma_{Wp}^{eff} \frac{4}{3} \frac{\mu_{WN}^2}{\mu_{Wp}^2} \langle S_p \rangle^2 \frac{J+1}{J} e^{-(\frac{v_{min}}{v_o})^2}. \tag{1.38}$$

For an example target of fluorine, $J = \langle S_p \rangle = \frac{1}{2}$, including this in Equation 1.38 along with other simplification and the inclusion of a parameter to account for the detector efficiency, ε, gives

$$\frac{dR^{SD}}{dE_R} = \frac{10^9 N_A \rho_W M_N M_D F^2(qr_N) \varepsilon \sigma_{Wp}^{eff}}{M_W \mu_{Wp}^2 v_o \sqrt{\pi}} e^{-(\frac{v_{min}}{v_o})^2}. \tag{1.39}$$

An overall rate of interactions in the detector can therefore be found by combining Equations 1.12 and 1.39 to give

$$R_{det} = \int_{E_{min}}^{E_{max}} \frac{dR}{dE_R} dE_R = \int_{E_{min}}^{E_{max}} \frac{10^9 N_A \rho_W M_N M_D F^2(qr_N) \varepsilon \sigma_{Wp}^{eff}}{M_W \mu_{Wp}^2 v_o \sqrt{\pi}} e^{-(\frac{v_{min}}{v_o})^2} dE_R. \tag{1.40}$$

Given a known rate of interactions in a detector, Equation 1.40 can be used to find the expected WIMP rate in the detector and thus set an upper limit on the possible SD WIMP-proton cross-section from those results. If there are WIMPs found in the dataset this would instead be used to find a signal region in the parameter space. The latest experimental limits on cross-sections will be shown in Section 1.3.2 along with a description of the experiments from which they were produced.

1.3.2 Direct Detection Experiments

The following section details the different experiments aiming to directly detect dark matter interactions, both the current experiments and some planned for operation in the near future.

Noble Liquid/Gas Detectors

The current leading detector technology, in terms of setting limits on spin-independent WIMP-nucleon interactions, is the use of dual-phase xenon detectors. There are three main groups attempting to discover WIMP signals in this way. The first is the LUX-ZEPLIN (LZ) collaboration [48], which consists of the ZEPLIN (ZonEd Proportional scintillation in LIquid Noble gases) collaboration [49–51] and the LUX (Large Underground Xenon) collaboration [52]. The ZEPLIN collaboration operated a series of detectors in Boulby Underground Lab, UK and the LUX collaboration have been running the LUX detector, which has recently finished running, in the Sanford Underground Research Facility (SURF), USA. The proposed LZ detector [48, 53], the first detector from the full LZ collaboration, uses the same dual-phase xenon technology and will be housed in the same location as the LUX detector in SURF utilising the previously developed infrastructure. The LZ detector will have over an order of magnitude increase on the previous detectors from LUX or ZEPLIN with a fiducial mass of 5.6 tonnes [53]; this is compared to the $\sim$ 100 kg of fiducial mass in LUX [52] and the 7.2 and 5.1 kg fiducial masses from the ZEPLIN-II and ZEPLIN-III detectors [50, 51]. The LZ detector is now under construction with detector installation expected in 2019 and data taking expected from 2020.

The second group using dual-phase xenon detectors is the XENON collaboration [54]. XENON have run a series of detectors of increasing mass in Gran Sasso National Laboratory (LNGS), Italy, from the 14 kg active mass (5.6 kg fiducial) of XENON10 [55], through to the 62 kg (48 kg fiducial) of XENON100 [56] to the latest incarnation XENON1T, with an active mass of 2 tonnes (1 tonne fiducial) [54]. The final group using this technology is the PandaX collaboration [57]. PandaX are currently running the PandaX-II 500 kg detector in the China Jin-Ping Underground Laboratory (CJPL).

The dual-phase Xe detectors consist of a large volume of liquid xenon (LXe) with an volume of gaseous xenon above, shown in Figure 1.13. An interaction occurs in the LXe causing primary scintillation (S1) and ionisation. The S1 signal is detected by photomultiplier tubes (PMTs) at the top and bottom of the detection region. The ionised electrons drift in the electric field upwards to the gaseous Xe, where there is an avalanche of charge with associated emission of proportional scintillation light (S2); this is again detected by the PMTs. The PMT detection gives a 2D location of the interaction and the time difference between S1and S2 signals gives the depth in the LXe that the interaction occurred. The ratio between the S1 and S2 signals also gives discrimination between background electron recoils and the nuclear recoils expected from WIMP interactions. The difference in the ratios is from the recombination of ionisation after nuclear recoil events, due to the high ionisation density. The recombination gives nuclear recoils a larger S1 scintillation signal and a lower charge signal (S2).

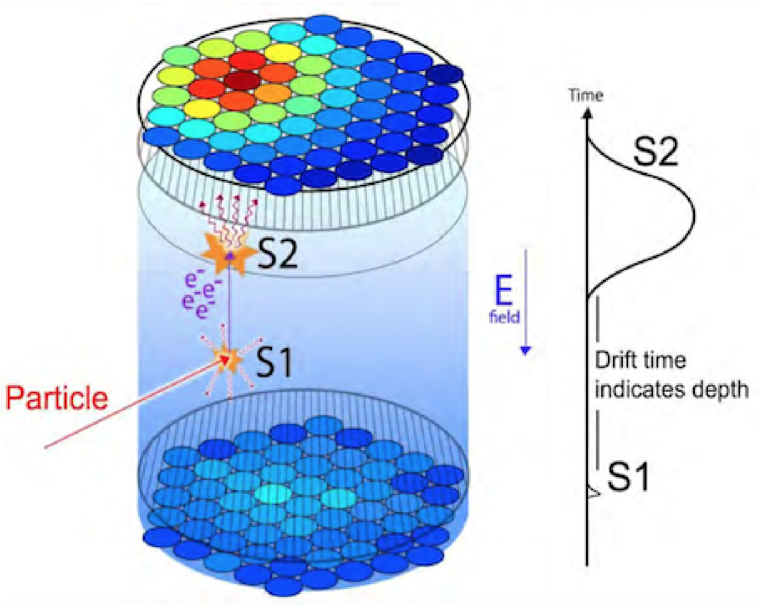

Fig. 1.13 The operation principle of the dual-phase Xe detectors is shown [48] with the initial interaction in the bulk liquid giving prompt scintillation light (S1) and the secondary scintillation (S2) coming from the ionised electrons avalanching when they reach the upper gas volume.

There are also two technologies being used with another noble gas, argon. These are a dual-phase argon experiment from the DarkSide collaboration [58] and a single-phase liquid argon (LAr) detector from the DEAP collaboration [59]. The latest detector from DarkSide is the DarkSide50 TPC, a 50 kg detector operating in LNGS. The detection method is very similar to that described above for the dual-phase xenon detectors, but using liquid and gaseous argon rather than xenon. The latest detector from the DEAP collaboration is the DEAP-3600 detector, a 3600 kg, spherical LAr detector surrounded by PMTs on all sides, a diagram of the detector is shown in Figure 1.14. Like the dual-phase detectors this also gives 3D reconstruction of interaction vertex from the comparison between the intensity in all of the PMTs.

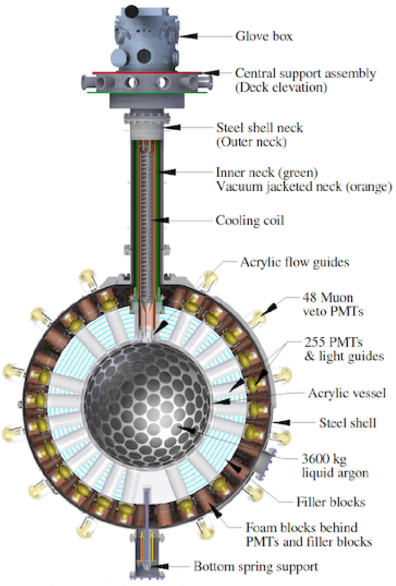

Fig. 1.14 A schematic of the DEAP-3600 detector is shown with the active LAr held in the spherical acrylic vessel and instrumented on all sides with PMTs connected to light guides [59].

The current leading spin-independent limit has been set by the LUX experiment, with PandaX-II [57] and XENON100 having slightly higher limits as shown in Figure 1.15 along with limits from the argon-based detectors. It is expected that PandaX-II, XENON1T and DEAP-3600 [59] will all produce limits lower than this in the next few years. As the LUX detector has stopped data taking to allow the LZ detector infrastructure to start moving into the laboratory space no new limits are expected from LUX, but LZ is expected to produce world-leading limits after it is operational.

Low-Threshold Crystal Detectors

The dual-phase xenon detectors are leading the way in spin-independent limit setting from a WIMP mass of > 10 GeV, but at masses below this the best limits are set by low-threshold, crystal-based bolometric detectors such as those from the SuperCDMS (Super Cryogenic Dark Matter Search) collaboration [60].

The SuperCDMS (previously CDMS) collaboration have used cryogenically-cooled germanium and silicon crystal detectors in Soudan Underground Laboratory, USA for many years [60], using a combination of ionisation and phonon signals to get discrimination between electron and nuclear recoils. The most recent SuperCDMS Soudan setup consisted of fifteen 0.6 kg Ge detectors [60]. The instrumented crystals are known as interleaved

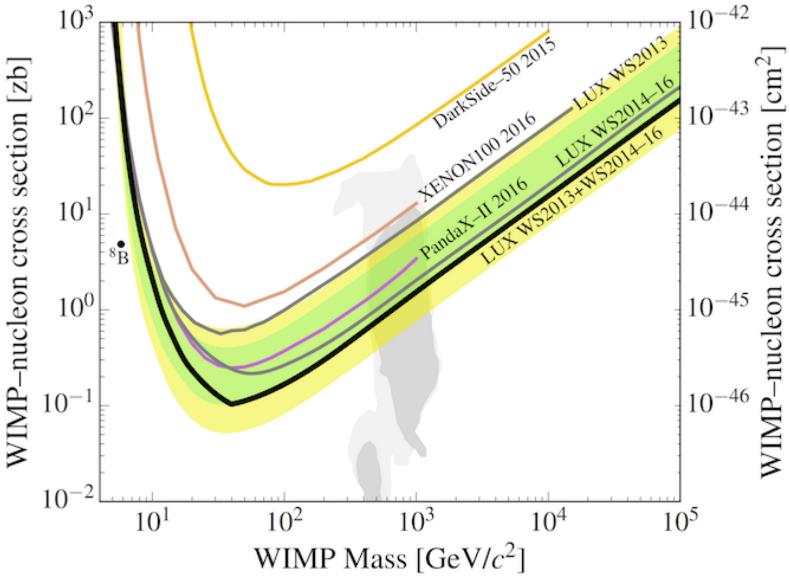

Fig. 1.15 The latest spin-independent WIMP cross-section limits are shown from the liquid noble detectors, with the lowest limit at time of writing coming from the LUX collaboration. The grey shaded area is the preferred parameter space of the SUSY CMSSM (constrained minimal supersymmetric model). Figure from Akerib et al. [52].

Z-sensitive Ionization and Phonon (iZIP) detectors. The iZIP detectors have both faces instrumented with two ionisation channels and 4 channels for phonons. The ionisation channels record the electron-hole pairs created by an event in the crystal. The detectors are designed with +2V and 0V sensors on one side and -2V and 0V sensors on the other. This design is so that surface events will have both electrons and holes detected on the same side and bulk events will have them collected on opposite sides of the crystal to give discrimination against background surface events. The phonon channels consist of superconducting transition edge sensors (TES) made of tungsten strips connected to aluminium fins used to collect the phonons.

The SuperCDMS Soudan experiment was run in two operational modes. The first was using the iZIP design described above to give higher discrimination of nuclear recoils. There has also been a low-threshold mode utilised, CDMSlite (CDMS low ionization threshold experiment) [61]. In this mode a SuperCDMS iZIP detector was operated at a higher voltage with one side of the detector held at 0V and the other at 70V. This mode takes advantage of Luke-Neganov amplification [62, 63] to give large phonon signals at the expense of the charge signal. This leads to a lower threshold to gain sensitivity to lower WIMP masses, but at the expense of nuclear-recoil discrimination.

The next generation of the SuperCDMS detector is to be run at the SNOLAB underground science laboratory, Canada [64], to give a lower background level than can be achieved at Soudan due to the increased overburden at SNOLAB. The initial setup for SuperCDMS SNOLAB will consist of 24 detectors with a mixture of iZIP and new high voltage detectors (HV) specifically designed to run in the low threshold mode. Both sets of detectors will be made with a combination of Ge and Si crystals and the detectors will be housed in four towers, each containing 6 detectors. There will be infrastructure in place to take a further 27 towers in the future to increase the exposure. The predicted limits from the initial SuperCDMS SNOLAB detectors are expected to set much improved limits in the spin-independent parameter space compared to previous experiments; Figure 1.16 shows these predicted limits.

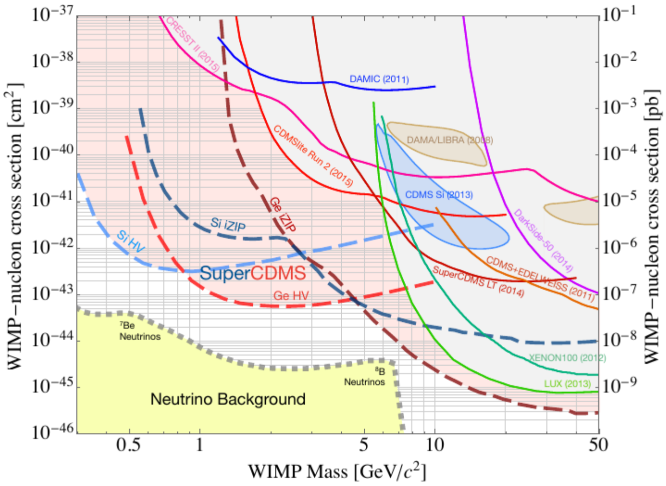

Fig. 1.16 The projected WIMP limits from the SuperCDMS SNOLAB detectors are shown for both the iZIP detectors and the HV mode along with recent limits from other collaborations. Plot from Calkins [64]. The limit from the Si detectors are shown in blue with the Ge limits in red.

SuperCDMS are the leading group in this field but there are also other experiments using similar crystal technology, including CRESST (Cryogenic Rare Event Search with Superconducting Thermometers) [65], running in LNGS, and EDELWEISS (Experience pour DEtecter Les WIMPs En Site Souterrain) [66], running in Modane underground laboratory, France. There is also another group, DAMIC (Dark Matter in CCDs) [67], who use CCD cameras with Si detectors to look for low mass WIMPs at SNOLAB.

Superheated Liquid Detectors

Where the previous detectors discussed have set the leading limits in spin-independent WIMP interactions, the leading limits from spin-dependant interactions currently come from detectors using superheated liquids as the target medium. The most recent of these detectors is PICO, which is the collaboration between the previous PICASSO (Project In Canada to Search for Supersymmetric Objects) [68] and COUPP (Chicagoland Observatory for Underground Particle Physics) [69] experiments that used a similar technique.

To date there have been two PICO detectors operated in SNOLAB: PICO-2L [70] and PICO-60 [71] . PICO-2L uses a chamber of superheated C_3F_8 liquid to search for dark matter. PICO-60 uses superheated CF_3I liquid. In both detectors CCD cameras are used to image the fiducial region, with bubbles being formed at the locations of interactions. The limits set by both PICO-2L and PICO-60 make up the lowest limits in spin-dependant WIMP interactions at low and high mass respectively. The latest spin dependant WIMP limits are shown in Figure 1.17.

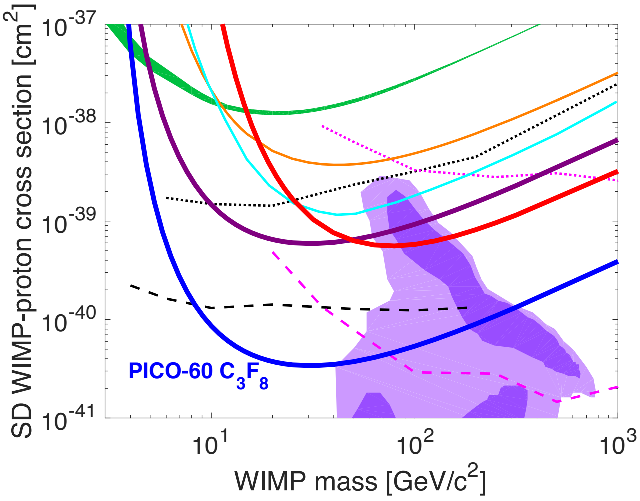

Fig. 1.17 This plot shows the latest limit from the PICO-60 detector (blue) along with previous direct detection results from PICO-60 (red), PICO-2L (purple), Panda-X (cyan), SIMPLE (orange) and PICASSO (green). Also plotted are indirect limits set by IceCube (pink) and SuperK (black) with the purple shaded region showing the favoured parameter space for the CMSSM SUSY model. Plot and limits from Ref. [71] and references therein.

Annual Modulation and Directional Detection

It has been shown that it is possible to detect the modulation of a dark matter signal in direct detection experiments, either detecting an annual modulation or the direction of the incoming particles [72, 73]. Both of these signals are discussed in detail in Chapter 2.

1.4 Alternative Methods of Dark Matter Detection

This section describes alternative methods for the detection of dark matter, with both indirect searches and collider searches discussed.

Indirect searches for dark matter look to detect SM particles from the annihilation or decay of DM particles. Indirect detection is usually undertaken by space or ground based telescopes: some examples include the space-based FermiLAT (Fermi Large Area Telescope) [74, 75] and the Chandra X-ray Observatory [76]. Some ground based examples include MAGIC (Major Atmospheric Gamma Imaging Cherenkov Telescopes) [74, 77, 78], CTA (Cherenkov Telescope Array) [79] and H.E.S.S (High Energy Stereoscopic System) [80]. In recent years both x-rays and gamma-rays as final states have had major interest due to possible excesses seen in data.

There has been an unexplained excess in x-ray emissions seen at 3.5 keV from several experiments. It was initially seen in stacked observations of 73 galaxy clusters in data from the XMM-Newton x-ray space observatory in 2014 [81], and has since been seen in several other experiments [76], although some other observations are in conflict with these [82]. The exact nature of the excess, if it exists, is unknown, but dark matter is a potential candidate. Also in 2014 an excess of gamma-rays was seen in the 1 - 3 GeV energy range [83]. This is thought to have been disproven as evidence for dark matter due to the evidence pointing towards the origin being from point sources, rather than a diffuse origin expected from dark matter [84, 85].

Indirect searches have also been made with neutrino detectors looking for the annihilation of dark matter in the Sun producing high energy neutrinos. The SuperK [86] and IceCube [87] collaborations have set limits competitive with direct detectors in the spin-dependant searches through this method, shown in Figure 1.17, although these limits have more model dependance than do the direct search results.

Collider searches look at the results of colliding standard model particles at high energies: Figure 1.10 shows that it should be possible. This is being tested at the LHC (Large Hadron Collider) at CERN, Switzerland, where the latest data is from proton-proton collisions with a centre-of-mass energy of 13 TeV. Both the ATLAS (A Toroidal LHC ApparatuS) [88] and CMS (Compact Muon Solenoid) [89] detectors are searching for a DM signal. The main method for searches is to look for events with missing transverse energy (MET) that cannot be reconstructed with standard model particles. Events that have MET are those containing particles that do not leave any signal in the detectors, with an example from the SM being neutrinos. The results from the detectors are plotted with detailed background models that show the expected results from the SM, and any significant excess in the data could be an indication of WIMPs or new physics. Many searches have been made in both detectors but, at the time of writing, there has been no indication of WIMPs in the LHC [90].

1.5 Conclusions

This chapter has shown that there is a vast amount of evidence showing there is missing matter in the universe. There are several possible candidates that could make up this missing matter that have been discussed, including the WIMP, which will be the candidate focused on in the remainder of the thesis. It has been shown that it is possible to set limits on the mass and cross section of WIMPs using Earth-based direct detection methods and many such experiments have been described along with their results. Chapter 2 will discuss two direct detection methods in more detail: these are searches for an annual modulation of a WIMP signal and searches for directional signatures of WIMPs. As well as direct detection this chapter also briefly mentioned the two other possible methods of dark matter detection, collider searches and indirect detection, with a description of the latest status of the field and a description of some of the experiments.

Chapter 2

Galactic Signals of Dark Matter

In the previous chapter it was seen that there are many experiments looking for the direct detection of dark matter. In this chapter, methods for direct dark matter detection using Galactic signals will be discussed. There are two methods for obtaining a Galactic signature of dark matter: annual modulation (discussed in Section 2.1) and directional detection (Section 2.2). Both of these methods use the assumption that the dark matter makes up a smooth, isothermal sphere of mass around the Galaxy. If the dark matter sphere, or 'halo', is assumed to be non-rotating, then the Earth and the whole solar system are travelling through it due to the rotation of the solar system around the Galactic centre. This leads to a 'wind' of dark matter particles towards the solar system at $\sim$ 220 km/s [91]. As the assumed dark matter candidate in this work is the WIMP, the dark matter wind is referred to as the 'WIMP wind' from here.

These methods of WIMP detection are of interest because they provide strong discrimination between signal and background compared to the direct detection experiments described in Chapter 1: this will be discussed in more detail in Sections 2.1 & 2.2.

2.1 Annual Modulation

The annual modulation signal is caused by the change in the velocity distribution of the incoming WIMPs throughout the year. The Earth's orbit around the Sun is angled at 60° to the motion of the solar system along the Galactic plane, as shown in Figure 2.3. Thus, as the Earth orbits the Sun, at $\sim$30 km/s, there will be a modulation of $\sim 27\%$ in the observed velocity of the WIMP-wind, with a maximum on June 1st and a minimum on December 1st [72, 73]. The modulation of the velocity distribution is expected to produce a modulation in the observed rate in an Earth-based detector dependant on the recoil energy. The change in the modulation amplitude is shown against energy in Figure 2.1. At low energies the modulation changes sign; this reversal can be used to constrain the mass of the recoiling WIMPs.

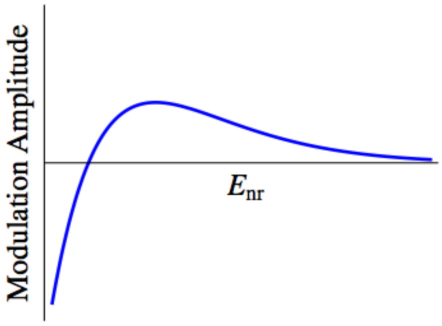

Fig. 2.1 Diagram of the change in modulation amplitude with recoil energy. Figure from Freese et al. [92].

This modulation is independent of terrestrial backgrounds so should remain constant independent of location on the detector on Earth. There are other seasonal modulations that could mimic this signal, which in the northern hemisphere will be of a similar timing to the WIMP annual modulation, with a peak around June. However any signal can be cross-checked by a detector placed in a different location, ideally in the southern hemisphere. If the modulation signal is from WIMPs, the signal would be identical in northern and southern hemisphere, but different signals would be seen if the modulation is from terrestrial effects. This section describes the current experimental searches and results for annual modulation, including a positive signal from the DAMA/LIBRA experiment (Section 2.1.1) and plans to test this in other locations, including the southern hemisphere with the DM-Ice experiment (Section 2.1.2). The section also includes a discussion of efforts towards lower background crystals and proposed future experiments.

2.1.1 DAMA/LIBRA

The DAMA/LIBRA (and previously DAMA/NaI) collaboration have been searching for the annual modulation signal for over two decades in LNGS [93, 94]. DAMA use scintillating thallium-doped sodium-iodide (NaI(Tl)) crystal detectors, with PMT used to read out the light signals from interactions. Results from the low energy (2-6 keV) DAMA data indicates a modulation signal, which is consistent with expectation for WIMP events with a peak in June, with a confidence level of 9.3 σ.

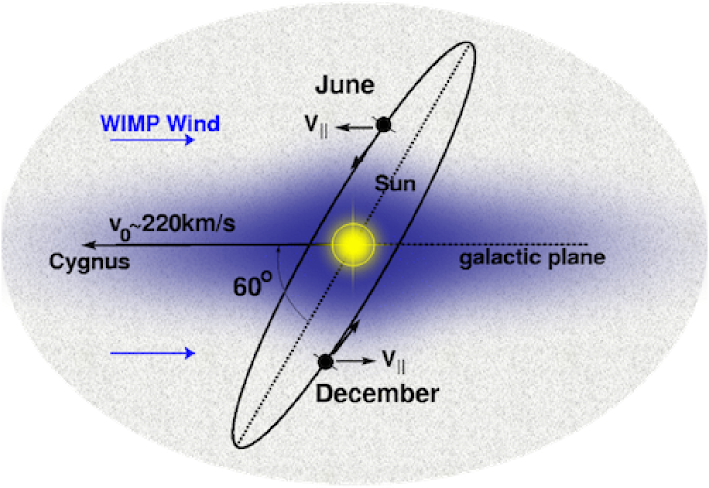

Fig. 2.2 Diagram of the earth travelling around the Sun over a year, causing a rise in WIMP interactions. Image credit: Sheffield Dark Matter Research

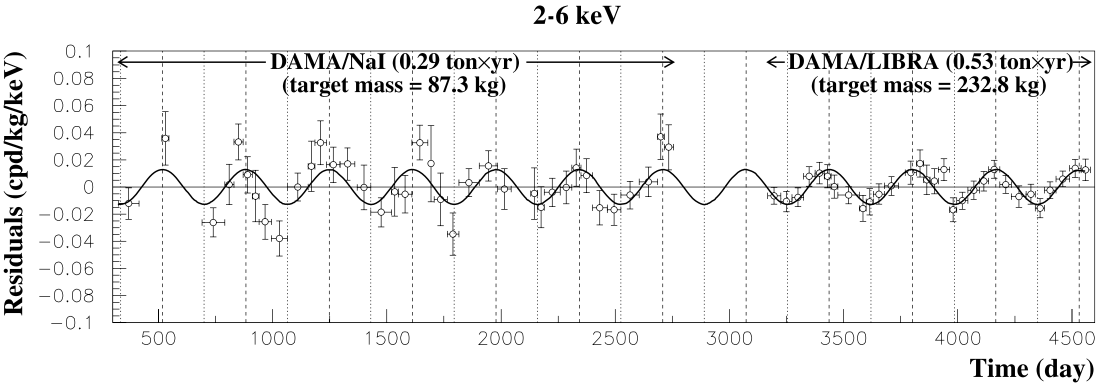

Fig. 2.3 Plot of the modulation signal seen across the DAMA/NaI and DAMA/LIBRA searches. Plot from Bernabei et al. [95].

These results are in disagreement with results from many other collaborations such as LUX, XENON and Panda-X, where exclusion limits have been set that exclude the area of phase space that contains the claimed DAMA result [96]: the results were discussed in Chapter 1. Several studies have been carried out in this area to try and find an alternative cause of this background e.g. [97, 98], but no backgrounds have yet been found to match the data. Other studies have been made to try and find compatibility between these results by looking at theoretical models that may allow agreement. One such model is looking at ionisation channelling in the crystals [99, 100]. In general the amount of energy converted into scintillation in NaI crystals is low compared to that lost as phonons/heat, with quenching factors of 0.3 for sodium recoils and 0.09 for iodine. Here the quenching factor, Q, is the amount of recoil energy transferred to electrons. However, if the recoils travel in the direction of a plane in the crystal, there will be fewer collisions with nuclei, and so more energy will go into electrons producing observable scintillation giving $Q \approx 1$. Taking this assumption into account allows some compatibility between the DAMA results and other experiments, although the allowed window is decreasing in size with every improvement in exclusion limit.

2.1.2 DM-Ice

Several experiments have been implemented which are designed to test the results from DAMA and conclusively prove whether the results are from dark matter or an unaccounted-for background. One such experiment is that from the DM-Ice collaboration, which aims to repeat the annual modulation experiment but in the southern hemisphere, specifically in the ice at the South Pole. Being located in the South Pole ice means that there will be a large suppression in any seasonal variations; however the modulation in the WIMP signal should be unaffected.

The DM-Ice17 experiment [101–103], shown in Figure 2.4, is made of two 8.5 kg NaI(Tl) crystals, previously used in the NAIAD experiment at Boulby [104]. The two detectors were deployed with the IceCube Neutrino Observatory and are located below separate IceCube DOMs (Digital Optical Modules) at a depth of 2457 m (2200 m.w.e.). One detector is located towards the centre of the IceCube array and the other towards the edge. As well as the depth of ice providing shielding from cosmic rays, the high hydrogen content of the ice is an excellent shield from neutrons and the ice is very radio-quiet [101].

The latest results from the DM-Ice17 detectors [105] show that no modulation signal was seen so a limit was set on spin-independent interactions. Due to the lower mass and higher background of the DM-Ice crystals the limit is above the DAMA allowed region; these results are shown in Figure 2.5. These results also show that it is possible to run an experiment in this environment with the primary physics run lasting for 3.6 years with an uptime of over 99%.

The DM-Ice collaboration has now merged with the KIMS (Korea Invisible Mass Search) collaboration to form COSINE (COnsortium of Sodium-IodiNe Experiments). KIMS and COSINE are described in Section 2.1.3.

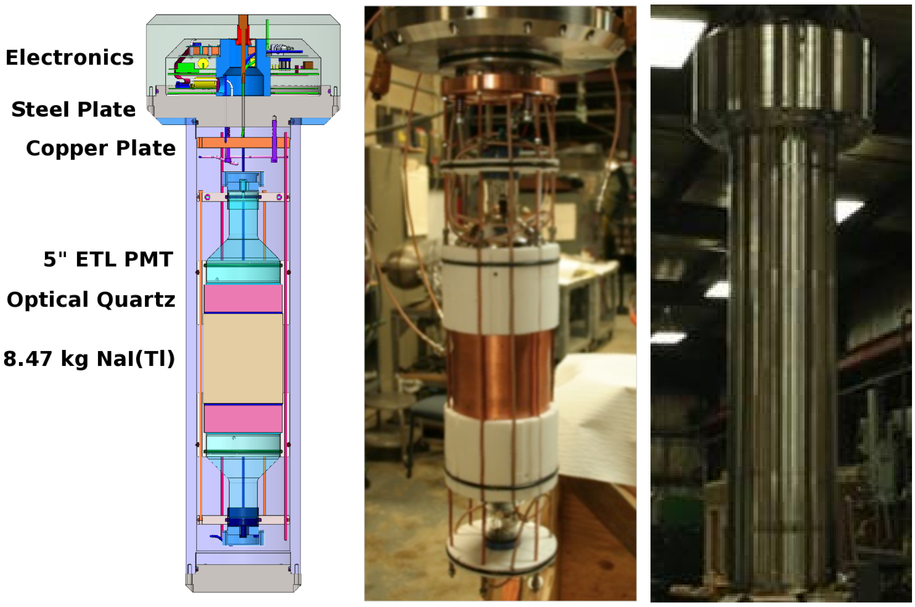

Fig. 2.4 Diagram and photographs of a single 8.5 kg detector from DM-Ice17 before being deployed in the South Pole ice. Diagram from Cherwinka et al. [102].

2.1.3 Other Annual Modulation Experiments

KIMS

The KIMS experiment (Korea Invisible Mass Search) [106] uses an array of 12 CsI(Tl) crystals with a combined mass of $\sim$ 100 kg to search for the annual modulation of dark matter. KIMS runs in the YangYang Underground Laboratory (Y2L) in South Korea with an overburden of 700 m (2400 mwe). The latest result from the KIMS experiment [106] is a search for WIMPs with a mass of below 20 GeV/c^2. This search gave no WIMP signal and has cut into the allowed region from the DAMA results as shown in Figure 2.6. The KIMS CsI(Tl) detectors are being upgraded and the next results should be able to exclude the entire DAMA region to 3σ assuming no signal is seen.

COSINE

COSINE (COnsortium of Sodium-IodiNe Experiments) [107] is the combination of the DM-Ice & KIMS collaborations. The first phase of detectors, known as COSINE-100, has been taking science data in Y2L with 107 kg NaI(Tl) crystals since September 2016. The plans for COSINE are to test the DAMA results initially in the northern hemisphere in Y2L,

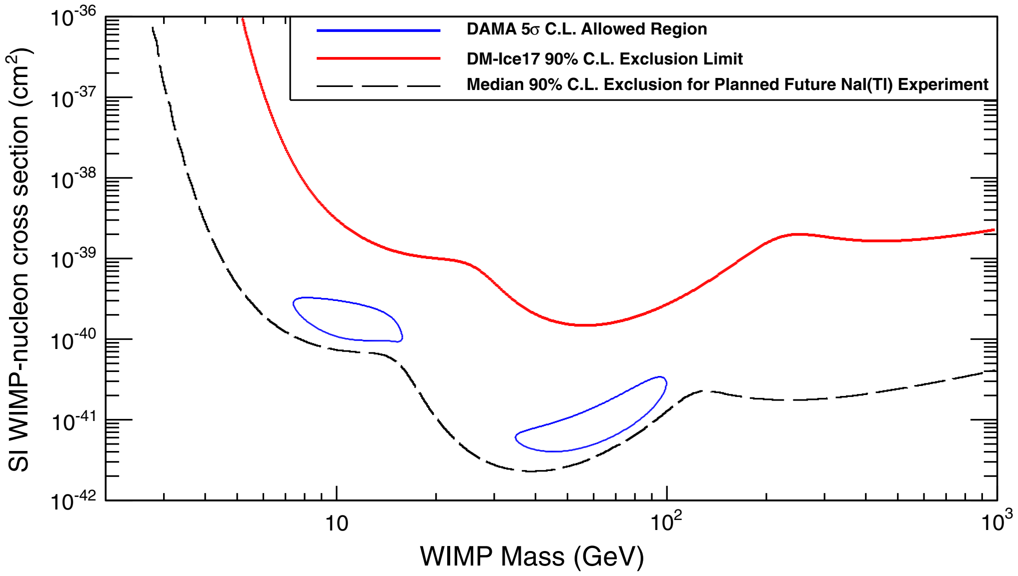

Fig. 2.5 Plot of the latest exclusion limits from the DM-Ice17 detectors running at the South Pole, together with the DAMA preferred regions and predicted future sensitivity. Figure from Barbosa de Souza et al. [105].

and then move to the southern hemisphere, and back to the South Pole ice in the future. The first results from COSINE-100 are currently in preparation.

ANAIS

The ANAIS (Annual modulation with NAI Scintillators) experiment [108] is running in Canfranc Underground Laboratory, in Canfranc, Spain. ANAIS also uses NaI(Tl) crystals to look for annual modulation and is currently using 112 kg of crystals in the ANAIS-112 detector [109]. The ANAIS-112 detector is predicted to provide a test of the DAMA results after a 5 year science run.

SABRE

The SABRE (Sodium-iodide with Active Background REjection) collaboration [110] are also looking to test the DAMA results using NaI(Tl) crystals. The main aim of SABRE is to develop ultra-low background NaI(Tl) crystals. Currently they are in the proof-of-principle phase and have recently produced a large crystal [111] with a lower background than the DAMA crystals, with a potassium level of 9.6 ppb, compared to 13 ppb for DAMA. Efforts are also ongoing to find low-background, high quantum efficiency PMTs. Initial underground operation is planned for LNGS, the same location as DAMA. The second stage for SABRE

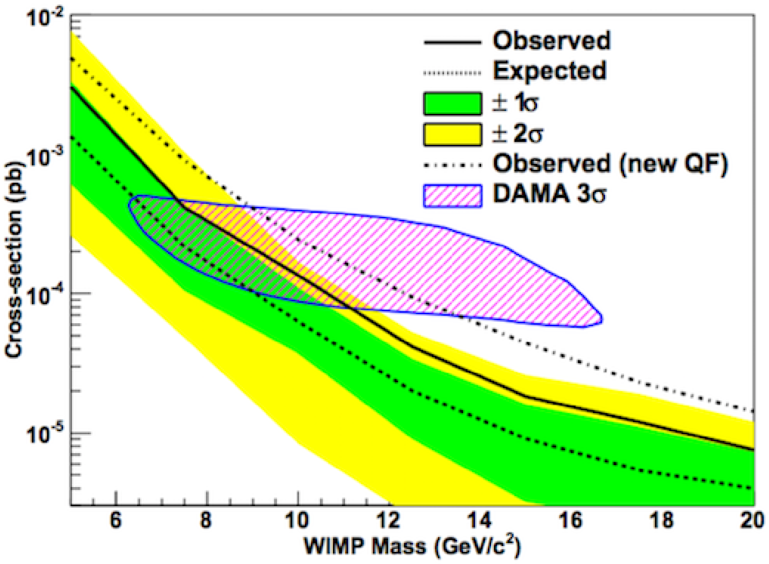

Fig. 2.6 Plot of the latest results from the KIMS CsI(Tl) detectors from Lee et al. [106]. It can be seen that KIMS is cutting into the DAMA allowed region.

is to run in the Stawell Underground Laboratory now under construction near Melbourne, Australia: this will give the southern hemisphere sanity-check gained by DM-Ice when using the South Pole.

2.1.4 Low-Background Crystal R&D

DM-Ice is one of a number of collaborations attempting to grow crystals with lower backgrounds and higher light yields. If it is possible to improve upon the crystals used by DAMA it will lead to a more accurate test of their modulation results. A reduction in the background will lower the chance that any modulation is from the crystal backgrounds and a higher light yield will allow lower energy interactions to be detected. One crystal tested by the DM-Ice collaboration was a crystal grown by SICCAS (Shanghai Institute of Ceramics, Chinese Academy of Sciences) [112]. The next sections show the analysis that has taken place on the SICCAS crystal, which was run in Boulby Underground Laboratory. The first analysis is to estimate the crystal background by looking at the events from alpha decays in the crystal. The second analysis is to look at the light yield of the crystal; this is calculated by using calibration sources of known energies to calibrate the energy deposited in the crystal. A brief description of the SICCAS crystal and setup will be given, along with calculations of the alpha contamination and light yield of the crystal.

Crystal Information

The SICCAS crystal is a 4"×4"⌀ NaI(Tl) crystal with a mass of 3.01 kg. The crystal was grown using Sigma-Aldrich crystal grade powder. The crystal has quartz windows at either end and is in an OFHC copper housing. The crystal is visibly less transparent than the two Alpha Spectra crystals (AS1 and AS2) that were previously used as part of the DM-Ice37 experiment at Boulby [113], so it was expected that the light yield would be worse. Images of both the SICCAS crystal and AS1 are shown in Figure 2.7.

Fig. 2.7 A Photograph SICCAS crystal on the left and the AS1 crystal from DM-Ice37 on the right.

Setup at Boulby

The crystal was installed in Boulby on 4th Dec 2015 and was placed in a light-tight copper box, repurposed from the NAIAD experiment [104], and this was housed in a lead castle with an internal copper layer. The crystal was instrumented with two Hamamatsu R12669 PMTs, FA0139 (Happy) on channel A and FA0134 (Dopey) on B. An image of the crystal in the NAIAD box is shown in Figure 2.8. The PMTs were powered with a CAEN V6533 HV power supply and were run at 1500 V for the first dataset, known as the ‘RivetCatcher’ dataset. The second dataset, known as the ‘SneckLifter’ dataset, had the PMTs operating at 1700 V. The data was taken at both high and low gain, with the high gain channels going through a ×10 NIM fast amplifier. All channels were digitised at 2 V dynamic range by a CAEN V1730B digitiser.

Alpha Contamination

One way to measure the contamination of a crystal is to count the number of alpha events seen in the crystal. The main alpha background in the crystals is from the decay of ^{210}Po.

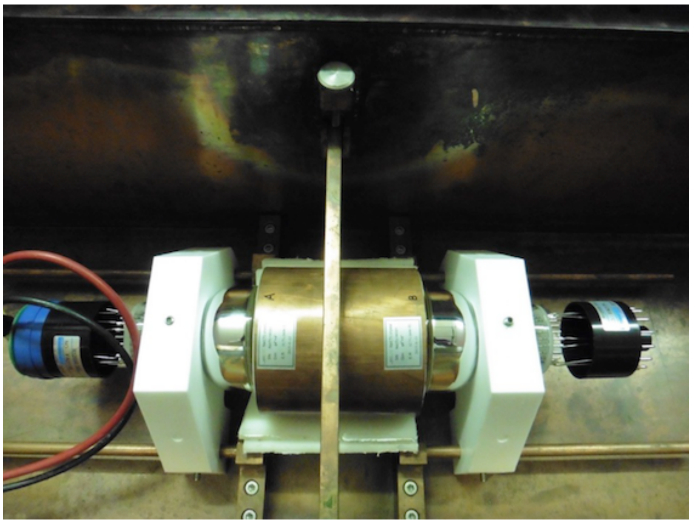

Fig. 2.8 Image of the SICCAS crystal inside a NAIAD box, inside the lead castle with the optically coupled Hamamatsu PMTs on either side.

^{210}Po is produced via the ^{238}U chain, but the main source of ^{210}Po in NaI crystals is from radon contamination during the crystal growing process. This has been shown by the KIMS collaboration [114] where a fit was made to the increase in alpha rate to point back to the date of contamination; an example of this is shown in Figure 2.9. The fit was shown to agree with the dates of crystal growing. Crystal growing teams are attempting to improve methods to reduce these contaminations as the alpha contamination is one of the major backgrounds in NaI(Tl) crystals.

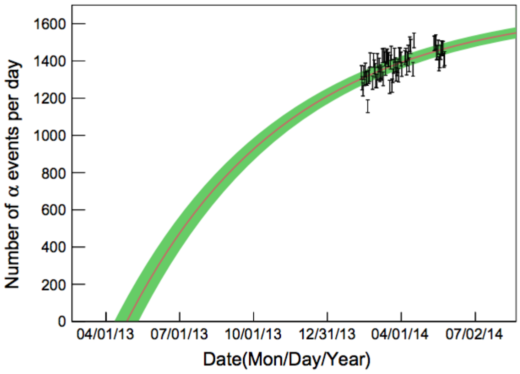

Fig. 2.9 A plot of alpha events against time from the KIMS study from Adhikari et al. [114]. The red line and associated 68% error band (green) show a fit to a model assuming a single instantaneous contamination event. The best fit line shows a match between the start date of the increase and the date of crystal growth.

A separation of alpha events from other events in the crystal can be found using one of two methods: plotting the pulse height against the integrated charge (integral) or by using the mean time of events, τ, as used in analysis of DM-Ice17 data [103] to separate events by their pulse shape. Figure 2.10 shows an average pulse shape from gamma, muon and alpha events with a clear difference between the alphas and the others[103]. The faster decay time from the alpha pulses is due to the shorter tracks from the alpha decays.

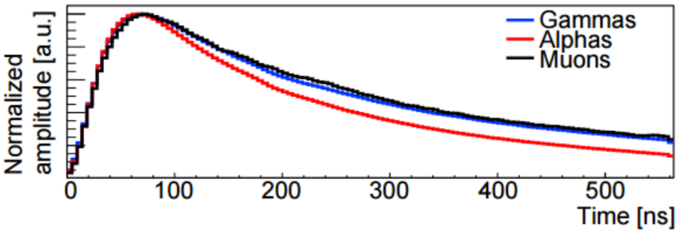

Fig. 2.10 A plot of average waveforms from muon, gamma and alpha events from Cherwinka et al. [103]. The difference between pulse shape of alphas provides the basis of the calculation of the τ parameter.

This difference is the basis of the τ parameter which is calculated by

$$\tau = \frac{\sum h_i t_i}{\sum h_i}, \tag{2.1}$$

where h is the pulse height, t is the time and i is the time bin.

A plot of the maximum pulse height against the integral of the pulse is shown in Figure 2.11 for PMT-A (left plot) and PMT-B (right). These plots are only for the low gain data as the high gain data caused saturation of the ADC. The alpha band can be seen separating from the main band at higher pulse heights.

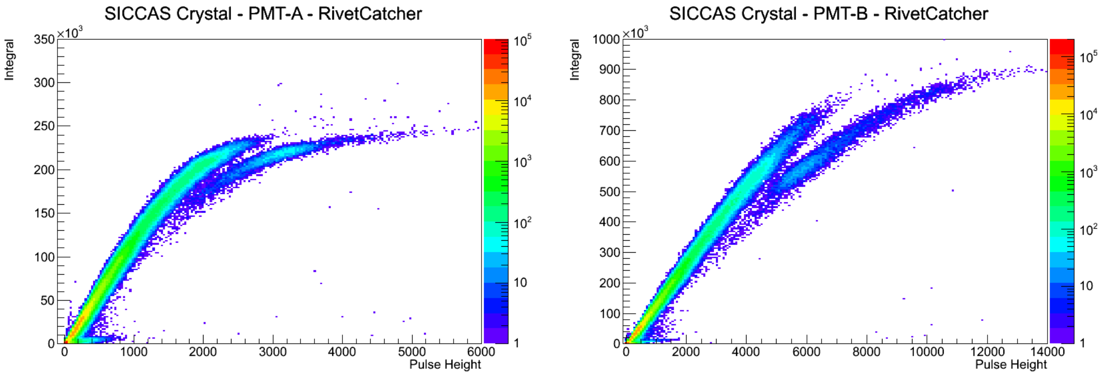

Fig. 2.11 Plot of integral vs pulse height for PMT-A (left) and PMT-B (right).

The alpha band in PMT-B was determined to have a better separation and was chosen to calculate the number of alphas in the dataset. Figure 2.12 shows the selection of alphas used to calculate the contamination of the crystal. The selection was made by eye and a 1% systematic error was determined for the measurement. The contamination of the crystal is calculated by taking the number of alphas in a dataset and assuming that these are all from ^{210}Po. This is assuming that the contamination in the crystal growing phase is dominant compared to the uranium or thorium content of the crystal. The next assumption is that ^{210}Po and ^{210}Pb are in equilibrium so the alpha rate is stable. With these assumptions we can take the rate of alphas and calculate a contamination in terms of mBq/kg. In the case of PMT-B here there are 7380 ± 160 events inside the box. The RivetCatcher castle-closed dataset used was 15 days long, using this and the 3.01 kg mass of the crystal, we obtain a contamination of 1.89 ± 0.04 mBq/kg. It can be seen that events in this band appear at lower pulse heights and integrals but due to the cross over with the main band of events these are not included here. This means that the figure shown here is a lower limit on the contamination.

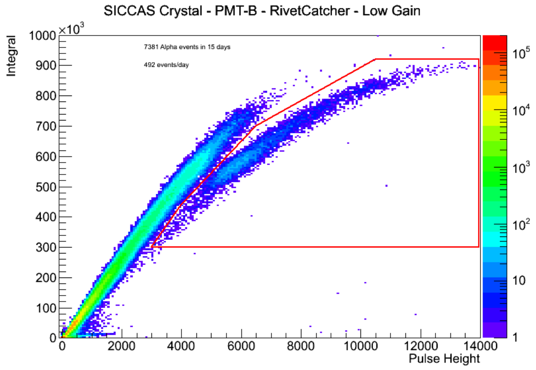

Fig. 2.12 Plot of integral vs pulse height for PMT-B showing the chosen alpha events.

To confirm the result found by using the pulse height vs integral plot, a comparison was made by using the τ parameter and plotting this against the integral. The plots for both PMTs at both high and low gain are shown in Figure 2.13. PMT-B shows better separation than PMT-A in both gains, as in the pulse height vs integral plots. The high gain plots were both used to calculate the contamination of the crystal, with the events chosen shown in Figure 2.14.

There were 7520 ± 160 events from PMT-A and 7600 ± 160 from PMT-B; this results in contaminations of 1.93 ± 0.04 mBq/kg and 1.95 ± 0.04 mBq/kg respectively, as with the previous measurement, these results are the lower limits of contamination.

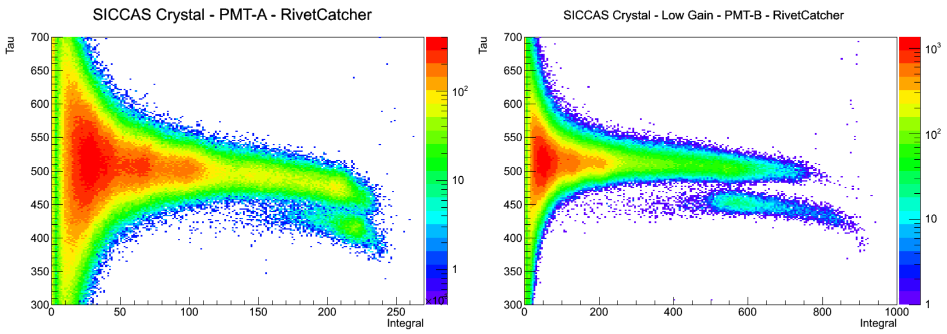

(a) PMT-A low gain

(b) PMT-B low gain

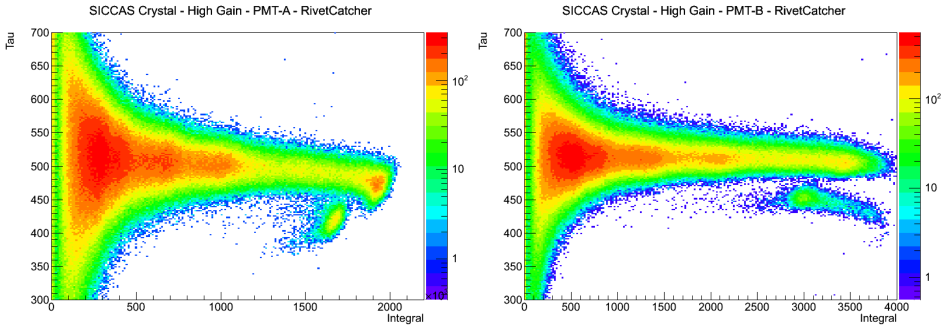

(c) PMT-A high gain

(d) PMT-B high gain

Fig. 2.13 Plots of τ (tau) vs integral for PMT-A and PMT-B at both high and low gains.

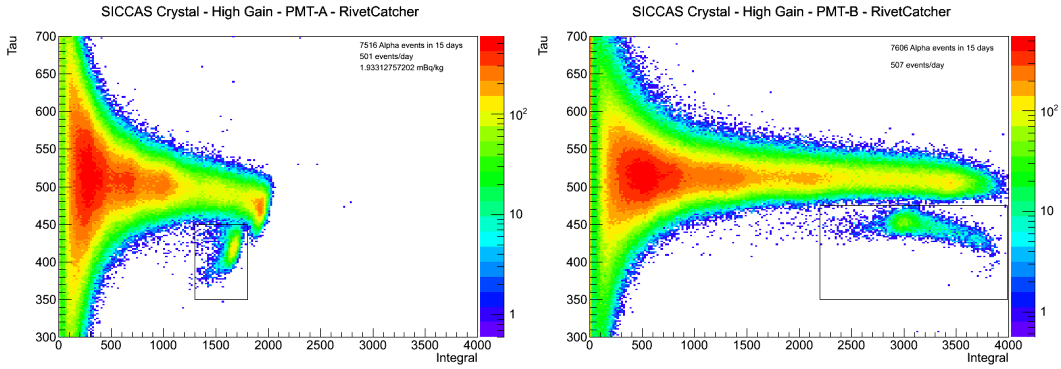

Fig. 2.14 Plots of τ vs integral for PMT-A and PMT-B at high gain, showing the chosen alpha events.

As the contamination calculation assumes that all the alphas are from ^{210}Po, to confirm this we look at the spectrum of the chosen alpha events to make sure that the ^{210}Po peak is dominant. The spectra of the events previously selected for PMT-A and PMT-B are shown in Figure 2.15.

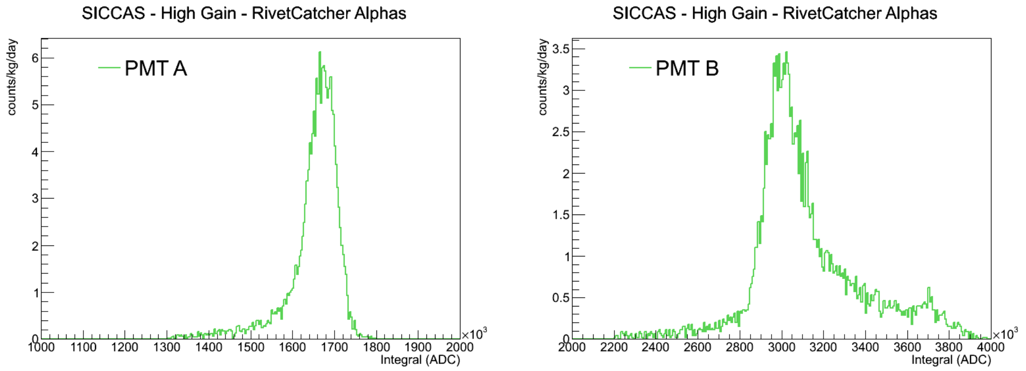

(a) PMT-A

(b) PMT-B

Fig. 2.15 Spectra of alpha events for PMT-A and PMT-B at high gain.

These plots both show a clear ^{210}Po peak from the alpha population, although there is a second small peak in the spectrum of PMT-B around 3700 ADC. This peak could indicate that there is a higher than expected uranium or thorium background in the crystal, but as the ^{210}Po peak is dominant it will be ignored for the purpose of this analysis. It should be noted that the difference in spectra between PMT-A and PMT-B is because PMT-A was close to saturation in the high-gain region, this can also be seen in Figure 2.13.

The results from all three checks of the alpha contamination are all slightly different, which is unexpected as all 3 calculations are using the same events. All the results are shown in Table 2.1. The differences between the results are likely to be from differing efficiencies of the methods with all missing some events that appear to be in the alpha band. As all three calculations have given lower limits the highest, 7600 ± 160 will be taken as the final value. This is $\sim$7% higher than the contamination calculated in the Alpha Spectra crystals that were in DM-Ice37, with both AS1 and AS2 having a contamination of 1.8 mBq/kg [115].

Method	PMT	Gain	Alpha Events	Contamination (mBq/kg)
PH vs Integral	PMT-B	Low	7380 ± 160	1.89 ± 0.04
τ vs Integral	PMT-A	High	7520 ± 160	1.93 ± 0.04
	PMT-B	High	7600 ± 160	1.95 ± 0.04

Table 2.1 Contamination results for SICCAS crystal from number of alpha events.

Light Yield

The light yield of a crystal is the amount of light produced per unit energy. The standard unit used to quote light yields is photo-electrons per keV of energy (PE/keV), this gives the number of photo-electrons inside the PMT from 1 keV of energy deposited into the crystal. The light yield is calculated by taking the ADC units corresponding to one PE (ADC/PE) for the PMTs and combining that with the conversion from keV to ADC calculated using calibration source runs. The ADC/PE values for the PMTs were previously measured to be 200 ADC/PE for PMT-A (known as 'Happy') and 250 ADC/PE for PMT-B ('Dopey') at PMT voltages of 1500 V (corresponding to the RivetCatcher dataset) [115].

There were two calibration runs taken for the RivetCatcher dataset, one with a ^{137}Cs source and one with a ^{60}Co source. A fit was made to the spectrum of both of these source runs to identify the 662 keV peak from ^{137}Cs, and the 1.17 and 1.33 MeV peaks from the ^{60}Co. This then permits a keV to ADC conversion. The resolution of the crystal (17 % for the ^{137}Cs 662 keV peak), along with the fairly low statistics meant that the two ^{60}Co peaks could not be separated. As the peaks have the same expected intensity they were then treated as a single peak at 1.25 MeV. The plots for both sources from PMT-A are shown in Figure 2.16, these were from the low gain data. This gives values of 75,800 $\pm$ 200 ADC for the 662 keV peak and 128,200 $\pm$ 1,700 ADC for the 1.25 MeV peak. It can be seen that these values are not consistent. As no other calibration data were taken to confirm which is correct an average was taken to be the most accurate result from PMT-A. Averaging these gives $9.24 \pm 0.13 \times 10^{-3}$ keV/ADC. Combining this with the 200 ADC/PE value gives a light yield of 0.54 ± 0.03 PE/keV for PMT-A.

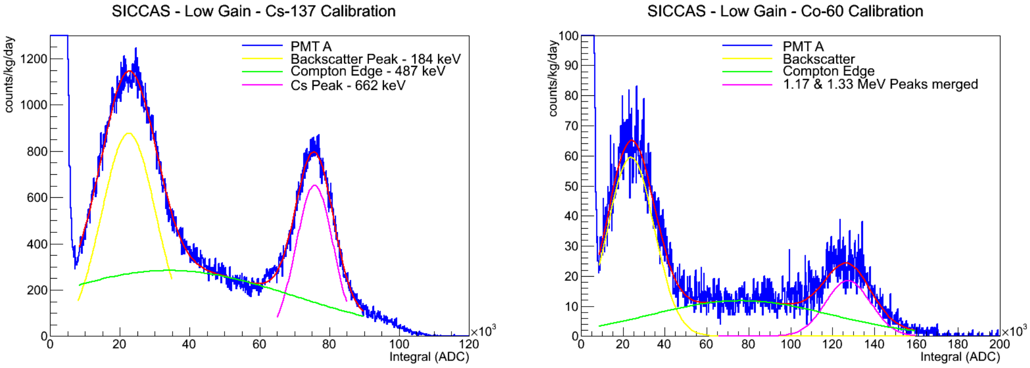

(a) ^{137}Cs calibration (b) ^{60}Co calibration

Fig. 2.16 Calibration spectra for PMT-A.

Similarly, the plots from PMT-B are shown in Figure 2.17, again using the low gain data. Here the value for the 662 keV peak is 190,600 ± 1,200 ADC and for the 1.25 MeV peak it is 355,500 ± 7,500 ADC. These give consistent results and so can be averaged. This gives $3.48 \pm 0.02 \times 10^{-3}$ keV/ADC. Combining this with the 250 ADC/PE value gives a light yield of 1.149 ± 0.007 PE/keV for PMT-B.

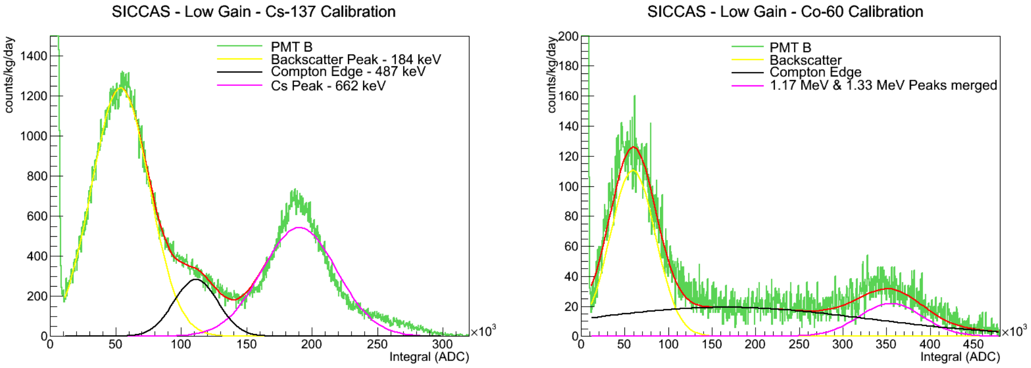

(a) ^{137}Cs calibration

(b) ^{60}Co calibration

Fig. 2.17 Calibration spectra for PMT-B.

The light yields from the SICCAS crystal are quite low, as expected from seeing the colour of the crystal (see Figure 2.7). The results from the SICCAS crystal are shown in Table 2.2; also shown are the light yields from AS1 and AS2 [115]. PMT-A on both the SICCAS crystal and AS2 gives the best comparison of the light yields, as both channels used the same PMT. This shows that the SICCAS crystal has a light yield over 5 times lower than AS2. As the coupling and system are slightly different from that used in DM-Ice37, this cannot be taken as an absolute difference between the crystals, but the dominant effect is from a lower light yield in the SICCAS crystal.

Crystal	PMT	Light Yield (PE/keV)
SICCAS	A (Happy)	0.54 ± 0.03
	B (Dopey)	1.149 ± 0.007
AS1	A (Doc)	2.5
	B (Sleepy)	3.00
AS2	A (Happy)	3.22
	B (Snow White)	2.15

Table 2.2 Light yield estimates for SICCAS crystal and AS1/2 crystals from DM-Ice37.

DM-Ice and other collaborations are using similar methods to determine the best crystals to be used in large-scale detectors to test the annual modulation signal in the DAMA data.

This crystal was an early attempt at crystal growing from the SICCAS group and there will be more crystals with better light yields and lower backgrounds grown and tested in the near future.

2.2 Directional Detection

The second method for using Galactic signals in the search for dark matter is directional detection. Directional detection aims to reconstruct the recoil tracks from WIMP interactions and thus deduce the direction of the incoming WIMPs [91, 116]. Assuming a non-rotating WIMP halo around the Galaxy, it is expected that as the solar system moves around the galactic centre, it will appear that the WIMPs are heading towards us, as a WIMP-wind. Due to the direction of travel, this wind is expected to come from the direction of the Cygnus constellation. This effect produces two observable signals: the first, in the lab frame, is that there should be a modulation of the direction over the course of a day, as the Earth rotates on its axis; this is shown pictorially in Figure 2.18. The second signal is that the direction of the incoming WIMPs is non-isotropic in the Galactic frame. This effect is shown in Figure 2.19 where the left plot shows the original WIMP direction in galactic coordinates and the plot on the right shows the reconstructed nuclear recoil direction. In both plots 'X' marks the position of the detector.

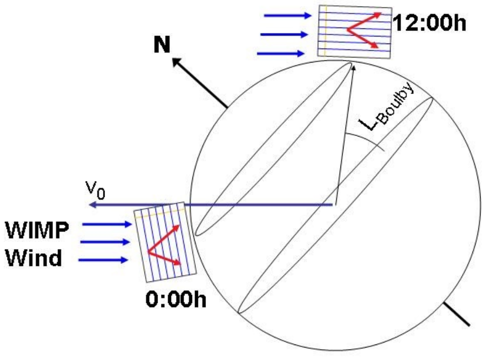

Fig. 2.18 Diagram of the movement of an earth-based detector compared to the WIMP-wind due to the Earth's rotation. Image credit: Sheffield Dark Matter Research.

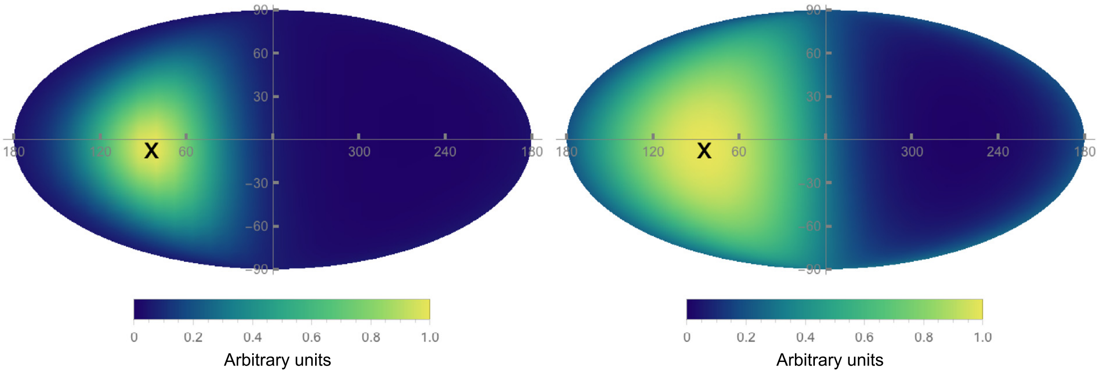

Fig. 2.19 Plot of the expected WIMP signal in the galactic frame, with the incoming direction of WIMPs on the left and the reconstructed nuclear recoil direction on the right. Plot from Mayet et al. [91].

It can be seen in Figure 2.19 that the signal is strongly anisotropic in both cases; this is a powerful tool in discrimination and background rejection as there are no terrestrial backgrounds that should mimic this anisotropy in the Galactic frame. This effect should also allow directional detectors to probe parameter space below what is known as the neutrino floor.

Neutrino Floor

The neutrino floor [91] is the name for the point at which detectors should become sensitive to recoils from coherent neutrino scattering on the nucleus; an example WIMP limit is shown in Figure 2.20 showing the location of the neutrino floor in this parameter space. The scattering from neutrinos is expected to be the major source of background for the typical direct detection experiments described in Section 1.3.2 when they begin to probe this parameter space. The neutrino floor is made of two major components. At low energies, corresponding to WIMP masses below 10 GeV, interactions will be dominated by solar neutrinos. The solar neutrinos are produced in the nuclear fusion reactions that occur in the Sun. The reactions of interest are from ^{7}Be and ^{8}B, these are [117]

$$^7Be + e^- \rightarrow ^7 Li + \nu_e; \tag{2.2}$$

$$^8B \rightarrow ^8 Be^* + e^+ + \nu_e. \tag{2.3}$$

These reactions produce neutrinos of 0.86 MeV from ^{7}Be and up to 15 MeV from ^{8}B.

At energies corresponding to >10 GeV WIMP masses, the interactions will be dominated by a combination of atmospheric neutrinos and neutrinos from distant supernovae; this is known as the diffuse supernova neutrino background (DSNB) [118].

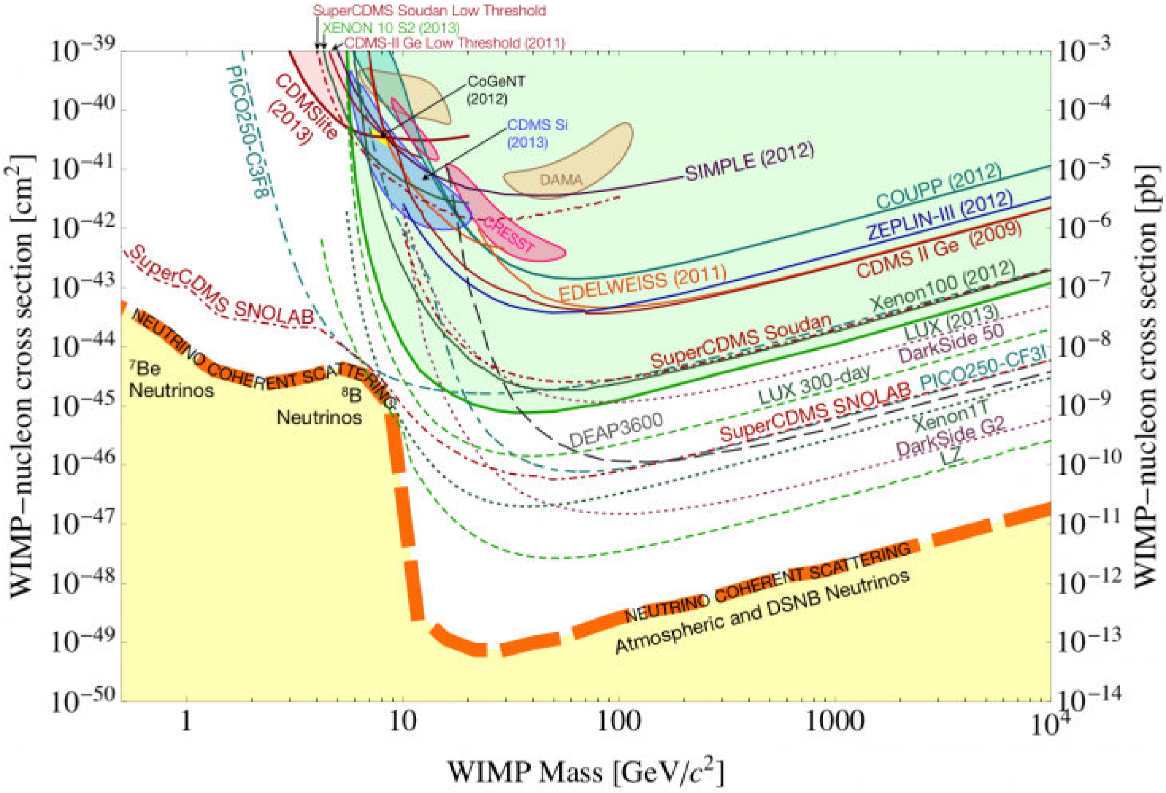

Fig. 2.20 An example plot of the WIMP mass against cross-section parameter space showing the neutrino floor (orange dashed line) along with current and future spin-independant limits set by direct dark matter searches from Cushman et al. [119]. Detectors with a sensitivities high enough to probe below this line are expected to start seeing coherent neutrino scatters.

Using directional detectors, given a high enough sensitivity, it is possible to probe below the neutrino floor in both the high and low energy regions. For the solar neutrinos at the low energies, the direction of the incoming neutrinos will change in the Galactic frame as the earth moves around the Sun. This is shown in Figure 2.21 [91], which is a plot of recoil directions in the laboratory frame. The signals of WIMPs and solar neutrinos will be at their closest point ($\sim 60^\circ$) in February, and at their furthest point ($\sim 120^\circ$) in September [91]. In this plot the WIMP signal is on the left of the neutrinos in the upper row of images and on the right in the lower row. Atmospheric neutrinos are expected to give a near-isotropic distribution in the lab so the anisotropic WIMP signal will be visible over the top of this background, similar to the signal shown in Figure 2.19.

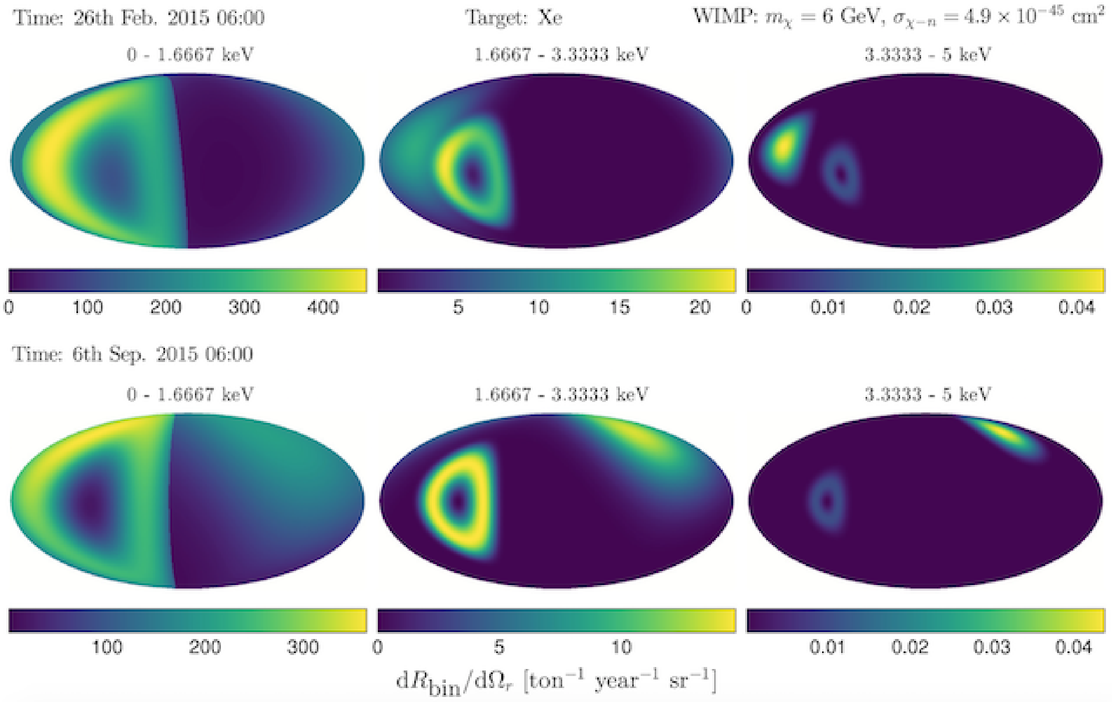

Fig. 2.21 Plot of the expected WIMP and solar neutrino signals in the lab frame from Mayet et al. [91]. In this plot the WIMP signal is on the left of the neutrinos in the upper row of images, corresponding to February 26, and on the right in the lower row, corresponding to September 6 2015. The plots from left to right represent different energy bins with 0-1.6667 keV on the left, 1.6667-3.3333 keV in the centre and 3.3333-5 keV on the right.

Track Reconstruction

When reconstructing nuclear recoil tracks there are two main components, the recoil orientation, which can be in 1, 2 or 3 dimensions, and the recoil direction, or sense, of the track. The recoil orientation of the track is determined by finding the projections in the x, y and z planes; these are also known as the axial range components. The recoil direction is found from an asymmetry in the track; one common example of this is the ‘head-tail’ effect. This is the property in low-energy nuclear recoil tracks that more charge is deposited at the beginning of the track (tail) compared to the end (head). This effect arises from the fact that as the recoil energy decreases for these low energy recoils, so does the dE/dx [120, 91]. It should be noted that the head-tail signature is dependant on the choice of readout, the W-value used (the amount of energy required to liberate one electron from the gas) and the straggling of the recoil track (the deviation of the track from the mean path). The head-tail effect is a powerful signature for rejecting an isotropic background with only $\mathcal{O}(10)$ events required if head-tail is included, as opposed to $\mathcal{O}(100)$ events for a purely axial signal [121]. An example showing this is seen in Figure 2.22 [91] which shows both the change in discovery limit and the limits achievable from detectors differentiated only by their directional capabilities. It can be seen that for a detector with no directional capabilities the number of events from ^{8}B neutrino interactions greatly reduces the discovery limit. It can also be seen that there is around an order of magnitude difference between the limits achievable from a 1D detector compared to 1D with head tail, with factor ∼5 reductions from 2D and 3D detectors. Looking at the WIMP mass vs cross-section parameter space shows that the head-tail sense also gives much stronger limits and probes deeper into the ^{8}B solar neutrino portion of the neutrino floor.

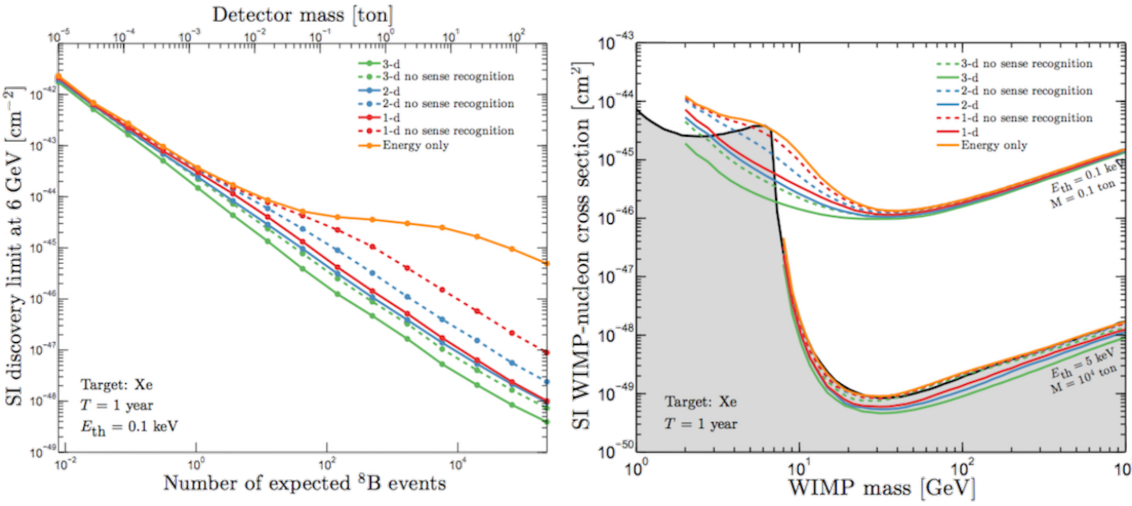

Fig. 2.22 The left plot shows how the discovery limit of a 6 GeV WIMP changes with increasing detector mass, and therefore increasing numbers of ^{8}B neutrino interactions for different levels of directional sensitivity. The right plot shows the limits set in the WIMP mass vs cross-section parameter space for changing levels of directional sensitivity and the inclusion of head-tail sense recognition. Plots from Mayet et al. [91].

The head tail signature has been shown experimentally [122, 123] and is tested in a one dimensional mode with a small THGEM detector in Chapter 7 and with a simplified DRIFT-IId detector in Chapter 8. The next section will discuss the progress of current experimental efforts in directional detection.

2.2.1 Directional detectors

This section describes the current and future efforts in directional detection. The main technology used in direction detection to date is low-pressure gaseous TPCs [91]. The interactions in lower pressures result in longer nuclear recoil tracks of mm-scale compared to nm scale tracks in solids; these longer tracks allow for more accurate track reconstruction in the gas TPCs. In addition to the number of gas TPCs, there are also some higher density targets being tested for their directional capabilities, such as detectors using nuclear emulsions [124] and carbon nanotubes [125]. As the main topic of this thesis is low-pressure gas TPCs, the higher density detection methods will not be discussed in detail. The next sections describe the different gaseous TPC detectors from the different collaborations before discussing the new proto-collaboration CYGNUS, which aims to bring together the whole directional community.

DRIFT

The DRIFT (Directional Recoil Identification From Tracks) collaboration have run a series of detectors in Boulby Underground Lab, UK for over a decade, starting with DRIFT I [126] and up to the currently running DRIFT-IId [127]. The DRIFT collaboration have pioneered the use of negative-ion drift in directional detection to reduce the effect of diffusion on track reconstruction [128] and were the first directional group to develop a m^3 scale detector [126]. The DRIFT experiments have shown sensitivity to the head-tail signature [122, 123] and have set the best WIMP-nucleon cross-section limit of any directional detector by over 3 orders of magnitude with a lowest limit at [127]. The DRIFT-IId detector is described in detail in Chapter 3 along with recent notable results.

DMTPC

The DMTPC (Dark Matter Time Projection Chamber) experiment [129] uses low pressure CF_4 gas and a readout made from a combination of charge signals from a triple-mesh avalanche region and optical signals from PMTs and CCD cameras imaging the avalanche region. The use of CF_4 with electron drift opposed to using negative-ion drift as in DRIFT means that shorter drift lengths are required to prevent results being dominated by diffusion. The DMTPC 10-litre detector produced dark matter results [130] from a surface run with a 35.7 g-day exposure; from this run a 90% C.L. limit was set at 2.0×10^{33} cm^2 for a 115 GeV/c^2 dark matter particle. The detector was then operated in WIPP (Waste Isolation Pilot Plant), New Mexico, USA [130], but no results have come from this underground running. A 20 litre detector, known as the 4-shooter, has also been operated with surface runs to test the directional capabilities of the technology before scaling up to a larger-scale detector [131]. The latest generation detector is a m^3 scale detector, the first for the DMTPC collaboration, and is currently undergoing calibration on the surface before possible deployment in SNOLAB [132]. The m^3 DMTPC detector uses four drift regions which are read out at either end of the detector by a combination of CCDs and PMTs with a different combination is used at either end to compare readout methods for future scale-ups. The charge signal is read out from the ground and +HV planes. A diagram of the detector is seen in Figure 2.23. The CCD cameras are used to image the nuclear-recoil tracks to recover the 2D directional information, with the third dimension coming from the charge readout timing.

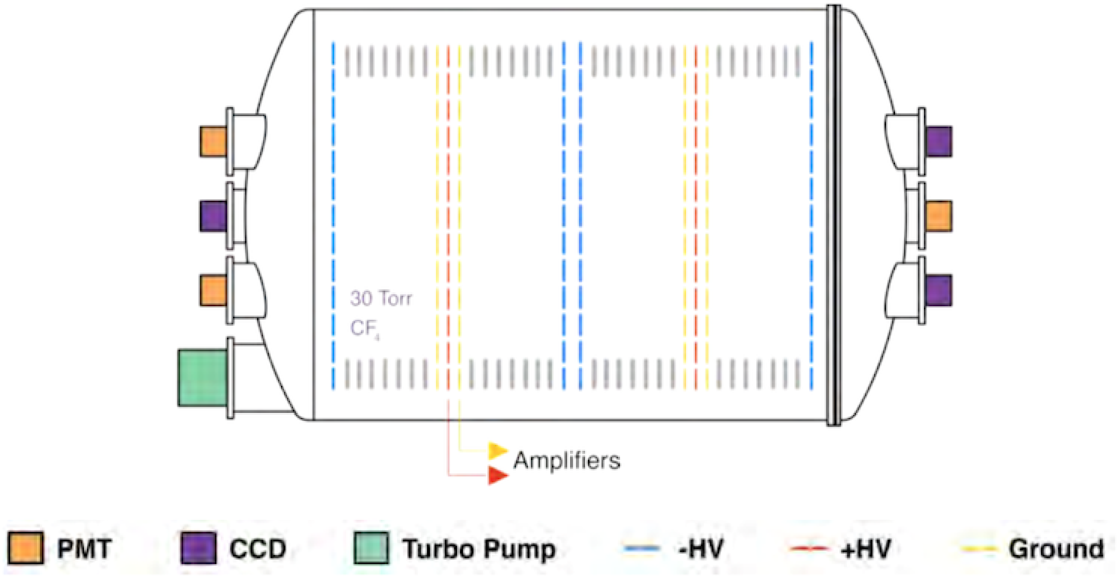

Fig. 2.23 Diagram of the m^3 DMTPC detector. Figure from Leyton [132].

NEWAGE

The NEWAGE detector is run in Kamioka Observatory, Japan [133, 134]. NEWAGE aims to produce a high-definition readout to reconstruct full 3D tracks. The currently running detector is the NEWAGE 0.3b' detector. This detector comprises of a TPC with a $30 \times 30 \times 41\ \text{cm}^3$ volume filled with 0.1 atm of CF_4 gas. The detector readout is a μPIC (micro pixel chamber) detector [133] made of a GEM (Gas Electron Multiplier) 4 mm above an array of pixels used to read out the charge; a diagram of this setup is shown in Figure 2.24. The GEM provides the charge gain to be read out by the pixels. The pixels are used to provide 2D reconstruction of tracks and the third dimension is found from the timing information.

In a recent data run, ‘Run 14’, NEWAGE have shown results on a ‘sky-map’ [134], shown in Figure 2.25, with the reconstructed recoils from the 3D readout used to point back

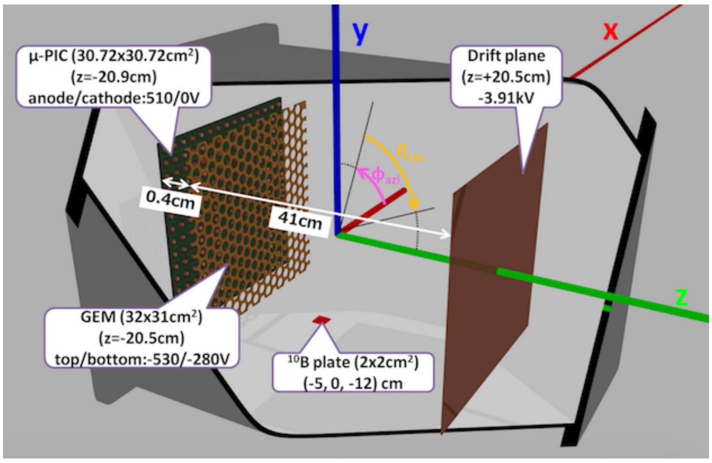

Fig. 2.24 Diagram of the NEWAGE 0.3b’ detector from Nakamura et al. [134].

towards the incoming particle direction in alt-az co-ordinates. Also shown is the position of the Cygnus constellation through the run, which would be the expected direction from WIMP recoils. The search did not produce a positive WIMP signal, but provided a limit on the WIMP mass and cross section with a lowest result at 557 pb for a 200 GeV WIMP.

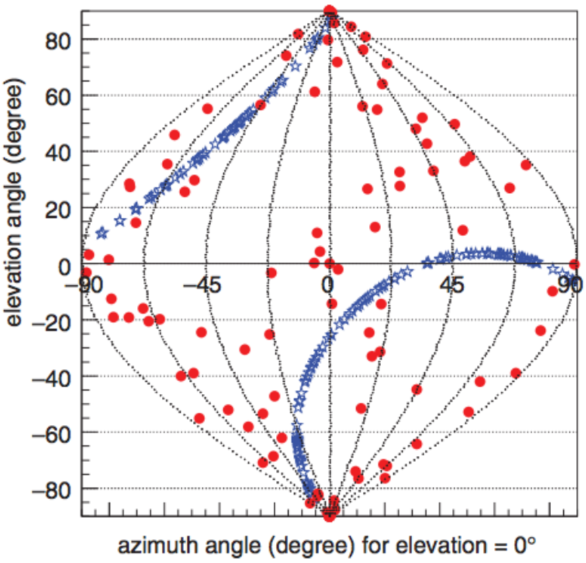

Fig. 2.25 A ‘sky-map’ plot from NEWAGE, showing the incoming particle directions in alt-az co-ordinates (red), also shown is the position of Cygnus through the run (blue). Plot from Nakamura et al. [134].

MIMAC

The MIMAC (MIcro-tpc MAtrix of Chambers) detectors operate in Modane Underground Laboratory (LSM), France [135, 136]. The currently operating MIMAC detector is the MIMAC bi-chamber prototype. The prototype is made of two back-to-back chambers with a detection volume of 10 × 10 × 25 cm^3. The readout is a micromegas-based [135] grid plane to produce the avalanche needed for charge-gain held above a pixelised anode plane used for the readout. A diagram of this is shown in Figure 2.26. The MIMAC detector uses a gas mixture of 70 % CF_4 + 28% CHF_3 + 2% C_4H_{10} at a pressure of 50 mbar. The prototype MIMAC detector has been installed in Modane since 2012 and has shown high definition 3D recoil tracks [137] but has not produced a dark matter limit. The next generation of MIMAC detector will be a m^3 detector made up of a matrix of 16 bi-chamber modules, based upon the design of the prototype.

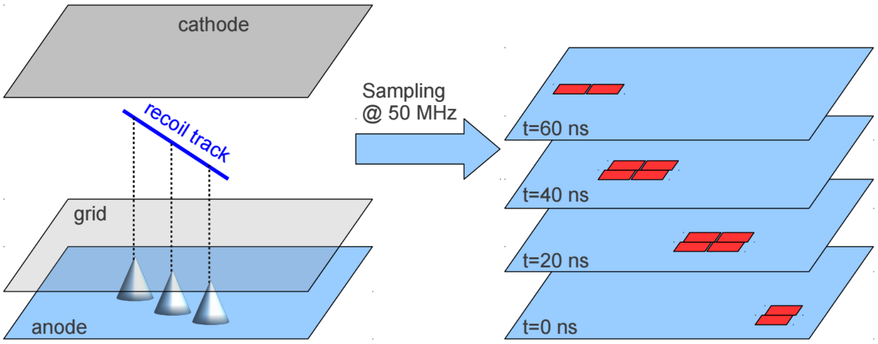

Fig. 2.26 Diagram of the MIMAC detector from Santos et al. [136].

2.2.2 The CYGNUS Collaboration

CYGNUS is a collaboration of the directional community with collaborators from the TPC side with DRIFT, DMTPC, NEWAGE, MIMAC as well as other projects such as D^3 (Directional Dark matter Detector) [138, 139] and NITEC (Negative Ion Time Expansion Chamber) [140]. There are also collaborators from the higher density side of the directional community, such as detectors using nuclear emulsions [124] and carbon nanotubes [125]. A proto-collaboration has now been formed with 5 working groups meeting regularly and a 1 m^3 test-bed for comparing readout methods is to be constructed in Kamioka [141] with first operation expected towards the end of 2017; a diagram of this is shown in Figure 2.27. Another CYGNUS test-bed is already operational in Boulby with tests of a large area detector described later in Section 7.3.

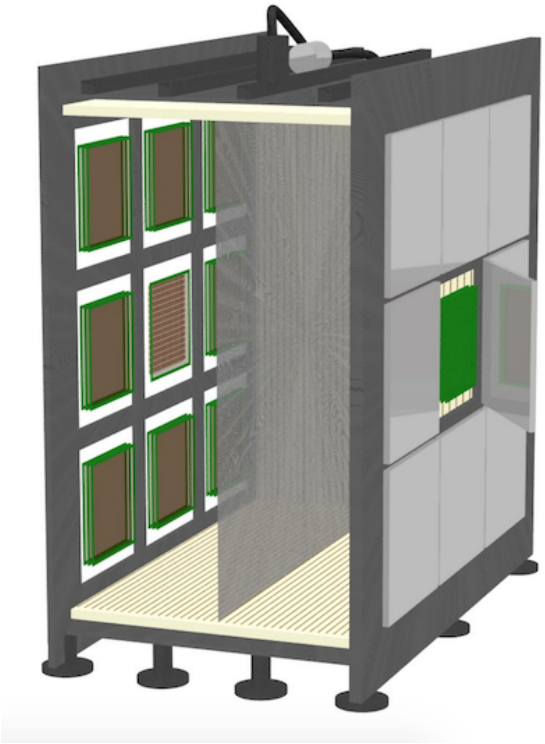

Fig. 2.27 Diagram of the CYGNUS test vessel to be built and run in Kamioka from Miuchi [141].

Currently the different TPC groups are using different readout techniques with different targets. One aim of the CYGNUS collaboration is to try and compare all of these technologies and select one to take forwards. A review of the different technologies has taken place [116] with a more in depth comparison of the technologies in preparation; Table 2.3 [116] gives a brief summary of the technologies used by the four main directional groups using low pressure TPCs.

2.3 Conclusions

This Chapter has discussed the current status of the searches for dark matter using Galactic signals from the WIMP wind: annual modulation and directional detection. The head-tail signature of a recoil track has been discussed and this will be the focus of work in Chapters 7 and 8 with work using a THGEM TPC in SF_6 gas and a simplified DRIFT-IId readout respectively. The current status of annual modulation experiments has been discussed along with an analysis of new crystals in the work towards NaI(Tl) detectors with lower backgrounds and better light yields. The current status of the presently operating directional detectors has been discussed as well as an introduction to the CYGNUS proto-collaboration that aims to combine the efforts of the directional community. The review of directional detectors will be continued in Chapter 3 where the DRIFT-IId detector will be discussed in detail and a review will be made of the recent results from the DRIFT collaboration.

Experiment	Readout	Drift	Granularity (x, y, z)	Fiducial Volume	Gas Gain	Energy Threshold	References
DRIFT	MWPC	Negative Ion	2 mm NA 1μs	0.8 m^3	~ 1000	30 keV$_r$	[123]
MIMAC	Micromegas	Electron	0.42 mm 0.42 mm 10 ns	5 L	2×10^4	1 keV$_{ee}$	[136]
NEWAGE	μPIC	Electron	0.4 mm 0.4 mm 10 ns	36 L	1000	50 keV$_{ee}$	[134]
DMTPC	Optical	Electron	0.3 - 0.6 mm 0.3-0.6 mm NA	20 L	NA	20 keV$_{ee}$	[142]

Table 2.3 A table comparing the main four directional dark matter detectors. Table modified from Battat et al. [116] with information from references within.

Chapter 3

DRIFT-IId Detector

The DRIFT-IId detector is a major part of this thesis in both operations, described in Chapter 4, and data analysis, described in Chapter 8. This chapter aims to give an overview of the current status of the DRIFT-IId (Directional Recoil Information From Tracks) dark matter detector. Section 3.1 introduces the detector technology that is utilised and Section 3.2 describes Boulby Underground Laboratory where the detector is run. Section 3.3 describes the advances required to enable DRIFT to run with zero background and Section 3.4 reviews the recent notable results produced from the DRIFT collaboration including papers on which the Author is a co-author [143–146, 123, 127] because of his contributions to detector operations and analysis.

3.1 The Detector

The DRIFT-IId detector is the latest in a line of negative-ion time projection chambers (NI-TPCs) used by the DRIFT collaboration to search for directional information from interactions of WIMPs [126, 49, 147, 45]. The current detector uses two back to back NI-TPCs with a combined active volume of 1 m^3 and is currently being run inside a $1.52 \times 1.52 \times 1.52$ m^3 stainless steel vacuum vessel at the Boulby Underground Laboratory (see Section 3.2). A schematic of DRIFT-IId is shown in Figure 3.1.

The aim of DRIFT-IId is to search for the interaction of WIMP particles with the target gas. In the early DRIFT detectors the gas was composed of 40 Torr of pure CS_2 gas. CS_2 is used to take advantage of its electronegative properties [128]. Using a electronegative gas results in electrons released from ionisation quickly attaching to a CS_2 molecule, producing a negative ion, CS_2^-. The negative ion then drifts in the electric field of the detector, and has a much lower diffusion effect compared to drifting electrons [128]. The diffusion from a drifting electron or ion is described by

$$\sigma^2 = \frac{4\varepsilon_k L}{3eE}, \tag{3.1}$$

where L is the drift distance, E is the drift field and ε_k is the average energy of the drifting ion or electron. For electrons, at high drift fields, ε_k will rise to several eV compared to thermal levels ($\sim k_B T$) at low drift fields. This increase in electron energy is because the difference between the masses of the electrons and the gas atoms means that the electron energy is not thermalised through elastic collisions. However ions, as they are of a similar mass to the gas, do collide elastically and this allows them to stay thermalised despite energy gained from collisions with the gas. This lower value of ε_k from drifting negative ions results in lower diffusion, as can be seen in Equation 3.1. This lower diffusion is the reason for the use of NI-TPCs by the DRIFT collaboration; for the DRIFT-IId detector the diffusion is < 0.4 mm over the 50 cm drift distance.

In late 2010 the DRIFT gas was modified to add CF_4 with a new operational mixture of 30-10 Torr CS_2-CF_4. The addition of CF_4 was to give the detector sensitivity to spin-dependent WIMP interactions [45]. The current operational gas has an additional 1 Torr of oxygen to give a mixture of 30-10-1 Torr CS_2-CF_4-O_2 [148]. The oxygen component was added to allow the z dimension of the detector to be fiducialised and will be discussed further in Section 3.3.2.

The readout in DRIFT-IId consists of two multi-wire proportional counters (MWPCs), each 50 cm from a central, texturised, thin-film cathode (see Section 3.3.1), as shown in Figure 3.1. The cathode is held at a potential of –31.9 kV to produce the drift field. A field cage of equally spaced stainless steel field rings is around the drift volume to keep the field uniform along. Each MWPC consists of 3 wire planes: a central anode plane of 552 × 20 μm vertical wires spaced 2 mm apart, and two outer orthogonal planes of 100 μm wires making up the outer grids, also with 2 mm spacing. The grid planes are located 1 cm from the anode plane and are held at –2.884 kV. The high field between the grids and the anode produces an avalanche of charge from incident electrons to give a charge gain of $\sim$1000.

As a CS_2^- ion reaches the high-field region in the MWPC the electron is stripped and avalanches in the field; the produced electrons are then detected by the anode wires. By looking at how many anode wires collected charge, along with the 2 mm wire separation, the ‘x’ dimension of the track can be reconstructed. The same can be done with the induced

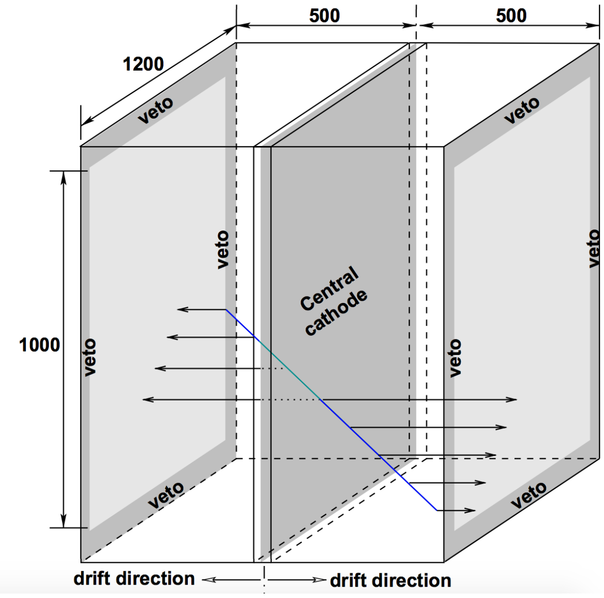

Fig. 3.1 Diagram of the DRIFT detector, showing positions of cathode and MWPCs with dimensions in mm. Diagram from S. Burgos et al. [149].

pulses on the grid wires to extract the ‘y’ dimension. The ‘z’ dimension can be reconstructed using timing information of the charge pulse, with the absolute z position being reconstructed using the fiducialisation method described in Section 3.3.2.

On each side of the anode planes are 11 guard wires (22 total) to step down from the voltage applied to the grids, then 41 veto wires (82 total) to allow rejection of events originating outside the fiducial volume: there are then 448 wires remaining to make up the fiducial area of the anode. The inner grid plane uses the outer 104 wires as a veto and also has a total of 448 wires read out in the centre of the plane. The anode and inner grid wirings are shown in Figures 3.2a and 3.2b respectively. The 448 central wires on both anode and inner grid are grouped, with every 8th wire being connected and read out as one channel; the outer grids are not instrumented. This allows 448 channels to be read out with only 8 channels of Data Acquisition (DAQ). This grouping is used to allow cheaper operation of the detector. As the average length of a nuclear recoil is much less than 16 mm, it does not affect the analysis of nuclear recoil events in the detector. The veto wires on each MWPC are joined together to be read out with one channel for the anode plane and one for the inner grid. Any hit in the veto region on either side will result in the event being rejected in the analysis. This channel grouping allows the entire detector to be read out with only 18 channels of DAQ.

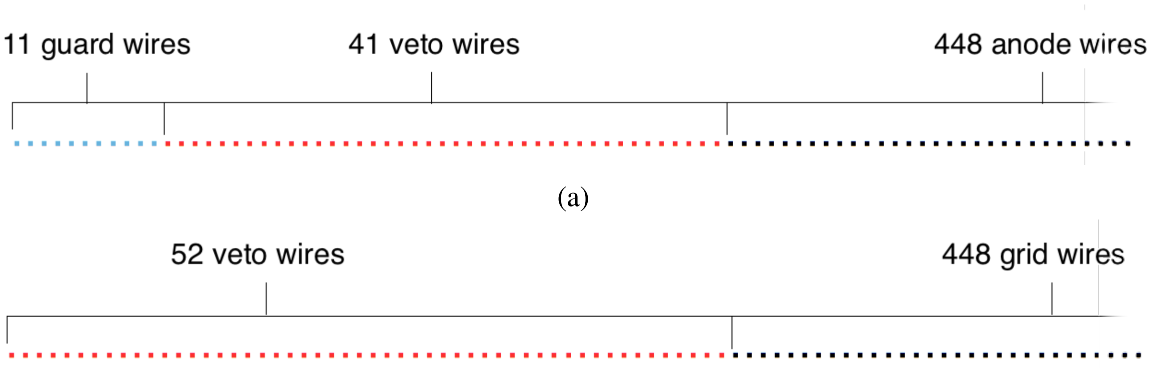

(a)

(b)

Fig. 3.2 A diagram of the guard and veto wires on one side of the anode plane (a) and the veto wires on one side of the inner grid plane (b).

The signals taken from the detector are run through a Cremat CR-111 preamplifier then a Cremat CR-200 shaping amplifier, with a 4 μs shaping time. The signals then go through a high-pass filter, with a time constant of 110 μs, to remove noise. Finally, the signals are digitised in a 14-bit National Instruments PXI-6133 ADC. This digitiser has an input voltage range of –1.25 to 1.25 V and sampling rate of 1 MHz.

3.2 Boulby Underground Laboratory

The DRIFT-IId detector is run in the STFC Boulby Underground Laboratory. The lab is situated 1100 m (2805 m.w.e) underground in Boulby Mine in the North-East of England. The DRIFT collaboration have run detectors in Boulby since the Palmer lab was constructed in 2001. Figure 3.3 shows the DRIFT-IId detector outside the vacuum vessel in the Palmer Lab. The DRIFT-IId detector has recently moved from the Palmer lab to the newly constructed lab at Boulby, and is currently being recommissioned after the move.

Although the lab has a substantial reduction in the cosmic ray flux compared to the surface [150], the detector is still in need of shielding from any neutrons produced by the cavern walls, as any neutrons in the fiducial volume will give a WIMP-like nuclear recoil signal. In the Palmer lab the vacuum vessel was surrounded by a wooden structure holding an average of 40 g cm^{-2} of shielding in all directions; in this case the shielding consisted of polypropylene pellets. In the new lab the shielding is largely composed of water, with a tiled wall of water blocks around the sides of the detector. A combination of polypropylene sheets

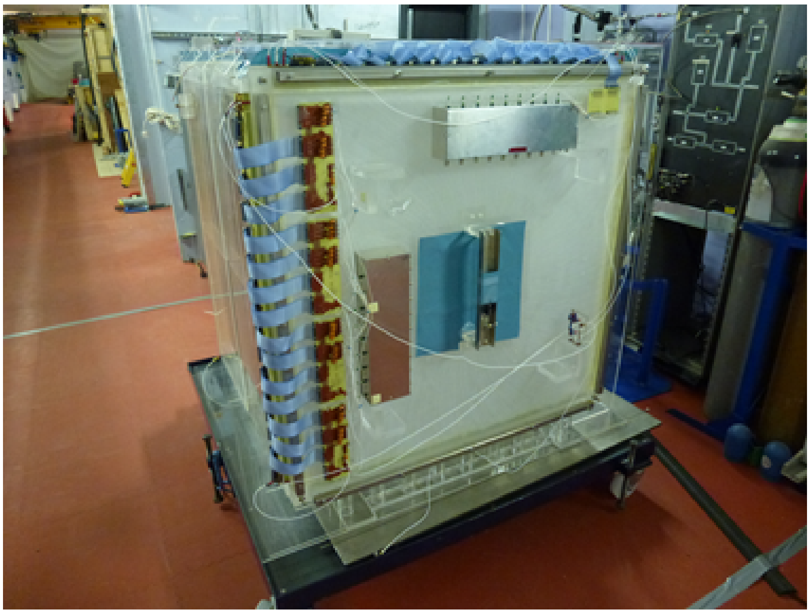

Fig. 3.3 Photograph of the DRIFT-IId detector outside the vacuum vessel in Boulby Underground Laboratory.

and water blocks provides the shielding above the detector and a mixture of polypropylene sheets and underfloor pellets provids the shielding below. This combination of shielding gives an average of over 47 g cm^{-2} of shielding. GEANT4 simulations have shown both shielding configurations give much less than 1 neutron induced recoil per year inside the detector per year.

3.3 Background-Free Operation

Through a combination of two main innovations, in addition to the previously mentioned shielding, the DRIFT-IId detector is now able to run background free. The first of these is the introduction of a 0.9 μm aluminised-mylar thin-film central cathode [146] with the other being the ability to fiducialise the detector using the addition of O_2 to the gas mixture [148].

In the past the main backgrounds of the DRIFT detector were from radon progeny recoil (RPR) events. These events come from the decay of radon gas inside the detector. The ^{218}Po ions from radon decays are generally positive and so drift to the cathode of the detector. When they arrive at the cathode they ‘plate out’ on the surface. Because of the alpha emitted in the decay these events are easily rejected and are dubbed ‘tagged RPR’ events. The events that caused the background in DRIFT are the subsequent decays of the plated out daughter nuclei, ^{218}Po, ^{214}Po and ^{210}Po. A diagram of the relevant part of the ^{222}Rn decay chain is shown in Figure 3.4. The result of these decays is an alpha particle and a recoiling nucleus. If the thickness of the cathode is large enough, the alpha particles can be stopped and not seen in the detector. In this case the recoiling nucleus produces a WIMP-like nuclear recoil event in the fiducial volume.

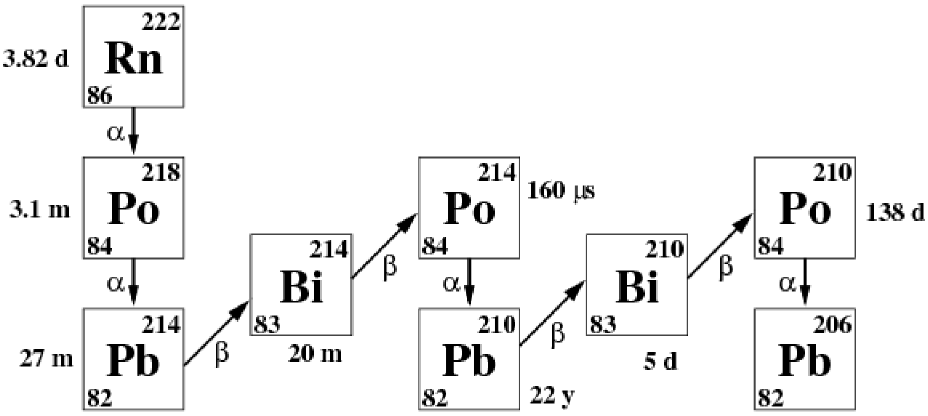

Fig. 3.4 A diagram of the ^{222}Rn decay chain which is the basis for the RPR backgrounds in the DRIFT-IId detector. Figure from [151].

3.3.1 Texturised Thin-Film Cathode

The original DRIFT cathode was made of an array of 20 μm stainless steel wires [146]. The decays from ^{218}Po(^{214}Po) give alphas with a path length of 12.4(17.8) μm in stainless steel, so the alphas could be fully stopped by the cathode. The introduction of a 0.9 μm aluminised-mylar thin-film central cathode, shown in Figure 3.5, led to a large reduction [146] in the number of untagged RPR events as a larger fraction of the alphas could now pass through the cathode, be detected and rejected as tagged RPR events.

The cathode has also been 'bead-blasted' using uniformly sized, spherical glass beads; this further reduces the chance of an alpha particle not appearing in the gas volume. A diagram illustrating the theory behind the bead blasting is shown in Figure 3.6.

In total the change to the new cathode has reduced the RPR background in DRIFT-IId by a factor of 70 ± 20 and now results in 99.97% of RPR events being rejected by alpha tagging [146].

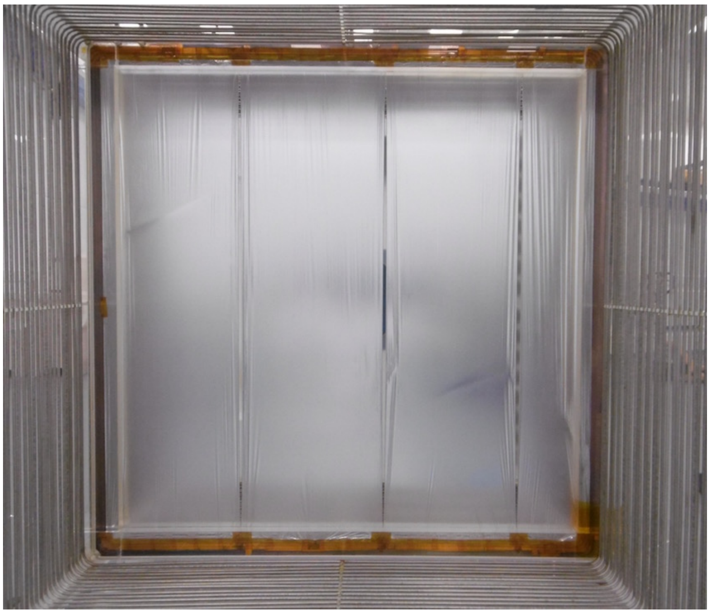

Fig. 3.5 Image of the 0.9 μm aluminised-mylar thin-film central cathode. In this image the cathode is shown in place in the DRIFT-IId field cage.

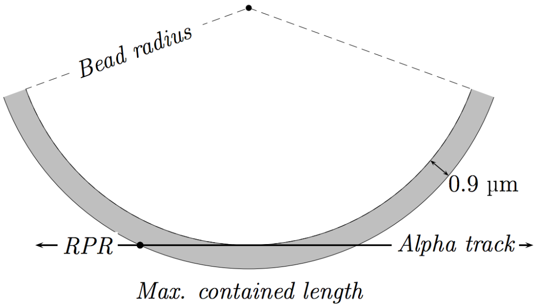

Fig. 3.6 Diagram of the effect from bead blasting the thin-film central cathode From Battat et al. [146]. The maximum contained length of an alpha particle from an RPR event is shown. This length is shorter than the length of an alpha track so the alpha particle enters the gas volume.

3.3.2 Z-fiducialisation

To run completely background free the DRIFT detector needs to be able to reconstruct where in the z-dimension the events are happening. This would allow any remaining RPR events to be rejected by placing a cut on events coming from the cathode. The addition of 1 Torr oxygen to the mixture gives this fiducialisation. When oxygen is added to the mixture, rather than a single peak from a drifting CS_2^- anion, four peaks are found [148]. An example event is shown in Figure 3.7 showing the main ionisation peak (I peak) and the three extra peaks that have been called minority carriers; these are known as the D, P & S peaks.

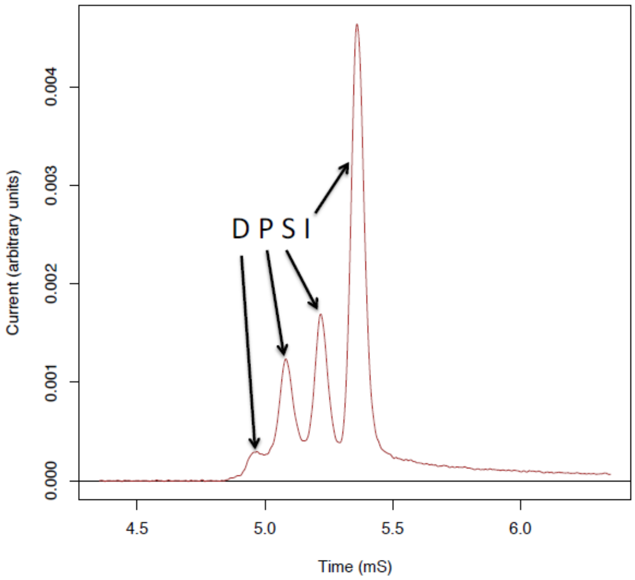

Fig. 3.7 Plot of the minority peaks appearing in a dataset from DRIFT-IId from Snowden-Ifft [148].

The cause of the minority carriers' appearance in the presence of oxygen is proposed to be from Bloch-Bradbury mechanisms [152–154], but this is still under investigation. Due to the fact that the peaks all have different drift velocities through the gas, the separation between the peaks can be used to calculate the z position of an event, as the further an event occurs from the MWPC, the larger the separation between the peaks when they reach the anode. The distance travelled, z, is calculated by

$$\Delta t_{S,P} = \left(\frac{1}{\mu_I} - \frac{1}{\mu_{S,P}}\right)\left(\frac{p}{E}\right) z, \tag{3.2}$$

where $\Delta t_{S,P}$ is the difference of arrival time between I peak and S or P peak, μ_I and $\mu_{S,P}$ are the mobilities of the respective peaks, p is the pressure, E is the electric field and z is the distance between ionisation and the MWPC. The relation is then calibrated by using the distribution of remaining RPR events that occur at the central cathode, as this distance is known to be 50 cm from the MWPCs.

Using a combination of the above techniques it is possible to run background free with DRIFT-IId. An example run is shown in Figure 3.8 where the tan line surrounds the fiducial volume, with a cut on the z at 48 cm to remove the RPR events from the cathode [127]. This location of this cut is chosen by taking the z distance of the lowest RPR multiplied by 5×Δz, where Δz is the z reconstruction precision described in [145]. From this plot it is seen that no events are inside the fiducial volume for the run of 45.4 days, thus the aim to run background free has been achieved for this run.

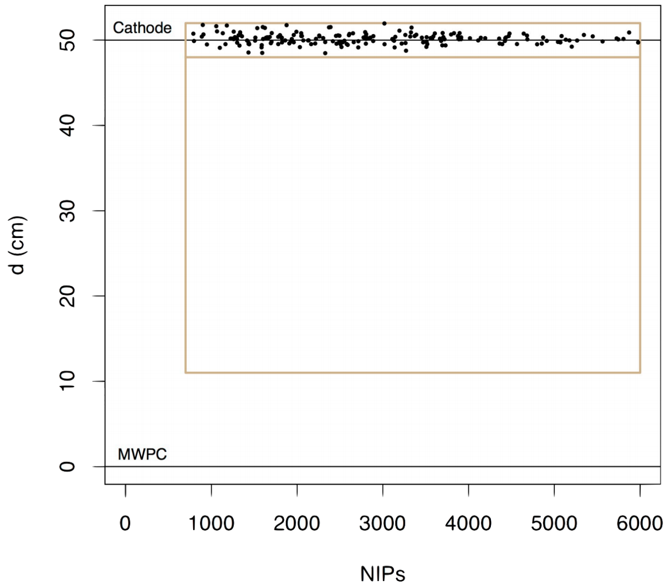

Fig. 3.8 A figure showing the background free fiducial volume from a 45.4 day shielded run with the DRIFT-IId detector in the z vs NIPs (Number of Ion Pairs) plane from Battat et al. [127]. The fiducial volume is enclosed in the tan box with the RPR population seen around the cathode.

3.4 Recent Results from DRIFT-IId

This section reviews results from the DRIFT experiments over the last few years and provides the basis for the later work described in Chapter 8. The latest results on the directional capabilities of DRIFT after the inclusion of oxygen to the gas mixture are discussed in Section 3.4.1. Section 3.4.2 describes the improvement in efficiency in analysis compared to previous results, Section 3.4.3 shows the results from unshielded running of the detector looking for neutrons from the rock at Boulby and Section 3.4.4 shows the latest limit on WIMP interactions from shielded runs.

3.4.1 Direction Sensitivity

In 2009 it was shown that DRIFT is sensitive to the head-tail effect when running in pure CS_2 gas [122]. This was demonstrated by placing a neutron source at different positions around the detector to look for a difference in the signal coming from the head-tail effect. This test was repeated with the new CS_2-CF_4-O_2 gas mixture to confirm that DRIFT-IId is still sensitive to the head-tail effect when fiducialisation is included [123]. The method for calculating the head-tail parameters was the same as used in Ref. [122], with only the I peak being used in the analysis of these runs. The head-tail is calculated by comparing the amount of charge in the beginning of the track compared to the end. In DRIFT-IId the best way to calculate this is to use the timing information from the incoming charge. This gives the ±z directions as the optimal directions for this work. For each incoming event, the charge in the first and second halves of the I peak is integrated to give the parameters η_1 and η_2 respectively. Figure 3.9 shows how these parameters are calculated.

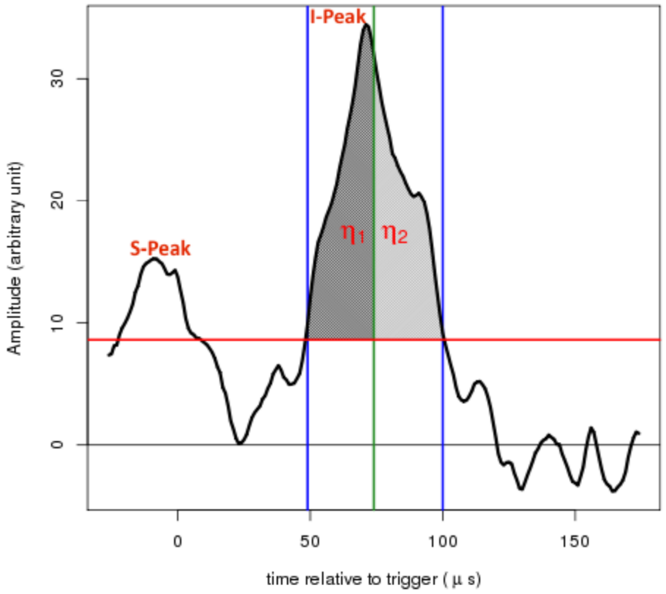

Fig. 3.9 An example event showing the method for calculating the head-tail parameters. Plot from Battat et al. [123].

The calculated η_1 & η_2, are used to define a ratio

$$\alpha = \frac{\eta_1}{\eta_2}. \tag{3.3}$$

Because more charge is deposited at the start of the track compared to the end, it is expected that an event pointing towards the cathode would have $\alpha > 1$, with an event with $\alpha < 1$ pointing towards the MWPC.

There is an asymmetry caused by the shaping electronics that affects the waveforms. This skews the waveforms slightly so a track parallel to the detector gives $\alpha \neq 1$. This skewing of the pulses is the same direction in the pulses in both detectors. However events travelling in the same direction would give a different signal in each readout due to the configuration of the detector. This can then be used to subtract the skewing of the pulses by combining the mean of α from each readout plane for each neutron exposure. A new parameter $\Delta\alpha$ is defined by

$$\Delta\alpha = \langle\alpha\rangle_L - \langle\alpha\rangle_R. \tag{3.4}$$

To quantify the level of the head-tail effect being seen the parameter δ, defined by

$$\delta = 100\frac{|\Delta\alpha|}{\frac{1}{2}(\langle\alpha\rangle_L + \langle\alpha\rangle_R)}. \tag{3.5}$$

This parameter gives the percentage difference of the head-tail asymmetry and can be used to show both the intrinsic head-tail signature and the sensitivity of the detector to that signature.

To get the data required to compute the δ parameter, a ^{252}Cf neutron source was set up in four configurations. The source was placed on either side of the detector, behind the left and right MWPCs; these runs were known as the +z and –z runs respectively. The source was placed in front of (–x run) and above (–y run) the detector for the other two runs. A diagram of the setup for all four exposures is shown in Figure 3.10. The source was placed 32 cm from the vacuum vessel in the ±z exposures and 132 cm from the vessel in the –x & –y exposures, with the distance helping to give some collimation to the neutrons. The shorter distance on the ±z runs was due to spatial constraints in the lab. The ±z runs were expected to give a positive head-tail result ($\delta > 0$) as they are parallel to the drift plane, so were known as the optimal runs. The orthogonal –x & –y runs were expected to give a null result ($\delta = 0$) to prove the analysis was working as expected; these were known as the anti-optimal runs.

The data from all runs were analysed as described above. The results from this are shown in Figure 3.11, with the blue points showing the results from the optimal data, the red showing the results from the anti-optimal directions and the black points showing the previous results from Ref. [122].

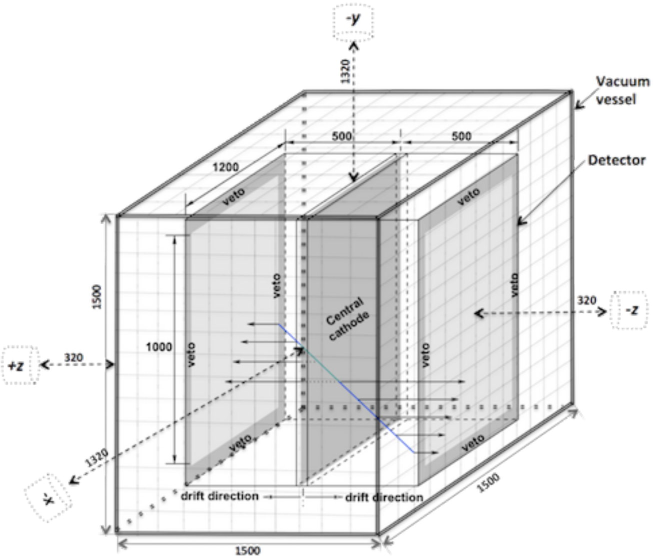

Fig. 3.10 The positions of the neutron source for each of the runs are shown, with the ±z runs being the optimal direction and the –x and –y directions being the anti-optimal directions used for an expected null result. Plot from Battat et al. [123].

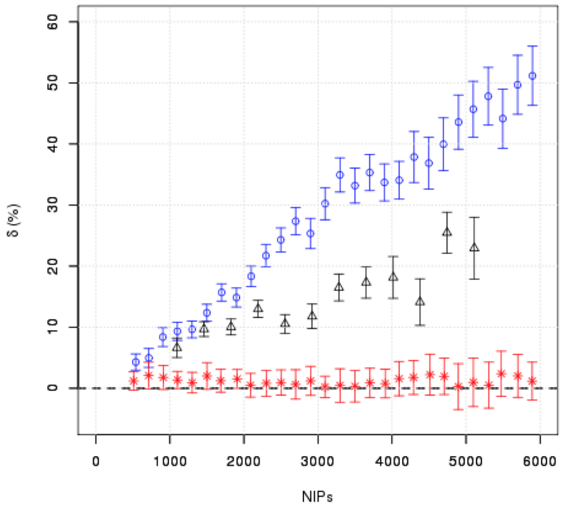

Fig. 3.11 Results from the head tail analysis, with the results from the ±z runs in blue, the –x & –y runs in red and the results from Ref. [122] in black. Plot from Battat et al. [123].

The results show, as expected, that the runs from the optimum direction see a head-tail signature and the anti-optimal runs do not. So it has been shown that DRIFT-IId can still see head-tail with the new fiducialisation mode. There is also what appears to be a greater head-tail effect compared to the results from [122]. This is because the previous work looked only at sulphur recoils where this work also sees carbon and fluorine recoils. As both carbon and fluorine are lighter than sulphur they will have longer recoil tracks; this makes the determination of the head-tail easier and so gives a higher value for δ.

3.4.2 Efficiency Improvement

Aside from the fiducialisation of the detector, the addition of oxygen to the DRIFT gas mixture and its associated minority carriers also caused a drop in the height in the main charge peak (I-peak). As the charge is split between the four peaks, the overall charge, and crucially the peak height, of the I-peak is reduced by $\sim$50% compared to pre-oxygen data. In the results presented in Ref. [145] this effectively doubled the detector threshold compared to the previous work using a CS_2-CF_4 gas mixture. Recently the DRIFT collaboration has lowered the hardware threshold from the previous 30 mV to 15 mV to achieve the same pulse height to threshold ratio, leading to an improved efficiency of the detector.

Figure 3.12a shows a plot of the detector efficiency from data using the high threshold [145]. This is compared to the latest efficiency map from data using the 15 mV threshold in Figure 3.12b [127]. The efficiency is calculated by splitting the detector into several bins in NIPs vs z parameter space. For each bin the number of events from a neutron exposure that pass the analysis is counted and compared to the expected number of events incident in the detector calculated from a GEANT4 simulation [155]. The detector efficiency has improved by a factor of 2 between the two runs which will allow greater sensitivity of the DRIFT-IId detector in future work.

3.4.3 Measurements of Neutrons from Boulby Rock

It was hypothesised that by using the DRIFT detector in an unshielded configuration it should be possible to measure the neutron flux from the cavern walls, and from this calculate the ^{238}U & ^{232}Th content of the rock. To test this the polypropylene shielding around DRIFT was fully removed apart from the shielding placed under the laboratory floor. The detector was run in this unshielded mode in the Palmer Lab at Boulby for 45.4 live-days. Figure 3.13 shows the results of this run, with 14 events passing all cuts.

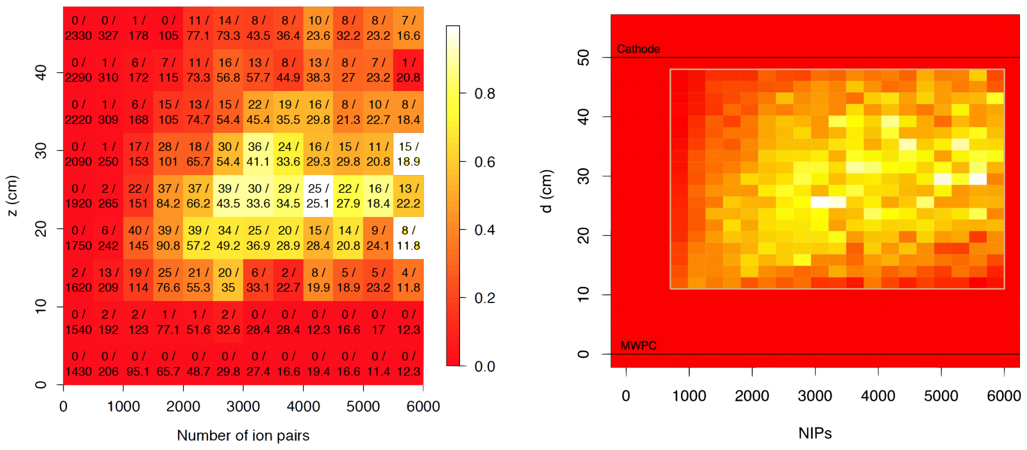

0 / 2330	0 / 327	1 / 178	0 / 105	11 / 77.1	14 / 73.3	8 / 43.5	8 / 36.4	10 / 23.6	8 / 32.2	8 / 23.2	7 / 16.6
0 / 2290	1 / 310	6 / 172	7 / 115	11 / 73.3	16 / 56.8	13 / 57.7	8 / 44.9	13 / 38.3	8 / 27	7 / 23.2	1 / 20.8
0 / 2220	1 / 309	6 / 168	15 / 105	13 / 74.7	15 / 54.4	22 / 45.4	19 / 35.5	16 / 29.8	8 / 21.3	10 / 22.7	8 / 18.4
0 / 2090	1 / 250	17 / 153	28 / 101	18 / 65.7	30 / 54.4	36 / 41.1	24 / 33.6	16 / 29.3	15 / 29.8	11 / 20.8	15 / 18.9
0 / 1920	2 / 265	22 / 151	37 / 84.2	37 / 66.2	39 / 43.5	30 / 33.6	29 / 34.5	25 / 25.1	22 / 27.9	16 / 18.4	13 / 22.2
0 / 1750	6 / 242	40 / 145	39 / 90.8	39 / 57.2	34 / 49.2	25 / 36.9	20 / 28.9	15 / 28.4	14 / 20.8	9 / 24.1	8 / 11.8
2 / 1620	13 / 209	19 / 114	25 / 76.6	21 / 55.3	20 / 35	6 / 33.1	2 / 22.7	8 / 19.9	5 / 18.9	5 / 23.2	4 / 11.8
0 / 1540	2 / 192	2 / 123	1 / 77.1	1 / 51.6	2 / 32.6	0 / 28.4	0 / 28.4	0 / 12.3	0 / 16.6	0 / 17	0 / 12.3
0 / 1430	0 / 206	0 / 95.1	0 / 65.7	0 / 48.7	0 / 29.8	0 / 27.4	0 / 16.6	0 / 19.4	0 / 16.6	0 / 11.4	0 / 12.3

(a) (b)

Fig. 3.12 Efficiency maps of the DRIFT detector from a 30 mV threshold (a) and a 15 mV threshold (b) are shown. Plots from Battat et al. in Refs [145] and [127] respectively.

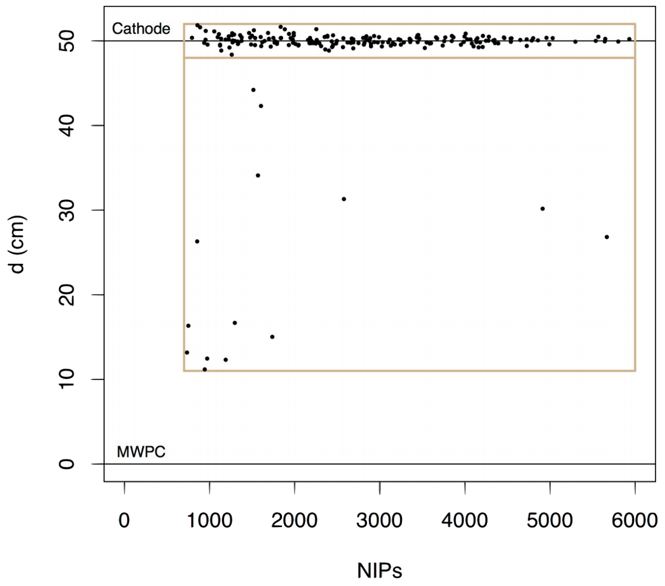

Fig. 3.13 Plot of z vs NIPs for the 45.4 days of unshielded data. There are 14 events seen passing all cuts inside the fiducial volume. Plot from Battat et al. [127].

To test that the 14 events were indeed neutrons and not rock-gammas the DRIFT detector was run exposed to a 56 kBq ^{60}Co source to simulate the rock-gamma flux. A GEANT4 simulation was made to show the similarity between the expected spectrum of rock-gammas and gammas from the ^{60}Co source. The comparison is shown in Figure 3.14. The comparison shows that the two spectra are similar, giving confidence to the test with ^{60}Co. During the ^{60}Co run no events were seen passing through the cuts. A GEANT4 simulation of the detector predicts a rate of 7.8±1.3 Hz from rock-gammas or 3.1 $\times 10^7$ events in the 45.4 live-days of unshielded data. As no events were seen in the ^{60}Co run a gamma rejection factor is calculated as 1.98×10^{-7} (90% CL). This also gives us an upper limit on contamination of 6 gamma events. These results give confidence that 14 events seen in the unshielded data are from rock-neutrons and not from rock-gammas.

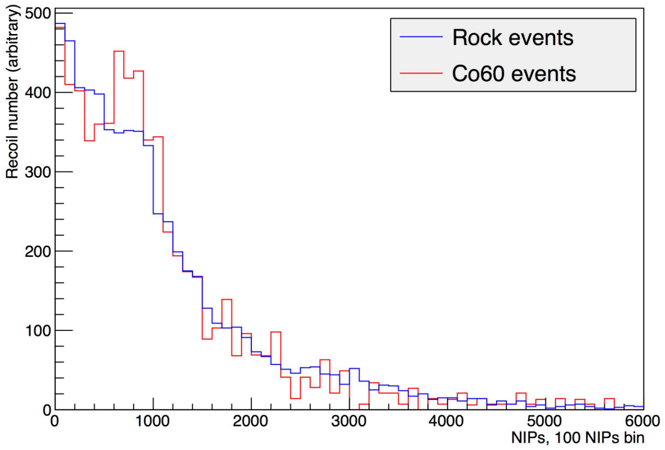

Fig. 3.14 Results from a comparison of gamma spectra from GEANT4 from Battat et al. [127]. The spectra from rock gammas is shown in blue with that of ^{60}Co shown in red.

A full GEANT4 simulation was done of the lab using 10 ppb of both U & Th in the rock [127]. Using the results from this and assuming the 14 events seen in the detector were all neutrons an estimate can be made of the U & Th content of the rock surrounding the Boulby lab. Assuming there is twice as much Th as U [156] and that both decay chains are in secular equilibrium the values are found to be 77 ± 20(stat) ± 7(sys) ppb for ^{238}U and 150 ± 40(stat) ± 10(sys) ppb for ^{232}Th. These results are in good agreement with previous results, Table 3.1 shows this comparison.

Source	Method	^{238}U (ppb)	^{232}Th (ppb)
Smith [157]	Ge Gamma Ray	67 ± 6	127 ± 10
Tziaferi [156]	Gd Scintillator	95 ± 34(stat) ± 21(sys)	190 ± 69(stat) ± 42(sys)
This work [127]	NI-TPC	77 ± 20(stat) ± 7(sys)	150 ± 40(stat) ± 10(sys)

Table 3.1 Results of ^{238}U (ppb) & ^{232}Th contamination from measurements in Boulby. Table reproduced from Battat et al. [127].

3.4.4 Latest WIMP Limit

The last result to be reviewed in this section is a background WIMP search [127]. A further WIMP search analysis is shown in Chapter 8 comparing the detector being read out in a single channel compared to the full DRIFT-IId readout. Here the detector was run in a fully shielded configuration for 54.7 live-days in the Palmer Lab at Boulby. After this run the data were analysed and the results are shown in Figure 3.8.

From these results it can be seen that no events are seen in the fiducial volume in the 54.7 day run. Using these results, along with an efficiency map as seen in Figure 3.12b and a simulation of expected WIMP recoils in the detector, a limit curve on the mass and cross-section of spin dependant (SD) WIMP interactions can be set. The resultant limit curve is shown in Figure 3.15 along with previous DRIFT limits and some other notable results from other collaborations.

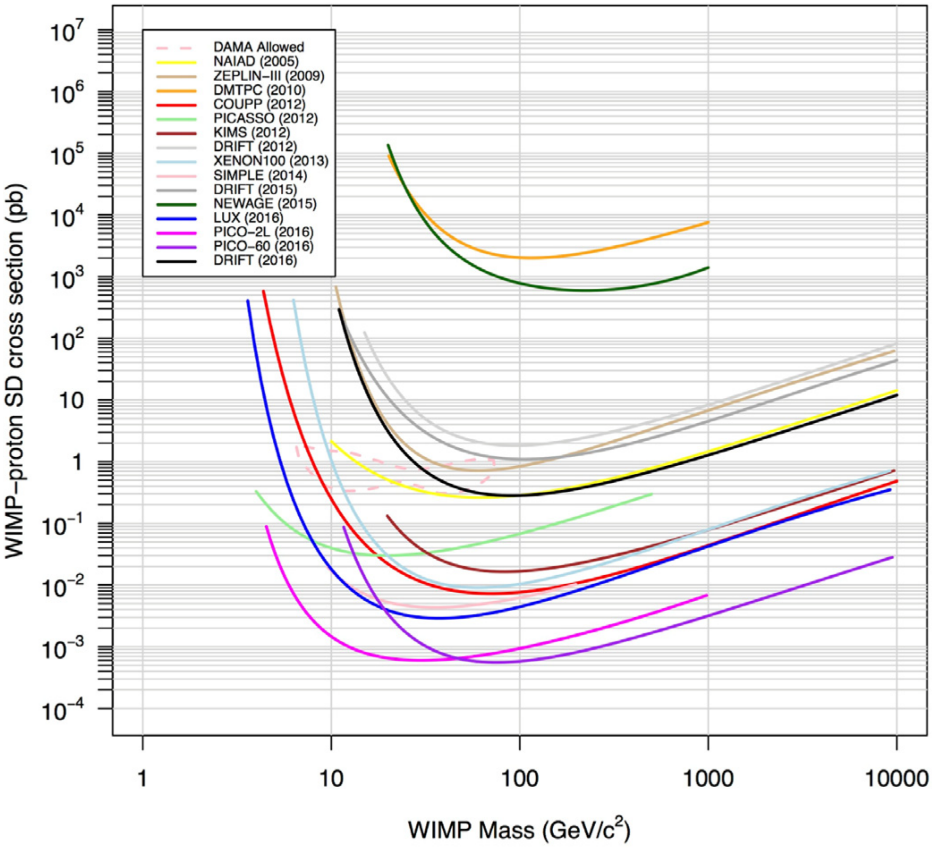

Fig. 3.15 The latest SD WIMP exclusion limit from the DRIFT detector is shown, along with previous limits from the DRIFT collaboration and other notable results from other groups. The plot is taken from Battat et al. [127].

The new limit has a minimum excluded cross-section at 0.28 pb for a 100 GeV WIMP. This is a factor of $\sim$3 lower than the previous published DRIFT result [145] and is lower than any other direction-sensitive detector by 3.5 orders of magnitude. It can also be seen that the new DRIFT limit is cutting into the allowed parameter space found by the DAMA collaboration [100].

3.5 Conclusions

This chapter gave an overview of the workings of the DRIFT-IId detector that is operational in the Boulby Underground Laboratory. It was shown that the DRIFT-IId detector is able to run in a background-free mode thanks to the introduction of a 0.9 μm aluminised-mylar thin-film central cathode and the addition of 1 Torr O_2 to the gas mixture to allow full z fiducialisation.

The chapter also reviewed recent results from the DRIFT experiments. After tests with directed neutrons it has been shown in that the DRIFT detector is still sensitive to the head-tail of a track in the optimal directions after the change of gas mixture. It has also been shown that the efficiency of the detector has been substantially improved by the lowering of the hardware threshold from 30 mV to 15 mV after the loss of charge in the main ionisation peak from the introduction of the minority carriers. A new result on the ^{238}U (ppb) & ^{232}Th contamination of the Boulby rock has been set at 77 $\pm$ 20(stat) $\pm$ 7(sys) for ^{238}U and 150 $\pm$ 40(stat) $\pm$ 10(sys) for ^{232}Th and these results are found to be in good agreement with previous results from other methods. Finally a new spin-dependant WIMP limit has been set from 54.7 live-days of background running, with a minimum of 0.28 pb for a 100 GeV WIMP.

The work presented in this chapter from the DRIFT collaboration provides the basis for the analysis shown in Chapter 8.

Chapter 4

Operations and Modifications of the DRIFT-IId Detector

This chapter describes the operations and modifications made to the DRIFT-IId detector during the author's period of work. Section 4.1 describes the author's contributions towards the running of the detector in Boulby Underground Laboratory. Section 4.2 describes the modifications made to the DRIFT gas system to allow safe running with the addition of O_2 to the gas mixture. Section 4.3 describes the construction and implementation of a cooling system for capturing CS_2 after use in the detector and Section 4.4 describe analysis of gas samples from the detector to assess options for recirculating the used gas after it has left the detector.

4.1 Detector Operations

During the author's period of work with DRIFT, the DRIFT-IId detector has had one of the most successful periods of stable running in the collaboration's history. At the time of writing, since the modifications were made to the gas system (described in Section 4.2), 150 days' shielded data have been taken, $\sim$200 days in total when including unshielded running and neutron exposures.

The author started work on DRIFT-IId in Sept 2013 and was given the responsibility of heading the organisation of operations in the UK since Jan 2014. In this time the author spent over 80 days working underground in Boulby and was in communication with the Boulby team most days when in Sheffield, along with taking 12 hour online shifts of remote monitoring for the detector when it was running.

4.2 Modification of Gas System for O_2

The addition of O_2 to the gas mixture that produced the minority carriers discussed in Section 3.3.2 also led to new safety features being required. CS_2 is a highly flammable substance with a lower flammability or explosion limit of 1.3% [158]; this is the level of oxygen at which a fire or explosion is possible in the mixture. As the nominal gas mixture for DRIFT operations is 30-10-1 Torr of CS_2-CF_4-O_2 it is already over that limit with an O_2 content of 2.4%. To try to lower any risk of fire or explosions three safety features were implemented. Section 4.2.1 describes the modification to the Mass Flow Controllers (MFCs) used with the gas mixing system, Section 4.2.2 describes the addition of flashback arrestors to the system and Section 4.2.3 describes the addition of a nitrogen ballast to the vacuum pump.

4.2.1 Mass Flow Controllers

To ensure a consistent gas mixture the DRIFT collaboration has used an automated gas mixing system since the introduction of CF_4 to the nominal detector gas [159]. The gas system, shown in Figure 4.1, consists of two main chambers, known as the mixing chamber and the supply chamber. The mixing chamber is filled from bottles of CS_2 and CF_4 to get the correct ratio for the detector. Once this is filled to the desired level it fills the supply chamber, which is connected directly to the DRIFT vessel. As the gas is pulled out of the detector by the vacuum pump it is replaced by the gas in the supply chamber to achieve a full gas change in the detector every day.

To control the flow of gas through the system, MKS Type 1479A mass flow controllers (MFCs) are used [160]. On the gas system four MFCs are used: MFC1 and MFC2 control the flow to the mixing chamber from the CS_2 and CF_4 bottles respectively, MFC3 controls the flow between the mixing and supply chambers and MFC4 controls the flow from the supply chamber to the vessel.

To calibrate the rate of flow, each MFC uses a heating element [161]. In normal operation this works well but as the gas mixture in the DRIFT vessel is over the flammable limit of CS_2 and O_2 this heating might produce a spark that could cause problems. It was found that it was possible to bypass the heating element in the MFC to avoid this problem. This led to the MFCs failing to accurately measure gas flow, but this problem is solved by using the pressure gauges in the gas system as triggers to open and close the MFCs at the desired pressures. This adjustment was made in September 2013.

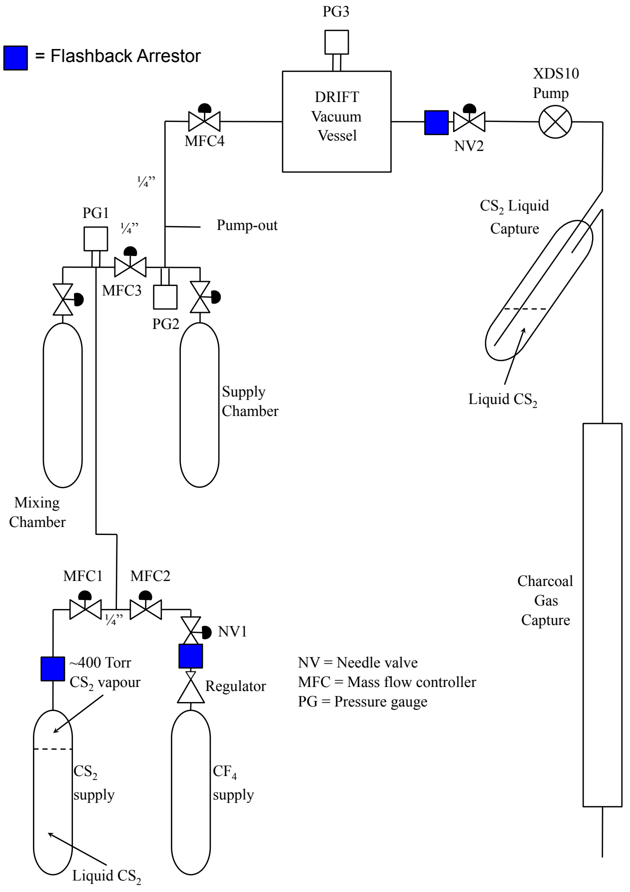

Fig. 4.1 Diagram of the gas mixing system used with the DRIFT-IId detector. Positions of flashback arrestors are shown in blue. Figure modified from Ref. [159].

4.2.2 Flashback Arrestors

To give another level of safety in the gas system three WITT RF53N Flashback Arrestors were added. Flashback arrestors seal up in the event of any fire in the gas system to prevent the fire reaching the gas cylinders and causing further harm. On the gas system the flashback arrestors were put between the CS_2 bottle and MFC1, between the CF_4 bottle and MFC2 and immediately after the vessel. The locations of these are shown in blue in Figure 4.1.

4.2.3 Nitrogen

The final safety feature to allow for the addition of O_2 to the gas mixture was to add a nitrogen ballast to the input of the Edwards XDS10 dry pump used to evacuate the vessel. By adding pure nitrogen to the mixture at the output the mixture can come below the flammability limit of CS_2. This allows the pump to be used as normal rather than any more complex modifications needing to be made as was necessary with the MFCs. The nitrogen flow was calibrated to reduce the mixture to a safe level and then the gas system was ready for constant flow with the new CS_2-CF_4-O_2 mixture. The final change was to swap the pure CF_4 bottle seen in Figure 4.1 for a CF_4-O_2 mixture.

4.3 CS_2 Cooling

On the output of the DRIFT-IId detector is a water-trap to capture the CS_2 after it has left the detector. This trap, shown in Figure 4.2, works via pumping the CS_2 below a layer of water. At atmospheric pressures CS_2 is a liquid with a density of 1.26 g cm^{-3}. When liquid the CS_2 is trapped under the water while the remaining gases from the detector will pass through the water layer to an exhaust system.

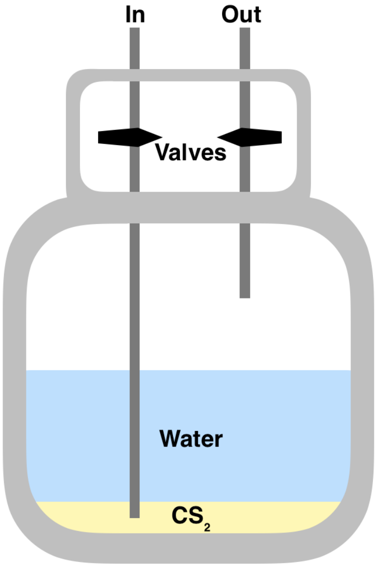

Fig. 4.2 Diagram of the water trap used to capture CS_2. Image credit: Chris Toth

After the introduction of the nitrogen ballast it was seen that the efficiency of CS_2 capture from the water trap went from ~90% to ~0%. It was hypothesised that this was due to bubbles of nitrogen going through the water layer and allowing CS_2 to escape. One method to raise the efficiency back up was to lower the flow of nitrogen, but this would then take the gas mixture back above the flammability limit. It was decided to try and lower the vapour pressure of the CS_2 to solve this problem. The Antoine equation [162] describes the relation between vapour pressure and temperature for a pure substance consisting of gas and liquid in equilibrium. It is given by

$$\log_{10}(P) = A - \frac{B}{T+C}, \tag{4.1}$$

where P is vapour pressure in bar and T is temperature in kelvin. A, B and C are constants. The values corresponding to CS_2 [163, 164] are shown in Table 4.1. The range of validity for these constants for CS_2 with the Antoine equation is 276.74-353.08 K [164]. However it has been shown that using these values with the Antoine equation is consistent with the KDB (Korean DataBank) Correlation Equation for CS_2, which is valid in the range of 161.58-552.00 K [165].

A	4.06683
B	1168.62 K
C	-31.616 K

Table 4.1 Values for the constants of the Antoine equation for CS_2 [163, 164].

Cooling the CS_2 going into and out of the water trap will lower the vapour pressure and thus reduce the risk that the CS_2 escapes as vapour. For convenience, Table 4.2 gives pressures in Torr and temperatures in °C.

To achieve this a cooling system was designed, with the main component being a Peltier cooler. A Peltier cooler takes advantage of the Peltier effect to remove heat from a system. The Peltier effect is the heating or cooling that takes place at a junction of two conductors when a current is flowing. When the current is applied one side of the cooler cools down and the other warms up. For this system a Peltier cooler was thermally coupled to a copper sheet. The cool side on the sheet and the warm side was connected to a computer heat sink to remove the heat from the system. Figure 4.3a shows the Peltier cooler and heatsink connected to the copper sheet. Attached to the copper sheet were two copper tubes through which the DRIFT gas mixture would flow, one on the input to the water trap and one on the output. These tubes were shaped so as to maximise the area in contact with the copper sheet and are

Temp (°C)	Pressure (Torr)
35	520
30	435
25	361
20	298
15	243
10	198
5	159
0	127
-5	100
-10	78
-15	61
-20	46
-25	35

Table 4.2 Comparisons of temperatures and corresponding vapour pressures of CS_2.

shown in Figure 4.3b.

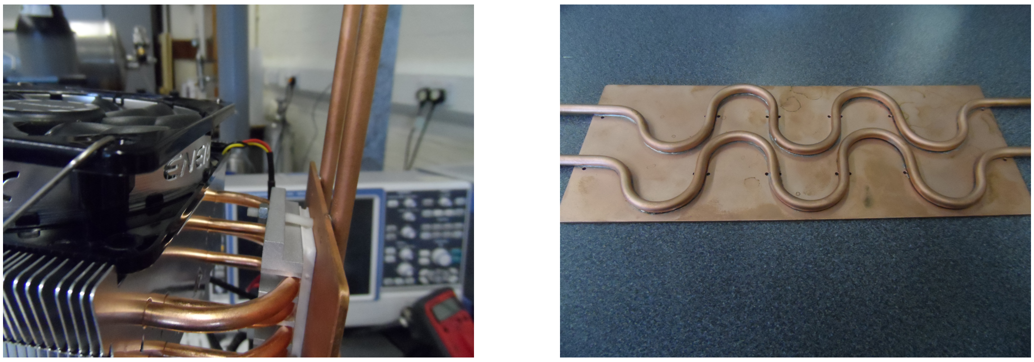
(a) (b)

Fig. 4.3 Image of the cooling system components with the Peltier with heatsink in (a) and the copper plate with copper tubes in (b).

A temperature probe was thermally coupled to the copper plate before the system was insulated to remove heating from the lab environment. The Peltier cooler was insulated and then tested with measurements made from the temperature probe every two minutes. The results of this test are shown in Figure 4.4 and it can be clearly seen that the Peltier cooler has a large effect on the temperature of the plate, with the temperature dropping from 27.1 °C to 15.7 °C over 40 minutes of running. Table 4.3 shows the corresponding pressure change from this cooling which would result in a drop in vapour pressure of 140 Torr.

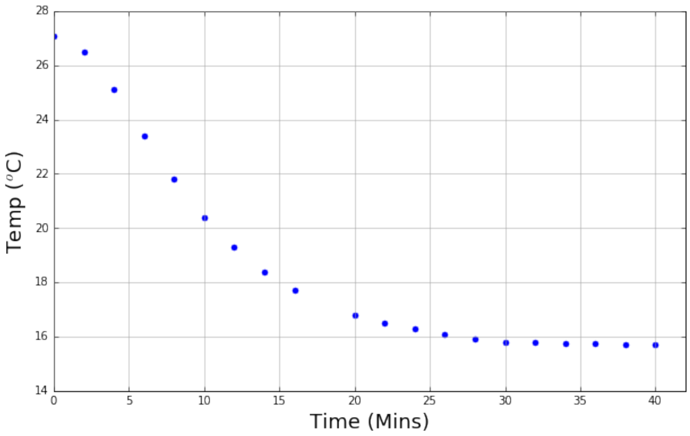

Fig. 4.4 Plot of the temperature drop of the insulated cooling system after power was applied to the Peltier cooler.

Temp ($^\circ C$)	Pressure (Torr)
27.1	391
15.7	251
Difference	140

Table 4.3 Drop in vapour pressure from use of Peltier cooler.

The cooler has now been installed on the DRIFT-IId output system in Boulby and will shortly be tested over long term running when the detector is running with full gas flow in the new lab.

4.4 Residual Gas Analyser Tests Towards CS_2 Recirculation

When the DRIFT detector is operating gas flows through the vessel at a rate of one change per day. This flow is needed to prevent impurities in the gas lowering the detector performance over time. Currently the waste CS_2 is captured in a water trap and disposed of after use. One key idea towards the scale up of the DRIFT detector technology is to recycle the used CS_2 after it has been captured and put it back in the detector. This would save £3000 - £5000/year in gas and waste removal costs.

As the CS_2 is captured below a level of water, the captured CS_2 must be tested for water contamination. To make this measurement a Hiden Analytical HPR-30 Residual Gas

Analyser (RGA) was used. The main component of the RGA is the HAL-201-RC mass spectrometer. The mass spectrometer has three main parts to it: the first is the ion source, whice is used to ionise the incoming gas. The newly produced ions are then accelerated in an electric field into the second part, the quadrupole mass filter. This filter uses an RF electric field which is tuned to only allow particles within a desired mass over energy ratio to pass through allowing detection of masses up to 200 a.m.u. The last part of the mass spectrometer is the detector, which is a dual Faraday and Single Channel Electron Multiplier (SCEM) detector. The SCEM is a secondary electron multiplier which gives the RGA a greater sensitivity than using only the Faraday detector.

A sample of CS_2 was taken after being collected in the water trap and connected to the RGA. The gas was sampled over 20 hours and the RGA measured the level of both CS_2 and water present. The results of this are shown in Figure 4.5 and it can be seen that there is a significant amount of water present in the sample.

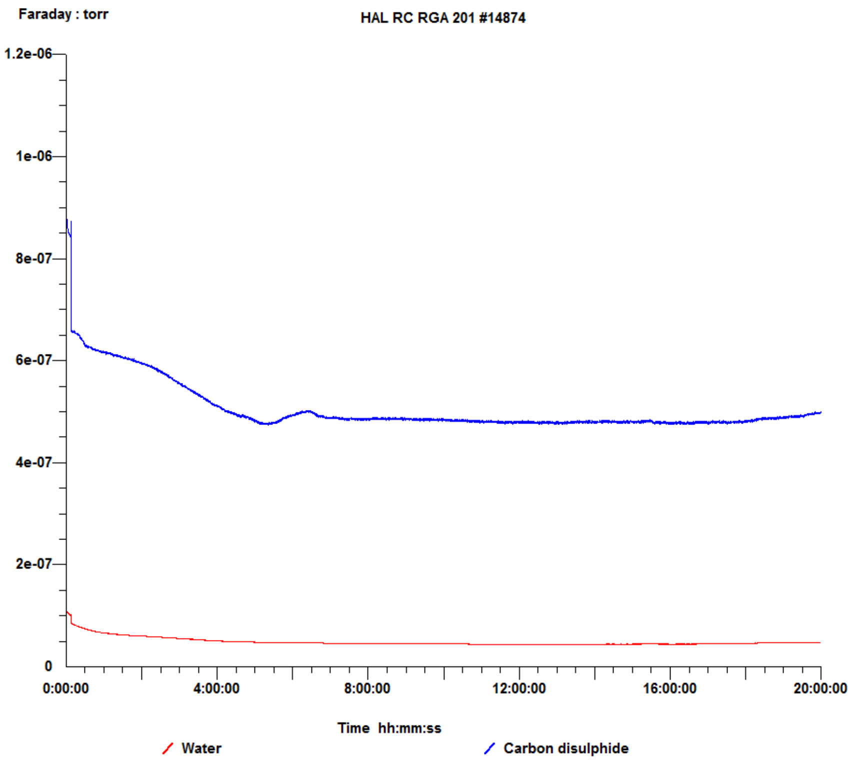

Fig. 4.5 Plot of the proportion of CS_2 and water in the sample. The level of CS_2 is shown in blue with the level of water shown in red.

The first 8 hours of the test were discounted as the levels needed time to settle and it took some time for any remaining gas from the previous tests to be removed from the system and stop having an impact on the results. Over the last 12 hours of the test, the sample consists of 9.3% water on average. The DRIFT detector has a maximum contamination limit of 1% when running, so this shows that in this state the captured CS_2 would not be ready to reuse in the DRIFT detector.

One option for improving upon this would be to change to a cold trap rather than a water trap. Like the cooling system discussed in Section 4.3, this would cool the incoming gas to a temperature such that the CS_2 would liquefy in the trap at the nominal DRIFT operating pressure of 41 Torr. From looking at Table 4.2, this would be in the region of -20 to -25 °C. If this trap was produced then it may be possible to extract pure CS_2 to reuse in the detector. Further study of this technique is planned.

4.5 Conclusions

The DRIFT-IId detector has recently run for the most consistent period since it started operations with 150 days of shielded data and almost 50 days of unshielded and calibration data taken. The recent modifications made to the DRIFT-IId gas system have been discussed which have allowed the DRIFT collaboration to run in a flowing, fiducialised mode to allow the recent background-free results shown in Section 3.4.4.

The design and construction of a cooling system to improve the CS_2 collection efficiency by reducing the CS_2 vapour pressure and has been discussed along with promising initial results.

Finally results from tests using an RGA on samples of captured CS_2 show that the water trap method for CS_2 collection is not adequate for reusing the CS_2 in the DRIFT-IId detector. An alternative method of CS_2 capture by use of a cold trap has been suggested as a suitable alternative and will be the subject of further study by the collaboration.

Chapter 5

Radon Emanation Measurements

Radon has been an important source of background in the DRIFT experiments for a long time [144, 166]. The recent addition of O_2 to the gas mixture and the use of the texturised thin-film central cathode, as discussed in Chapter 3, has led to a reduction in the limitations caused by radon. However in a scaled up detector a large amount of radon inside the detector could still have potential to cause unidentified background events that could mimic WIMP recoils. In the decay of radon and its daughters an alpha particle is ejected leaving a recoiling nucleus. If the alpha particle is not seen in the detector, for example if it were fully stopped in the cathode, as described in Section 3.3, then the nuclear recoil would mimic a WIMP signal. To lower the amount of radon in the detection volume it is necessary to measure the emanation of materials and replace any materials that have a high radon background. In the DRIFT collaboration much work has already been done in this area and the system used for detecting radon emanation from materials in previous work [144, 166] is discussed in Section 5.2. This system is based on the commercially available Durridge RAD7 radon detector, with the aim being to work closely with Durridge to improve the sensitivity of the instrument for precision emanation measurements. Section 5.3 describes the recent improvements that have been made to the emanation system which have led to an improved sensitivity and a lower background. Section 5.4 describes the sample emanation measurements made using the improved system, including materials likely to be used in future low background experiments.

5.1 Radon in Low Background Experiments

One of the biggest and hardest to control backgrounds in rare-event searches such as dark matter or neutrinoless double-beta decay experiments is radon [144, 166–170]. Radon is a decay product in both the Uranium-238 (^{222}Rn) and Thorium-232 (^{220}Rn) decay chains and is the only gaseous element in either chain. Being a gas means that radon can seep out of materials and be released into the surrounding environment, as discussed in [171]. This is especially the case for ^{222}Rn because of the relatively long half-life of 3.82 days [172]. Due to the much shorter half-life of ^{220}Rn (55.6 seconds), it does not have as much time to escape and so poses less of a problem for low background experiments.

5.2 Radon Emanation System

The radon emanation system described in [144] is the starting point for this work. For convenience a brief summary will be provided here. The main component of the emanation system is the commercially available Durridge RAD7 radon detector [173], shown in Figure 5.1a. The RAD7 uses electric fields applied to an internal dome to drift the positively charged radon daughters onto a Canberra PIPS (Passivated Implanted Planar Silicon) detector [174]. The alpha particle from the subsequent decay of the daughters has a 50% chance of interacting with the detector and being recorded. A diagram of the internal dome and detector is shown in Figure 5.1b. In the case of the particle interacting in the detector, the full alpha energy is captured. The amount of energy deposition is then used to identify the decaying nucleus. The PIPS detector measures the alpha energy to a precision of 50 keV in a 0-10 MeV window.

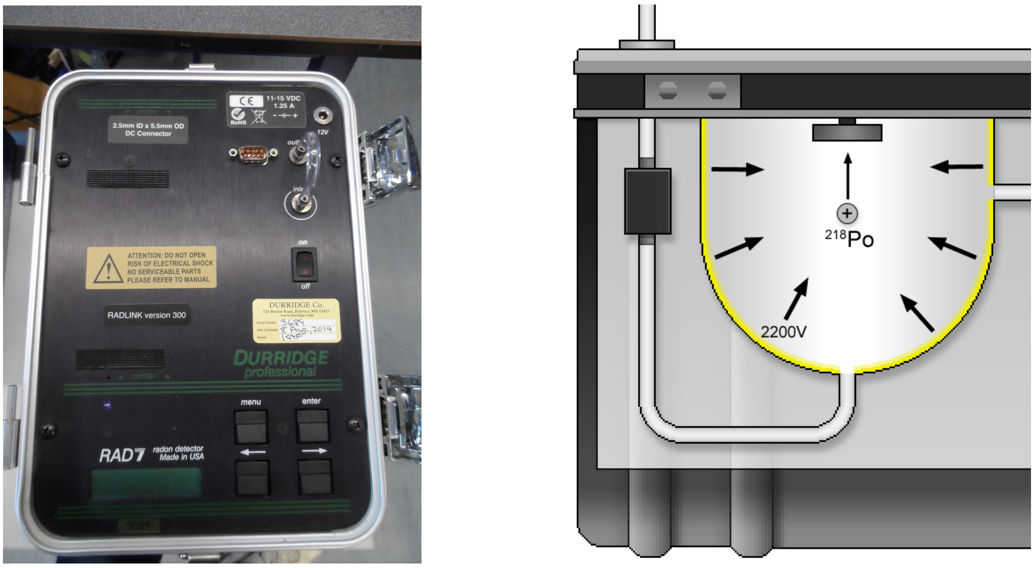

(a) (b)

Fig. 5.1 An image of the Durridge RAD7 detector is shown in (a) with a diagram of the internal dome and detector shown in (b). Image (b) from Durridge [173].

Durridge quote an intrinsic background of "0.005 pCi/L (0.2 Bq/m^3) or less, for the life of the instrument" [173]. Using a given RAD7 internal volume of 0.954 litres for a large-domed detector this can be used to get the final background in atoms/minute

$$0.005 \text{ pCi} = 0.2 \text{ mBq} = 0.01 \text{ atoms/min.} \tag{5.1}$$

The other major part of the emanation system is the emanation chamber itself. Two sizes of emanation chamber were used with the system, with vacuum vessels of 3.5 l and 35 l; the chambers are shown in Figures 5.2a and 5.2b respectively. A sample is placed inside the appropriate chamber and a vacuum pump is then used to evacuate the chamber to less than 0.1 Torr. The chamber is then left to outgas for 2 days. After the two day period the chamber is pumped again, and this time it is sealed for 7 days for the emanation of radon from the sample. Because of the electric fields in use, the RAD7 can only be used at a pressure of 1 atm; this is compensated for by using dry nitrogen to backfill the sample chamber. This backfill is done after the seven day emanation period. The dry nitrogen is also used to purge the RAD7 detector. Dry nitrogen flows through the RAD7 for 20 minutes to remove any radon left in the system from any prior tests. After the emanation period and the nitrogen purge, the chamber and RAD7 are connected in a closed loop. An emanation test is then begun with the RAD7. Each test consists of 12 consecutive cycles of counting decays in the detector, with each cycle lasting 4 hours. A diagram of the emanation system is shown in Figure 5.3.

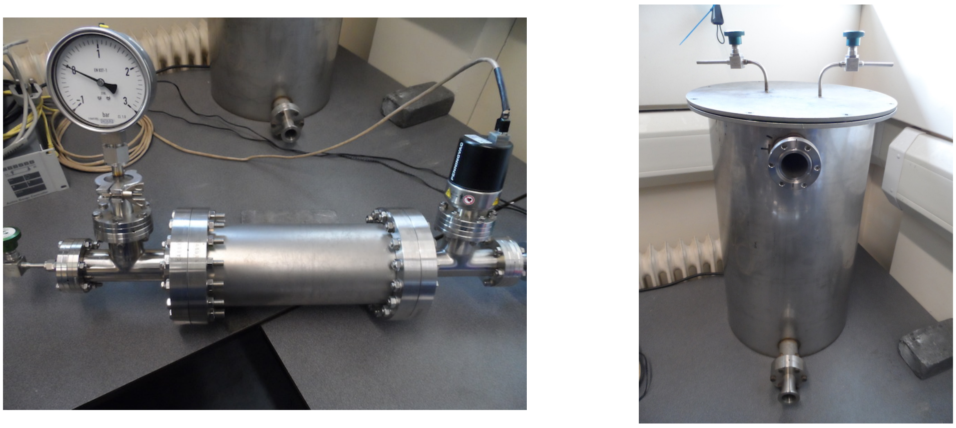

(a)

(b)

Fig. 5.2 The small, 3.5 litre, and the large, 35 litre, emanation chambers are shown in (a) and (b) respectively.

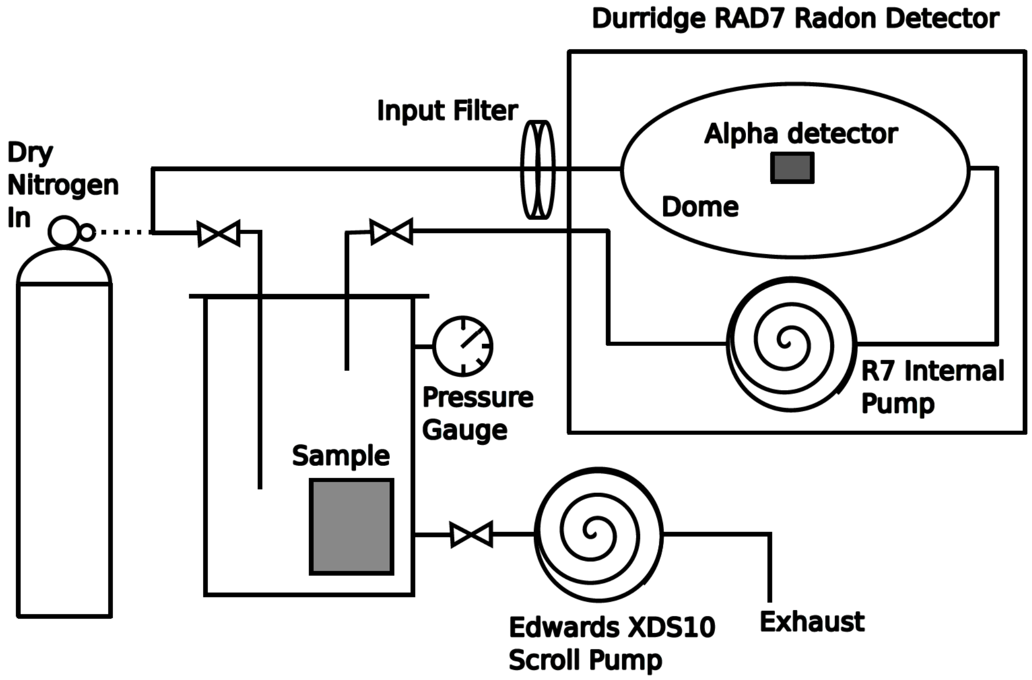

Fig. 5.3 Diagram of the emanation system described above. Figure from Sadler [166].

After the test is completed the results are transferred from the RAD7 to the software CAPTURE which is provided by Durridge. CAPTURE gives the results from the 4 hour cycles in units of Bq m^{-3}. The data is then exported from CAPTURE to allow three corrections to the data take place.

The first correction to take place is a volume correction to convert the Bq m^{-3} output from CAPTURE into Bq. This is given by

$$\mathrm{Bq} = \mathrm{Bq\ m}^{-3} \times (V_{\mathrm{vessel}} + V_{\mathrm{RAD7}} - V_{\mathrm{sample}}). \tag{5.2}$$

The next correction applied is to correct for the relative humidity (RH) in the chamber. An increase in RH causes the efficiency of the detector to decrease due to the water molecules slowing the drifting nuclei, causing a higher fraction to neutralise before reaching the detector. This correction is supplied by Durridge [173] and is applied if the RH for the associated point is above 15%; it takes the form

$$A_{\mathrm{corr}} = A_{\mathrm{meas}} \times \frac{100}{116.67 - 1.1 \times RH}, \tag{5.3}$$

where A_{corr} is the corrected level of radon, A_{meas} is the measured level of radon and RH is the relative humidity measured by the RAD7 in %.

The final correction applied to the data is to compensate for the emanation time. The half-life, $t_{1/2}$, of radon is 3.82 days, which is not negligible compared to the 7 day emanation time; this results in the samples not reaching equilibrium, so a correction must be made for this:

$$A_{\mathrm{corr}} = A_{\mathrm{meas}} \times \frac{1}{1 - e^{-t/\tau}}, \tag{5.4}$$

where A_{corr} is the corrected level of radon, A_{meas} is the measured level of radon, t is the emanation time and τ is the lifetime of radon. After these corrections are calculated for each data point, the average of the points is calculated along with the associated error. The result from a sample is then background corrected by subtracting the measurement from a background run. The background run is set up identically to the procedure described above, but with the chamber empty.

5.3 Emanation System Improvements

This section will describe the individual improvements that were made by the author to the system described above, and then describe the final system as a whole. There were two main roads to improving the system: one is to improve the sensitivity to allow lower levels of radon emanation to be recorded, and the other is to lower the intrinsic background of the system. The modifications to the system described in the remainder of this section aim to give a more sensitive emanation system to allow improved radon screening capabilities.

5.3.1 Activated Charcoal Filter

One hypothesis on a cause of background in the system is that it is from the nitrogen being used to purge the detectors and backfill the vessel. The nitrogen is stored in a steel vacuum vessel: as steel is known to have a uranium content of between 1 - 5 ppb it follows that radon would be found inside the gas cylinder.

To try and remove as much radon as possible from the nitrogen an activated charcoal filter was placed in the gas line. It has previously been shown that activated charcoal can be used to capture radon as it flows past [175, 176]. Tests were made using the filter at room temperature and the filter cooled with liquid nitrogen (LN) using the normal background procedure in the small vacuum vessel. The results from these tests are shown in Table 5.1 and are compared to the previous background from [144] which did not use a charcoal filter.

Test	Radon (atoms/min)
No Filter [144]	0.63 ± 0.08
Filter (Room Temp)	0.32 ± 0.06
Filter (Cooled)	0.21 ± 0.03

Table 5.1 Results from tests using the activated charcoal filter.

The tests show that the inclusion of the filter gives a reduction in the background of ~50%. It is also shown that with a cooled filter another reduction of >30% is obtained, giving a total reduction of 67% from inclusion of the filter. At the same time the filter was implemented, a dedicated pressure gauge along with a pressure relief valve and a manual valve were installed on the system. These were included due to the large pressure changes inside the filter when cooled to LN temperatures and warmed up again.

5.3.2 Multiple Detectors

The next modification made to the system was to use a second RAD7 detector in the system to improve the sensitivity. Due to the $\frac{1}{\sqrt{n}}$ in the calculation of the error this gives a factor $\sqrt{2}$ reduction in the error of the measurements. The detectors are run in series in a closed loop with the emanation chamber, with the detector pump only running in the first RAD7; this is to avoid an under-pressure in either RAD7 during the run. The detectors were also tested in a parallel configuration but this caused a high pump current due to an under-sized output hose. Because of this the RAD7s were run in series for the remainder of this work.

5.3.3 Component Swaps on Emanation Chamber

The next modification was to swap some known radon emitters from the system to try to lower the background. It was shown in [144] that rubber o-rings were a source of radon. The emanation chamber had several of these in KF vacuum connections. All but one of these connections were changed for CF connections, which use copper gaskets to produce a seal. In this process the size of the ‘arms’ on the chamber was reduced; this lowers both the amount of material contributing to emanation and the volume of the chamber. After these modifications were made the volumes of the small and large vacuum vessels were remeasured and found to be 2.7 litres and 34.1 litres respectively.

5.3.4 Desiccant

The final improvement made to the system was to attempt to lower the humidity of the sample gas. As described in Section 5.2, extra water molecules in the dome cause a higher fraction of decayed nuclei to neutralise before reaching the detector. This lowers the overall efficiency of the system. It was hoped that by lowering the initial humidity of the backfill gas, the use of the RH correction would no longer be necessary, increasing the accuracy of the measurements.

To lower the humidity a tube of desiccant was placed in line with the detector. Ideally this would be used in the closed loop of the emanation system while the test was taking place, but the desiccant was found to emit a small amount of radon. To remove this issue, but still lower the humidity of the system, the desiccant tube was placed before the activated charcoal trap. This allowed any radon that was produced in the desiccant to be removed before reaching the detectors or emanation chamber.

5.3.5 Final Post-Improvements System

After the modifications previously described in this section were finalised, they were all put together in a single system, as shown in Figure 5.4. The new procedure for an emanation test starts off as described in Section 5.3, with the vessel being pumped to below 0.1 Torr using an Edwards XDS10 vacuum pump. This is left for two days for outgassing before being pumped once more. After this the chamber is left to emanate radon for 7 days.

After the emanation period the RAD7 detectors are purged with nitrogen for 20 minutes. The nitrogen flows through the desiccant and then the cooled charcoal trap before entering the detectors. After the 20 minutes the nitrogen is connected to the vessel to backfill the emanation volume to a pressure of 1 atm. The complete new system is shown in Figure 5.4.

The new system was used to take a background reading in both the large and the small emanation chambers. The results from these are 0.28 ± 0.11 atoms/min and 0.09 ± 0.03 atoms/min respectively. These are compared to the previous best background measurements from the previous method in Table 5.2. From these results it is seen that the overall radon background of the system has been reduced by a factor of 5.6 for the large chamber and

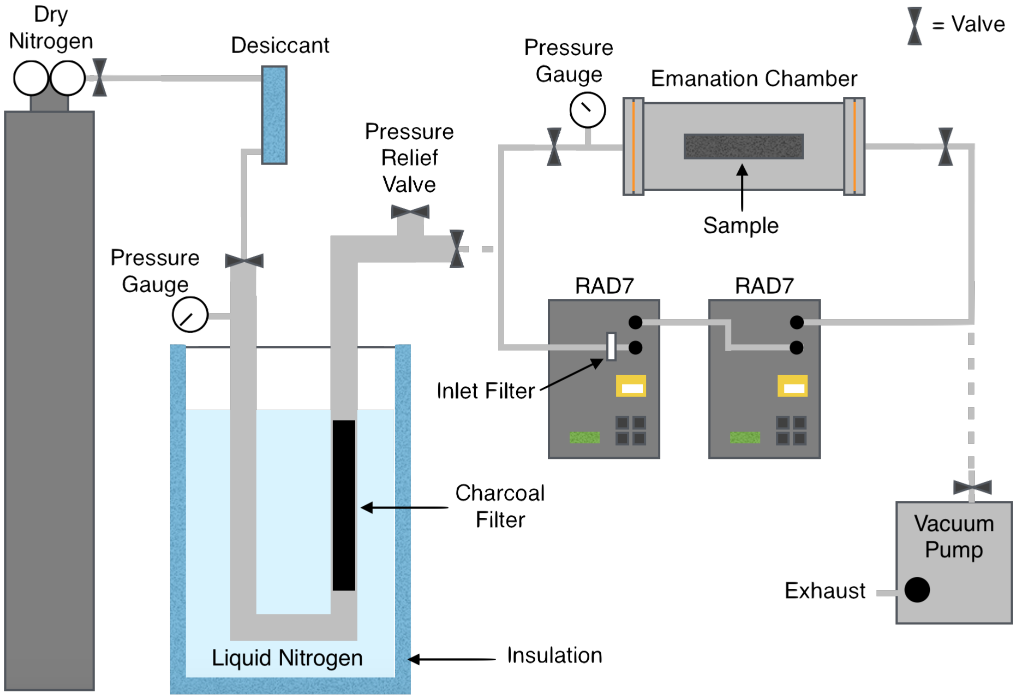

Fig. 5.4 Diagram of the emanation system including all described improvements.

a factor of 7 for the small chamber. A reduction is also seen in the error on these values corresponding to an increased sensitivity of the system of a factor ∼3. So a large improvement in both background and sensitivity of the emanation system has been shown.

Test	Radon (atoms/min)
Small Vessel [144]	0.63 ± 0.08
Large Vessel [144]	1.56 ± 0.30
Small Vessel - This work	0.09 ± 0.03
Large Vessel - This work	0.28 ± 0.11

Table 5.2 Comparison between background results from old and new emanation systems.

5.4 Emanation Measurements

After the improvements described in Section 5.3 were implemented the system was used to take measurements of emanation rates from material samples. This Section consists of two main parts: Section 5.4.1 describes the results from materials proposed for use in low background experiments such as DRIFT and the scaled-up detectors to be used by the CYGNUS collaboration, and Section 5.4.2 investigates the radon emanation from the individual components of the RAD7 detectors with a view to swapping these components for lower emanation alternatives.

5.4.1 Samples for Low Background Experiments

This section shows the results from using the improved emanation system to measure material samples proposed for use in future low background experiments. The procedure for these tests is nearly identical to that described in Section 5.3.5, with the only difference being that a sample is placed in the chamber as opposed to the empty chamber used in the background tests.

The first materials tested were samples of G10 plastic. These have been proposed as cathode materials for future TPC experiments including CYGNUS. Because of the sample sizes (three $151 \times 152 \times 1.7$ mm^3 sheets) they were initially tested in the larger vessel. There was no measurable emanation above background in the large vessel so an upper limit was set for the sample using Feldman-Cousins [177].

To fit inside the small vessel the G10 samples were cut in half to give six $151 \times 76 \times 1.7$ mm^3 sheets. The six sheets were then held together with a nylon rod (4 mm $\oslash$) before being placed inside the small vessel for testing. Due to the cylindrical shape of the smaller vessel this was the only way to fit all the sheets inside while maintaining the maximum possible surface area open to the gas. Like the tests in the large vessel, these tests did not give any emanation above background, so an improved upper limit was set for each sample.

The results from all of these tests are shown in Table 5.3. The results are shown in both the raw number of radon emanation for the sample and also in mBq/m^2 to allow extrapolation for larger quantities of the material to be used in future experiments.

The same method was used with other samples to get the results for each material in both raw emanation of the sample and the emanation per unit surface area. The results from the G10 and all the other samples tested are shown in Table 5.4.

5.4.2 Emanation Measurements of RAD7 Components

This section describes the results of testing internal components of the Durridge RAD7 detectors. This is with the aim of identifying high radon emitters and attempting to find replacements for them, as done with the DRIFT-IId detector [144]. As the emanation system

Test	Radon	Units
Background (Large vessel)	0.28 ± 0.11	atoms/min
G10 (Inc. large bg)	0.22 ± 0.09	atoms/min
Upper Limit of Emanation (90% CL)	< 0.088	atoms/min
Upper Limit of Emanation (90% CL)	< 10.4	mBq/m^2
Background (Small vessel)	0.09 ± 0.03	atoms/min
G10 (Inc. small bg)	0.10 ± 0.02	atoms/min
Upper Limit of Emanation (90% CL)	< 0.085	atoms/min
Upper Limit of Emanation (90% CL)	< 9.9	mBq/m^2

Table 5.3 Emanation results from G10 sample tests.

Sample	Vessel Size (litres)	Radon	Units
Background	2.7	0.09 ± 0.03	atoms/min
	34.1	0.28 ± 0.11	atoms/min
G10	2.7	< 0.085 (90% CL)	atoms/min
		< 9.9 (90% CL)	mBq/m^2
Carbon Fibre	2.7	0.15 ± 0.05	atoms/min
		48 ± 15	mBq/m^2
Steel	34.1	< 0.24 (90% CL)	atoms/min
		< 38.8 (90% CL)	mBq/m^2

Table 5.4 Results from all material emanation tests made with improved system.

has improved it is thought that the RAD7 itself is now the major contributor to the background of the tests. The majority of Durridge customers use the RAD7 for measuring relatively high radon levels, so the detector has not been designed with low background in mind. To test the emanation of the detector the individual components that will be in contact with the sample gas were tested. The initial components tested are the dome gasket that provides a seal around the measurement dome, the plastic pods that cover the RH and temperature monitors and the gaskets that create a seal for the pods. These tests were all done using the previously described method. The other major component to be tested was the internal pump. The pumps are not designed to work at vacuum so to avoid unnecessary damage to the sample pumps a modified test procedure was designed. This is described later in this section.

The next subsections describe the results from each component, giving the results from the tests and then the final area-corrected contribution to the overall radon emanation of the RAD7.

Pods

The pod tests were done in the small (2.7 l) chamber. Six pods were placed in the chamber for the test. The results from this are shown in Table 5.5. The final contribution to background of a RAD7 from the area of the pod open to the sample gas is 0.006 ± 0.002 atoms/min.

Test	Radon (atoms/min)
Background (Small vessel)	0.09 ± 0.03
6 Pods (Inc. bg)	0.27 ± 0.04
6 Pods	0.17 ± 0.05
1 Pod	0.028 ± 0.008
Pod contribution	0.006 ± 0.002

Table 5.5 Results from the emanation tests of the pods.

Pod Gaskets

The tests of the pod gaskets were also performed in the small (2.7 l) chamber. The chamber was filled with 18 gaskets during the test. Final contribution to background of a RAD7 from the pod gasket was found to be 0.0031 ± 0.0003 atoms/min. The results from this test are shown in Table 5.6.

Test	Radon (atoms/min)
Background (Small vessel)	0.09 ± 0.03
18 Pod Gaskets (Inc. bg)	0.90 ± 0.08
18 Pod Gaskets	0.81 ± 0.09
1 Pod Gasket	0.045 ± 0.005
Pod Gasket contribution	0.0031 ± 0.0003

Table 5.6 Results from the emanation tests of the pod gaskets.

Dome Gasket

The dome gasket tests again were performed in the small (2.7 l) chamber. For this test 5 dome gaskets were placed inside the vessel. Radon emanation is normally assumed to scale with surface area for solid materials, but as the gasket is a ‘spongy’ material there is an uncertainty on the propagation length of radon. To compensate for this uncertainty we have only given this result as the range of possible values from the minimum value from the surface area to the maximum of the whole gasket contribution. The final contribution towards the background of a RAD7 is $0.0009 \pm 0.0003 < A_{gasket} < 0.024 \pm 0.008$ atoms/min.

The full results from this test are shown in Table 5.7.

Test	Radon (atoms/min)
Background (Small vessel)	0.09 ± 0.03
5 Dome Gaskets (Inc. bg)	0.21 ± 0.03
5 Dome Gaskets	0.12 ± 0.04
1 Gasket	0.024 ± 0.008
Gasket contribution	0.0009 ± 0.0003 - 0.024 ± 0.008

Table 5.7 Results from the emanation tests of the dome gaskets.

Internal Pump

As previously mentioned, the test for the internal pump was modified to prevent damaging the sample pumps. For the modified test 6 pumps were all connected between the two RAD7s, and instead of being pumped for outgassing and held at vacuum for a week of emanation, the pumps were purged with dry, clean nitrogen along with the two RAD7s and then a 7 day test was made. The test was made for 7 days, rather than the normal 2 day tests to attempt to show the increase of radon over time, so a fit could be made to replace the equilibrium correction provided by Durridge (see Equation 5.4), to account for the fact the samples were not at equilibrium during the test.

The background test for this was made in the same way but with the pumps removed, so the two RAD7s were in a closed loop with each other. Again the test was run for 7 days, rather than the normal 2 day tests to attempt to fit to the emanation time. The plot of emanation as a function of time is shown in Figure 5.5. This plot shows the data after the RH correction but before emanation time and volume corrections. Unlike the expectation this result does not show an obvious increase in the emanation over time, so a different method was chosen for this test.

In light of this development it was decided to take the result from the pumps from the last two days of the analysis, so starting after 5 days of emanation. This was done for both pump and background tests with the results shown in Table 5.8. The final contribution from a pump to the background of a single RAD7 is 0.032 ± 0.008 atoms/min. This is higher than expected, and as the test is the first of a new experimental mode there may be some associated errors that have not been accounted for.

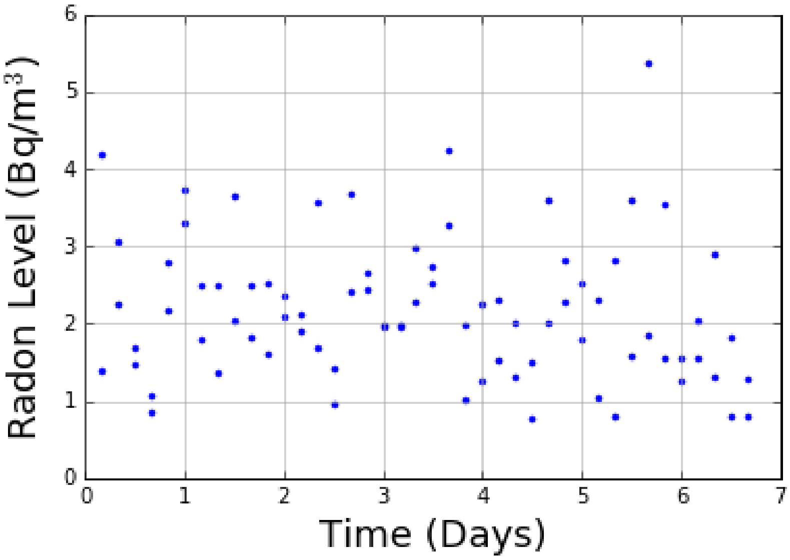

Fig. 5.5 Plot of the radon emanation from the pump setup over the 7 day test.

Test	Radon (atoms/min)
Background	0.16 ± 0.02
6 Pumps (Inc. bg)	0.35 ± 0.04
6 Pumps	0.19 ± 0.05
Pump contribution	0.032 ± 0.008

Table 5.8 Results from the emanation tests of the internal pumps.

Total Contribution

After taking measurements of these components a number for the total background contributions of a single RAD7 can be estimated and compared to the given value from Durridge. The results give a $\sim$ 4 times higher value that the given background when the pump is included. When the pump is omitted however, the results are in agreement with those from Durridge. The results from the tests are shown in Table 5.9 including the total radon. The difference when including the pump is likely to be from the uncertainties in the new measurement mode for the pumps. One possible error not accounted for is the extra pipe connections when using the pumps that may allow air to get in the system, causing the level of radon to rise. Additionally, it may be possible that air is getting into the system through the pumps themselves. This new mode will be analysed and modified in the future to try and improve this measurement. Discussions are also ongoing with Durridge to fully understand the circumstances under which the stated background was measured. But the main conclusion from these tests is that the main radon contributors inside the RAD7 have been identified, and replacements of lower radon emanation can now be sourced. If the majority of these emanation from these components can be removed that would allow a reduction in background to ~0.05 atoms/min for the small vessel, giving a total reduction of a factor ~13.

Test	Radon (atoms/min)
Pod	0.006 ± 0.002
Pod Gasket	0.0031 ± 0.0003
Dome Gasket	$> 0.0009 \pm 0.0003$
Pump	0.032 ± 0.008
Total	$> 0.042 \pm 0.008$

Table 5.9 Total contribution of radon emanation from the internal RAD7 components. This should be compared to the RAD7 background of < 0.01 atoms/min given by Durridge.

RAD7 component swaps

After measuring the emanation of the materials the next step is to test new, cleaner materials to replace them. The first part of the detector to be swapped was the dome gasket. From previous tests for emanation from DRIFT [144], teflon encapsulated o-rings were determined to be a good, low emanation alternative to the current o-ring used in the RAD7. O-rings from the PAR group [178] were used; these were custom made to fit the size of the dome. For the first test an o-ring was used with FEP teflon encapsulating a Viton core. Due to the lack of flexibility of the new o-rings compared to the sponge-like gaskets that are used in RAD7 detectors a groove was cut into the underside of the dome to allow a good seal.

Background tests were made with the RAD7 before and after the swap. The method differed from the regular method used for sample emanation because the RAD7 cannot be subjected to a vacuum. The detector was purged with clean, dry nitrogen as in the normal procedure and was immediately put into a closed loop with itself. It was then run on the normal 2 day cycle with results being taken every 4 hours. After the first test the detector had the old gasket removed, the dome groove cut and then the new gasket connected. High-vacuum grease was applied to the new gasket to allow a good seal and a leak test was then made which proved the seal was good. After the gasket swap an identical test was made on the new configuration. The results for both tests are found in Table 5.10.

These results show no significant variation between the two methods. As the uncertainties on the measurements are higher than the lower limit of emanation from the original gasket

Test	Radon (atoms/min)
Original Gasket (1)	0.068 ± 0.014
Original Gasket (2)	0.051 ± 0.016
Original Gasket (Average)	0.060 ± 0.011
New O-ring	0.050 ± 0.018

Table 5.10 Results for comparing the background levels before and after the dome gasket swap of the RAD7.

(0.009 ± 0.003 atoms/min) this not unexpected. Improvements to this measurement mode are the subject of further work. Currently work is ongoing to find suitable replacement parts for the other internal components of the RAD7 detector and these should be tested in the near future to allow for the further reduction of the backgrounds.

5.5 Conclusions

In this chapter significant improvements to the radon emanation system used in [144] have been described. These were achieved primarily by the addition of a cooled activated charcoal trap to capture radon from the nitrogen line. A reduction in the background of a factor of 5.6 for the large chamber and a factor of 7 for the small chamber has been shown along with an improvement in sensitivity of a factor $\sim$3. The newly improved system has then been used to measure several different components for proposed low background experiments such as CYGNUS. The system has also been used to show the emanation of different materials in the Durridge RAD7 detector. A first test on a replacement part for the RAD7 has been conducted and the acquisition of more low background components is underway which, if successful, would allow a further reduction of the background to 0.05 atoms/min giving a total reduction of a factor $\sim$13.

Chapter 6

Operation of THGEM Detectors in CF_4 Gas with Charge and Optical Readouts

This chapter describes the operation of a THGEM (Thick Gas Electron Multiplier) based TPC, constructed by the author, operating in low pressure CF_4 gas. Section 6.2 describes operation using a charge readout with the aim of testing the performance of the THGEM for possible use as an alternative readout for directional dark matter detectors. The system was also used with an optical readout (Section 6.3) with the objective to see if the head-tail effect is observable in sub-10 keV nuclear recoils.

6.1 Introduction to THGEM Detectors

The THGEM detector [179–183] is a variant of the GEM (Gas Electron Multiplier) [184]. The GEM detector was invented by Fabio Sauli in 1996 at CERN's Gaseous Detector Development Group [185]. GEMs are made of an insulator separating two layers of copper. Many holes are made through the GEM foil; these become areas of high electric field when a potential difference is applied across the two copper plates. Figure 6.1a shows an image of the field lines through a GEM hole and Figure 6.1b shows an image of a GEM foil. When an electron reaches this area of high field an electron avalanche occurs resulting in high gas gains. Typical GEM dimensions are a thickness of 50 μm, a hole diameter of 70 μm and a pitch between holes of 140 μm. The small thickness means very large fields are produced when a relatively low voltage is applied.

One of the disadvantages of the GEM detectors is that the small thickness of the GEM foils leads to them being very fragile and very sensitive to any change in the electric field.

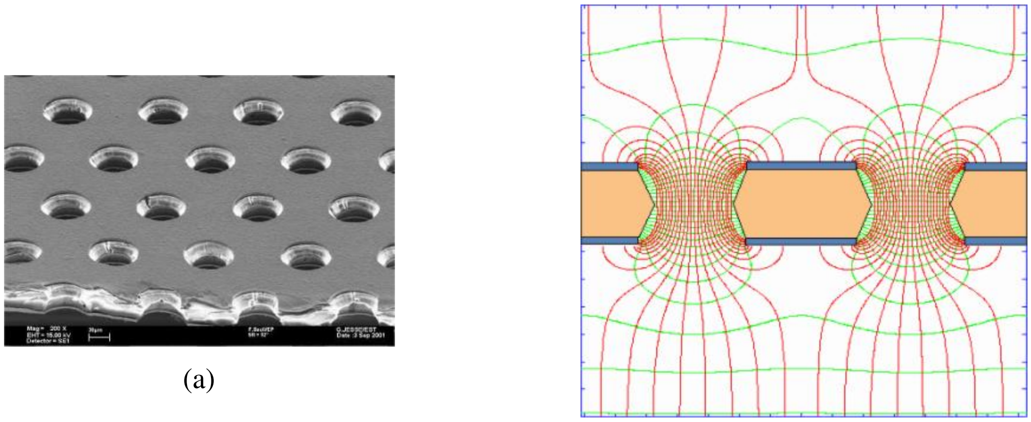

(a)

(b)

Fig. 6.1 (a) A magnified image of a GEM foil. (b) A diagram of the electric fields through a GEM. Image and diagram from CERN's Gaseous Detector Development Group [186].

Just a small amount of dust on the detector can lead to a damaging discharge. They also have a limited gain of $\sim 10^4$ [179], after which a discharge occurs, potentially destroying the detector. The THGEM detectors have been designed to try and overcome some of these disadvantages. THGEMs have thicknesses of 0.4 - 2 mm, which means that they are more robust and less prone to discharges caused by small non-uniformities in the field. They also have small rims etched around the holes, around 0.04 - 0.1 mm thick, to help reduce unwanted discharges; an example image of THGEM holes with rims is shown in Figure 6.2. These detectors can also achieve high gains, with a single THGEM detector able to reach gains of 10^5 in 740 Torr of Ar/5%CH_4 and $10^4 - 10^6$ in 1 - 10 Torr of isobutane [179]. These higher gains make the THGEM highly suitable for low pressure particle detection for low energy particles. Applications run from medical imaging to WIMP detection, as is relevant for this work. The main advantage of the GEM compared to the THGEM is that the spatial resolution of the THGEM is worse due to the large pitch, ~0.5 mm compared to 0.14 mm for a GEM. However, it is possible to get sub-mm precision with a THGEM detector, which provides better resolution than the DRIFT-IId MWPCs with 2 mm wire spacing, so would allow reconstruction of shorter tracks.

Current research on THGEMs has shown that they can be used to provide the high gains [179] and sub-mm resolution needed for the directional detection of dark matter. THGEMs are also robust and costs are relatively low for the THGEM foil itself, with the major cost coming from the readout that is needed to get two-dimensional information from the THGEM (THGEMs cost £100s, where the readouts are £1000s). This information can be extracted by using the THGEM with a 2D readout plane, such as a strip readout, or with an optical readout

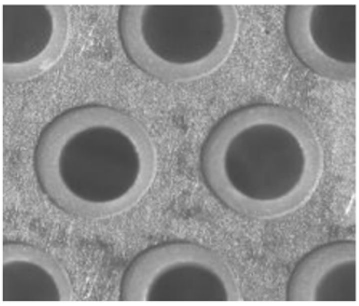

Fig. 6.2 Image of a THGEM detector and the rims around the holes from Shalem et al. [182].

as will be described in Section 6.3. Another method is to use just the charge readout from the THGEM with no 2D information. This charge is used along with timing information from a TPC to obtain directional information through the head-tail effect. Results from this method using an SF_6 based NI-TPC are shown in Chapter 7. Non-directional results using the charge directly from the THGEM in low pressure CF_4 are described in Section 6.2.

6.2 Operation of a THGEM TPC in Low Pressure CF_4

This section will describe the operation of a THGEM-based TPC in low pressure CF_4 using only information from the charge signal read out directly from the THGEM electrode. The aim of the work was to show the high gains that can be achieved with a THGEM detector and are a good starting point before using a gas with negative-ion drift as described in Chapter 7. The experimental setup used in the work in this section is described in Section 6.2.1 and Section 6.2.2 describes the calibration of the detector and measurements of the gains achieved with varying pressures and applied voltages. Section 6.2.3 uses the performance of the detector shown in Section 6.2.2 to directly calculate the Rose-Korff coefficients of the gas.

6.2.1 Description of THGEM TPC

The setup used in this work consists of a THGEM electrode mounted 2 cm from a cathode plane, creating a time projection chamber. Any electrons liberated in the 2 cm drift region of the detector will be drifted to the THGEM in the electric field between the cathode and the THGEM. The THGEM used in this work, obtained from CERN's Gaseous Detector Development Group, is circular with a 10 cm diameter and thickness of 0.4 mm. The hole diameter is 0.4 mm, the pitch is 0.6 mm and the rim around each hole is 0.04 mm. A diagram of the THGEM dimensions is shown in Figure 6.3 with a photograph of the THGEM shown in Figure 6.4.

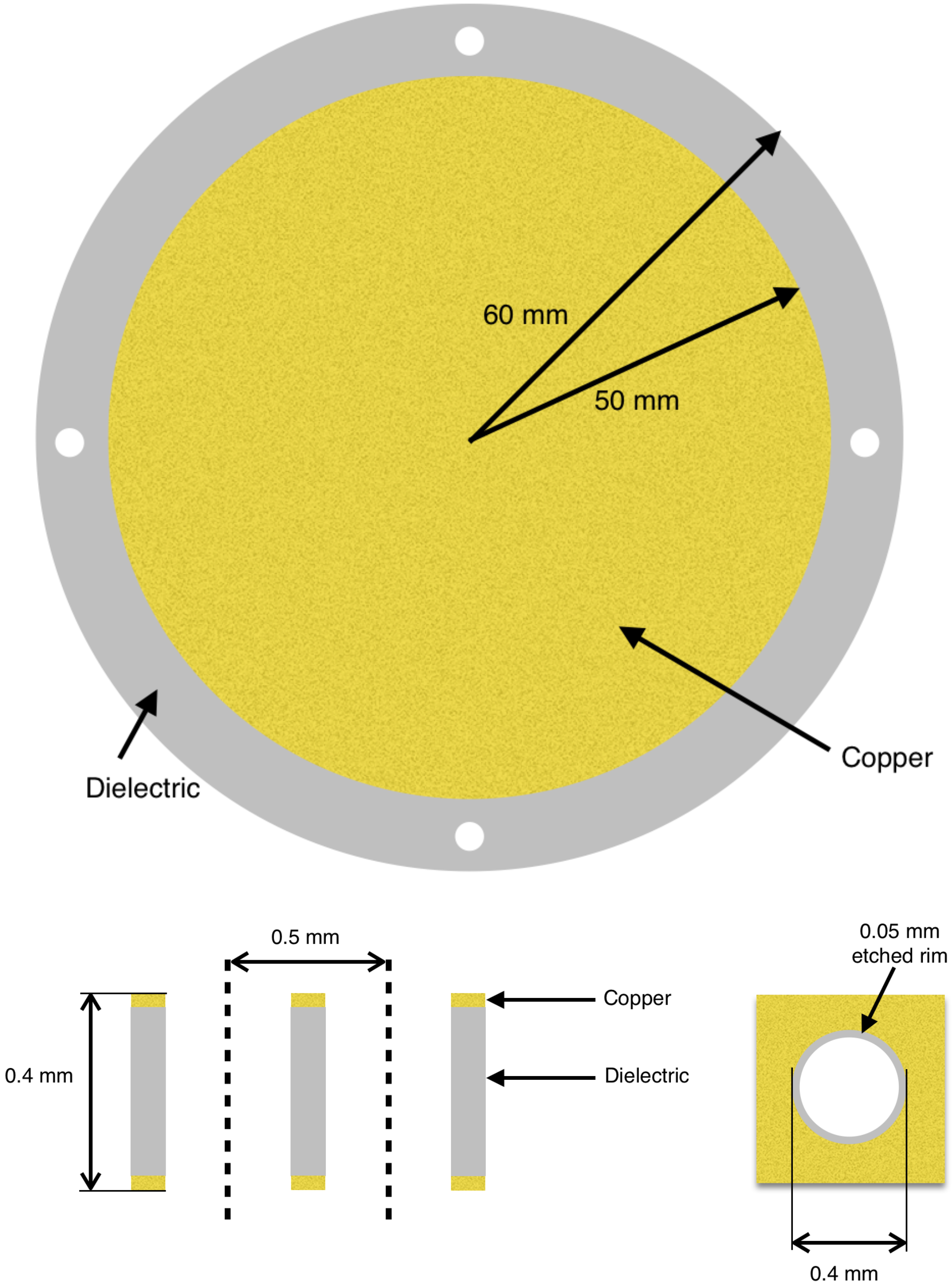

Fig. 6.3 A diagram of the dimensions of the CERN THGEMs used in this work.

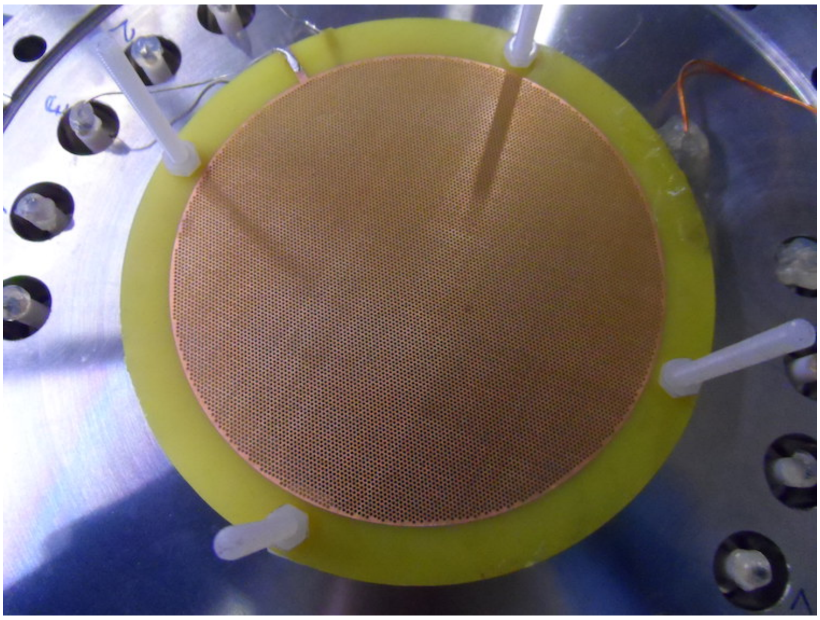

Fig. 6.4 A photograph of the THGEM used in this work.

The setup is located inside a 10 litre vacuum vessel with a quartz window on the top. There are two radioactive sources in the vessel for calibration and analysis, ^{241}Am and ^{55}Fe; these produce 5.49 MeV alpha particles and 5.89 keV x-rays respectively. Both sources are connected to magnets which allow them to be moved into and away from the detection region to give a background result without the need to open the vessel. A diagram of this geometry is shown in Figure 6.5.

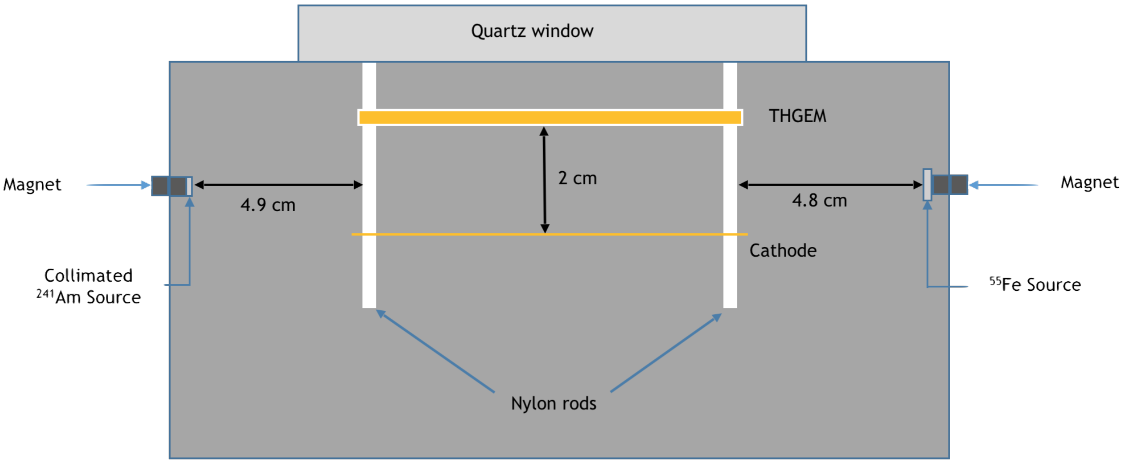

Fig. 6.5 Setup of THGEM TPC inside the 10 litre vacuum vessel. Also shown are the ^{241}Am and ^{55}Fe sources used for calibration.

The upper plane of the THGEM is powered by a Bertan model 377P positive high voltage (HV) power supply, with the lower plane (closest to the cathode) grounded. The cathode voltage is applied by a Bertan model 377N negative HV power supply. The signal of the THGEM is read out from the upper plane through an Ortec 142 IH preamplifier, the signal then goes to an Ortec 572 shaping amplifier before being recorded via an Ortec 926 ADCAM MCB (multi-channel buffer). The voltage was measured constantly with a voltmeter with ± 1 V accuracy. A diagram of the electronics setup is shown in Figure 6.6.

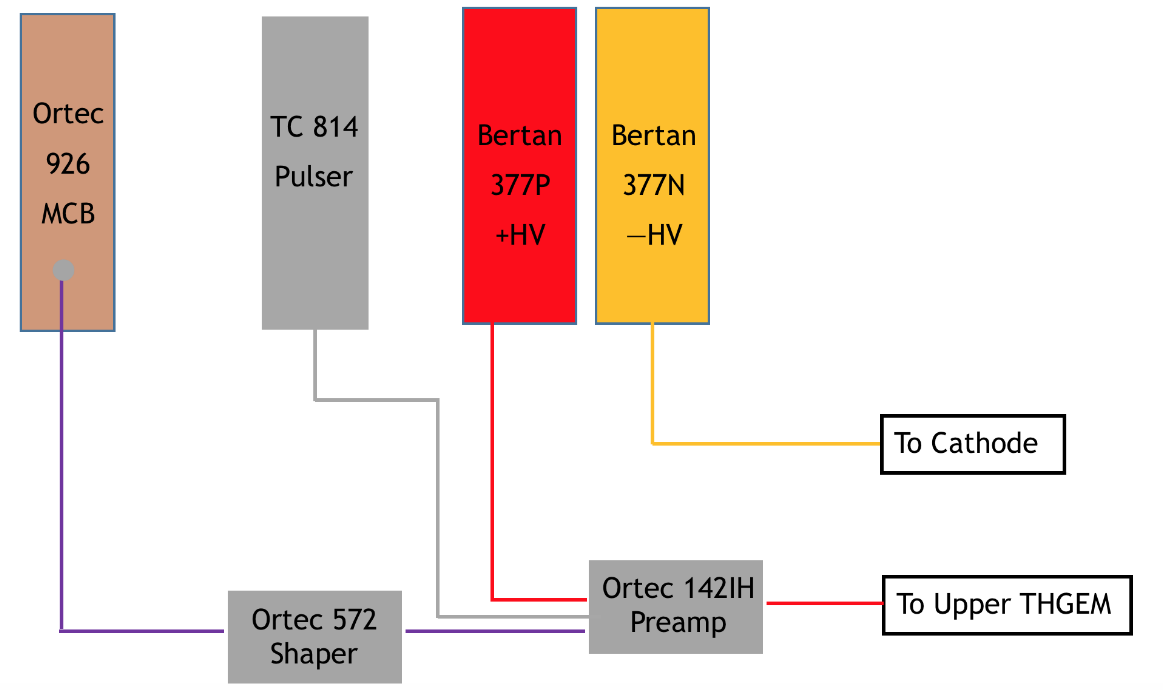

Fig. 6.6 A diagram of the electronics setup used with the THGEM TPC.

6.2.2 Gain Calibration

The setup described above was used to calibrate the performance of the THGEM detector. In this section the gain of the detector is calculated for varying amplification fields and pressures. Calibration runs with an ^{55}Fe x-ray source were used along with the Ortec-926 MCB to take an energy spectrum of the 5.89 keV x-rays that are emitted from the source. An example energy spectrum, along with a background run for comparison, is shown in Figure 6.7.

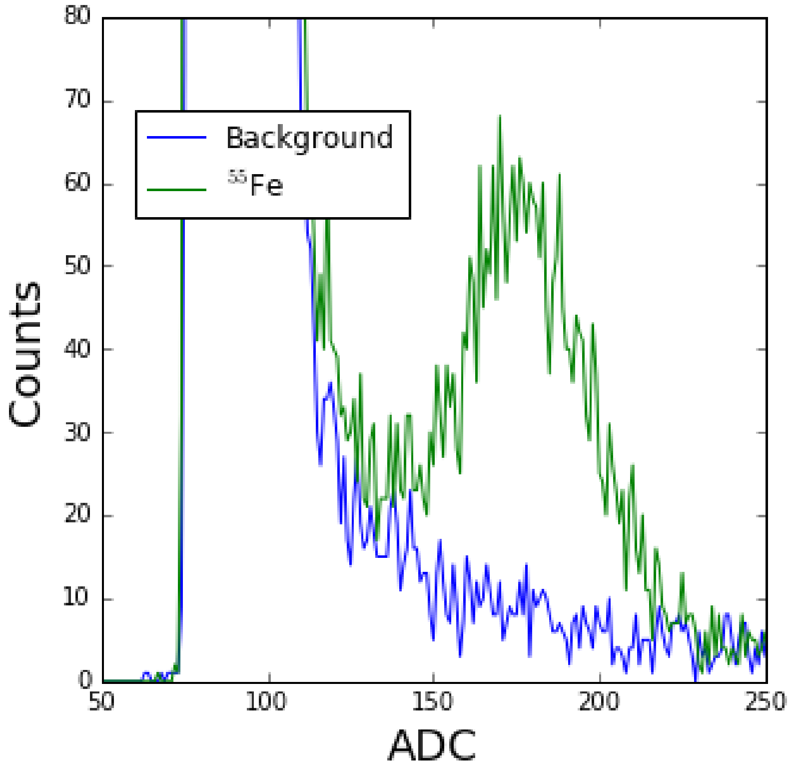

Fig. 6.7 An example energy spectrum from the 5.89 keV ^{55}Fe x-rays is shown (green) along with a background measurement for comparison (blue). These data were taken in 30 minute runs with 100 Torr CF$_4$. The voltage across the THGEM was 750 V with a drift field of 300 V/cm.

A Tennelec TC 814 pulser was connected to the test input of the Ortec 142 IH preamplifier to give simulated input pulses. From the recorded spectra on the MCA, a charge to ADC conversion was calculated. Seven different pulse heights were used with the pulser and the peak location for each was found in ADC units. The initial pulse heights and peak locations found from the MCA are shown in Table 6.1. Errors on the peak locations are ± 1 ADC.

The pulse heights can be used to calculate a conversion from ADC units on the MCA to a measurement of gain from an ^{55}Fe spectrum. The initial step is to use the known value of the input capacitor of the preamp test input (1 pF) to get the initial charge; this is then divided by the electron charge (1.6×10^{-19} C) to get a final number of electrons. Using the W-value for CF$_4$ (34 eV [187]) and the known energy of the incident x-rays (5.89 keV), the initial number of electrons produced is found to be 173. The gain is then calculated by dividing the final number of electrons by the initial number of electrons. This conversion was done for all pulse heights and Figure 6.8 shows the plot of gain against ADC. A least squares linear fit is

Pulse Height (mV)	Peak Location (ADC)
200	322
400	612
600	897
800	1190
1000	1485
1200	1766
1400	2049
1600	2335

Table 6.1 Calibration numbers

used on the data of this plot to get a gain to ADC conversion. The result of the fit was

$$Gain = (25.10 \times ADC) - 921.23 \tag{6.1}$$

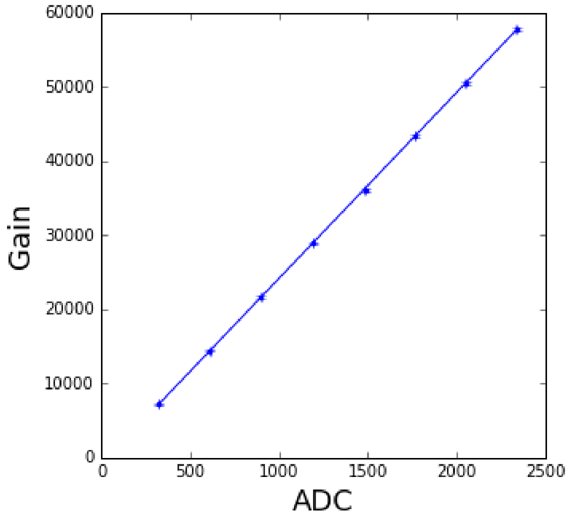

Fig. 6.8 Plot of the gain against ADC of the MCA from the calibration with a test pulses.

After the conversion from ADC to gain was found, measurements of the gain can be made from the detector. The detector was tested in pressures from 50 - 100 Torr with voltages across the THGEM varying between 620 V and 900 V, producing fields in the THGEM of 15,500 V/cm to 22,500 V/cm. For each combination of voltage and pressure an ^{55}Fe calibration was made and the peak was found on the MCA that corresponded to the 5.89 keV x-rays. This is then converted to a gain via the calibration shown above. The results from these measurements are shown in Figure 6.9, with the gain rising exponentially with increasing voltage. Very high gains were achieved with a highest gain of over 9×10^4

recorded in 50 Torr CF_4 with a voltage of 770 V across the THGEM.

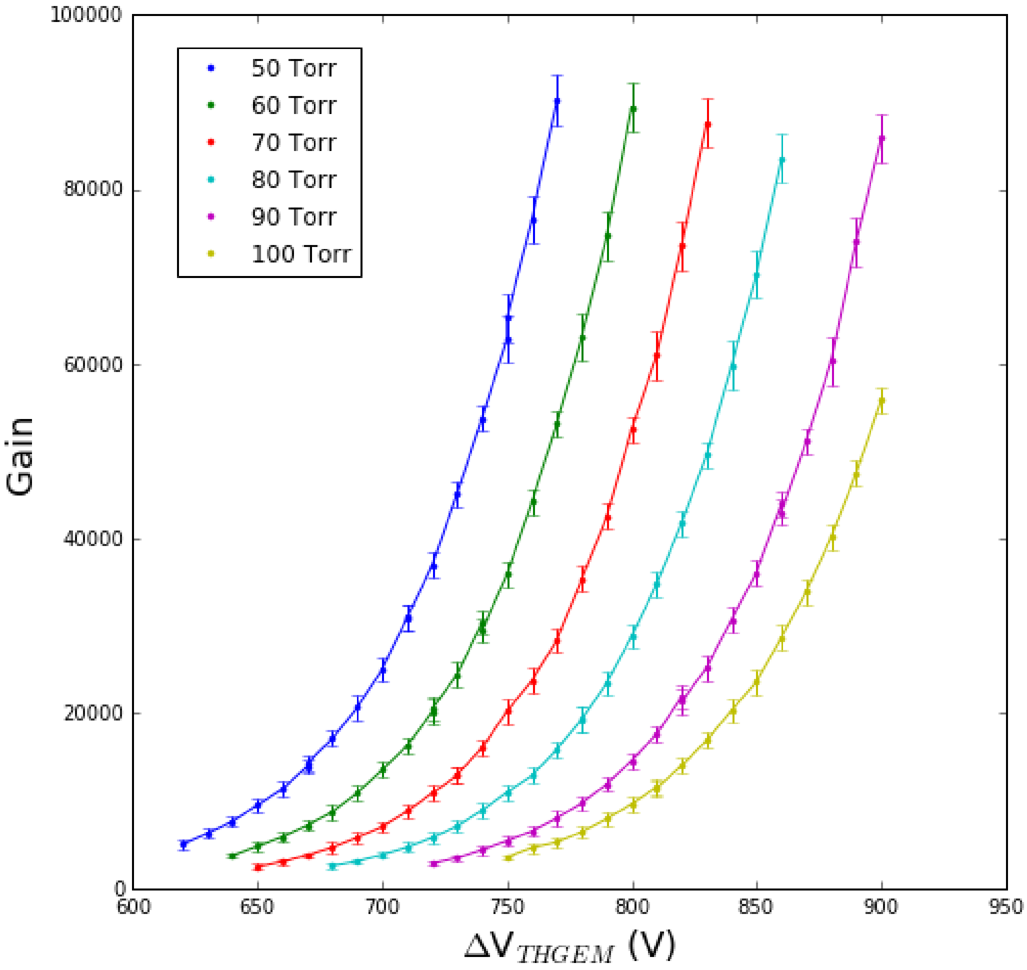

Fig. 6.9 Plot of THGEM gain against voltage across the THGEM for different pressures of CF_4 gas.

6.2.3 Calculation of Rose-Korff Coefficients

The Rose-Korff model [188] expresses the relation between the first Townsend coefficient, α, the pressure P, and the electric field E as

$$\frac{\alpha}{P} = Ae^{\frac{-BP}{E}} \tag{6.2}$$

where A and B are the constants which depend on the gas mixture. The first Townsend coefficient is defined as the number of ion pairs per unit length, and is given, assuming a pair of parallel plates by $\frac{ln(Gain)}{d}$ where d is the separation between plates. Here the plates are the THGEM electrodes and d assumed to be the 0.4 mm separation between the THGEM electrodes. Rearranging Equation 6.2, we can plot ln(ln(Gain)) against $1/E$ to find values for the constants A and B:

$$ln(ln(Gain)) = ln(APd) - \frac{BP}{E} \tag{6.3}$$

Figure 6.10 shows the plot of ln(ln(Gain)) against $1/E$ for each pressure from 50 to 100 Torr and the least squares polynomial fit for each.

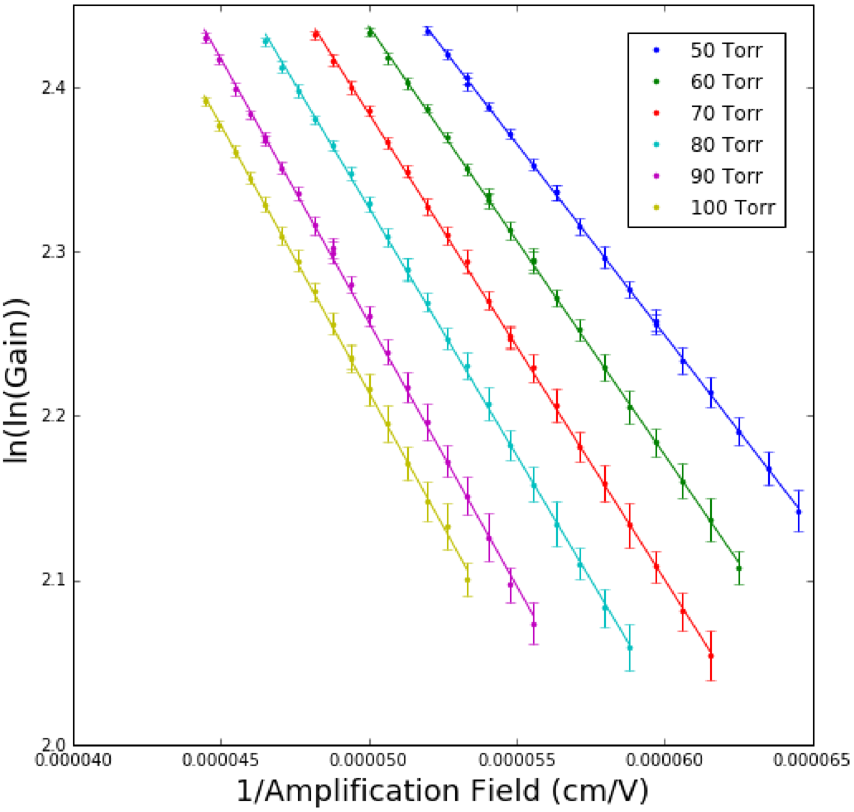

Fig. 6.10 Plot of the ln(ln(gain)) against the reciprocal of the amplification field inside the THGEM holes for different pressures of CF_4 gas.

The resulting values of A and B are shown in Table 6.2. It can be seen that the values of both A and B decrease with increasing pressure, this is the same effect as seen by Lightfoot et al. using CS_2 [189]. The only previous known measurement of the constants of the Rose and Korff formula in CF_4 is from Ref. [190] where a parallel plate chamber was used in CF_4 at atmospheric pressure. The result from Ref. [190] gives A = 203.5 ± 1.0 cm^{-1} Torr^{-1} and B = 401.2 ± 2.2 V cm^{-1} Torr^{-1}. If the trend of decreasing A and B with increasing pressure continues this result would be inconsistent with the results here, but given the different operational parameters it is hard to draw a firm conclusion.

Pressure (Torr)	A (cm^{-1} Torr^{-1})	B (V cm^{-1} Torr^{-1})
50	19.2 ± 0.5	465 ± 14
60	17.6 ± 0.4	435 ± 13
70	16.0 ± 0.4	405 ± 12
80	14.5 ± 0.3	377 ± 11
90	13.2 ± 0.3	356 ± 11
100	11.6 ± 0.2	325 ± 12

Table 6.2 Values for the gas constants for different pressures of CF_4.

This section has shown that the THGEM is producing high gains and smooth operation which is very promising for moving towards using THGEMs in directional WIMP detectors. The next section describes the operation of a THGEM TPC in CF_4 using an optical readout to get 2D track information.

6.3 A CCD-Based Optical Readout with a THGEM TPC

This Section describes work done with the THGEM detector using an optical readout to image particle tracks in the detector giving two-dimensional position information as opposed to the one-dimensional charge readout described in the previous section. This allows a 2D reconstruction of recoils that occur in the THGEM TPC as required for directional dark matter detectors. This work aims to detect nuclear recoils from a neutron source that will simulate the expected recoils from WIMP interactions and look for an observable head-tail signature in the events. This work uses the same TPC setup as shown in Figure 6.5 but in addition has an external CCD camera to image the particle tracks. The CCD camera is an FLI Microline M1001 and is placed above the quartz window. A 20 mm extension tube and 50 mm f/1.4 Nikon Nikkor lens are used with the camera for focusing the images, with the camera focused on a 1 cm × 1 cm area of the upper THGEM foil; this modified setup is shown in 6.11 with a photograph of the setup shown in Figure 6.12.

As CF_4 is a scintillating gas it is possible to use the CCD camera to image particle tracks in the TPC. After an electron is liberated it drifts to the THGEM where an avalanche occurs inside the high field region in the holes. During the electron avalanche in CF_4 0.34 ± 0.04 photons (200 - 800 nm) are produced for every electron [191]. Given the high gains shown

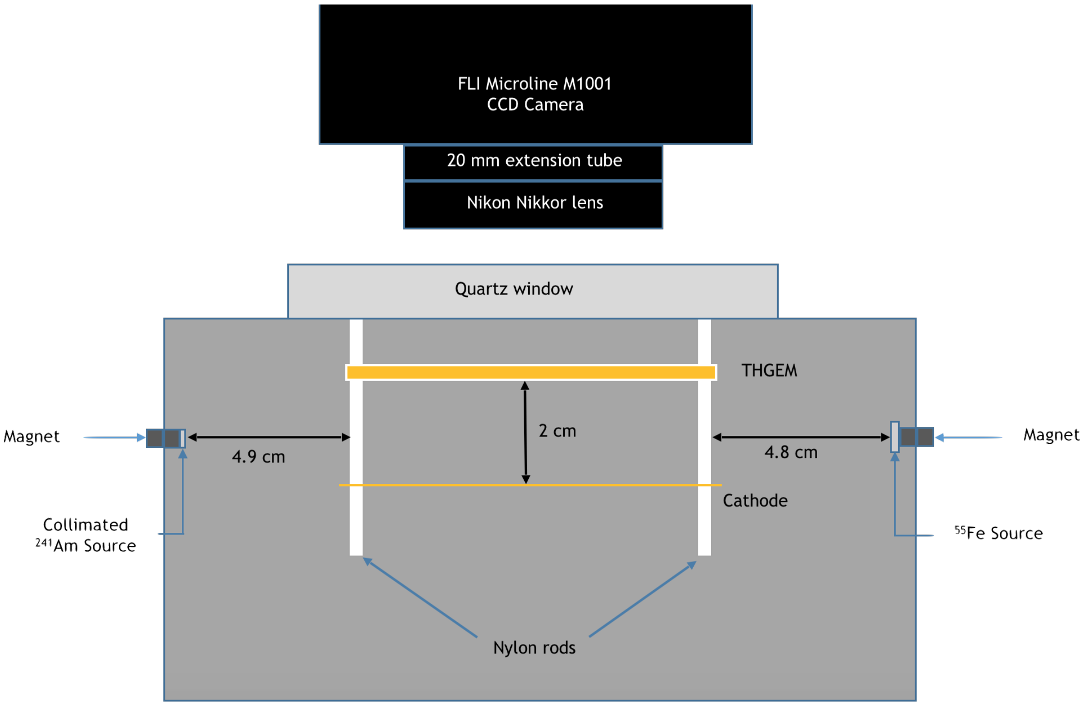

Fig. 6.11 Setup of THGEM TPC inside the vessel with CCD camera positioned above the quartz window.

in Section 6.2.2, this leads to a large number of photons being produced inside the THGEM holes; the photons that are incident on the CCD can then be recorded to give a 2D image of a particle track. Here it is also important to note that the optics must be set up correctly or the images will be very distorted. The use of the 20 mm extension tube was to focus the image to allow a smaller THGEM to camera distance, allowing a smaller imaging area to produce a more detailed image.

6.3.1 Detection of Alpha Tracks

The first measurements made with the optical readout were of alpha particles from the ^{241}Am source. An example track is shown in Figure 6.13 where the alpha particle was travelling downwards from the top of the image. Here the Bragg peak of the track can clearly be seen where more charge is deposited at the end of the track. Images were taken over varying drift fields and the track width was measured to look for change due to diffusion, with a lower diffusion expected from a higher drift field as diffusion is proportional to $1/\sqrt{E}$ [128]. For these tests the vessel was filled with 100 Torr CF_4 and a voltage of 860 V was applied across the THGEM. The voltage applied to the cathode ranged from –200 V to –1300 V in steps of 50 V, giving a drift field ranging from 100 V/cm to 650 V/cm. For

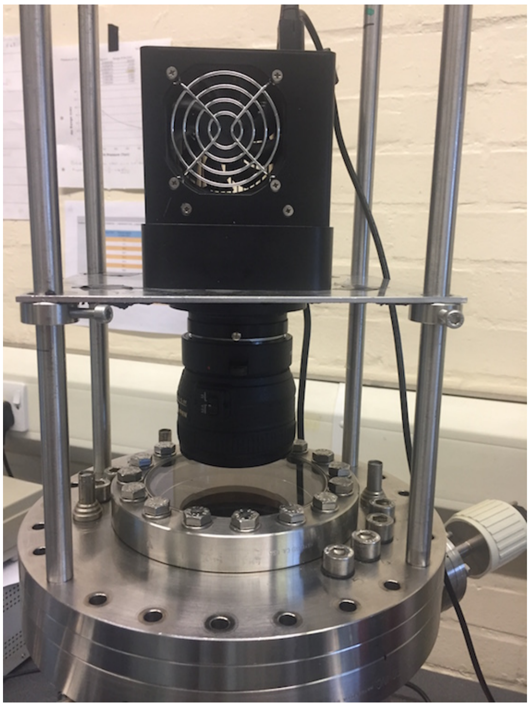

Fig. 6.12 A photograph of the CCD camera positioned above the quartz window.

these tests the camera was run untriggered and for each drift field took 100 consecutive images with a 2 second exposure, with 6 × 6 pixel binning used to increase signal to noise levels.

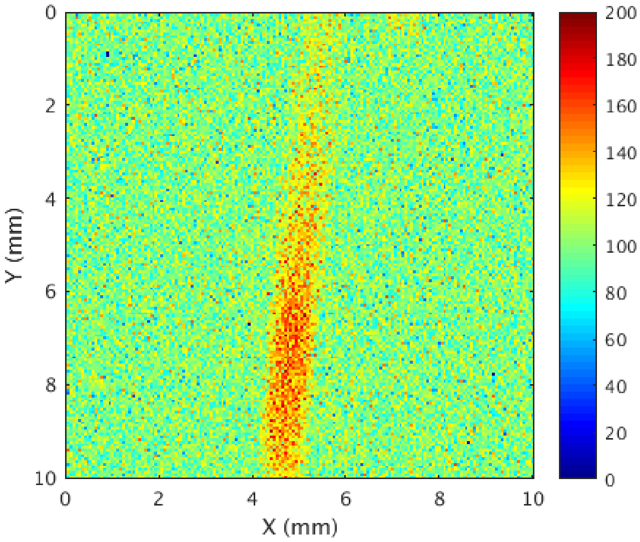

Fig. 6.13 Example alpha track.

For each image the MATLAB function *improfile* was used to look at the profile across the track to extract the width. An example profile is shown Figure 6.14 where the track can clearly be seen above background. A gaussian fit was made to each profile and the FWHM (full width at half maximum) of the peak was calculated from this. A histogram was made of the FWHM for each drift field and a fit was made to this to obtain the average FWHM for each drift field. The results of the average FWHMs for the varying drift fields are shown in Figure 6.15 along with a linear fit calculated in MATLAB.

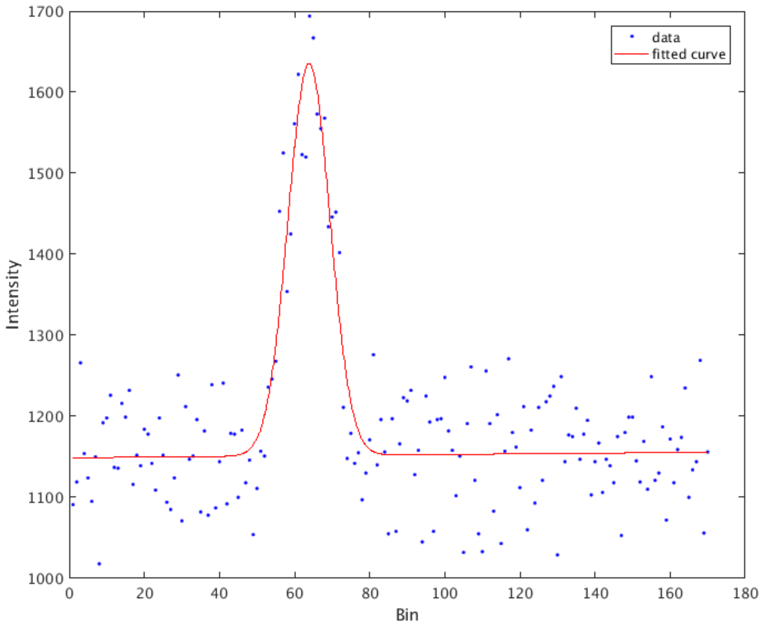

Fig. 6.14 Example profile across an alpha track.

The gradient from the linear fit is –0.0008 ± 0.0011. The mean of the gradient shows a decrease in track width with larger drift field, with a reduction of ∼5% from 100 V/cm to 650 V/cm. However the uncertainty means that the gradient is consistent with zero. To check the goodness of fit the χ^2 was calculated. Using all the points shown in Figure 6.15 the fit gave a normalised χ^2 of 2.19, showing that it is a poor fit to the data. This bad fit was mostly caused by the outlying point at 350 V/cm, removing this gives a normalised χ^2 of 1.31. As this is close to 1 it shows good agreement between the fit and the data.

Diffusion, σ, is described by:

$$\sigma^2 = \frac{4\varepsilon_k L}{3eE}. \tag{6.4}$$

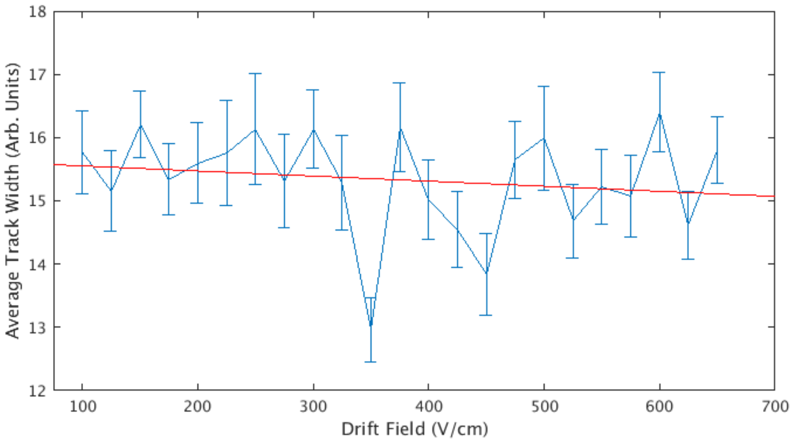

Fig. 6.15 Plot of track width against drift distance with errors included. Best fit line shown in red.

Here L is the drift distance, E is the drift field and ε_k is the average energy of the drifting electron [128]. It is seen that the diffusion is proportional to $1/\sqrt{E}$. This results in the expectation that when going from a field of 100 V/cm to a field of 650 V/cm the reduction should be $\sim$60%. This is quickly seen to be much larger than the observed 5% reduction. The reason for the discrepancy is the size of the THGEM holes (0.4 mm diameter) leading to the observed width of the alpha tracks ($\sim$1 mm); there will also be some distortion from the CCD but on a smaller scale. Using Equation 6.4 the expected diffusion of a track is 0.083mm. The combination of the THGEM holes and CCD distortion results in a smeared track compared to the initial track before the THGEM so the true difference between diffusion and drift field cannot be measured with this setup. Using GEMs, with hole diameters of 70 μm, opposed to THGEMs may allow improved track width reconstruction and allow the effect of electric field on the diffusion to be seen more clearly.

6.3.2 Optical Energy Calibration

As previously mentioned the optical results are from a camera exposure of 2 seconds. This length of exposure means that the charge and optical signals cannot be combined for each event in the current setup, so a calibration as seen in Section 6.2.2 is not possible. Two possible ways were investigated to find a calibration for the optical data: one was to take an optical spectrum of ^{55}Fe x-rays and the other was to use data from the alpha tracks. Although ^{55}Fe interactions were seen with the CCD, with examples shown in Figure 6.16, due to the small area of the THGEM imaged by the CCD (1 cm × 1 cm) and the low rate of the ^{55}Fe source, it was determined that taking an ^{55}Fe spectrum would not be suitable in this situation.

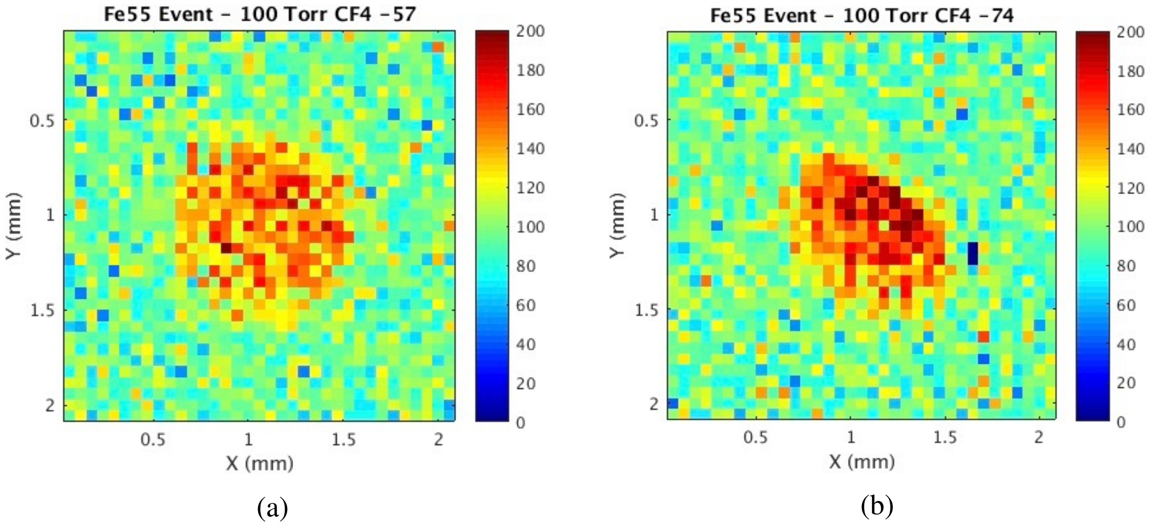

(a) (b)

Fig. 6.16 Example ^{55}Fe events in 100 Torr CF_4

The alternative to using the optical ^{55}Fe spectrum was to use the charge from alpha particles. The range of alpha particles from ^{241}Am in 100 Torr CF_4 is $\sim$13 cm (calculated in the software SRIM (Stopping and Range of Ions in Matter) [192]). As the imaging area is much smaller than this it was decided to look at the energy deposited after the Bragg peak of the alpha track to perform the energy calibration as the source position could be adjusted to have this peak appear in the imaged region. There are two stages to this calibration: the first is to find the amount of energy deposited in the gas after the Bragg peak, and the second it to use experimental data to find the intensity of light detected in the CCD after the peak.

To find the amount of energy deposited after the peak the simulation program TRIM (Transport of Ions in Matter), part of the SRIM software package, is used [192]. Here 1000 alpha particles were fired into 100 Torr of CF_4 and the recoil energies and locations of the interactions along the track were recorded. Example plots from the TRIM software are shown in Figure 6.17 showing the path of the tracks and the energy deposition as a function of distance into the CF_4.

The data from TRIM were then analysed to find the average sum of recoil energy after the Bragg peak. The results of this sum for the 1000 events were plotted and fitted by a gamma distribution, giving an average of 3090 ± 120 eV deposited after the maximum of

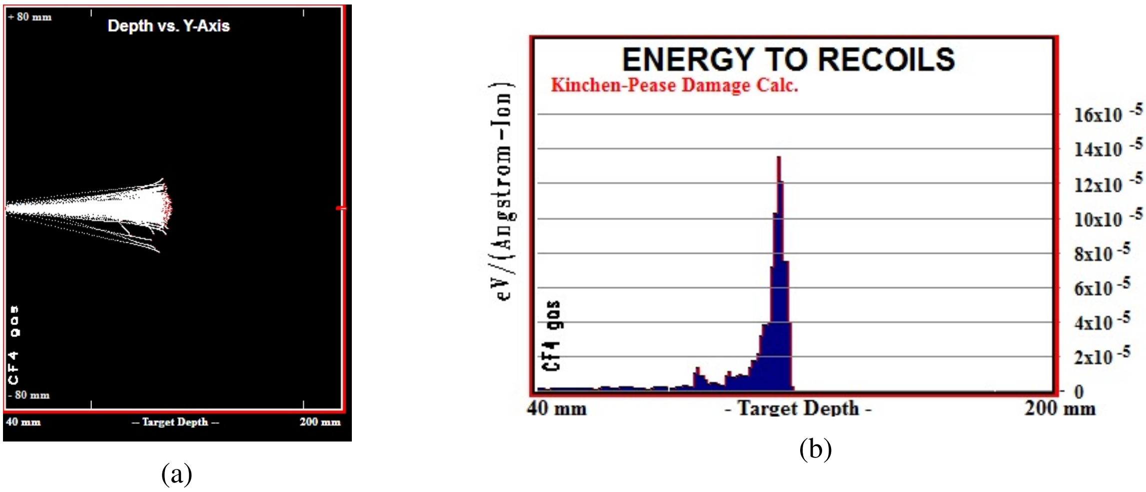

Fig. 6.17 Plots from TRIM of alpha particles in 100 Torr CF_4. (a) shows the distance travelled by the particles and (b) shows the energy deposited along the track.

the Bragg peak. This result is shown in Figure 6.18.

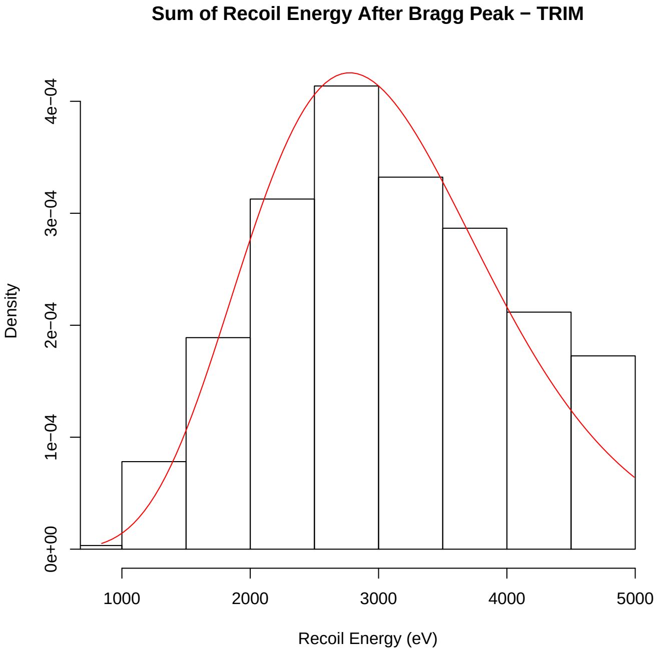

Fig. 6.18 Histogram of the sum of recoil energy deposited after the maximum of the Bragg peak. Energies calculated from TRIM.

To calibrate the system an equivalent measurement needs to be taken experimentally. This is done by taking a set of alpha calibration images using an ^{241}Am source. For the alpha calibrations the vessel was filled with 100 Torr and a drift field was set at 300 V/cm. The THGEM was operated at 880 V, this was chosen to give high gains but limit the number of sparks in the detector. A sample of 500 alpha images was taken, with a 2 second exposure for each image as discussed above. After the data were taken they were imported into MATLAB for analysis. The first step was to implement cuts on the data, the first cut being to remove images with no events. The following cut was to remove multiple hit images as the current algorithm used for the track finding only works for a single track. The final cuts are to remove any alpha track that is not downward going, to remove any background alpha events, to remove tracks that pass through the bottom edge of the image and remove events where the track length is less than half the length of the image. The track length cut removes low energy background events and allows the Bragg peak to be visible in the image. After all the cuts only 34 of the 500 remained. Of the removed images ∼46% had no events and ∼20% had multiple events.

After the event selection a track-finding algorithm was used to find the profile along the track. For each image a noise filter was applied and then a Gaussian fit was applied to every line of the image looking for a peak. If a peak was found the point of maximum value was recorded; if the fit failed it was determined that there was no peak present on that line. After the image was processed a linear fit was made to the saved points to reconstruct the track. An example event is shown in Figure 6.19 showing the maximum points from the Gaussian fit (red) and the linear fit (white). It is seen that the final linear fit is in good agreement with the alpha track seen in the image. An example of a bad fit is shown in Figure 6.20, where a second hit in the image has confused the tracking algorithm and resulted in a bad fit. In future the algorithm could be modified to allow for multiple hit events to give higher statistics for future calibrations, but for this work, as described above, any event with two hits was removed from further analysis.

After the fit is made to the track the maximum point, corresponding to the Bragg peak, is found. The sum is then taken of all the pixels in the track from the Bragg peak to the first pixel that reaches the average background level. The background is calculated from taking the average of a 10 pixel by 10 pixel square in the top left corner of image. After the previously described cuts no images has any signal in this area. The average background was then subtracted from the total sum from after the Bragg peak to give a final value for the image in ADU (analogue to digital units). The same procedure was applied to all events passing the cuts. The average value of the summed energy was calculated to be 42,000 ± 3,000 ADU, where ± 3,000 ADU is the standard error. From the TRIM result and the experimental result a conversion from the ADU of the camera to eV can be made. This gives a calibration conversion of $(7.36 \pm 0.60) \times 10^{-2}$ eV/ADU.

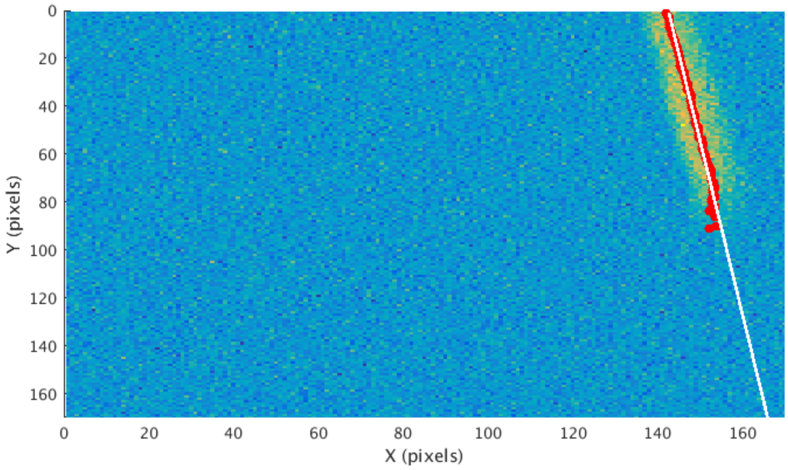

Fig. 6.19 An example alpha event with the results of the track finding algorithm. The maximum points from the Gaussian fit are shown (red) along with the linear fit made to these points to reconstruct the track direction (white).

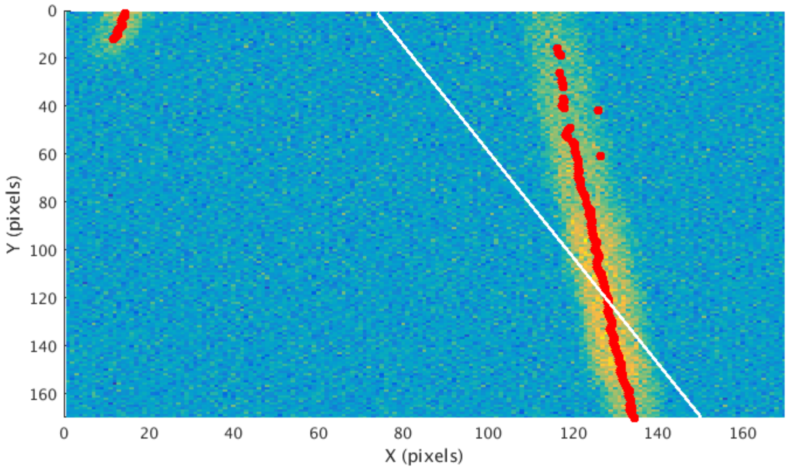

Fig. 6.20 An example multiple-event image with the results of the track finding algorithm. It is seen that the extra track confuses the algorithm.

6.4 Optical Observation of Nuclear Recoils

Immediately after the alpha calibration runs, data were taken with a ^{252}Cf neutron source to look at nuclear recoil events. Several events were seen, although the event rate was low due to the low activity of the source (9.26 kBq) and the small imaging area of the camera (1 cm × 1 cm). Some example nuclear recoil events are shown in Figure 6.21. From taking the sum of the light recorded in the image and using the conversion calculated earlier the energies are found to be 12.3 ± 1.2 keV$_R$ for event (a) and 6.4 ± 0.5 keV$_R$ for event (b).

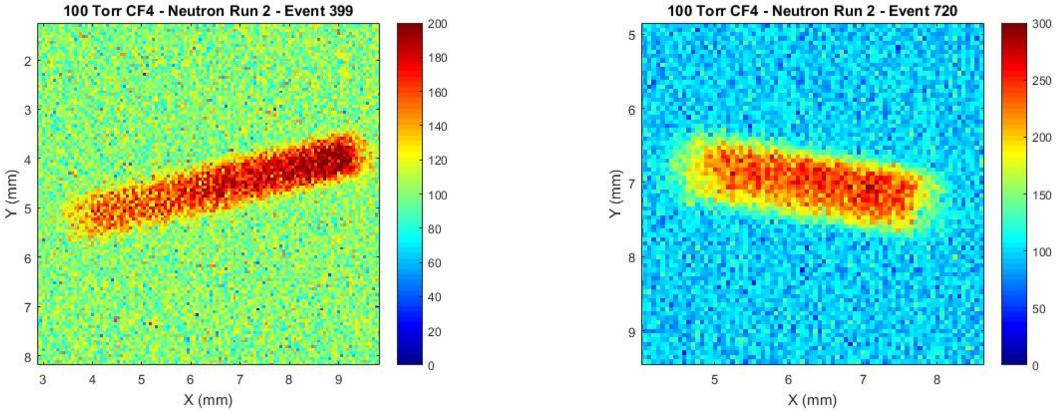

(a) 12.3 ± 1.2 keV$_R$ (b) 6.4 ± 0.5 keV$_R$

Fig. 6.21 Example nuclear recoil events from a ^{252}Cf run in 100 Torr CF$_4$.

These results have shown that it is possible to perform an energy calibration using only the optical signal from recoil tracks in low-pressure CF$_4$. It can also be seen by eye, looking at Figure 6.21, that more energy is deposited towards the right of the track compared to the left. As the source was placed to the right of the imaging area this is a visual signature of the head-tail asymmetry in the nuclear recoil, with more energy deposited at the start of the track compared to the end, as described in Chapter 2. These results have shown that this effect is still observable down to ∼6 keV which is promising for directional detectors looking to observe low energy WIMP recoils. This effect will now be studied in more detail with a higher activity source to achieve higher statistics and test the lowest possible recoil energies that directional information can be extracted from.

6.5 Conclusions

The results from this chapter have shown the potential for using a THGEM TPC in low pressure CF$_4$ gas for directional dark matter detection. High gains have been shown with the charge readout with gains of over 90,000 achieved. The stability and operation across varying pressures and electric fields across the THGEM has permitted for a direct measurement of the Rose-Korff coefficients of CF_4, this is the first known measurement of these coefficients using a THGEM-based detector.

The results from Section 6.3 have shown the potential for using a CCD-based optical readout with the THGEM to obtain 2D track information. Clear nuclear-recoil track images have been recorded and an energy calibration has been performed showing recoils detected down to 6.4 ± 0.5 keV$_R$. From the images the directional information can be clearly seen in terms of the head-tail signature and analysis of this information is the topic of further study. Although the optical readout has potential in directional detection, it also has some drawbacks that may cause issues when trying to scale up the detector size. The imaging area of this system was only 1 cm × 1 cm, whereas typical TPC readout planes are much larger; for example the DRIFT MWPCs are 1 m × 1 m. To do this would require many more CCD cameras and a current cost of ~£6,000/cm^2 is not feasible. Also using a longer drift distance between cathode and detector is complicated in the electron-drift gas of CF_4 due to the added diffusion compared the the negative-ion drift of the CS_2 used in DRIFT. It has been shown that by adding CS_2 to CF_4 it is possible to get negative-ion drift with scintillation remaining [193] but the light output reduces with CS_2 in the mixture.

The following chapter looks at using a new electronegative gas SF_6 as an alternative target gas with the THGEM TPC. The detector is also used with a single channel charge-readout mode to search for head-tail asymmetry from directed neutron exposures. This would allow a directional signal to be recorded without the high costs associated with the optical readout or a readout with a large number of channels.

Chapter 7

Head-Tail Measurements from a THGEM Detector in SF_6

This chapter aims to build upon the work shown in Chapter 6 with the THGEM TPC. This chapter will introduce the use of SF_6 gas in place of CF_4 to take advantage of the negative-ion drift provided by SF_6. In Section 7.1 the properties of SF_6 will be discussed along with initial operation of the detector with this target gas and measurements of gain.

Section 7.2 describes the operation of back-to-back THGEM TPCs along with directed neutron exposures to test the directional sensitivity of the detector and look for a head-tail signal. These tests are looking towards a large scale, single channel readout for future directional dark matter detectors, specifically as part of the CYGNUS collaboration as discussed in Section 2.2.2. Section 7.3 looks at initial results from a large area THGEM in CF_4 gas; this is the first test of a large area THGEM in low pressure gas and is the first step towards operation of a large scale THGEM-based directional detector.

7.1 Operation in SF_6

7.1.1 SF_6 Gas

SF_6 gas has recently been tested for its suitability for directional dark matter detection by Phan et al. at the University of New Mexico (UNM) [194]. The UNM group has shown that it is possible to get good gains in SF_6 with a THGEM TPC with a maximum achieved gain of 3000 in both 30 and 40 Torr of SF_6. It has also been shown that it should be possible to get fiducialisation of event positions from the drifting SF_5^- formed in an interaction. An example event is shown in Figure 7.1 [194] showing the main peak from SF_6^- and the smaller SF_5^- peak. As with the minority carriers described in Chapter 3, the time difference between these peaks can be used to locate the initial interaction location. As SF_6 is an electronegative gas and has a high fluorine content (so sensitive to spin dependent WIMP interactions) it has all of the desirable properties of the current, more complex gas mixture used in the DRIFT-IId detector (30-10-1 Torr CS_2-CF_4-O_2). Also SF_6 is non-toxic, unlike CS_2, which simplifies the health and safety aspect of detector operations in an underground lab considerably.

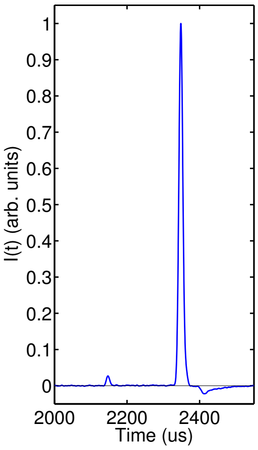

Fig. 7.1 An averaged waveform from Phan et al. [194] showing the SF_5 peak at about 2150 μs, along with the main SF_6 peak ($\sim$2350 μs).

7.1.2 Detector Setup & Data Acquisition

In the work described in this chapter the setup is similar to that described and used in Chapter 6. The main difference is the addition of a second THGEM electrode below the cathode; a diagram of this modified setup is shown in Figure 7.2 with a photograph shown in Figure 7.3. This setup gives the same back-to-back configuration used in the DRIFT-IId detector and is necessary for the directionality measurements that will be described in Section 7.2.

The other difference in this setup compared to Chapter 6 is a new electronics chain and data acquisition (DAQ). The two outer THGEM planes (those furthest from the cathode) are powered by a Bertan model 377P positive HV power supply with the inner planes grounded. The cathode is powered by a Bertan model 377N negative HV power supply. The signals from the THGEMs are read out from the outer THGEM planes and go to a Cremat CR-111 preamplifier. The CR-111 preamplifier is powered by a Cremat CR-150 board. From the

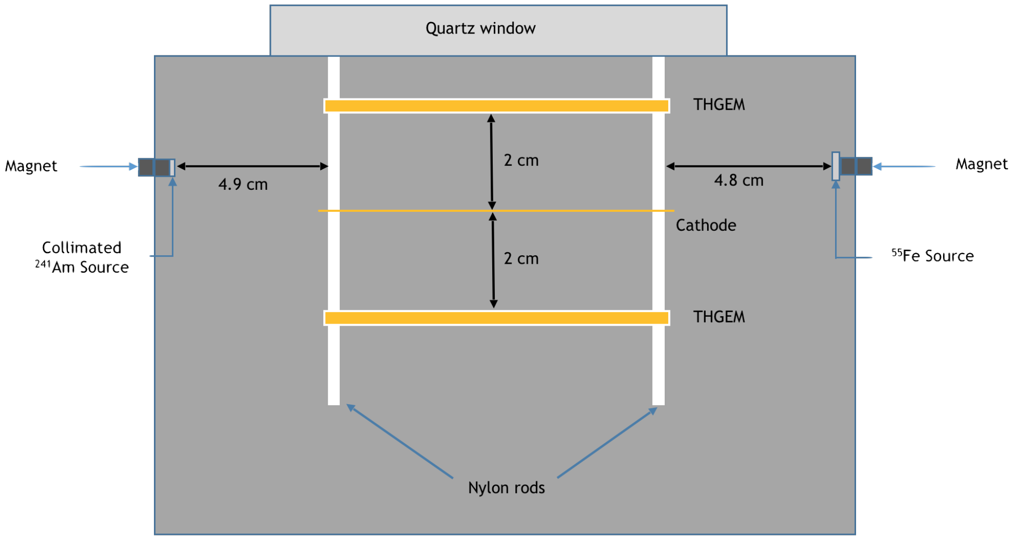

Fig. 7.2 A diagram of the experimental setup used in this work; the major difference from the setup shown in Chapter 6 is the addition of the lower THGEM electrode.

preamplifier the signals go to a Cremat CR-200-4μs shaping amplifier before going to a National Instruments 5751 card and being digitised. A diagram of the electronics is shown in Figure 7.4.

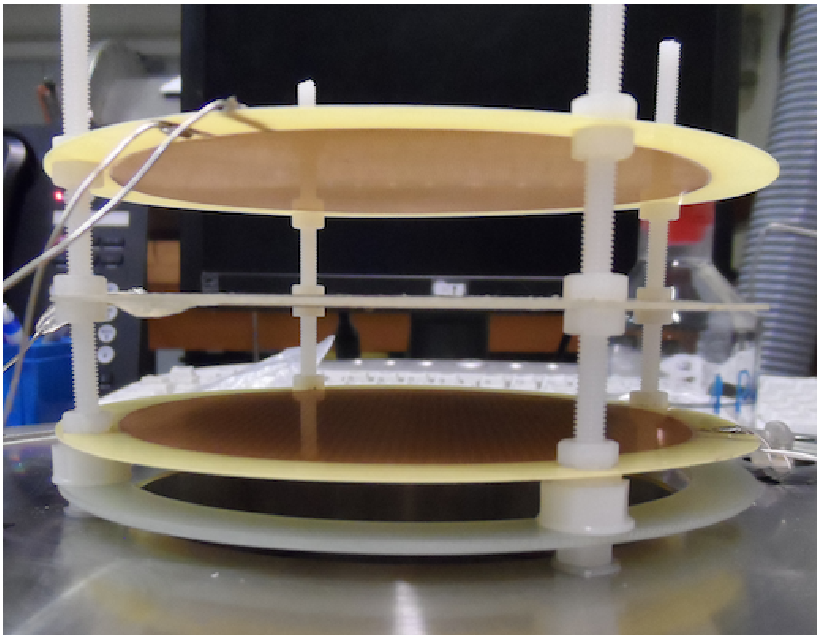

Fig. 7.3 A photograph of the experimental setup used in this work showing the upper and lower THGEM electrodes in place either side of the cathode.

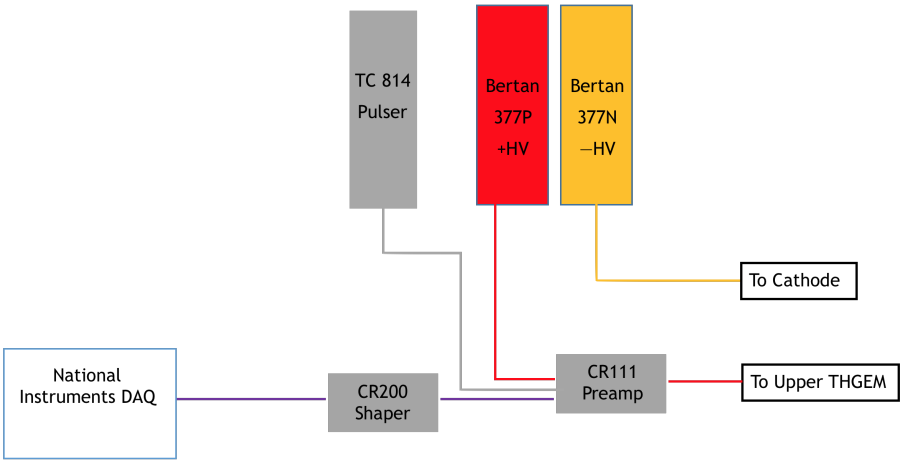

Fig. 7.4 A diagram of the electronics and power supplies used with the upper THGEM. An identical setup is used for the lower THGEM.

The DAQ software is written in LabVIEW and takes in the data from the two THGEM channels. If an event passes the trigger threshold (set at 10 mV in this work) the waveforms are printed to screen and saved to disk. The saved waveforms were then analysed using the programming language R. The first step in the data analysis was to correct for the baseline offset from the electronics; this was done by taking the first 50 μs of each waveform and taking an average. This average was then subtracted from every point in the waveform to give a baseline-corrected event. As the pre-trigger is set at 2 ms, the first 50 μs of the waveform are away from the main region of interest, and so do not contain extra charge from the event. This baseline restoration has been shown to work well with an example event shown in Figure 7.5 with the baseline-corrected event shown on the same plot.

After the baseline restoration other parameters can then be calculated for the waveform, such as the maximum pulse height and integral charge. These parameters can then be used to calibrate the THGEMs and calculate the charge gain achieved in SF_6.

7.1.3 Gain Calculation & Calibration

The gain of the THGEMs was calculated using a similar method to Chapter 6. The first step was to use a Tennelec TC 814 Pulser to inject a pulse into the test input of the CR-111 preamp. In this analysis the saved waveforms are used to plot a histogram of the integral charge of the pulses opposed to using the pulse height spectrum from the MCA as used in Chapter 6. As the THGEM gain is lower in SF_6 the use of integral charge helped in the

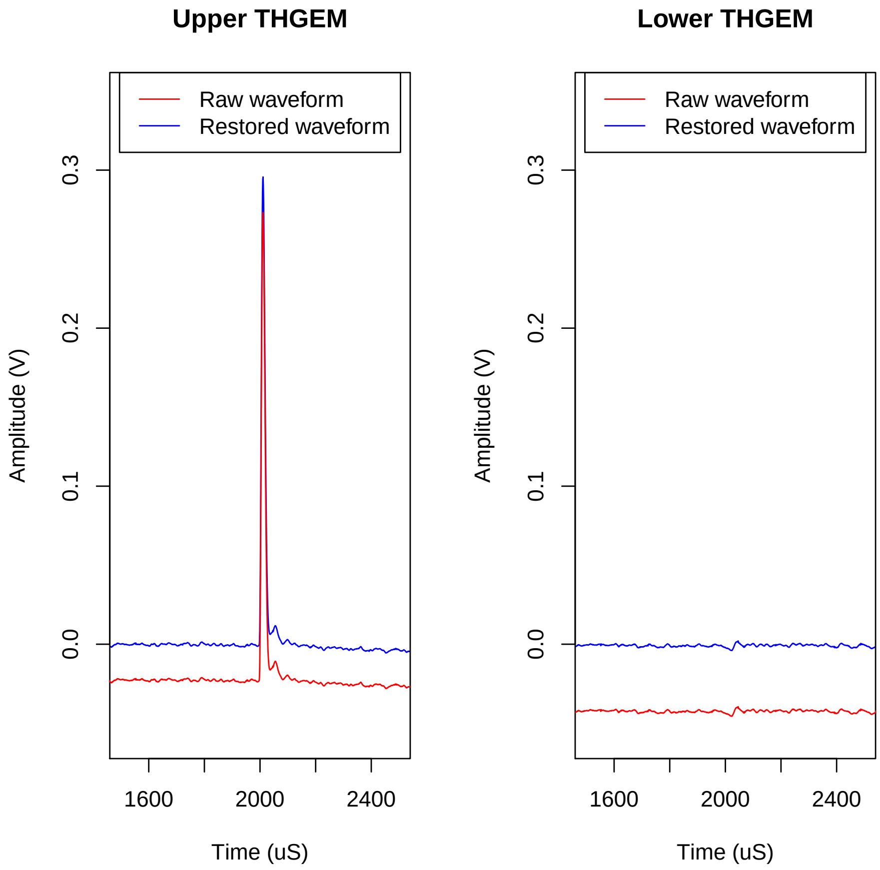

Fig. 7.5 A plot of an example raw waveform (red) along with the baseline corrected waveform (blue). It can be seen that the restoration accurately brings the baseline to 0 V.

separation of signal and noise compared to using the pulse heights. An example histogram of integral charge from a test pulse is shown in Figure 7.6.

The mean of the histogram was taken and from using multiple pulse heights a conversion was calculated from input charge to integral charge, similar to the input charge to ADC conversion found in Chapter 6. Using the W-value of SF_6 as 34.0 ± 0.4 eV [195] a gain to integral charge conversion can be obtained. The next step was to take calibration data with ^{55}Fe x-rays. This was done at various pressures of SF_6, and a integral charge spectrum was plotted for 20, 30, 40 and 50 Torr of SF_6; these spectra are shown in Figure 7.7. These spectra are from the upper THGEM only, but the lower THGEM was seen to operate with similar results.

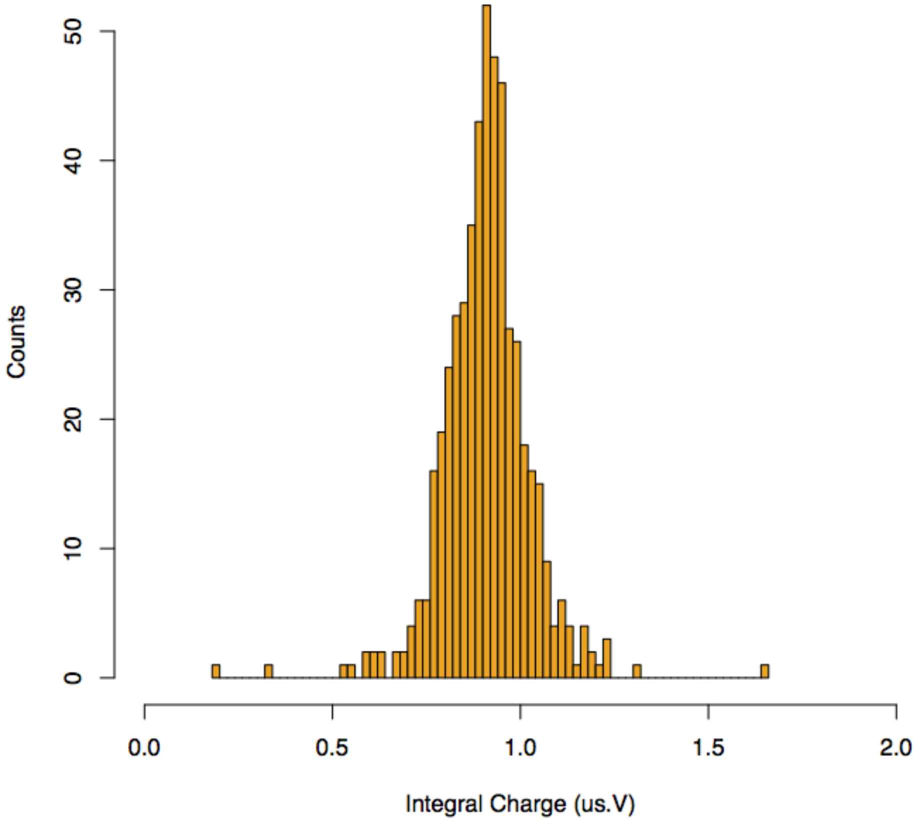

Fig. 7.6 A spectrum of the integral charge from a 300 mV pulse in the preamp test input.

From these spectra a clear ^{55}Fe peak can be seen for each. From taking the peak of these spectra, from the fitted gamma distribution, and using the integral charge to gain conversion, a gain was calculated for each pressure; these are shown in Table 7.1. The highest recorded gain here was 8600 ± 150 at 20 Torr of SF_6 with the error in the gain measurements taken from the error in the peak position of the fits. The resolution of the peaks, calculated from the mean divided by the FWHM, is calculated to be from 17 - 20 %. To the author's knowledge these are the highest gains and best resolutions produced in SF_6 to date.

Pressure (Torr)	THGEM Voltage (V)	Gain	Resolution (%)
20	770	8600 ± 150	19
30	845	8100 ± 180	20
40	900	8100 ± 130	17
50	940	7800 ± 300	20

Table 7.1 Gain measurements for different pressures of SF_6.

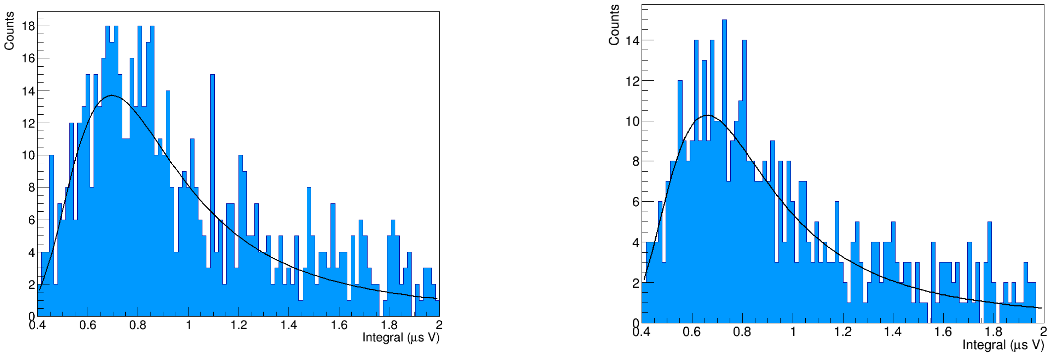

(a) 20 Torr.

(b) 30 Torr.

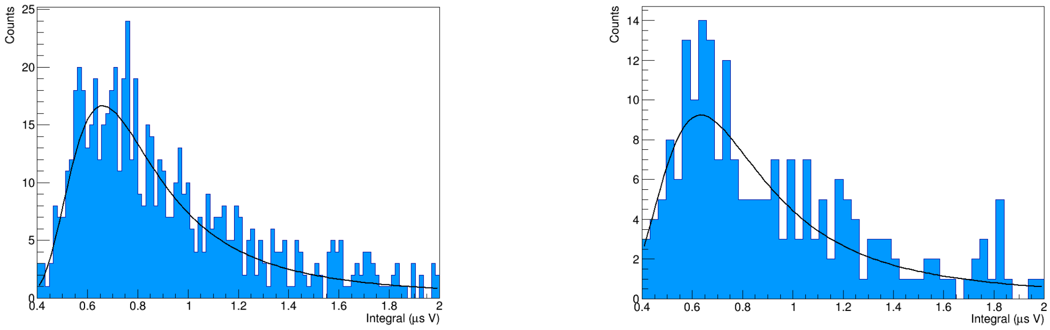

(c) 40 Torr.

(d) 50 Torr.

Fig. 7.7 ^{55}Fe spectra in pressures of 20 - 50 Torr of SF_6.

It can be seen that the shape of the peaks is not the expected gaussian shape but is skewed towards low energies. Initial simulations [196] suggest that this is due to the short shaping time of the Cremat CR200 (4 μs) compared to the drift velocity. The drift velocity is calculated to be 68.4 ± 0.3 μm μs^{-1} for 30 Torr of SF_6 with a drift field of 500 V cm^{-1} and a reduced mobility of 0.540 ± 0.002 cm^2 V^{-1} s^{-1} [194]. The 4 μs shaping time results in the shaped pulse from tracks with a z extent of over 0.27 mm missing some of the energy. This causes more events to be reconstructed with lower energies producing the skewed plots seen above. If confirmed this effect would also mean that the gains stated here are underestimated. For future work a shaping amplifier with a longer shaping time will be used to test this effect further.

It should be noted that these gains were taken at voltages where sparks occurred every few minutes. The THGEMs used in this work have been operating for several years and it is possible that some dust etc. has accumulated on the surfaces in this time. If they were to be cleaned, etched in acid for example, it may be possible for them to operate at these voltages with no breakdowns. However if this is not the case the THGEMs would need to be operated at a lower voltage for long term running, so the gains would be slightly lower.

The integral charge spectrum from ^{55}Fe was also used for calibrating the energy deposited into the detector from other interactions, such as the neutron-induced nuclear recoils that will be reported in Section 7.2. Because it is not known if a nuclear interaction is with a sulphur or fluorine nucleus, we cannot give a precise measurement of the energy, but the DRIFT model can be adopted whereby the number of ion pairs (NIPs) from the event is used in lieu of this. From the W value (34.0 ± 0.4 eV) and the ^{55}Fe energy (5.89 keV) the NIPs from ^{55}Fe x-rays is calculated to be 173 ± 2. By finding the peak of the ^{55}Fe spectrum a NIPs to integral charge conversion can be found by assuming this is equivalent to 173 electrons. This calibration is made for each run, with every neutron exposure preceded by ^{55}Fe exposures for the upper THGEM, then the lower THGEM. These runs are known as the *ucal* and *lcal* runs respectively, and are to calibrate for any difference in gain between runs and between THGEM electrodes. In future work they will also be useful for tracking the stability of the detector performance.

7.2 Head-Tail Measurements with Single Plane THGEM Readout

This section follows the method used by the DRIFT collaboration [122, 123] and discussed in Section 3.4.1. The aim of this work is to see the head-tail effect, i.e. see the difference in charge in the beginning of the track compared to the end, as discussed in Chapter 2. Using this effect could allow directional dark matter detectors to reject isotropy and show there is a signal coming from the Cygnus constellation. In this work the THGEM was read out using only the charge signal from the outer THGEM electrodes. This results in no information about the x or y dimensions, with z information coming from the timing signal. As the DRIFT results used only the charge signal for the head-tail measurement a similar analysis can be performed with the THGEM setup.

The detector was set up in the back-to-back configuration described in Section 7.1.2 and shown in Figure 7.2. A ^{252}Cf neutron source was used to perform three directed neutron runs. The source was placed above the vacuum vessel for the +z run, with the source 7 cm from the upper THGEM. The source was placed below the vacuum vessel for the –z run, 40 cm from the lower THGEM, and at the side of the vessel for the –x run, with the source 7 cm from the edge of the THGEMs. A diagram showing these source positions is shown in Figure 7.8. Ideally the source would be placed further from the fiducial volume for these tests to allow for a more directed neutron exposure, but laboratory constraints resulted in the +z and –x distances and the low rate of the source prevented the source being placed further away in the –z run. As only the timing information, corresponding to the z direction, is being used in the analysis we only expect a head-tail signal in the ± z runs. As the x run is perpendicular to the ± z runs it is expected to give a null result to confirm the head-tail signal seen in the ± z runs. As the THGEM planes are circular there should be no difference between exposures in the x or y directions so the –x run was the only exposure taken to give the expected null result.

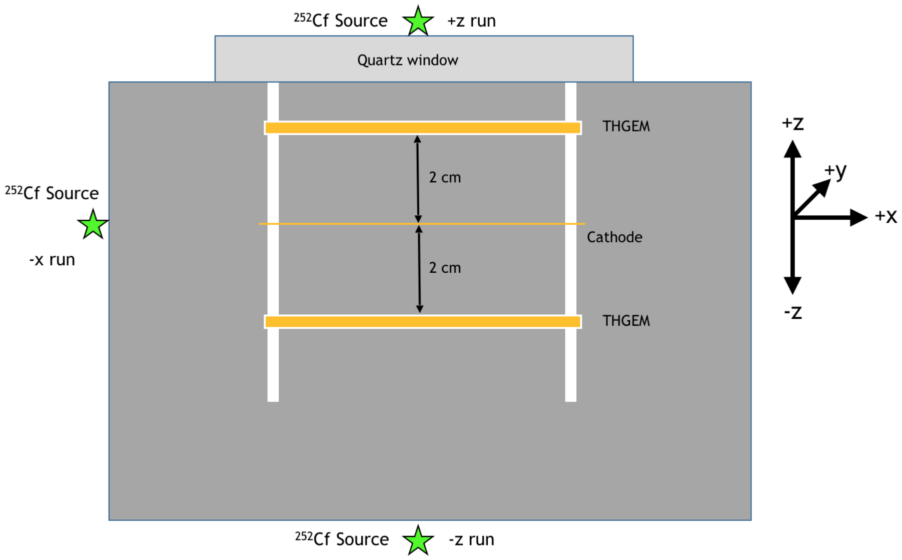

Fig. 7.8 Diagram of the ^{252}Cf source locations for the directed neutron exposures.

For the neutron runs the vessel was filled with 30 Torr SF_6 and the detectors were operated with $\Delta V = 830$ V with an expected gain of $\sim$6500. The cathode was held at –1000 V to give a drift field of 500 V/cm in both drift volumes. The voltage was lower than the value used in Section 7.1.3 to try and reduce the number of sparks as these can damage the detector over longer runs and cause a sharp spike in the rate of the detector which wastes memory and computing time when running the analysis.

Before the main head-tail analysis could occur data reduction had to take place. After the calibration from the *ucal* and *lcal* runs, a cut was made on all neutron events of less than 400 NIPs. This removed most low level noise events and events from the wandering baseline caused by sparks on the THGEMs. A cut was also placed on events with more than 2000 NIPs: this was to remove background events in the detector such as alpha particles. The next major cut was to remove all events that were above threshold in both detectors. Due to the low cross-section of the neutrons in the low pressure gas double scatters of neutrons are very unlikely so these events are rejected. After these cuts the head-tail analysis can begin.

The first part of the head-tail calculation is to find the peak of the event; a region of interest (ROI) is then set at 50 μs before and after the peak. This was found to contain all charge from nuclear-recoil events. If any events extended beyond the ROI they were also cut from the analysis. After the peak was found the points before and after the peak where the charge reaches 25% of the maximum were located to form a second ROI; these will be referred to as *roistart* and *roistop* respectively. The point in time half way between these was also calculated; this will be known as *roimid*. An example event from the lower THGEM is shown in Figure 7.9 with lines representing *roistart*, *roimid* and *roistop*. Two parameters, η_1 and η_2, are then calculated from this event. These are the sum of charge from *roistart* to *roimid* and from *roimid* to *roistop* respectively. The red shaded region in Figure 7.9 shows η_1 and the green shows η_2.

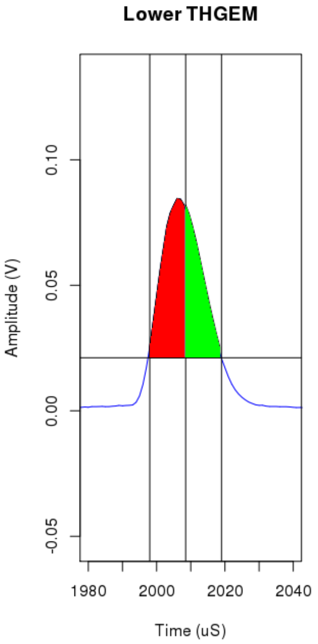

Fig. 7.9 An example event from the +z run showing the areas used for η_1 (red) and η_2 (green). This calculation is the main basis of the head-tail analysis looking in the difference in charge in the start and end of the tracks.

After η_1 and η_2 are calculated, the ratio of these, α, can be found, where $\alpha = \frac{\eta_1}{\eta_2}$. Here the expectation would normally be that if $\alpha > 1$ (more charge in the first half of the pulse) the recoil is travelling towards the cathode and if $\alpha < 1$ the recoil is travelling towards the THGEM. However due to shaping effects from the electronics where the incoming charge is integrated across the shaping time this statement is not true. To compensate for this an analysis over the whole data set has to be made looking at the difference between events in the two detectors. This is done by calculating the differences of the mean values of α from each detector for each run. This gives us $|\Delta\alpha|$ defined by

$$|\Delta\alpha| = \langle\alpha\rangle_U - \langle\alpha\rangle_L, \tag{7.1}$$

where $\langle\alpha\rangle_U$ is the average α from the upper detector and $\langle\alpha\rangle_L$ is the average α from the lower detector. This is known as the head-tail asymmetry parameter. The significance of the head-tail signal can be calculated by taking the head-tail asymmetry parameter divided by the standard error. This result, along with the other significant numbers from the calculations is shown in Table 7.2.

Run	N_{events}	N_U	N_L	$\langle\alpha\rangle_U$	$\langle\alpha\rangle_L$	$\Delta\alpha$	Significance
+z	213	82	131	1.514 ± 0.032	1.535 ± 0.018	-0.021 ± 0.037	–0.57
–z	511	205	306	1.456 ± 0.019	1.539 ± 0.011	-0.083 ± 0.022	–3.8
–x	313	131	182	1.462 ± 0.020	1.475 ± 0.018	-0.013 ± 0.027	–0.48

Table 7.2 Results of the head-tail measurements from the THGEM detector in 30 Torr SF_6.

These results clearly show a significant result in the –z run compared to the null result from the –x run. However it was expected that the +z run would give a positive significance as the source was facing down, towards the cathode for the upper detector and towards the THGEM in the lower detector, but instead no significance was seen in the result. This may be due to the source placement for the +z run as it was only 7 cm from the upper THGEM, where the source was 40 cm from the lower THGEM in the –z run. This will cause a higher spread of neutron angles in the detectors causing a smearing of the result. As previously mentioned the source position for the +z run was due to spatial constraints in the lab. A future test is planned and it should be a priority to allow a source placement further from the upper THGEM to allow for better collimation of the neutron source.

More efficiency would also be possible by having a veto region around the THGEM plane. This would allow the removal of the upper threshold at 2000 NIPs as any background alphas in the active volume would be expected to cross the side of the detector. The veto region could be created by etching an isolated outer ring onto the THGEM plane and having this operated and read out separately from the active region of the THGEM. A diagram of a possible THGEM design with a veto is shown in Figure 7.10, showing a 5 mm thick veto region around the current 10 cm diameter THGEM. This veto will be a vital part of background rejection for the simplified one-dimensional readout described here.

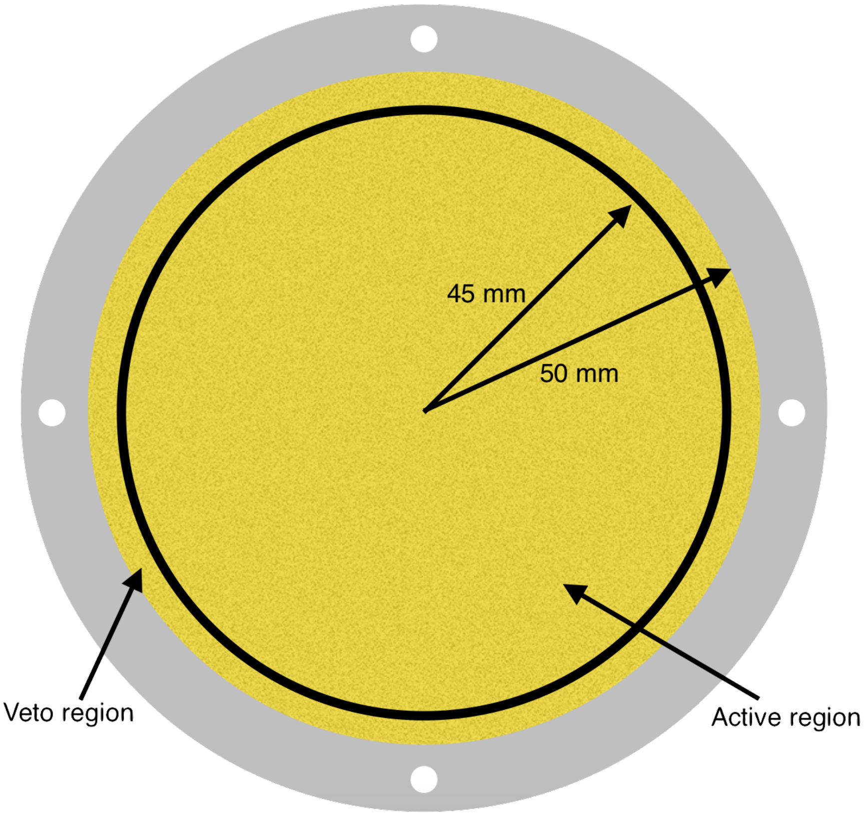

Fig. 7.10 A diagram of a THGEM plane with a 0.5 cm veto around the edge. This would be a vital part of background rejection in one-dimensional THGEM readouts.

7.3 Testing a Large Area THGEM

This section describes the first tests of a large area THGEM for directional dark matter work. This is an important step towards producing a large-scale detector. A 0.4 mm thick, 50 × 50 cm^2 THGEM was produced in collaboration with AWE; an image of the THGEM is shown in Figure 7.11a. The pitch was 1.2 mm, hole diameter was 0.4 mm and there was an etched rim of 0.15 mm around each hole to prevent sparking. The THGEM was operated in Boulby Underground Laboratory in a 1.5 × 1.5 × 1.5 m^3 stainless steel vacuum vessel. The THGEM and cathode were placed vertically to prevent sagging of the boards disrupting the electric fields. The two boards were placed 1 cm apart to produce the drift region with an ^{241}Am alpha source placed below the fiducial volume for calibrations. This setup is shown in Figure 7.11b.

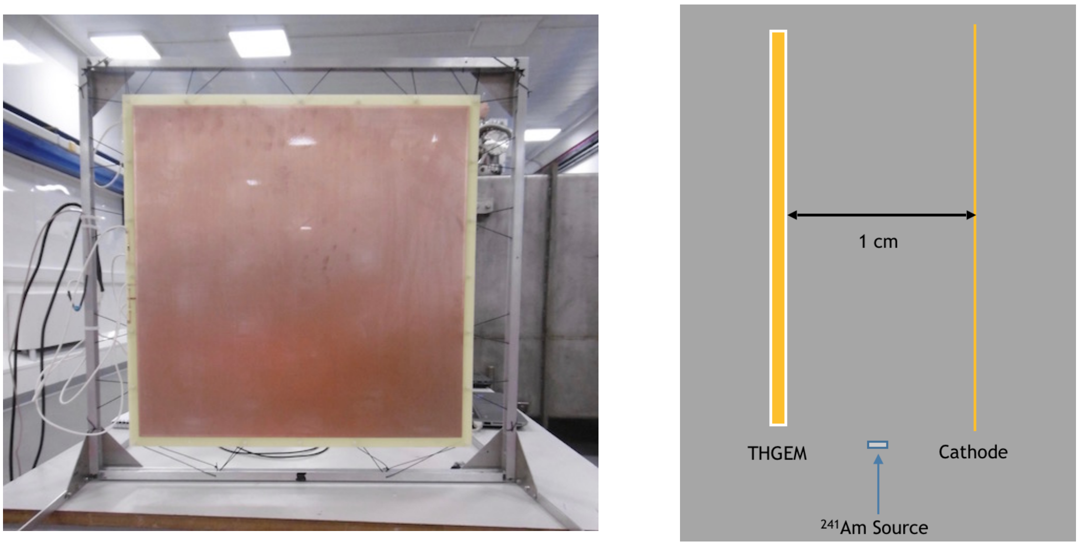

(a) (b)

Fig. 7.11 A photograph of the 50 x 50 cm THGEM at Boulby (a) and a diagram of the THGEM TPC setup inside the vessel, showing the 1 cm drift gap between THGEM and cathode and the placement of the ^{241}Am alpha source.

The THGEM was initially operated in CF_4 gas at low pressures between 30 and 100 Torr. The THGEM was powered using a similar setup to that described in Chapter 6, with the side of the THGEM closest to the cathode at 0 V, with the opposing side held at a positive voltage. The cathode was held at –300 V in all tests. The THGEM signal was taken to an Ortec 142 IH preamplifier, then through an Ortec 572 shaping amplifier before a pulse height spectrum is recorded via an Ortec 926 ADCAM MCB (multi-channel buffer). This is the same as the setup shown in Figure 6.6. The spectrum was calibrated using a pulser using the method described in Chapter 6. Results from initial tests have indicated low gains from the THGEM, with a maximum gain found of 124 in 50 Torr CF_4 at a voltage of 740 V. Figure 7.12 shows an example alpha spectrum taken in 50 Torr CF_4 with 700 V across the THGEM [197].

The current theory for the low gains is that it is due to the comparatively large rim sizes around the THGEM holes, with 0.15 mm rims on the large THGEM compared to 0.04 mm in the CERN THGEMs used in Chapter 6 and in the earlier work in this chapter. The extra rim size increases the metal to metal distance of the THGEMs, reducing the electric fields

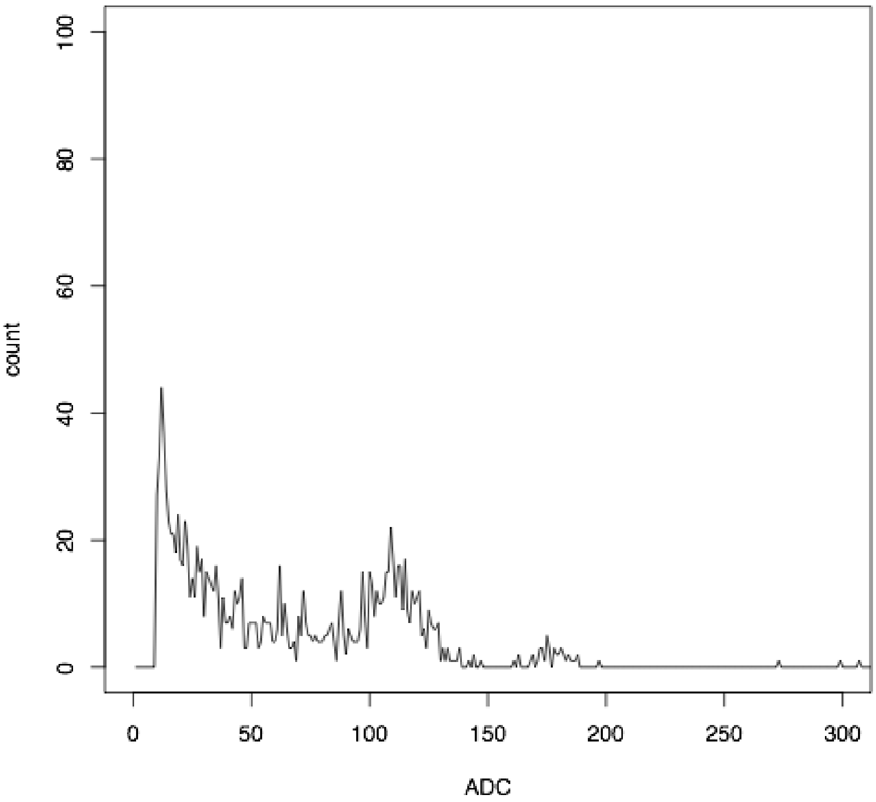

Fig. 7.12 An example alpha spectrum from the latest runs with the large area THGEM. The spectrum was taken in 50 Torr CF_4 with 700 V across the THGEM [197] and recorded on an Ortec 926 ADCAM MCB.

produced in the holes for a given voltage difference. For example, 740 V across the CERN THGEM produces a field of $\sim$15,400 V/cm, compared to $\sim$10,600 V/cm from the large area THGEM. Simulations of both THGEMs will be tested to confirm the cause of the low gains in the boards, with the results being used to help design new THGEMs with a design optimised to produce high gains.

7.4 Conclusions

This chapter has shown the initial operation of a THGEM TPC in low pressure SF_6 gas. Gain measurements have been made from ^{55}Fe calibration runs in pressures from 20 to 50 Torr of SF_6, with gains of up to 8600 ± 150 found. These gain measurements are, to the author's knowledge, the highest made to date using a gas TPC in SF_6 gas, with the energy resolutions of 17 to 20 % also being the best seen to date.

Two THGEM TPCs were operated in a back-to-back mode and directed neutron runs were made to look for the head-tail effect using a one-dimensional detector. A signal of the head-tail effect was seen in the –z run, but the results of the +z run did not give a head-tail signal. A null-result was obtained from the –x run as expected, a result that rules out some systematic errors in the analysis as the cause of the significance seen in the –z run. The cause of the lack of signal in the +z run has been discussed and a modified experimental setup has been described to be tested in the future. A design for a modified THGEM board has also been shown with a veto region around the edge of the THGEM to allow improved background rejection capabilities.

Initial operations of a large area THGEM have been discussed with initial gain measurements made using ^{241}Am calibration runs. These have shown low gains with a maximum of 124 in 50 Torr CF_4 at a voltage of 740 V. The size of the rim around the THGEM holes has been discussed as a cause of the low gains and simulations are underway to confirm this and optimise future THGEM designs.

Chapter 8

Directionality and WIMP Limit with a Simplified DRIFT-IId Readout

This chapter will describe the analysis of data from the DRIFT-IId detector. The analysis will focus on the operation of the detector in a simulated one-dimensional readout mode, described further in Section 8.1. Two analyses were performed in this readout mode, the first of which is a directional analysis looking for the head-tail signature of recoils from directed neutron runs. This will use the method discussed in Section 3.4.1 and the method and results of this are shown in Section 8.2. The second analysis considered is the calculation of a WIMP exclusion limit using data from DRIFT-IId background runs, shown in Section 8.3. This result will be compared to a new WIMP limit calculated using the same data but with the original readout used in past DRIFT analyses (as described in Section 3.4.4).

8.1 The Simplified Readout Mode

As described in Chapter 3, each DRIFT MWPC is made of 3 wire planes, each of 552 wires. The instrumented anode and inner grid planes are composed of 448 central signal wires and 52 outer veto wires, with the anode having stepped guard wires in place of the outer 11 veto wires. The central signal wires of these planes are grouped, with every 8th wire connected and read out in one channel, with each channel containing the signal from 56 wires. The grouping is done for the anode and inner grid planes on both left and right MWPCs. All 82(104) veto wires are connected together for each anode(grid) plane. The combination of these results in 9 channels of readout for each wire plane, with 36 channels needed to instrument the entire detector. An example event is shown in Figure 8.1 showing the signal from each of these channels. The labels represent the left/right anode channels (LA/RA), left/right grid channels (LG/RG) and the left/right anode and grid veto channels(LVA/RVA/LVG/RVG). The other channels shown are known as the ‘sum lines’. These lines are the sum of all the respective channels: for example, the left anode sum (LAS) is the sum of all left anode channels (LA1 to LA8).

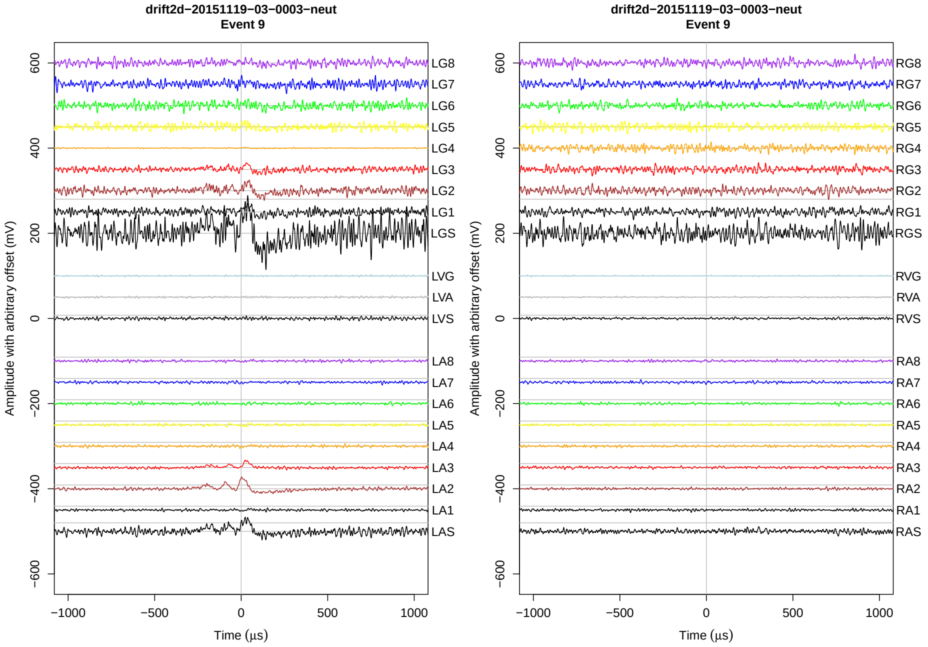

Fig. 8.1 An example event from the DRIFT-IId detector. The labels represent the left/right anode channels (LA/RA), left/right grid channels (LG/RG) and the left/right anode and grid veto channels(LVA/RVA/LVG/RVG). The other channels shown are known as the ‘sum lines’. These lines are the sum of all the respective channels, for example the left anode sum (LAS) is the sum of all left anode channels (LA1 to LA8)

The sum lines described above are the main basis for the simplified readout mode used in this work and previously used by Ezeribe [198] where a one-dimensional WIMP limit was obtained using 54.7 days of shielded DRIFT data. Using only the sum lines on both the left and right MWPCs simulates a one dimensional detector, such as a single THGEM electrode as discussed in Chapters 6 and 7. The aim of this chapter is to show that it is still possible to maintain directional sensitivity in terms of a head-tail signal with just a single plane of readout. The simplified readout technique could confirm a lower cost route to a scaled up detector. A key issue with the technique is in background rejection: new cuts for background reduction are discussed in Section 8.2. Measurements of the efficiency and the ability for the simplified readout to run background free and set a WIMP limit from ∼100 days of shielded

DRIFT data will be shown in Section 8.3 along with a comparison to the original 36 channel readout mode.

^{55}Fe Calibration

The calibration of the DRIFT-IId detector for this analysis is unchanged from Ezeribe [198] but will be briefly described here. While data taking, a calibration run with an ^{55}Fe source is taken to calculate the energy deposited in the detector. A source is installed behind each MWPC and every 6 hours a remotely operated shutter is opened to allow the ^{55}Fe x-rays to be incident in the fiducial volume, first on the left, then on the right. As the energy from ^{55}Fe x-rays is lower than the nominal DRIFT threshold, 5.89 keV compared to $\sim$30 keV for a fluorine recoil, these runs are taken in an untriggered mode and 100 waveforms of 13 ms are recorded for each MWPC calibration.

To obtain a calibration constant from the ^{55}Fe data an analysis threshold is set at 2.3 mV. A charge integral is taken of any pulse on the sum line above this threshold, and an average value is taken of all the pulses to obtain a value that is equivalent to 173 NIPs, the amount from ^{55}Fe in the DRIFT gas mixture. This calibration constant can then be applied to data taken in the following 6 hours of operation to give NIPs values for each event. The energy is given in terms of NIPs as it is unknown which nucleus is recoiling for a given event so the exact energy cannot be reconstructed.

The calibration on the sum line has previously been shown to be $\sim$18% higher than the same calibration from the normal DRIFT analysis leading to an underestimate of the energy of an event [198]. As the sum line is the combination of all 8 channels on a single detector, the noise is higher than for a single channel and as the ^{55}Fe signal from an event is only on a single wire, this lowers the signal to noise. This results in many ^{55}Fe events becoming lost in the noise reducing the efficiency of this analysis. Although the calibration is a known issue, it is the topic of future work and for this analysis it will be used as it was previously [198].

8.2 Head-Tail Sensitivity with the Simplified Readout

This section describes the calculation of the sensitivity of the simplified DRIFT readout to the head-tail effect. This work uses the same head-tail data used by Battat et al. [123] but using the simplified readout described above, rather than the nominal DRIFT analysis. To test the detector sensitivity to the head-tail effect, four directed neutron runs were made.

The source was placed to the left of the detector for the +z run, to the right of the detector (–z run), above the detector (–y run) and in front of the detector (–x run). The ±z runs are known as the optimal directions as they are expected to give a significant head-tail signal. The –x and –y runs are known as the anti-optimal runs, as they are expected to give a null result to give a sanity check on the analysis. The source positions for all four runs are shown in Figure 3.10 [123]. The live times for each run are shown in Table 8.1 and for reference the datasets used are shown in Table A.1 in Appendix A. During these runs the detector was operated with all of the polypropylene pellet shielding removed from the top and sides of the detector. To preserve the structure of the lab the underfloor shielding remained in place.

Source Position	Live Time (Days)
+z	1.793
–z	3.320
–x	0.774
–y	0.561

Table 8.1 Live time of the directed neutron runs.

Waveform Processing

After data passing the 15 mV hardware threshold were imported the waveforms were processed to remove noise and electronics effects. The first part of the processing is to remove high frequency noise, specifically the 55 kHz sinusoidal noise originating from the central cathode [159]. This noise is removed by using a Fourier transform notch filter, which takes the Fourier transform and then removes the 55 kHz noise and its harmonics. An inverse Fourier transform is then used to obtain the original waveform without the noise. The following step is to remove the low frequency noise which originates from the 50 Hz of the mains electricity. This is removed by fitting and subtracting a 50 Hz sine wave to the data with 5 harmonics. The fitted sine wave is then subtracted from the waveforms. A Savitzky-Golay smoothing filter [199] with a 50 μs smoothing window is then applied to the data. The final step in the waveform processing is to correct for the undershoot that occurs after every pulse. This is an effect of the Cremat shaping amplifier and the baseline is restored before analysis of the data begins.

Data Selection

After the waveforms are processed cuts were made to remove background events from the analysis. Any events passing the software threshold of 9 mV for the anode lines (full analysis only) or 20 mV on the sum line were analysed further. An ROI was set up from –700 to 700 μs then an energy threshold is set at 700 to 6000 NIPs; any events not inside this region were removed. After this any events that produced a signal in both detectors simultaneously were removed, as neutron- or WIMP-induced nuclear recoils will only have a range of a few mm and only single hits are expected.

A cut to remove sparks is made on the rise time of the pulse: the time from the start of the event to reaching the peak charge must be over 3 μs. Next a cut is made on the minority carriers, described in Chapter 3. If the ratio of charge in the minority peaks compared to the main peak is not between 0.3 and 0.6 then the events are removed. This cut has a slightly lower upper bound in this work compared to [145] as some spark-like events were found to be passing the cut between 0.6 and 0.65. The cut is discussed in more detail in Refs. [145, 166, 198]. Any events with a hit on the veto wire were also removed. This has been modified from the previous method to include the entire veto wire, compared to just the veto signal in the ROI, because the previous cut failed to remove some background events. Such an event is shown in Figure 8.2: this is clearly identified as a bad event due to the hit on the left anode veto channel. This event passed the current cuts because of the ROI set on the analysis of –700 to 700 μs. As the charge on the veto crosses the threshold outside of this region the analysis does not remove it. To remove this event the additional cut is made to remove events with a hit on the veto wire at any point in the 13 μs window.

The previously described cuts are all used with both the simplified and full DRIFT analyses. However, two cuts that are not possible with the simplified readout are to remove events that hit more than 8 wires in the MWPC and to remove any events with non-contiguous wire hits. These cuts are designed to remove long events such as alpha particles, but due to the use of the sum line this is not possible in this work. To replace these a new cut was made on the charge before and after the ROI. The region from beginning of the waveform to the start of the ROI is known as the ‘up veto’, with the area from the end of ROI to the end of the waveform being the ‘down veto’. If there is charge in these areas of the waveform it indicates a long event has been recorded in the detector. Any event with a value over 3 mV on either the up veto or down veto will be removed. The final data selection applied is to remove events with z positions less than 15 cm or more than 48 cm from the MWPC. The higher z cut has been lowered from the 50 cm used previously [145] as this will include background

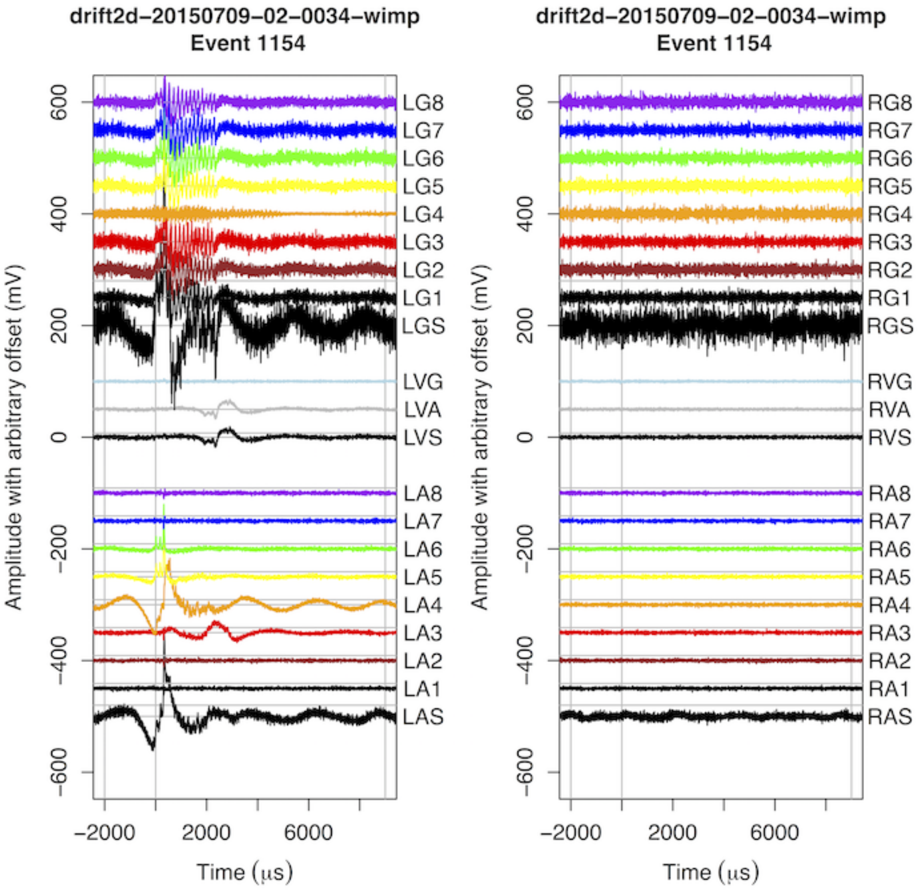

Fig. 8.2 The waveform of the event that passed the cuts to appear in the fiducial volume. It can be seen that there was a hit on the LVA veto line that indicates a background event.

RPR events on the central cathode. The lower z cut is due to limitations of the z calculation at z values lower than this.

Head-Tail Calculation

After the events for analysis have been selected the parameters to look for the head-tail effect are calculated. The method followed is identical to that shown in Ref. [123] and described in Chapter 3, with the only difference being the use of the simplified analysis here compared to the full DRIFT analysis used previously. As in Ref. [123] with DRIFT and Chapter 7 with the THGEM TPC the α parameter is calculated for each event. This is the ratio of charge in the first half to charge in the second half of the pulse. The start and end points of the ROI for this calculation are set at the point where the pulse crosses 25% of the maximum pulse height before and after the pulse. As previously discussed a combination of the left and right detectors is required due to the shaping effects on the pulses. This is calculated by finding $\Delta\alpha$, where $\Delta\alpha = \langle\alpha_L\rangle - \langle\alpha_R\rangle$ and $\langle\alpha_L\rangle$ and $\langle\alpha_R\rangle$ are the mean values of α for the left and right detectors respectively. From this a significance of the result can be calculated by taking $\Delta\alpha/\sigma_{\Delta\alpha}$. The results from the head-tail analysis are shown in Table 8.2 showing the significance from each run as well as other important numbers from the calculation. Also shown are the combined significances from the optimal and anti-optimal runs using $|\Delta\alpha|$ from each run and the corresponding numbers from [123] for comparison.

Run	N_{events}	$\langle\alpha\rangle_L$	$\langle\alpha\rangle_R$	$\Delta\alpha$	Significance
+z	12285	1.032 ± 0.002	1.060 ± 0.001	-0.028 ± 0.002	–14
–z	17348	1.057 ± 0.002	1.011 ± 0.002	0.046 ± 0.003	15
–x	229	1.069 ± 0.022	1.054 ± 0.023	0.015 ± 0.032	0.47
–y	236	1.060 ± 0.020	1.057 ± 0.022	0.003 ± 0.030	0.10
Optimal	29633	-	-	0.074 ± 0.004	18.5
Anti-Optimal	465	-	-	0.018 ± 0.044	0.409
Optimal [123]	121281	-	-	0.235 ± 0.004	59
Anti-Optimal [123]	7967	-	-	0.008 ± 0.021	0.38

Table 8.2 Results of the head-tail measurements from the simplified DRIFT-IId readout.

It is clearly seen here that there is a large significance in the head-tail measurement from the optimal directions, both separately and combined, showing the sensitivity of this new readout mode to the head-tail signature. It is also seen that there is no significance in the anti-optimal directions as expected. The sign flip between +z and –z and the lack of significance in the anti-optimal directions helps to validate the optimal result by showing the significance is not from a systematic error in the calculation. This is the first time the head-tail signature has been shown in this simplified read out mode.

It is seen that the significance is reduced compared to [123]; this may be due to the lower efficiency of neutron detection in this work, with this work having only 23% the number of neutrons per run on average. A part of this number will be from the extra events located between 48 and 50 cm in the detector as these were not included in this run, with the energy calibration also a possible cause of this lower detection efficiency. A comparison between the efficiency of the simplified analysis and the full DRIFT analysis will be shown in Section 8.3.1 to see how large an effect this is. But even with the lower efficiency there is still a clear sign of head-tail using the simplified analysis which along with the results from Chapter 7 with the THGEM shows that it may be possible to construct a large detector with one-dimensional readout and directional sensitivity.

8.3 Calculation of a WIMP Limit

This section describes the calculation of a spin dependant WIMP limit from the DRIFT-IId detector. Two limits will be presented, one from the simplified readout scheme described above, and another from the normal DRIFT analysis for comparison. The data presented are from 106.1 days of background data from the DRIFT-IId detector operated in the Palmer Lab at Boulby. The detector was operated in a fully shielded mode with > 40 g/cm^2 of polypropylene pellets on all sides to shield from background neutron events. The background runs were separated by calibration runs using a ^{252}Cf neutron source placed on the top of the DRIFT-IId vessel. These runs were used to calibrate the efficiency of the detector throughout the background runs. The background and neutron datasets used are shown in Appendix A in Tables A.2 and A.3.

8.3.1 Efficiency Map

The first step towards producing a WIMP limit is to calculate the efficiency of the detector. This is done using neutron calibrations spread throughout the data taking period. To perform the calibrations the ^{252}Cf source is placed in a tube through the shielding to sit on top of the vacuum vessel. The data from the neutron exposure are processed through the analysis, with the data selection process described in Section 8.2. It was found that the ‘up veto’ and ‘down veto’ cuts described above helped to remove background events in the regular analysis, so this was also used in addition to the 8-wire hit cut with a cut at 1.9 mV on the up veto and 1.7 mV on the down veto.

The events that passed all of the selection cuts from the full DRIFT analysis are shown in Figure 8.3 with the fiducial volume shown in the black box between 11 - 48 cm and 700 - 6000 NIPs. The events passing the cuts from the simplified analysis are shown in Figure 8.4. It is seen that many more events pass the cuts in the full analysis compared to the simplified analysis, with event rates of 9447 neutrons per day in the fiducial volume from the full analysis compared to 1942 neutrons per day in the fiducial volume from the simplified analysis.

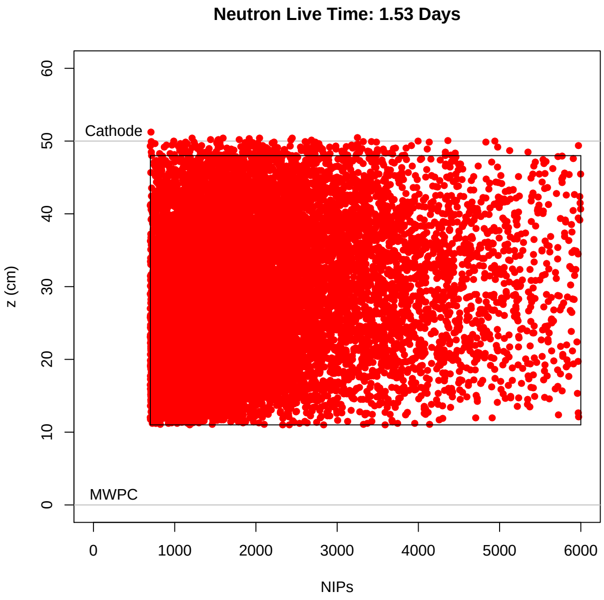

Fig. 8.3 The neutron events passing all the cuts from the full DRIFT analysis are shown in z vs. NIPs parameter space.

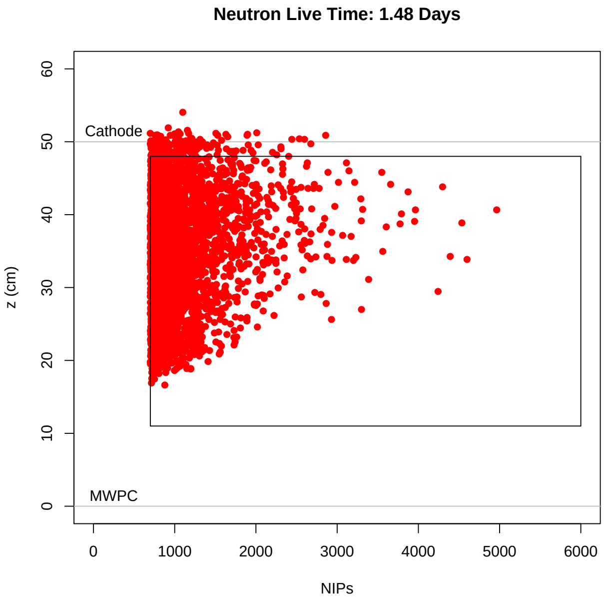

Fig. 8.4 The neutron events passing all the cuts from the simplified DRIFT analysis are shown in z vs. NIPs parameter space.

To get a better understanding of the differences between the results and to find the detector efficiencies in both cases, the results are compared to simulations from GEANT4 of the expected neutron events inside the detector. The simulations used were provided by Frederic Mouton and are the same simulations used in [127] and [198]. The simulation results are scaled to match the neutron exposure and the results from both experiment and simulation are plotted in z vs NIPs parameter space and split into bins to see how the efficiency changes with position of the event in the detector and energy deposition. In each bin the ratio of neutrons detected/neutrons expected is taken to give the efficiency. Figure 8.5 shows the efficiency map computed from this ratio for the full DRIFT analysis with Figure 8.6 showing the efficiency map for the simplified analysis. A comparison of how the efficiency changes with energy for both the simplified readout and the full DRIFT readout is shown in Figure 8.7. Here it is clearly seen again that the efficiency of the full analysis is much higher than the simplified analysis with an average overall efficiency of 27 ± 3% compared to 2.8 ± 0.1% from the simplified analysis. It should also be noted that the analysis used here is an older version of the DRIFT analysis code compared to that used in Ref [127] with a poorer energy calibration and lower efficiency, hence the difference in efficiency map compared to Figure 3.12b. This version has been used to allow for comparison with the simplified readout which has not yet been implemented in the latest version of the code.

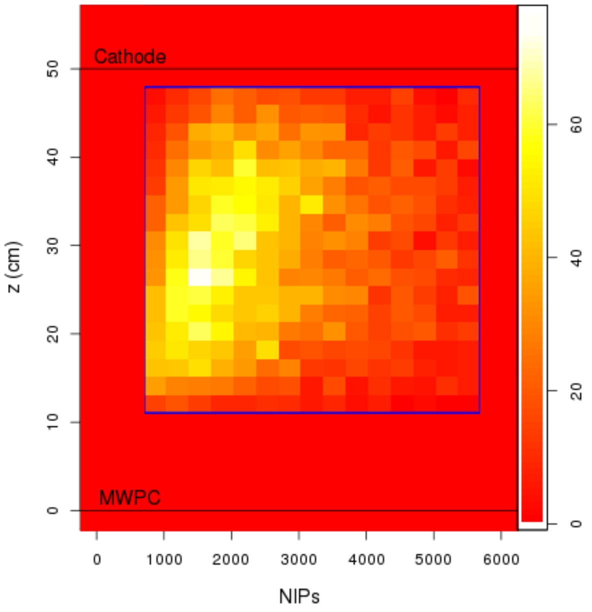

Fig. 8.5 A map of efficiency showing how the neutron detection efficiency changes for the full DRIFT analysis with varying position in the detector and deposited energy.

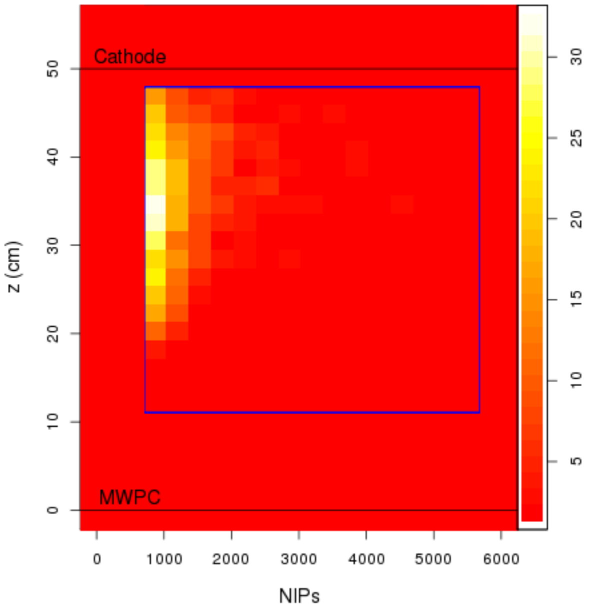

Fig. 8.6 A map of efficiency showing how the neutron detection efficiency changes for the simplified DRIFT analysis with varying position in the detector and deposited energy.

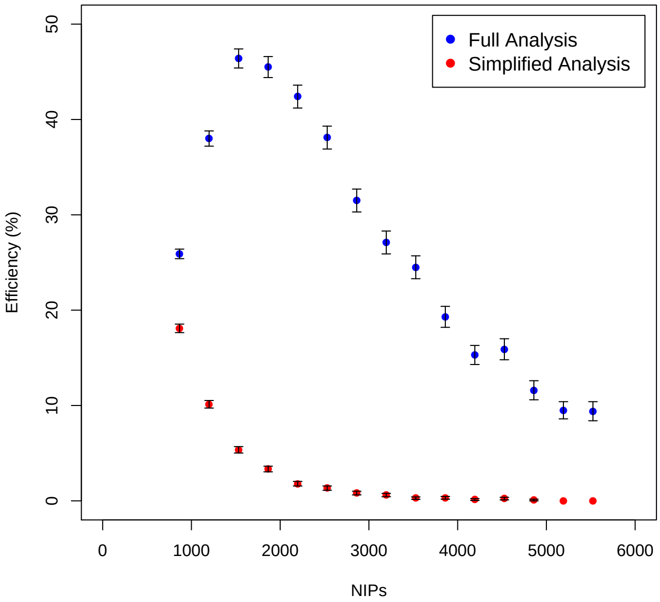

Fig. 8.7 A plot of efficiency against NIPs for both analyses, with the full analysis shown in blue and the simplified analysis shown in red.

One major difference between the analysis modes is the efficiencies at higher energies. In the simplified readout this efficiency drops to below 1% from around 3000 NIPs and comparing Figures 8.3 and 8.4 instantly shows many extra events in the higher energy region in the full analysis compared to the simplified mode. This is a further indication that the energy reconstruction is a big factor in the lower efficiency with events being reconstructed with a lower energy in the simplified analysis. Work is ongoing to understand the energy calibration and to improve the energy reconstruction. It is also seen that events at lower z positions are detected more efficiently in the full DRIFT analysis. This may be due to the minority peaks being lost in the noise at lower energies and the reconstruction algorithm not being able to fit them correctly. This may be improved in the future by implementing the new fitting algorithm that has been developed in the DRIFT collaboration and may allow a better efficiency when applied to the simplified readout.

8.3.2 Calculation of a WIMP Limit

After the efficiency is calculated the shielded WIMP run must be analysed. The plot of z vs NIPs for the normal DRIFT-IId readout from 106.1 days of shielded data is shown in Figure 8.8 with the same plot from the simplified readout shown in Figure 8.9.

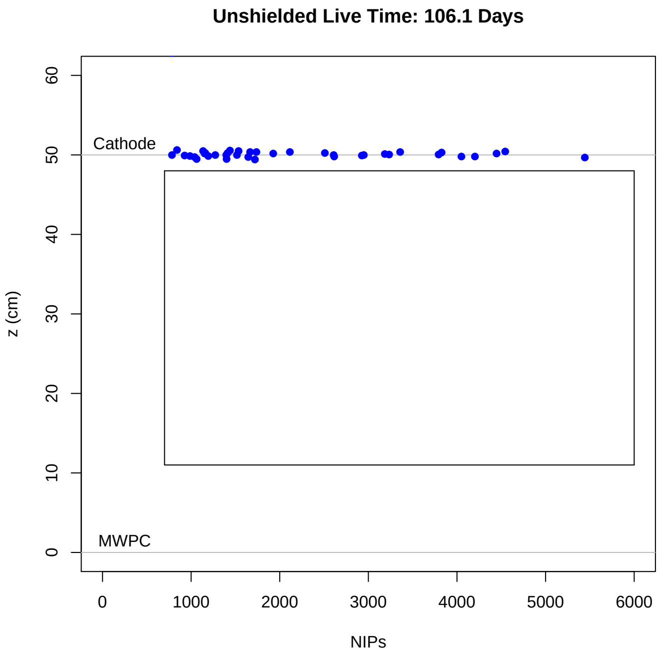

Fig. 8.8 A plot of z against NIPs showing that no events in the fiducial volume passed the cuts from the full DRIFT analysis. The fiducial volume is shown by the black box.

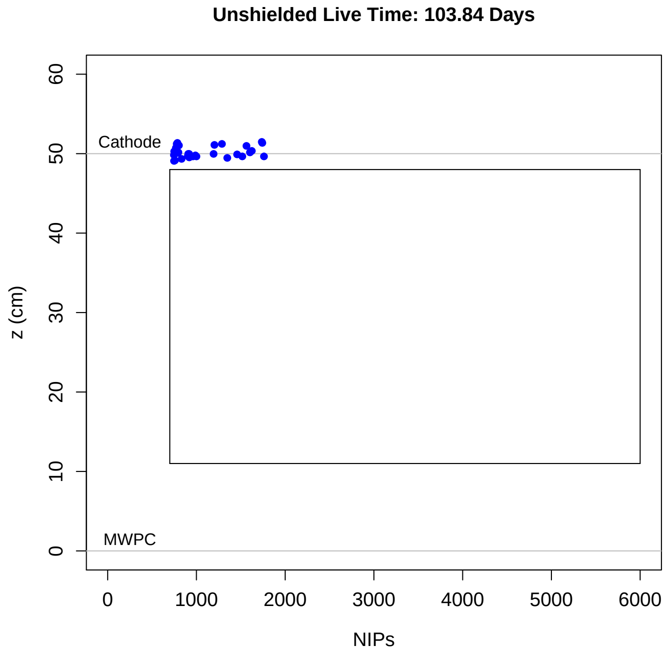

Fig. 8.9 A plot of z against NIPs showing no thatevents in the fiducial volume passed the cuts in the simplified DRIFT analysis. The fiducial volume is shown by the black box.

From these plots it can be seen that no events passed the cuts to appear in the fiducial region (shown in the black box) in the 106.1 live days of operation so a limit can be set on the WIMP-nucleon cross section from each analysis. This also shows that both analysis modes are able to operate background free for the 100 days. The limit is set by using the rate equation derived in Chapter 1:

$$R_{det} = \int_{E_{min}}^{E_{max}} \frac{10^9 N_A \rho_W M_N M_D F^2(qr_N)\varepsilon\sigma_{Wp}^{eff}}{M_W \mu_{Wp}^2 v_o \sqrt{\pi}} e^{-(\frac{v_{min}}{v_o})^2} dE_R, \tag{8.1}$$

where ρ_W = 0.3 GeV c^{-2} cm^{-3} and v_o = 0.000847 c [21]. Using this equation a limit on the cross section is set for WIMP masses from 10 to 10,000 GeV. For each mass an arbitrary cross section of 1 picobarn is used. The rate equation is then used to calculate an expected rate of WIMP events inside the detector for that mass and cross section, using the detection efficiencies calculated above and the detector target mass (34.2 g) and the live time. After the initial expected number of events is calculated the cross section is scaled until it corresponds to 2.3 events in the fiducial volume to represent a 90% confidence level. An exclusion limit can then be set in the cross section against WIMP mass parameter space. The limit is calculated for both the full DRIFT analysis and the simplified analysis; both limits are shown in Figure 8.10, with the full analysis in blue and the simplified analysis in red. From this plot the lowest excluded cross section was found to be 0.16 pb at 130 GeV/c^2 for the full analysis and 0.30 pb at 120 GeV/c^2 for the simplified analysis. The result from the full analysis is the lowest excluded limit from the DRIFT-IId detector to date, with the previous best being the 0.28 pb in Ref. [127]. The simplified analysis result is also lower than the result from Ref. [198] as expected from the longer run time. It should also be noted that these limits are expected to reduce further following the implementation of the latest DRIFT analysis mode.

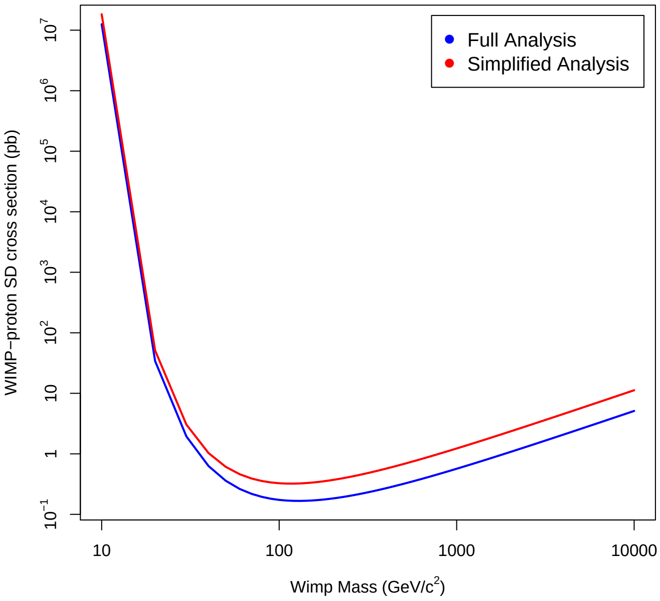

Fig. 8.10 The exclusion limits set on the spin dependant WIMP-proton cross section as a function of WIMP mass. Here both the full analysis (blue) and the simplified analysis (red) are shown.

These results show that it is possible to produce a WIMP limit using a detector with a one-dimensional readout with the result from the full analysis being less than a factor of two lower than the simplified analysis. Further work is ongoing on the energy calibration on the simplified analysis and is expected to reduce this difference further once it is completed. These results also show that the DRIFT-IId detector is capable of running in a background-free mode for over 100 days in both the full and simplified readout modes. The lack of background events in the fiducial volume is one important factor that allows DRIFT to set the lowest limits on the cross section of any directionally sensitive detector. The other directional limits are from the NEWAGE collaboration with a limit of 557 pb at 200 GeV/c^2 [134] and the DM-TPC collaboration with a limit of 2000 pb at 115 GeV/c^2 [130], both over 3 orders of magnitude larger than either limit shown here from DRIFT-IId.

8.4 Conclusions

This chapter has built upon the initial work in [198] where the simplified DRIFT readout using only the sum line was shown. This simplified mode simulates DRIFT as a one dimensional detector. This work has shown for the first time that the simplified readout is sensitive to the head-tail signature from neutron recoils showing that the technique may be a viable option for future directional dark matter detectors such as those proposed by the CYGNUS collaboration.

It has also been shown that it is possible for the DRIFT detector to operate background free for over 100 live-days with a spin-dependent limit set from both the simplified and the full DRIFT readout modes. The lowest excluded cross sections were 0.16 pb at 130 GeV/c^2 for the full analysis and 0.30 pb at 120 GeV/c^2 for the simplified analysis with the result from the full analysis being the lowest limit set by DRIFT-IId or any directional detector. The simplified readout has shown a lower efficiency compared to the full readout but this difference is expected to reduce after the future work on correction the energy calibration is completed.

Chapter 9

Conclusions

It has been shown in Chapter 1 that there is a wide array of evidence pointing towards some unknown component of matter, known as dark matter, making up the majority ($\sim$85%) of the matter in the universe. Several candidates have been discussed with the focus on the WIMP, one of the leading candidates. The current experimental efforts were discussed with the best direct detection limits at the time of writing coming from dual-phase xenon detectors.

Chapter 2 describes the efforts among some direct detection experiments to use the Galactic signals from the movement of the solar system to identify the dark matter. The current status of annual modulation experiments has been discussed with the current detection from the DAMA/LIBRA experiment and a discussion about other collaborations looking to test this result and tests for purer crystals for future experiments. Searches for directional detection of dark matter have been discussed as well as the ability for future large-scale directional detectors, as planned by the CYGNUS collaboration, to probe below the neutrino floor.

The current detector from the DRIFT collaboration, DRIFT-IId, was described in Chapter 3 along with a review of the latest results from the DRIFT collaboration such as the ability to run background-free and new tests of the directional sensitivity of the detector in a new operational mode. Recent modifications to the DRIFT-IId detector to allow for gas flow with the new oxygen component have been discussed in Chapter 4. It has also been shown that the current water-based CS_2 trap is not suitable for recirculating the gas and a cold-trap has been discussed as a replacement.

The reduction of radon backgrounds is a large part of all low background experiments, especially for dark matter searches, and the improvements to a radon emanation chamber have been shown in Chapter 5. A reduction in the background of a factor of 5.6 for the large test chamber and factor 7 for the small chamber has been shown along with an improvement in sensitivity of a factor $\sim$3. The modified system has been used to test proposed component for future low background experiments such as CYGNUS. Also shown is the work from a collaboration with Durridge UK on reducing the background of the Durridge RAD7 detector. The main contributors to the background have been identified and lower background alternatives are currently being sought.

A newly constructed THGEM-based TPC has been shown in Chapter 6 and the results from this have shown the potential of the setup in low pressure CF_4 gas for directional dark matter detection. High gains have been shown with the charge readout with gains of over 90,000 achieved. The stability and operation across varying pressures and electric fields across the THGEM has allowed a direct measurement of the Rose-Korff coefficients of CF_4; this is the first known measurement of these coefficients using a THGEM-based detector. A CCD-based optical readout has been shown with initial results showing the potential of this readout to obtain 2D track information. Clear nuclear-recoil track images have been recorded and an energy calibration has been performed showing recoils detected down to 6.4 $\pm$ 0.5 keV_R. From the images the directional information can be clearly seen and analysis of this information is the topic of further study.

The use of electronegative gases is important for limiting diffusion in large-scale detectors. A back-to-back THGEM TPC has been shown in Chapter 7 with high gains up to 8,600 $\pm$ 150 shown in low pressure SF_6. These results are the highest known achieved gains in SF_6 and the resolution of 19% is also the best seen to date. The directional sensitivity of the system using only a one-dimensional readout has been tested with the results showing signs of the head-tail signature. Further tests have been suggested to provide more conclusive results. Also shown were the first tests of a large-area THGEM looking towards a scaled up THGEM-based TPC. Initial results show low gains but it is expected that modifications to the THGEM design should allow higher gains to be achieved.

Analysis of data from the DRIFT-IId detector is shown in Chapter 8 with the directional sensitivity of a simplified, one-dimensional DRIFT-IId readout shown. Results indicate that the head-tail effect is still visible in this simplified mode with a combined significance of 18.5 seen from the optimal directions with the expected null result seen from the anti-optimal directions. This is the first measurement of head-tail in this simplified readout mode. Reasons for the lower head-tail sensitivity compared to the full DRIFT readout have been discussed with the energy calibration on the sum line being a possible cause of discrepancy.

A spin-dependant WIMP limit has been calculated from over 100 days of shielded DRIFT-IId data using both the full DRIFT analysis and the simplified analysis. The results show that it is possible for the DRIFT-IId detector to run background free for over 100 days and from the results the lowest excluded cross sections are calculated to be 0.16 pb at 130 GeV/c^2 for the full analysis and 0.30 pb at 120 GeV/c^2 for the simplified analysis. The exclusion limit from the full analysis is the lowest limit seen from the DRIFT-IId detector and both limits are over 3 orders of magnitude lower than any other directional detector. It has been seen that the simplified analysis produces an exclusion limit within a factor of 2 of the full analysis showing the viability of the technique for WIMP searches. This difference should reduce when the work on the efficiency of the simplified analysis mode is completed.

References

[1] F. Zwicky. Die Rotverschiebung von extragalaktischen Nebeln. *Helvetica Physica Acta*, 6:110–127, 1933.

[2] F. Zwicky. Republication of: The redshift of extragalactic nebulae. *General Relativity and Gravitation*, 41(1):207–224, 2009.

[3] F. Zwicky. On the Masses of Nebulae and of Clusters of Nebulae. *The Astrophysical Journal*, 86:217, 1937.

[4] Simon D. M. White, et al. The baryon content of galaxy clusters: a challenge to cosmological orthodoxy. *Nature*, 366(6454):429–433, 1993.

[5] Jürgen Ehlers. Editorial note to: F. Zwicky The redshift of extragalactic nebulae. *General Relativity and Gravitation*, 41(1):203–206, 2009.

[6] P. A. R. Ade, et al. Planck 2015 results. *Astronomy & Astrophysics*, 594:A13, 2016.

[7] Vera C. Rubin and Jr. Ford, W. Kent. Rotation of the Andromeda Nebula from a Spectroscopic Survey of Emission Regions. *The Astrophysical Journal*, 159:379, 1970.

[8] Jeffrey Bennett, et al. *The Essential Cosmic Perspective, Sixth Edition*. Pearson, 2014.

[9] Douglas Clowe, Anthony Gonzalez, and Maxim Markevitch. Weak-Lensing Mass Reconstruction of the Interacting Cluster 1E 0657-558: Direct Evidence for the Existence of Dark Matter. *The Astrophysical Journal*, 604(2):596–603, 2004.

[10] Maxim Markevitch, et al. Direct Constraints on the Dark Matter Self-Interaction Cross Section from the Merging Galaxy Cluster 1E 0657-56. *The Astrophysical Journal*, 606(2):819–824, 2004.

[11] Douglas Clowe, et al. A Direct Empirical Proof of the Existence of Dark Matter. *The Astrophysical Journal*, 648(2):L109–L113, 2006.

[12] B. Ragozzine, et al. Weak-Lensing Results for the Merging Cluster A1758. *The Astrophysical Journal*, 744(2):94, 2012.

[13] Lindsay J. King, et al. The distribution of dark and luminous matter in the unique galaxy cluster merger Abell 2146. *Monthly Notices of the Royal Astronomical Society*, 459(1):517–527, 2016.

[14] A. Mahdavi, et al. A Dark Core in Abell 520. *Astrophysical Journal*, 668(806):806–814, 2007.

[15] J. Merten, et al. Creation of cosmic structure in the complex galaxy cluster merger Abell 2744. *Monthly Notices of the Royal Astronomical Society*, 417(1):333–347, 2011.

[16] A. A. Penzias and R. W. Wilson. A Measurement of Excess Antenna Temperature at 4080 Mc/s. *The Astrophysical Journal*, 142:419, 1965.

[17] R. H. Dicke, et al. Cosmic Black-Body Radiation. *The Astrophysical Journal*, 142:414, 1965.

[18] George R. Blumenthal, et al. Formation of galaxies and large-scale structure with cold dark matter. *Nature*, 311(5986):517–525, 1984.

[19] Joshua A. Frieman, Michael S. Turner, and Dragan Huterer. Dark Energy and the Accelerating Universe. *Annual Review of Astronomy and Astrophysics*, 46(1):385–432, 2008.

[20] George F. Smoot. COBE Observations of the Early Universe. *Journal of the Royal Astronomical Society of Canada*, 88:114, 1994.

[21] C Patrignani et. al. Review of Particle Physics. *Chinese Physics C*, 40(10):100001, 2016.

[22] Brian D. Fields. The Primordial Lithium Problem. *Annual Review of Nuclear and Particle Science*, 61(1):47–68, 2011.

[23] C.S. Frenk and S.D.M. White. Dark matter and cosmic structure. *Annalen der Physik*, 524(9-10):507–534, 2012.

[24] J. Richard Gott III, et al. A Map of the Universe. *The Astrophysical Journal*, 624(2):463–484, 2005.

[25] M. J. Geller and J. P. Huchra. Mapping the Universe. *Science*, 246(4932):897–903, 1989.

[26] Matthew Colless, et al. The 2dF Galaxy Redshift Survey: spectra and redshifts. *Monthly Notices of the Royal Astronomical Society*, 328(4):1039–1063, 2001.

[27] Marco Taoso, Gianfranco Bertone, and Antonio Masiero. Dark matter candidates: a ten-point test. *Journal of Cosmology and Astroparticle Physics*, 2008(03):022, 2008.

[28] Stephen P. Martin. A Supersymmetry Primer. In *Perspectives on Supersymmetry*, pages 1–98, 1998.

[29] Thomas Appelquist, Hsin-Chia Cheng, and Bogdan A. Dobrescu. Bounds on universal extra dimensions. *Physical Review D*, 64(3):035002, 2001.

[30] ATLAS Collaboration. ATLAS Run 1 searches for direct pair production of third-generation squarks at the Large Hadron Collider. (June), 2015.

[31] T Kaluza. Zum Unitatsproblem in der Physik. *Sitzungsber. Preuss. Akad. Wiss. Berlin (Math. Phys.)*, page 966, 1921.

[32] Oskar Klein. Quantentheorie und funfdimensionale Relativitatstheorie. *Zeitschrift fur Physik*, 37(12):895–906, 1926.

[33] Oskar Klein. The Atomicity of Electricity as a Quantum Theory Law. *Nature*, 118(2971):516–516, 1926.

[34] Yoshiharu Kawamura. Gauge hierarchy problem, supersymmetry, and fermionic symmetry. *International Journal of Modern Physics A*, 30(25):1550153, 2015.

[35] Debajyoti Choudhury and Kirtiman Ghosh. Bounds on universal extra dimension from LHC run I and II data. *Physics Letters B*, 763:155–160, 2016.

[36] R. D. Peccei and Helen R. Quinn. CP Conservation in the Presence of Pseudoparticles. *Physical Review Letters*, 38(25):1440–1443, 1977.

[37] Jihn E. Kim. Weak-Interaction Singlet and Strong CP Invariance. *Physical Review Letters*, 43(2):103–107, 1979.

[38] M.A. Shifman, A.I. Vainshtein, and V.I. Zakharov. Can confinement ensure natural CP invariance of strong interactions? *Nuclear Physics B*, 166(3):493–506, 1980.

[39] Michael Dine, Willy Fischler, and Mark Srednicki. A simple solution to the strong CP problem with a harmless axion. *Physics Letters B*, 104(3):199–202, 1981.

[40] A.R. Zhitnitskij. On possible suppression of the axion-hadron interactions. *Yadernaya Fizika*, 31(2):497–504, 1980.

[41] Ed Daw. Overview of axions, axion-like particles. In *DMUK Meeting - UCL, London*, 2017.

[42] Q. R. Ahmad, et al. Measurement of the Rate of ve + d -> p + p + e- Interactions Produced by 8B Solar Neutrinos at the Sudbury Neutrino Observatory. *Physical Review Letters*, 87(7):071301, 2001.

[43] R. Adhikari, et al. A White Paper on keV sterile neutrino Dark Matter. *Journal of Cosmology and Astroparticle Physics*, 2017(01):025–025, 2017.

[44] Takehiko Asaka and Mikhail Shaposhnikov. The νMSM, dark matter and baryon asymmetry of the universe. *Physics Letters B*, 620(1-2):17–26, 2005.

[45] Ed Daw. A Review of the theory of WIMP scattering off target nuclei. *Priv. Commun.*, 2012.

[46] J.D. Lewin and P.F. Smith. Review of mathematics, numerical factors, and corrections for dark matter experiments based on elastic nuclear recoil. *Astroparticle Physics*, 6(1):87–112, 1996.

[47] D.R. Tovey, et al. A new model-independent method for extracting spin-dependent cross section limits from dark matter searches. *Physics Letters B*, 488(1):17–26, 2000.

[48] The LZ Collaboration, et al. LUX-ZEPLIN (LZ) Conceptual Design Report. Technical Report March, 2015.

[49] G.J. Alner, et al. First limits on nuclear recoil events from the ZEPLIN I galactic dark matter detector. *Astroparticle Physics*, 23(5):444–462, 2005.

[50] G.J. Alner, et al. First limits on WIMP nuclear recoil signals in ZEPLIN-II: A two-phase xenon detector for dark matter detection. *Astroparticle Physics*, 28(3):287–302, 2007.

[51] D.Yu. Akimov, et al. WIMP-nucleon cross-section results from the second science run of ZEPLIN-III. *Physics Letters B*, 709(1-2):14–20, 2012.

[52] D. S. Akerib, et al. Results from a Search for Dark Matter in the Complete LUX Exposure. *Physical Review Letters*, 118(2):021303, 2017.

[53] B. J. Mount, et al. LUX-ZEPLIN (LZ) Technical Design Report, 2017.

[54] E. Aprile, et al. Physics reach of the XENON1T dark matter experiment. *Journal of Cosmology and Astroparticle Physics*, 2016(04):027–027, 2016.

[55] E. Aprile, et al. Design and performance of the XENON10 dark matter experiment. *Astroparticle Physics*, 34(9):679–698, 2011.

[56] E. Aprile, et al. XENON100 dark matter results from a combination of 477 live days. *Physical Review D*, 94(12):122001, 2016.

[57] Andi Tan, et al. Dark Matter Results from First 98.7 Days of Data from the PandaX-II Experiment. *Physical Review Letters*, 117(12):121303, 2016.

[58] P. Agnes, et al. Results from the first use of low radioactivity argon in a dark matter search. *Physical Review D*, 93(8):081101, 2016.

[59] B. (DEAP Collaboration) Cai. The DEAP-3600 Dark Matter Experiment. In *American Physical Society Division of Particles and Fields Meeting, 4-8 August 2015, Ann Arbor, USA*, 2015.

[60] R. Agnese, et al. Projected Sensitivity of the SuperCDMS SNOLAB experiment. *Submitted to: Physical Review D*, 2016.

[61] R. Agnese, et al. New Results from the Search for Low-Mass Weakly Interacting Massive Particles with the CDMS Low Ionization Threshold Experiment. *Physical Review Letters*, 116(7):071301, 2016.

[62] P.N. Luke, et al. Calorimetric ionization detector. *Nuclear Instruments and Methods in Physics Research Section A: Accelerators, Spectrometers, Detectors and Associated Equipment*, 289(3):406–409, 1990.

[63] B. Neganov and V. Trofimov. USSR patent No 1037771. *Otkrytia i izobreteniya*, 146:215, 1985.

[64] R Calkins. The SuperCDMS Soudan high threshold WIMP search and the planned SuperCDMS SNOLAB experiment. *Journal of Physics: Conference Series*, 718:042009, 2016.

[65] J Schieck, et al. Direct Dark Matter Search with the CRESST II Experiment. In *ICHEP 2016, Chicago*, 2016.

[66] L. Hehn, et al. Improved EDELWEISS-III sensitivity for low-mass WIMPs using a profile likelihood approach. *The European Physical Journal C*, 76(10):548, 2016.

[67] A. Aguilar-Arevalo, et al. Search for low-mass WIMPs in a 0.6 kg day exposure of the DAMIC experiment at SNOLAB. *Physical Review D*, 94(8):082006, 2016.

[68] E. Behnke, et al. Final results of the PICASSO dark matter search experiment. *Astroparticle Physics*, 90:85–92, 2017.

[69] E. Behnke, et al. Direct measurement of the bubble-nucleation energy threshold in a CF3I bubble chamber. *Physical Review D*, 88(2):021101, 2013.

[70] C. Amole, et al. Improved dark matter search results from PICO-2L Run 2. *Physical Review D*, 93(6):061101, 2016.

[71] C. Amole, et al. Dark Matter Search Results from the PICO-60 C3F8 Bubble Chamber. *Preprint - arXiv:1702.07666*, 2017.

[72] Andrzej K. Drukier, Katherine Freese, and David N. Spergel. Detecting cold dark-matter candidates. *Physical Review D*, 33(12):3495–3508, 1986.

[73] Katherine Freese, Joshua Frieman, and Andrew Gould. Signal modulation in cold-dark-matter detection. *Physical Review D*, 37(12):3388–3405, 1988.

[74] M. L. Ahnen, et al. Limits to dark matter annihilation cross-section from a combined analysis of MAGIC and Fermi-LAT observations of dwarf satellite galaxies. *Journal of Cosmology and Astroparticle Physics*, 2016(02):039–039, 2016.

[75] A. Albert, et al. Searching for Dark Matter Annihilation in Recently Discovered Milky Way Satellites with Fermi-LAT. *The Astrophysical Journal*, 834(2):110, 2017.

[76] Nico Cappelluti, et al. Searching for the 3.5 keV Line in the Deep Fields with Chandra: the 10 Ms observations. *Preprint - arXiv:1701.07932*, 2017.

[77] J. Aleksić, et al. The major upgrade of the MAGIC telescopes, Part II: A performance study using observations of the Crab Nebula. *Astroparticle Physics*, 72:76–94, 2016.

[78] J. Aleksić, et al. The major upgrade of the MAGIC telescopes, Part I: The hardware improvements and the commissioning of the system. *Astroparticle Physics*, 72:61–75, 2016.

[79] Valentin Lefranc, Gary A. Mamon, and Paolo Panci. Prospects for annihilating Dark Matter towards Milky Way's dwarf galaxies by the Cherenkov Telescope Array. *Journal of Cosmology and Astroparticle Physics*, 2016(09):021–021, 2016.

[80] H. Abdalla, et al. H.E.S.S. Limits on Linelike Dark Matter Signatures in the 100 GeV to 2 TeV Energy Range Close to the Galactic Center. *Physical Review Letters*, 117(15):151302, 2016.

[81] Esra Bulbul, et al. Detection of an unidentified emission line in the stacked x-ray spectrum of galaxy clusters. *The Astrophysical Journal*, 789(1):13, 2014.

[82] F. A. Aharonian, et al. Hitomi Constraints on the 3.5 keV Line in the Perseus Galaxy Cluster. *The Astrophysical Journal*, 837(1):L15, 2017.

[83] Tansu Daylan, et al. The characterization of the gamma-ray signal from the central Milky Way: A case for annihilating dark matter. *Physics of the Dark Universe*, 12:1–23, 2016.

[84] Richard Bartels, Suraj Krishnamurthy, and Christoph Weniger. Strong Support for the Millisecond Pulsar Origin of the Galactic Center GeV Excess. *Physical Review Letters*, 116(5):051102, 2016.

[85] Samuel K. Lee, et al. Evidence for Unresolved Gamma-Ray Point Sources in the Inner Galaxy. *Physical Review Letters*, 116(5):051103, 2016.

[86] K. Choi, et al. Search for Neutrinos from Annihilation of Captured Low-Mass Dark Matter Particles in the Sun by Super-Kamiokande. *Physical Review Letters*, 114(14):141301, 2015.

[87] M. G. Aartsen, et al. Search for annihilating dark matter in the Sun with 3 years of IceCube data. *The European Physical Journal C*, 77(3):146, 2017.

[88] G. Aad, et al. The ATLAS Experiment at the CERN Large Hadron Collider. *JINST*, 3:S08003, 2008.

[89] S Chatrchyan, et al. The CMS experiment at the CERN LHC. *JINST*, 3:S08004, 2008.

[90] Felix Kahlhoefer. Review of LHC dark matter searches. *International Journal of Modern Physics A*, 32(13):1730006, 2017.

[91] F. Mayet, et al. A review of the discovery reach of directional Dark Matter detection. *Physics Reports*, 627:1–49, 2016.

[92] Katherine Freese, Mariangela Lisanti, and Christopher Savage. Colloquium : Annual modulation of dark matter. *Reviews of Modern Physics*, 85(4):1561–1581, 2013.

[93] R. Bernabei, et al. Dark Matter Particles in the Galactic Halo: Results and Implications from DAMA/NaI. *International Journal of Modern Physics D*, 13(10):2127–2159, 2004.

[94] R. Bernabei, et al. Final model independent result of DAMA/LIBRA–phase1. *The European Physical Journal C*, 73(12):2648, 2013.

[95] R. Bernabei, et al. First results from DAMA/LIBRA and the combined results with DAMA/NaI. *The European Physical Journal C*, 56(3):333–355, 2008.

[96] D. S. Akerib, et al. Results from a Search for Dark Matter in the Complete LUX Exposure. *Physical Review Letters*, 118(2):021303, 2017.

[97] R. Bernabei, et al. No role for neutrons, muons and solar neutrinos in the DAMA annual modulation results. *The European Physical Journal C*, 74(12):3196, 2014.

[98] J. Klinger and V. A. Kudryavtsev. Muon-Induced Neutrons Do Not Explain the DAMA Data. *Physical Review Letters*, 114(15):151301, 2015.

[99] Paolo Gondolo and Graciela Gelmini. Compatibility of DAMA dark matter detection with other searches. *Physical Review D*, 71(12):123520, 2005.

[100] C Savage, et al. Compatibility of DAMA/LIBRA dark matter detection with other searches. *Journal of Cosmology and Astroparticle Physics*, 2009(04):010–010, 2009.

[101] J. Cherwinka, et al. A search for the dark matter annual modulation in South Pole ice. *Astroparticle Physics*, 35(11):749–754, 2012.

[102] J. Cherwinka, et al. First data from DM-Ice17. *Physical Review D*, 90(9):092005, 2014.

[103] J. Cherwinka, et al. Measurement of muon annual modulation and muon-induced phosphorescence in NaI(Tl) crystals with DM-Ice17. *Physical Review D*, 93(4):042001, 2016.

[104] G.J. Alner, et al. Limits on WIMP cross-sections from the NAIAD experiment at the Boulby Underground Laboratory. *Physics Letters B*, 616(1-2):17–24, 2005.

[105] E. Barbosa de Souza, et al. First search for a dark matter annual modulation signal with NaI(Tl) in the Southern Hemisphere by DM-Ice17. *Physical Review D*, 95(3):032006, 2017.

[106] H. S. Lee, et al. Search for low-mass dark matter with CsI(Tl) crystal detectors. *Physical Review D*, 90(5):052006, 2014.

[107] Reina Maruyama. COSINE-100. In *Lake Louise Winter Institute, Lake Louise, Canada, February 19-25, 2017*, 2017.

[108] J. Amaré, et al. The ANAIS Dark Matter Project: Status and Prospects. *Proceeding of the MG14 conference, July 2015, Rome*, 2016.

[109] María Luisa Sarsa. Status and Prospects of ANAIS-112 at the Canfranc Underground Laboratory. In *IDM2016, Sheffield, UK, 17-22 July 2016*, 2016.

[110] Emily Shields, Jingke Xu, and Frank Calaprice. SABRE: A New NaI(T1) Dark Matter Direct Detection Experiment. *Physics Procedia*, 61:169–178, 2015.

[111] Francis Froborg. The SABRE Dark Matter Search Experiment. In *DMUK Meeting - UCL, London*, 2017.

[112] Mark Hull. Shanghai Institute of Ceramics. *Powder Metallurgy*, 49(3):203–205, 2006.

[113] Walter C. Pettus. DM-Ice: Current Status and Future Prospects. In *12th Conference on the Intersections of Particle and Nuclear Physics, Vail, CO, USA, May 18 – 24, 2015*, 2015.

[114] P. Adhikari, et al. Understanding internal backgrounds in NaI(Tl) crystals toward a 200 kg array for the KIMS-NaI experiment. *The European Physical Journal C*, 76(4):185, 2016.

[115] M. Kauer. DM-Ice Private Communication. *Priv. Commun.*, 2016.

[116] J.B.R. Battat, et al. Readout technologies for directional WIMP Dark Matter detection. *Physics Reports*, 662:1–46, 2016.

[117] John N. Bahcall. Solar Neutrinos: A Popular Account. *Encyclopedia of Physics, 3rd edition, eds. G. Trigg and R. Lerner (Wiley-VCH, Weinheim 2005)*, 2004.

[118] L Borodikhina. Perspectives of DSNB neutrino researches in modern detectors. *Journal of Physics: Conference Series*, 675(1):012005, 2016.

[119] P. Cushman, et al. Snowmass CF1 Summary: WIMP Dark Matter Direct Detection. *Snowmass CF1 Final Summary Report*, 2013.

[120] N.J.C. Spooner, et al. Simulations of the nuclear recoil head–tail signature in gases relevant to directional dark matter searches. *Astroparticle Physics*, 34(5):284–292, 2010.

[121] Ben Morgan, Anne M. Green, and Neil J. C. Spooner. Directional statistics for realistic weakly interacting massive particle direct detection experiments. *Physical Review D*, 71(10):103507, 2005.

[122] S. Burgos, et al. First measurement of the head-tail directional nuclear recoil signature at energies relevant to WIMP dark matter searches. *Astroparticle Physics*, 31(4):261–266, 2009.

[123] J.B.R. Battat, et al. First measurement of nuclear recoil head-tail sense in a fiducialised WIMP dark matter detector. *Journal of Instrumentation*, 11(10):P10019–P10019, 2016.

[124] A. Alexandrov, et al. Intrinsic neutron background of nuclear emulsions for directional Dark Matter searches. *Astroparticle Physics*, 80:16–21, 2016.

[125] L.M. Capparelli, et al. Directional dark matter searches with carbon nanotubes. *Physics of the Dark Universe*, 9-10:24–30, 2015.

[126] Ben Morgan. DRIFT: A directionally sensitive dark matter detector. *Nuclear Instruments and Methods in Physics Research, Section A: Accelerators, Spectrometers, Detectors and Associated Equipment*, 513(1-2 SPEC. ISS.):226–230, 2003.

[127] J.B.R. Battat, et al. Low threshold results and limits from the DRIFT directional dark matter detector. *Astroparticle Physics*, 91:65–74, 2017.

[128] Tohru Ohnuki, Daniel P. Snowden-Ifft, and C.Jeff Martoff. Measurement of carbon disulfide anion diffusion in a TPC. *Nuclear Instruments and Methods in Physics Research Section A: Accelerators, Spectrometers, Detectors and Associated Equipment*, 463(1-2):142–148, 2001.

[129] Gabriella Sciolla and the DMTPC Collaboration. The DMTPC project. *Journal of Physics: Conference Series*, 179:012009, 2009.

[130] S. Ahlen, et al. First dark matter search results from a surface run of the 10-L DMTPC directional dark matter detector. *Physics Letters B*, 695(1-4):124–129, 2011.

[131] Cosmin Deaconu, et al. Measurement of the directional sensitivity of DMTPC detectors. *Accepted for publication in Phys. Rev. D.*, 2017.

[132] Michael Leyton. Directional dark matter detection with the DMTPC m 3 experiment. *Journal of Physics: Conference Series*, 718:042035, 2016.

[133] K. Miuchi, et al. Direction-sensitive Dark Matter Search –NEWAGE–. *EAS Publications Series*, 36:243–248, 2009.

[134] Kiseki Nakamura, et al. Direction-sensitive dark matter search with gaseous tracking detector NEWAGE-0.3b'. *Progress of Theoretical and Experimental Physics*, 2015(4):43F01–0, 2015.

[135] F J Iguaz, et al. Micromegas detector developments for Dark Matter directional detection with MIMAC. *Journal of Instrumentation*, 6(07):P07002–P07002, 2011.

[136] D Santos, et al. MIMAC : A micro-tpc matrix for dark matter directional detection. *Journal of Physics: Conference Series*, 460:012007, 2013.

[137] D. Santos. MIMAC (MIcro-tpc MAtrix of Chambers). In *IDM2016, Sheffield, UK, 17-22 July 2016*, 2016.

[138] S.E. Vahsen, et al. The Directional Dark Matter Detector (D 3). *EAS Publications Series*, 53:43–50, 2012.

[139] S.E. Vahsen, et al. 3-D tracking in a miniature time projection chamber. *Nuclear Instruments and Methods in Physics Research Section A: Accelerators, Spectrometers, Detectors and Associated Equipment*, 788:95–105, 2015.

[140] Elisabetta Baracchini. NITEC: a Negative Ion Time Expansion Chamber for directional Dark Matter searches. In *IDM2016, Sheffield, UK, 17-22 July 2016*, 2016.

[141] Kentaro Miuchi. NEWAGE. In *IDM2016, Sheffield, UK, 17-22 July 2016*, 2016.

[142] C. Deaconu. *A model of the directional sensitivity of low-pressure CF4 dark matter detectors*. PhD thesis, MIT, 2015.

[143] J. Brack, et al. Long-term study of backgrounds in the DRIFT-II directional dark matter experiment. *Jinst*, 9(07):P07021–P07021, 2014.

[144] J.B.R. Battat, et al. Radon in the DRIFT-II directional dark matter TPC: emanation, detection and mitigation. *Jinst*, 9(11):P11004–P11004, 2014.

[145] J. B R Battat, et al. First background-free limit from a directional dark matter experiment: Results from a fully fiducialised DRIFT detector. *Physics of the Dark Universe*, 9-10:1–7, 2015.

[146] J. B R Battat, et al. Reducing DRIFT backgrounds with a submicron aluminized-mylar cathode. *Nuclear Instruments and Methods in Physics Research, Section A: Accelerators, Spectrometers, Detectors and Associated Equipment*, 794:33–46, 2015.

[147] D. Muna. The DRIFT-II Directional Dark Matter Detector. *Nuclear Physics B - Proceedings Supplements*, 173:172–175, 2007.

[148] Daniel Snowden-Ifft. Discovery of multiple, ionization-created anions in gas mixtures containing CS2 and O2. *Review of Scientific Instruments*, 85(1):013303, 2014.

[149] S Burgos, et al. Track reconstruction and performance of DRIFT directional dark matter detectors using alpha particles. *Nuclear Instruments and Methods in Physics Research Section A: Accelerators, Spectrometers, Detectors and Associated Equipment*, 584(1):114–128, 2008.

[150] M. Robinson, et al. Measurements of muon flux at 1070 m vertical depth in the Boulby underground laboratory. *Nuclear Instruments and Methods in Physics Research, Section A: Accelerators, Spectrometers, Detectors and Associated Equipment*, 511(3):347–353, 2003.

[151] V E Guiseppe, et al. A radon progeny deposition model. In *AIP Conference Proceedings*, volume 1338, pages 95–100, 2011.

[152] Felix Bloch and Norris E. Bradbury. On the Mechanism of Unimolecular Electron Capture. *Physical Review*, 48(8):689–695, 1935.

[153] Horishi Shimamori and Yoshihiko Hatano. Thermal electron attachment to O2 in the presence of various compounds as studied by a microwave cavity technique combined with pulse radiolysis. *Chemical Physics*, 21(2):187–201, 1977.

[154] N L Aleksandrov. Three-body electron attachment to a molecule. *Soviet Physics Uspekhi*, 31(2):101–118, 1988.

[155] J. Allison, et al. Recent developments in G eant 4. *Nuclear Instruments and Methods in Physics Research Section A: Accelerators, Spectrometers, Detectors and Associated Equipment*, 835:186–225, 2016.

[156] E. Tziaferi, et al. First measurement of low intensity fast neutron background from rock at the Boulby Underground Laboratory. *Astroparticle Physics*, 27(5):326–338, 2007.

[157] P. F. Smith, et al. Simulation studies of neutron shielding, calibration and veto systems for gaseous dark matter detectors. *Astroparticle Physics*, 22(5-6):409–420, 2005.

[158] Sigma-Aldrich. Carbon Disulfide Safety Data Sheet V5.2, 2017.

[159] Mark Pipe. *Limits on spin-dependent WIMP-proton cross-sections using the DRIFT-IId directional dark matter detector*. PhD thesis, University of Sheffield, 2011.

[160] MKS-Instruments. Type 1479A Metal-Sealed Mass-Flo® Controller, 2006.

[161] Wilfred J. Maginnis Jr., Thomas O., Baxter Jr. Thermal mass flow sensor with improved sensitivity and response time, 2003.

[162] George Wm. Thomson. The Antoine Equation for Vapor-pressure Data. *Chemical Reviews*, 38(1):1–39, 1946.

[163] P.J. Linstrom and W.G. Mallard, editor. *NIST Chemistry WebBook, NIST Standard Reference Database Number 69*. National Institute of Standards and Technology, Gaithersburg MD, 20899, 2017.

[164] Guy Waddington, et al. Carbon Disulfide as a Reference Substance for Vapor-Flow Calorimetry; the Chemical Thermodynamic Properties. *The Journal of Physical Chemistry*, 66(6):1074–1077, 1962.

[165] Korean Data Bank. CHERIC, https://www.cheric.org/research/kdb/, 2017.

[166] Stephen W Sadler. *Towards the DRIFT-III Directional Dark Matter Experiment*. PhD thesis, University of Sheffield, 2014.

[167] A. Bradley, et al. Radon-related Backgrounds in the LUX Dark Matter Search. *Physics Procedia*, 61:658–665, 2015.

[168] P. A. Amaudruz, et al. Radon backgrounds in the DEAP-1 liquid-argon-based Dark Matter detector. *Astroparticle Physics*, 62:178–194, 2015.

[169] Xin Ran Liu. UK low-background infrastructure for delivering SuperNEMO. pages 1–5, 2015.

[170] James Mott. *Search for double beta decay of 82 Se with the NEMO-3 detector and development of apparatus for low-level radon measurements for the SuperNEMO experiment*. PhD thesis, UCL, 2013.

[171] G. Keller, B. Hoffmann, and T. Feigenspan. Radon permeability and radon exhalation of building materials. *Science of the Total Environment*, 272(1-3):85–89, 2001.

[172] H. Schrader. Half-life measurements with ionization chambers - A study of systematic effects and results. *Applied Radiation and Isotopes*, 60(2-4):317–323, 2004.

[173] Durridge Company Inc. Durridge RAD7 Radon Detector, http://www.durridge.co.uk/products_rad7.shtml, 2017.

[174] Canberra. Canberra PIPS Detector, http://www.canberra.com/products/detectors/pips-detectors.asp, 2017.

[175] E. Rutherford. Absorption of the Radio-active Emanations by Charcoal. *Nature*, 74(1930):634–634, 1906.

[176] N. Karunakara, et al. Evaluation of radon adsorption characteristics of a coconut shell-based activated charcoal system for radon and thoron removal applications. *Journal of Environmental Radioactivity*, 142:87–95, 2015.

[177] Gary J. Feldman and Robert D. Cousins. Unified approach to the classical statistical analysis of small signals. *Physical Review D*, 57(7):3873–3889, 1998.

[178] PAR-Group. PAR Group, http://www.par-group.co.uk/, 2017.

[179] R. Chechik, et al. Thick GEM-like hole multipliers: Properties and possible applications. *Nuclear Instruments and Methods in Physics Research, Section A: Accelerators, Spectrometers, Detectors and Associated Equipment*, 535(1-2):303–308, 2004.

[180] R. Chechik, et al. Thick GEM-like (THGEM) detectors and their possible applications. In *Proceedings, International Symposium on Detector Development for Particle, Astroparticle and Synchrotron Radiation Experiments (SNIC 2006): Menlo Park, California, April 3-6, 2006*, volume C0604032, page 0025, 2006.

[181] C. K. Shalem, et al. Advances in thick GEM-like gaseous electron multipliers Part II: Low-pressure operation. *Nuclear Instruments and Methods in Physics Research, Section A: Accelerators, Spectrometers, Detectors and Associated Equipment*, 558(2):468–474, 2006.

[182] C. Shalem, et al. Advances in Thick GEM-like gaseous electron multipliers—Part I: atmospheric pressure operation. *Nuclear Instruments and Methods in Physics Research Section A: Accelerators, Spectrometers, Detectors and Associated Equipment*, 558(2):475–489, 2006.

[183] A. Breskin, et al. A concise review on THGEM detectors. *Nuclear Instruments and Methods in Physics Research, Section A: Accelerators, Spectrometers, Detectors and Associated Equipment*, 598(1):107–111, 2009.

[184] F. Sauli. GEM: A new concept for electron amplification in gas detectors. *Nuclear Instruments and Methods in Physics Research, Section A: Accelerators, Spectrometers, Detectors and Associated Equipment*, 386(2-3):531–534, 1997.

[185] Fabio Sauli. Progress with the gas electron multiplier. *Nuclear Instruments and Methods in Physics Research, Section A: Accelerators, Spectrometers, Detectors and Associated Equipment*, 522(1-2):93–98, 2004.

[186] CERN Gas Detectors Development Group. CERN Gas Detectors Development Group.

[187] G. F. Reinking, L. G. Christophorou, and S. R. Hunter. Studies of total ionization in gases/mixtures of interest to pulsed power applications. *Journal of Applied Physics*, 60(2):499–508, 1986.

[188] Y. Giomataris. Development and prospects of the new gaseous detector "Micromegas". *Nuclear Instruments and Methods in Physics Research Section A: Accelerators, Spectrometers, Detectors and Associated Equipment*, 419(2-3):239–250, 1998.

[189] P.K. Lightfoot, et al. First operation of bulk micromegas in low pressure negative ion drift gas mixtures for dark matter searches. *Astroparticle Physics*, 27(6):490–499, 2007.

[190] A. Arefev, et al. A Measurement of the first Townsend coefficient in CF-4, CO-2, and CF-4/CO-2 mixtures at high, uniform electric field. *CERN-PPE-93-82*, 1993.

[191] A. Kaboth, et al. A measurement of photon production in electron avalanches in CF4. *Nuclear Instruments and Methods in Physics Research Section A: Accelerators, Spectrometers, Detectors and Associated Equipment*, 592(1-2):63–72, 2008.

[192] James F. Ziegler, M.D. Ziegler, and J.P. Biersack. SRIM – The stopping and range of ions in matter (2010). *Nuclear Instruments and Methods in Physics Research Section B: Beam Interactions with Materials and Atoms*, 268(11-12):1818–1823, 2010.

[193] Dinesh Loomba. R and D with Implications for a Directional Low Mass Dark Matter Search. In *CYGNUS 2013, 4th Workshop on Directional Detection of Dark Matter, 10 June - 12 June 2013, Toyama, Japan*, 2013.

[194] N.S. Phan, et al. The novel properties of SF 6 for directional dark matter experiments. *Journal of Instrumentation*, 12(02):P02012–P02012, 2017.

[195] I Lopes, H Hilmert, and W F Schmidt. Ionisation of gaseous and liquid sulphur hexafluoride by 60 Co γ-radiation. *Journal of Physics D: Applied Physics*, 19(6):L107–L110, 1986.

[196] J.B.R. Battat. Private Communication. 2017.

[197] Warren Lynch. Private Communication. 2017.

[198] Anthony C. Ezeribe. *Towards a massive directional dark matter detector: CYGNUS-TPC*. PhD thesis, University of Sheffield, 2017.

[199] Abraham. Savitzky and M. J. E. Golay. Smoothing and Differentiation of Data by Simplified Least Squares Procedures. *Analytical Chemistry*, 36(8):1627–1639, 1964.

Appendix A

DRIFT Data used for Analysis

The data used in Chapter 8 will be shown here. Table A.1 shows the data used for the head-tail analysis in Section 8.2.

Source Position	File Name
+z	drift2d-20141118-01
-z	drift2d-20141114-01
-x	drift2d-20151112-04
-y	drift2d-20151119-03

Table A.1 Datasets corresponding to the directed neutron runs.

Table A.2 shows the background data used in the WIMP limit calculation in Section 8.3 and the neutron calibration data files are shown in Table A.3.

Data Run	File Name
Background	drift2d-20141204-03
	drift2d-20141209-02
	drift2d-20141218-02
	drift2d-20141219-01
	drift2d-20141219-05
	drift2d-20150219-03
	drift2d-20150220-02
	drift2d-20150226-02
	drift2d-20150302-02
	drift2d-20150308-03
	drift2d-20150312-02
	drift2d-20150317-02
	drift2d-20150319-01
	drift2d-20150322-02
	drift2d-20150326-02
	drift2d-20150522-02
	drift2d-20150527-02
	drift2d-20150528-02
	drift2d-20150612-03
	drift2d-20150618-02
	drift2d-20150626-02
	drift2d-20150701-02
	drift2d-20150709-02
	drift2d-20150716-02
Live Time:	106.1 Days

Table A.2 Datasets corresponding to the shielded background runs.

Data Run	File Name
Neutron	drift2d-20141209-01
	drift2d-20141218-01
	drift2d-20150220-01
	drift2d-20150223-01
	drift2d-20150226-01
	drift2d-20150302-01
	drift2d-20150312-01
	drift2d-20150317-01
	drift2d-20150326-01
	drift2d-20150528-01
	drift2d-20150610-01
	drift2d-20150619-01
	drift2d-20150625-01
	drift2d-20150701-01
	drift2d-20150716-01
Live Time:	

Table A.3 Datasets corresponding to the neutron calibration runs.